Examining the Links Between Organic Photovoltaic Operation and Complex Morphological Structures

MATTHEW LEWIS JONES

Examining the Links Between Organic Photovoltaic Operation and Complex Morphological Structures

Matthew Lewis Jones

A Thesis presented for the degree of

Doctor of Philosophy

School of Engineering and Computing Sciences

University of Durham

England

October 2015

Dedicated to

My beloved Dangat - the reason I became a scientist

Examining the Links Between Organic Photovoltaic Operation and Complex Morphological Structures

M. L. Jones

Submitted for the degree of Doctor of Philosophy

October 2015

Abstract

This thesis utilises computational simulations to investigate the relationship between morphological structure of the active layer within organic photovoltaic devices, and its impact on the device performance. Specifically, the effects of hot charge transfer states, the mixed molecular phase and fullerene aggregation on organic photovoltaic performance, and polymer crystallinity on carrier mobility, are explored using kinetic Monte Carlo simulations. These investigations agree with experimental results and shed new light on the processes of recombination, ultrafast charge separation and the utility of the amorphous phase within the context of tie-chains.

A more accurate charge separation kinetic model is proposed in order to correctly describe the biexponential carrier recombination determined from Monte Carlo investigations. The model incorporates a 'quasi-free' state where charges are still Coulombically bound but sufficiently separated to prevent recombination. This is conceptually similar to the cooled remains of hot charge transfer states, the effects of which are investigated on device operation and shown to provide a benefit that is

strongly dependent on the aggregation of the fullerene phase, the limitation of the molecularly mixed phase and the relative charge carrier mobilities. Crystallisation within the polymer medium is then comprehensively explored using a combination of molecular dynamics and Monte Carlo simulations, along with quantum chemical calculations to help elucidate the observed annealing temperature and molecular weight dependencies of the carrier mobility for a poly(3-hexylthiophene-2,5-diyl) test system. The annealing temperature trend can be explained by increased crystallite size and order, but the molecular weight dependence is not satisfactorily explained by the crystalline regions. Instead, mobility is shown to be limited by the availability of tie-chains in the amorphous phase of the morphology, linking together crystals and providing regions of high mobility through the amorphous material.

Declaration

I hereby declare that the work carried out in this thesis has not been previously submitted for any degree and is not currently being submitted in candidature for any other degree.

Publications From This Work

- **M. L. Jones**, B. Chakrabarti and C. Groves. "Monte Carlo Simulation of Geminate Pair Recombination Dynamics in Organic Photovoltaic Devices: Multi-Exponential, Field-Dependent Kinetics and its Interpretation." *The Journal of Physical Chemistry C*, **118**, 85-91

- **M. L. Jones**, R. Dyer, N. Clarke and C. Groves. "Are Hot Charge Transfer States the Primary Cause of Efficient Free-Charge Generation in Polymer:Fullerene Organic Photovoltaic Devices? A Kinetic Monte Carlo Study." *Physical Chemistry Chemical Physics*, **16**, 20310-20320 - **hot article, selected for cover of themed PV issue**

- **M. L. Jones**, D. M. Huang, B. Chakrabarti and C. Groves. "Relating Molecular Morphology to Charge Mobility in Semi-Crystalline Conjugated Polymers." *Under review*

Attended Conferences

- **UK Semiconductors Conference**, "The Efficacy of Hot Charge Transfer States" (Oral Presentation), *Sheffield, UK*, July 2014

- **MRS Fall Meeting and Exhibition**, "The Role of Hot Charge Transfer States in Polymer-Fullerene Organic Photovoltaic Devices, Explored Using Kinetic Monte Carlo Methods" (Oral Presentation), *Boston, MA*, December 2014

- **British Science Festival**, "Can We Secure Our Energy Future? - Solar Power" (Oral Presentation), *Bradford, UK*, September 2015

Acknowledgements

Firstly, I would like to extend my most sincere gratitude to my supervisors, Dr Chris Groves and Dr Buddhapriya Chakrabarti, who have been constant sources of inspiration, teaching and support from day one. After funding fell through on my originally intended PhD project, Buddho was somehow able to rally around and find me an exceptionally exciting and stimulating project with Chris at the very last minute - a fact for which I am extremely grateful as I cannot imagine a more fitting subject that I could be more passionate about. Chris has been fully committed to furnishing me with the most complete and fulfilling PhD experience, gently leading me out of my various comfort zones and helping me become a far more well-rounded research scientist. His dedication and professionalism are unparalleled and I believe that, because of this, we have accomplished fantastic work together. I am so grateful for their praise and encouragement. I strongly believe that they have provided me with the best possible start to my research career. Beyond my supervision team, I would also like to thank my collaborators who assisted me with preparing my publications: Reesha Dyer, Professor Nigel Clarke and Dr David Huang.

As a theoretical physicist by training, it must have been most unusual for the electronics group at the School of Engineering and Computing Sciences to have

someone in their midst who sits at a computer all day and does not have lab work to do. However, each and every member of staff and student - postgraduate and postdoctoral alike - have accepted me and encouraged me, making me feel far less like an outsider and far more at home. Discussions with them all have led me to learn far more than I ever have before about their own fields of expertise and indeed my own project, when an extra pair of eyes can sometimes make all of the difference. Beyond our research, the countless games of Monopoly Deal, Hearts, Office Funtimes and Blobby Volley gave us all some valuable downtime to regroup and then attack our respective problems with renewed vigour. A good working environment is absolutely paramount to efficient and productive research, and everyone has contributed to making it a pleasure to come into work each and every day.

They say that if you don't have an annoying housemate, then you are it. Perhaps that is the case, because my two housemates Thomas Morgan and Ben Dobson have been the absolute best friends that I could have wished for. From discussing coding issues and molecular chemistry, to picking up the slack on my chores when I work late, they have supported me endlessly and made home life a precious sanctuary to retreat to after the day's graft. I will miss you both terribly and I am so proud to call myself your friend. Thank you for making my entire university experience so enjoyable, and I wish you all the best for completing your own PhDs.

Often, it can be difficult to see the 'big-picture' and instead get stuck on the tiny details that mean little in the grand scheme of things. Thanks to both Cait Brunkhorst and Dr Eric Jankowski, I have had a very specific and precise objective to aim for since very early on in my PhD. I would like to thank them both for giving

me something important to strive to, as it has motivated me and forced me to apply myself in the best possible way to achieve my goal.

Finally, I would like to express my extra special thanks to my parents, Darren and Ann-Marie. By their example, they have always encouraged me to commit my all to every task - no matter how small and trivial it might seem. They constantly help me to strive for excellence in everything that I turn my hand to, and then help me back up to my feet when I stumble and lose my way. The love and support they continually show has been more valuable to me than I could ever put into words and, without them, I would not have got nearly as far as I have. For this, I will always be indebted to them both.

Contents

List of Figures

List of Tables

Abbreviations

BHJ	Bulk Heterojunction
C8-BTBT	2,7-dioctyl[1]benzothieno[3,2-b][1]benzothiophene
CG	Coarse-Grained
CH	Cahn-Hilliard (Morphology generation theory)
CT	Charge-Transfer (State)
D:A	Donor:Acceptor (Morphology)
DD	Drift-Diffusion (Simulations)
DFT	Density Functional Theory
DoS	Density of States
DRCN7T	2,2'-((5Z,5'Z)-5,5'-((3,3"",3""',3"""",4',4"-hexaoctyl-[2,2':5', 2":5",2"':5"',2"":5"",2""':5"'',2"""-sepithiophene]-5,5"""-diyl)bis (methanylylidene))bis(3-ethyl-4-oxothiazolidine-5, 2-diylidene))dimalononitrile
DSC	Differential Scanning Calorimetry
DTS($PTTh_2$)$_2$	5,5'-bis(4-(7-hexylthiophen-2-yl)thiophen-2-yl)-[1,2,5]thiadiazolo[3,4-c]pyridine-3,3'-di-2-ethylhexylsilylene-2,2'-bithiophene
F8	Poly(9,9'-dioctylfluorene)
FC	Free Charge (State)
FET	Field-Effect Transistor
FF	Fill-Factor
FRET	Förster Resonance Energy Transfer
FRM	First Reaction Method
GIWAXS	Grazing-Incidence Wide-Angle X-ray Scattering
GS	Ground State
HCT	Hot Charge-Transfer (State)

HOMO	Highest Occupied Molecular Orbital
IQE	Internal Quantum Efficiency
ITO	Indium Tin Oxide
KM	Kinetic Model
LAMMPS	Large-scale Atomic/Molecular Massively Parallel Simulator
LUMO	Lowest Unoccupied Molecular Orbital
MC	Monte Carlo (Simulations)
MD	Molecular Dynamics
ME	Master Equation (Simulations)
MEH-PPV	Poly(2-methoxy-5-(2-ethylhexyloxy)-1,5-phenylenevinylene)
Mx:Ag	Mixed:Aggregate (Morphology)
NPT	A simulation that keeps the number of particles (N), pressure (P) and temperature (T) constant
NVT	A simulation that keeps the number of particles (N), volume (V) and temperature (T) constant
OB	Onsager-Braun (Recombination model)
OED	Organic Electronic Device
OFET	Organic Field-Effect Transistor
OLED	Organic Light-Emitting Diode
OPLS-AA	Optimised Potentials for Liquid Simulations - All Atom
OPV	Organic Photovoltaic Device
OTFT	Organic Thin Film Transistor
p-DTS(FBTTh$_2$)$_2$	7,7'-[4,4-bis(2-ethylhexyl)-4H-silolo[2,3-b:4,5-b']dithiophene-2,6-diyl]bis[6-fluoro-4-(5'-hexyl-[2,2'-bithiophen]-5-yl)benzo-[c]-[1,2,5]thiadiazole]
P3HT	Poly(3-hexylthiophene-2,5-diyl)
PBDTTPD	Poly([5-(2-ethylhexyl)-5,6-dihydro-4,6-dioxo-4H-thieno[3,4-c] pyrrole-1,3-diyl][4,8-bis[(2-ethylhexyl)oxy]benzo[1,2-b:4,5-b']dithiophene-2,6-diyl])
PBTTT	Poly(2,5-bis(3-tetradecylthiophen-2-yl)thieno[3,2-b]thiophene)
PC$_{61/71}$BM	Phenyl-C$_{61/71}$-butyric acid methyl ester

PCDTBT	Poly(N-9'-heptadecanyl-2,7-carbozole-alt-5,5-(4',7'-di-2-thienyl-2',1',3'-benzothiadiazole))
PDI	Polydispersity Index
PEDOT	Poly(3,4-ethylenedioxythiophene)
PFB	Poly(9,9'-dioctylfluorene-co-bis-N, N'-(4-butylphenyl)-bis-N,N'-phenyl-1,4-phenylenediamine)
PIA	Photoinduced Absorption (Spectroscopy)
PL	Photoluminescence
PNDT-DTBT	Poly(naphtho[2,1-b:3,4-b']dithiophene-4,7-di(thiophen-2-yl) benzothiadiazole)
PP(P)M	Particle-Particle(-Particle)-Mesh method - a Fourier-based method used to calculate the potentials for N-body simulations
PPV	Poly(1,4-phenylene-1,2-ethenediyl)
PSS	Poly(4-vinylbenzenesulfonic acid)
PTB7	Poly([4,8-bis[(2-ethylhexyl)oxy]benzo[1,2-b:4,5-b']dithiophene-2,6-diyl][3-fluoro-2-[(2-ethylhexyl)carbonyl]thieno[3,4-b] thio-phenediyl])
QF	Quasi-Free (state)
SHAKE	A computational chemistry algorithm that applies a number of constraints to a system to satisfy a required bond geometry
ToF	Time-of-flight
UV	Ultraviolet
XRD	X-ray Diffraction
ZINDO	Zerner's Intermediate Neglect of Differential Overlap (Quantum chemical calculation to determine the excited states and electronic spectrum of a molecule)

Chapter 1

Introduction

1.1 Motivation

As concerns for the environment and worries about global warming grow across the world, there is a stronger emphasis on looking at renewable energy sources to help replace non-renewable energy generation. Currently, the majority of the UK's total energy production comes from non-renewable, imported sources[1,2], with renewable energy accounting for around 25% of the total electricity generation in Q2 2015[3].

Solar power generation is becoming increasingly popular, as misconceptions about solar cells functioning poorly in temperate climates, on non-south-facing rooftops or during high levels of cloud cover are alleviated. The adoption rate of solar power is set to increase as new solar farms are completed around the country, with government projections predicting 22 000 MW of installed photovoltaic capacity in Britain by 2020[4]. This seems attainable, as solar power has proved successful elsewhere in Europe; for instance, nearly 7% of Germany's total power generation comes from solar sources[5]. However, generating electricity from the sun is not without its

challenges. Conventional silicon-based photovoltaics cost around £220 m^{-2} to manufacture, using processes that have been developed for almost 50 years[6]. This is often regarded as prohibitively expensive and so researchers are exploring alternatives using cheaper materials.

Recent decades have seen the emergence of a variety of new solar technologies[7–11], not least of which is the idea of using organic compounds (*i.e.* carbon-containing materials) in the manufacture of solar cells, ranging from small molecules to polymers and fullerene derivatives[12,13]. Organic photovoltaic devices (OPVs) like these have become promising alternatives to their inorganic counterparts. They exhibit many advantages over conventional solar cells, such as the capability to modify the composition of the molecules to tune their absorption to better match the solar spectrum[14] and a wealth of compatible, low-cost, scalable manufacturing processes[15,16]. In fact, the synthesis of the carbon-containing molecules in OPVs costs around £95 m^{-2} using processes less than two decades old[17]. It is likely then that, in the near future, these processes will become further optimised and the cost of OPVs will drop even more.

The invention of the solution-processed bulk heterojunction (BHJ) solar cell in 1995[13,18] heralded a jump in performance compared to earlier devices as new component materials and deposition processes became viable[15,16]. Today, some OPVs have reached laboratory power-conversion efficiencies as high as 12% for single-junction cells[19]. Unfortunately, this falls far short of the near 40% laboratory efficiencies and 20% commercially-available efficiencies of various inorganic devices[6]. It is estimated, after factoring in the drastically reduced manufacturing costs of OPVs,

that an energy conversion efficiency of 15% is required in order to make organic devices more commercially viable than conventional, silicon-based solar cells[20,21]. The focus of the research community has therefore been the optimisation of the power conversion efficiency.

Morphology, which is a description of the physical arrangement of the constituent molecules within the active layer responsible for charge conduction, plays a key role in the operation of all organic electronic devices (OEDs). It can be strongly influenced by the material selection, solvent and thermal annealing processes, as well as the mixing of the component phases[22–24]. There has been much research on the effects that device processing has on the morphology, however the direct relationship between the morphology and the resultant device performance, especially in terms of the charge carrier mobility, is more complex and it can be time consuming and expensive to explore. An alternative method is to utilise computer simulations, which can permit the control of device characteristics in order to determine which most strongly affect the device efficiency.

Such simulations must be capable of treating all of the important physical processes that occur in OPVs, such as photoinjection, transport and recombination. This can be achieved through *ab initio* calculations, or through calibration to experimental results. In particular, the results of spectroscopy or microscopy investigations are important as they are often able to highlight the population of excited states within the device in the case of photoluminescence (PL) studies[25–27], or determine molecular structure such as crystalline lattice packing using x-ray diffraction (XRD)[28,29] or microscopy[30]. In general, simulation code is often developed over

a period of many years, in order to obtain the most accurate results. The eventual aim is to construct a virtual photovoltaic device, where enough parameters can be tested that a set of optimised design rules can be created for manufacturers.

1.2 Outline

In this thesis, a variety of computational methods are employed in order to clarify the relationship between morphology of organic thin films, and the overall device performance. In chapter 2, the constituent materials and operation of typical OEDs are discussed, with particular focus on the characterisation of OPVs. Then, in chapter 3, an overview of some of the available simulation methods exploring OPV behaviour is given, including a description of the Monte Carlo (MC) code used in the bulk of the investigations that were performed in chapters 4-6. In chapter 4, an investigation of the recombination dynamics of geminate charge pairs within OPVs is reported. Some commonly used theories are found to not satisfactorily describe the observed behaviour from the MC simulations, suggesting that a new theoretical framework is required in order to explain spectroscopy results. The new framework attempts to describe carriers that are physically close enough to be Coulombically bound but sufficiently separated to avoid recombination. In chapter 5, the MC code is upgraded in order to probe the efficacy of hot charge-transfer states (HCTs) in efficient OPVs. The benefit from HCTs is found to be strongly morphology dependent and particularly linked to the aggregation of the fullerene acceptor material in two-phase devices. In the final results chapter 6, an investigation of the crystal properties of a thin film of polymer donor phase is discussed, with the aim of relating charge

mobility to nanoscale molecular structure. This investigation is broadly applicable to OEDs and unites several theoretical methods such as the coarse-graining of an interaction forcefield, molecular dynamics (MD) simulations, quantum chemical calculations and MC simulations. Finally, chapter 7 outlines the main conclusions drawn from this work, and suggests the possible directions of future investigations.

References

[1] D. J. Evans and R. A. Chadwick. *Underground Gas Storage: Worldwide Experiences and Future Development in the UK and Europe.* Geological Society Special Publications, 2009.

[2] Department of Energy & Climate Change. "Coal Statistics." `http://www.gov.uk/government/collections/coal-statistics`, 2015. [Online; Accessed 01-oct-2015].

[3] Department of Energy & Climate Change. "Renewables Statistics." `https://www.gov.uk/government/collections/renewables-statistics`, 2015. [Online; Accessed 01-oct-2015].

[4] Department of Energy & Climate Change. "UK Solar PV Strategy." `http://www.gov.uk/government/publications/uk-solar-pv-strategy-par-1-roadmap-to-a-brighter-future`, 2014. [Online; Accessed 01-oct-2015].

[5] Fraunhofer-Institut. "Für Solare Energiesysteme Ise." `http://www.ise.fraunhofer.de`, 2015. [Online; Accessed 01-oct-2015].

[6] R. M. Swanson. "A Vision for Crystalline Silicon Photovoltaics." *Prog. Photovolt. Res. Appl.*, **14**, 443–453, 2006.

[7] M. Ohmori, T. Takamoto, E. Ikeda, and H. Kurita. "High Efficiency InGaP/GaAs Tandem Solar Cells." *Technical Digest, International PVSEC-9*, **1**, 525–528, 1996.

[8] M. A. Contreras, B. Egaas, K. Ramanathan, J. Hiltner, A. Swartzlander, F. Hasoon, and R. Noufi. "Progress Towards 20% Efficiency in Cu (In,Ga)Se Polycrystalline Thin-Film Solar Cell." *Prog. Photovolt: Res Appl.*, **7**, 311–316, 1999.

[9] A. Hinsch, J. Kroon, K. Rainer, R. Sasrawan, A. Meyer, and I. Uhlendorf. "Long-Term Stability and Efficiency of Dye-Sensitised Solar Cells." *Proceedings of the 17th European Photovoltaic Solar Energy Conference*, **1**, 51–54, 2001.

[10] G. J. Bauhuis, P. Mulder, J. J. Schermer, E. J. Haverkamp, J. van Deelen, and P. K. Larsen. "Thin Film GaAs Solar Cells with Improved Radiation Hardness." *Proceedings of the 20th European Photovoltaic Solar Energy Conference*, **1**, 6–10, 2005.

[11] M. A. Green, K. Emery, Y. Hishikawa, W. Warta, and E. D. Dunlop. "Solar Cell Efficiency Tables (Version 45)." *Prog. Photovolt: Res Appl.*, **23**, 1–9, 2015.

[12] C. W. Tang. "Two-Layer Organic Photovoltaic Cell." *Appl. Phys. Lett.*, **48**, 183–185, 1986.

[13] G. Yu, J. Gao, J. C. Hummelen, F. Wudl, and A. J. Heeger. "Polymer Photovoltaic Cells: Enhanced Efficiences via a Network of Internal Donor-Acceptor Heterojunctions." *Science*, **270**, 1789–1791, 1995.

[14] Y Li. "Molecular Design of Photovoltaic Materials for Polymer Solar Cells: Toward Suitable Electronic Energy Levels and Broad Absorption." *Acc. Chem. Res.*, **45**, 723–733, 2012.

[15] A. C. Arias, J. D. MacKenzie, I. McCulloch, J. Rivnay, and A. Salleo. "Materials and Applications for Large Area Electronics: Solution-Based Approaches." *Chem. Rev.*, **110**, 3–24, 2010.

[16] F. C. Krebs, T. Tromholt, and M. Jørgensen. "Upscaling of Polymer Solar Cell Fabrication Using Full Roll-to-Roll Processing." *Nanoscale*, **2**, 873–886, 2010.

[17] J. Kalowekamo and E. Baker. "Estimating the Manufacturing Cost of Purely Organic Solar Cells." *Sol. Energ.*, **83**, 1224–1231, 2009.

[18] J. J. M. Halls, C. A. Walsh, N. C. Greenham, E. A. Marseglia, R. H. Friend, S. C. Moratti, and A. B. Holmes. "Efficient Photodiodes from Interpenetrating Polymer Networks." *Nature*, **376**, 498–500, 1995.

[19] S. Ali-Oettinger. "Heliatek Announces World Record for Organic Cell." `http://www.pv-magazine.com/news/details/beitrag/heliatek-announces-world-record-for-organic-cell_100009859`, 2013. [Online; Accessed 01-oct-2015].

[20] C. J. Brabec, S. Gowrisanker, J. J. M. Halls, D. Laird, S. Jia, and S. P. Williams. "Polymer:Fullerene Bulk-Heterojunction Solar Cells." *Adv. Mater.*, **22**, 3839–3856, 2010.

[21] S. E. Shaheen, D. S. Ginley, and G. E. Jabbour. "Organic-Based Photovoltaics: Toward Low-Cost Power Generation." *MRS Bull.*, **30**, 10–19, 2005.

[22] W. Ma, C. Yang, X. Gong, K. Lee, and A. J. Heeger. "Thermally Stable, Efficient Polymer Solar Cells with Nanoscale Control of the Interpenetrating Network Morphology." *Adv. Funct. Mater.*, **15**, 1617–1622, 2005.

[23] M. C. Scharber, D. Mühlbacher, M. Koppe, P. Denk, C. Waldauf, A. J. Heeger, and C. J. Brabec. "Design Rules for Donors in Bulk-Heterojunction Solar Cells - Towards 10% Energy-Conversion Efficiency." *Adv. Mater.*, **18**, 789–794, 2006.

[24] J. K. Lee, W. L. Ma, C. J. Brabec, J. Yuen, J. S. Moon, J. Y. Kim, K. Lee, G. C. Bazan, and A. J. Heeger. "Processing Additive for Improved Efficiency from Bulk Heterojunction Solar Cells." *J. Am. Chem. Soc.*, **130**, 3619–3623, 2008.

[25] P. Peumans, A. Yakimov, and S. R. Forrest. "Small Molecular Weight Organic Thin-Film Photodetectors and Solar Cells." *J. Appl. Phys.*, **93**, 3693–3723, 2003.

[26] A. Mani, J. Schoonman, and A. Goossens. "Photoluminescence Study of Sexithiophene Thin Films." *J. Phys. Chem. B.*, **109**, 4829–4836, 2005.

[27] Y. C. Zhou, Y. Wu, L. L. Ma, J. Zhou, X. M. Ding, and X. Y. Hou. "Exciton Migration in Organic Thin Films." *J. Appl. Phys.*, **100**, 023712:1–023712:5, 2006.

[28] S. Ko, E. T. Hoke, L. Pandey, S. Hong, R. Mondal, R. Rajib, C. Risko, Y. Yi, R. Noriega, M. D. McGehee, J.-L. Brédas, A. Salleo, and Z. Bao. "Controlled Conjugated Backbone Twisting for an Increased Open-Circuit Voltage while Having a High Short-Circuit Current in Poly(hexylthiophene) Derivatives." *J. Am. Chem. Soc.*, **134**, 5222–5232, 2012.

[29] A. M. Schneider, L. Lu, E. F. Manley, T. Zheng, V. Sharapov, T. Xu, T. J. Marks, L. X. Chen, and L. Yu. "Wide Bandgap OPV Polymers Based on Pyridinonedithiophene Unit with Efficiency >5%." *Chem. Sci.*, **6**, 4860–4866, 2015.

[30] A. Zen, J. Pflaum, S. Hirschmann, W. Zhuang, F. Jaiser, U. Asawapriom, J. P. Rabe, U. Scherf, and D. Neher. "Effect of Molecular Weight and Annealing of Poly(3-hexylthiophene)s on the Performance of Organic Field-Effect Transistors." *Adv. Funct. Mater.*, **14**, 757–764, 2004.

Chapter 2

Organic Electronic Devices

2.1 Introduction

Organic electronic devices are becoming attractive alternatives to their silicon-based counterparts due to the growth of new technologies over the last decade that allow for cheaper and more versatile manufacturing and materials synthesis. In this chapter, a brief overview of organic semiconductors will be presented in §2.2, considering various types of small molecules and conjugated polymers that are suitable for the active layer in devices. The function and operation of organic field-effect transistors (OFETs) and OPVs will then be discussed in §2.3 and §2.4, with particular emphasis on the structure and morphology of OPV devices, as these will form the majority of the investigations in the thesis. Some commonly used characterisation methods for OPVs will be outlined in §2.5, before summarising in §2.6.

2.2 Organic Electronic Materials

A key consideration for any organic electronic device is its material composition, as this can strongly affect its performance characteristics[1]. Most devices consist of a combination of several materials, from conductive metals in the electrodes, through semiconducting materials forming the active layer and insulating dielectrics as substrates that control the flow of current in OFETs[2]. This thesis is concerned with investigations into the semiconducting active layer of organic devices, particularly in OPVs, and so this will be the main focus of the materials selection.

The conductivity of materials is generally characterised by a bandgap - the energetic spacing between the valence band that denotes the energy of the outermost, bound electrons of the material, and the conduction band. Hence, the bandgap describes the energy required for charge carriers to move freely throughout the medium. In an electrical conductor there is no bandgap and the two bands overlap. Therefore, there is a high probability that electrons will occupy part empty levels, allowing them to move easily in an electric field. Conversely, insulators have a large bandgap ($\sim 5\,\mathrm{eV}$), meaning that the probability that electrons will be promoted from the valence to the conduction band is low. In these materials, the available mobile charge is also low, restricting current flow. In organic semiconducting materials, the bandgap is of the order $\sim 1\,\mathrm{eV}$, which is still significantly greater than k_BT at device operating temperatures. This leads to generally few thermally excited carriers in the material, and so the availability of charges is instead controlled through injection from metal electrodes or, in the case of photovoltaics, through the absorption of energy from incident photons[3,4]. Semiconducting materials are therefore preferred in the active

layer in electronic devices because their electrical properties and conductivity can be controlled in this way.

In inorganic semicondcutors, the electronic properties can be further controlled by incorporating impurity atoms (dopants) into the material's lattice structure. This process, called doping, increases the number of available charge carriers by modifying the bandgap and Fermi level, E_F, of the material, which describes its highest occupied energy level at a temperature of 0 K[5–7]. Schematic examples of the band structure of p-type (where E_F is closer to the valence band and there is a deficiency of electrons in the material) and n-type doped semiconductors (where E_F is closer to the conduction band and there is an excess of electrons in the material) are shown in figure 2.1. Note that it is common within electronics to think of a deficiency of electrons as identical to an abundance of 'holes' - positively-charged fermions that correspond to the absence of electrons in the valence band. Although they are not physical particles, the motion of holes throughout a medium can be a useful concept, especially when considering p-doped materials. Pure polycrystalline silicon can be doped with boron or gallium atoms to reduce E_F, resulting in p-type semiconducting behaviour, or with phosphorus or antimony to result in an n-type semiconductor[8].

Organic semiconductors, on the other hand, can exhibit p- or n-type 'behaviour' without doping, as the arrangement of their energy levels (with respect to the electrodes) gives rise to an increased population of charge carriers[9,10]. Of particular importance are the frontier molecular orbitals - the highest occupied molecular orbital (HOMO) and lowest unoccupied molecular orbital (LUMO) levels - which are

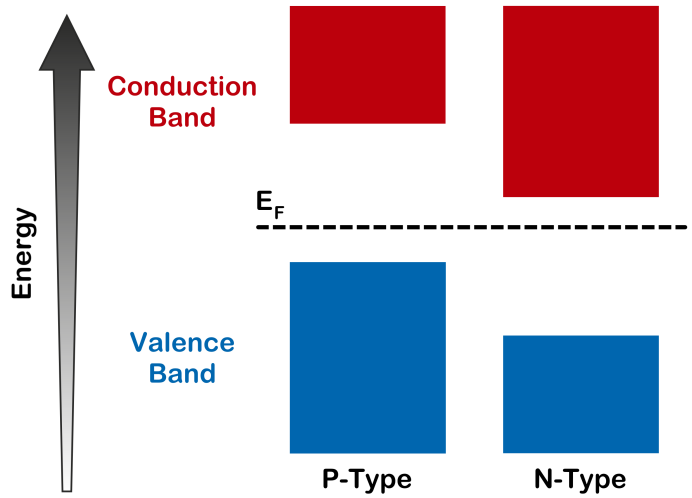

Figure 2.1: *Schematic of the p-type and n-type band structure in semiconducting materials.*

analogous to the top of the valence band, and the bottom of the conduction band in inorganic materials respectively[11]. The difference between the HOMO and LUMO levels of a material corresponds to its bandgap, and is typically around 1−2 eV for most conjugated polymers[12]. The behaviour of the semiconductor, *i.e.* the carrier type that is injected and propagates through it, can be determined by selecting an electrode with an appropriate energy level. The work function of the electrode (the energy required to move a charge carrier from the Fermi level of a material to infinity[13]) can be aligned to match the HOMO (if holes are to be injected) or the LUMO (if electrons are to be injected) of the semiconductor, as shown in figure 2.2[11]. In this example, the electron-transporting fullerene molecule $PC_{61}BM$ has a LUMO level of ∼−4 eV and a HOMO of ∼−6.5 eV. By connecting an electrical contact made of aluminium (which has a work function of around −4.2 eV) to a $PC_{61}BM$ film, electrons can be injected into the LUMO with a higher probability than holes are injected into the HOMO, as the electron injection barrier is smaller (0.2 eV for electrons, 2.3 eV for holes). In this configuration, $PC_{61}BM$ will trans-

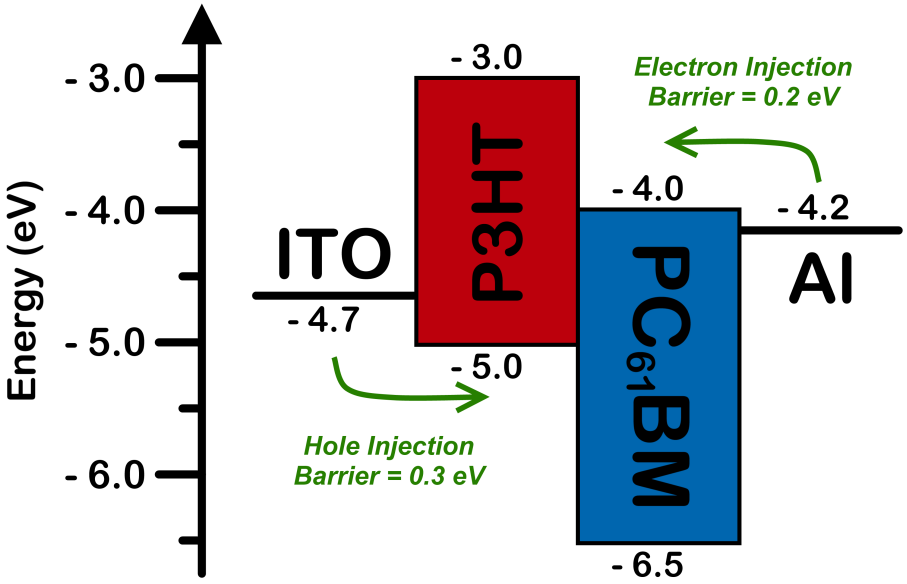

Figure 2.2: *Example energy level diagram for a system consisting of a P3HT donor, a $PC_{61}BM$ acceptor, an ITO anode and an Al cathode, as are often used in OPVs.*

port electrons preferentially, leading to n-type behaviour. Materials of this type are known as 'acceptors'. Conversely, hole-transporting organic semiconductors such a P3HT, typically have HOMOs of around −5 eV. Indium tin oxide (ITO) has a Fermi level of −4.7 eV, making it a suitable hole-injection anode and leading to p-type, 'donor' behaviour in these materials.

Both donor and acceptor materials form molecular orbitals based on the configuration of the electron wavefunctions, due to the covalent chemical bonds of the constituent carbon atoms[14]. This mixing of the orbitals is known as hybridisation and is depicted in figure 2.3. Consider two carbon atoms, each forming a trigonal planar bond with three other atoms, with electrons in sp^2 orbitals, leaving the final valence electron in an additional p-orbital. In the bonding case (*i.e.* in a C=C double bond), the proximity of the two p-orbitals causes them to hybridise, forming a π-bond. The π-bond is weaker than the standard C−C σ-bond, as there is an

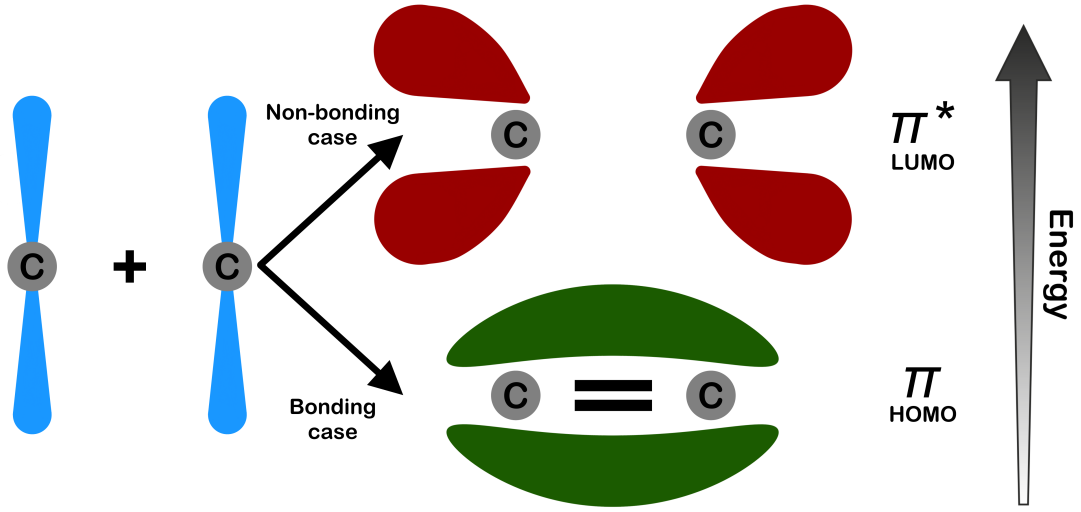

Figure 2.3: *Schematic of the p-orbital hybridisations for the bonding (bottom, green) and non-bonding (top, red) cases. The coloured regions denote the orbitals, which describe the probability of electron density.*

excess electron density above and below the plane of the double bond. This is the HOMO configuration for the bond. In the non-bonding case, the electron wavefunctions separate, forming a high-energy π^* configuration, that produces the LUMO. The magnitude of the π-π^* splitting can be modified by altering the chemical structure of the material, which affects the wavelength of light that it can absorb. This method has been used in conjugated polymers in order to make their absorption better match the solar spectrum, improving the power conversion efficiency, η, of the material (the ratio of output current to input fluence)[15].

Charge transport in organic semiconductors occurs *via* consecutive quantum tunnelling events ('hops') between regions of increased π-orbital overlap[16], so it is common for materials to contain aromatic functional groups that have several double bonds to increase π-conjugation[17]. The ability of a material to transport a particular carrier is quantified by its mobility, μ. This is a measure of the drift velocity, v_d of a charge through a medium in a given electric field, E, and is related

to the electrical conductivity, σ:

$$\sigma = nq\frac{v_{\text{drift}}}{E} = nq\mu, \tag{2.2.1}$$

where n is the carrier concentration and q is the unit charge carried. Molecules with increased π-conjugation tend to exhibit higher mobilities, with both small molecules and conjugated polymers finding extensive use in OFETs and OPVs[18]. There are two main methods to calculate the mobility. Time-of-flight (ToF) mobility is measured from the transient photocurrent induced from a laser excitation[19], whereas field-effect mobility can be inferred from OFET measurements[20]. As charges are not injected from the contacts in ToF measurements, the carrier densities are significantly lower and so field-effect mobility measurements tend to be several orders of magnitude greater than ToF measurements in the same material[21]. The nature of how the orbital overlap affects the mobility is explored more deeply in chapter 6, where charge transport in a conjugated polymer is related to its backbone conformation.

2.2.1 Molecules

Organic small molecules are advantageous to use in organic devices due to simple synthesis and purification processes resulting in well-defined structures that allow for good batch-to-batch reproducibility of results[22,23]. However, these molecules tend to be rigid with low viscosity, making it more difficult to dissolve them in a solvent or form a phase-separated mixture with an acceptor material[24]. As such, precise and controllable vacuum deposition processes tend to be favoured over solution process-

ing for such materials, although they are more expensive[25]. Pentacene is often used as the benchmark against which new materials are compared[18]. Although early investigations reported a field-effect mobility $\sim 0.7\,\mathrm{cm^2\,V^{-1}\,s^{-1}}$[26] for pentacene, incorporating triisopropylsilylethynyl groups on the central ring to make TIPS-pentacene increases the solubility of the molecule and permits mobilities $> 1\,\mathrm{cm^2\,V^{-1}\,s^{-1}}$ in solution-processed transistors[27,28]. Oligothiophenes and their derivatives can also be used as a donor medium, reporting mobilities of up to $0.08\,\mathrm{cm^2\,V^{-1}\,s^{-1}}$ for unsubstituted sexithiophene[29], which can be increased to $\sim 0.5\,\mathrm{cm^2\,V^{-1}\,s^{-1}}$ by substituting the terminating hydrogens with cyclohexane[30,31]. Recently, a spin-coated blend of the small molecule C8-BTBT with conjugated polymer polystyrene has produced a thin film transistor exhibiting a hole mobility of $25\,\mathrm{cm^2\,V^{-1}\,s^{-1}}$[32].

Perhaps the first OPV device consisted of a layer of the small molecular donor copper pthalocyanine, vacuum deposited on a layer of an electron-deficient perylene tetracarboxylic derivative. This resulted in devices with $\eta \sim 1\%$[33]. By substituting the acceptor with a C_{60} fullerene, η was increased to 3.6%[34]. This highlights the importance of pairs of materials within the active layer of OPVs, an idea that will be revisited more thoroughly in §2.4. Other successful uses of small molecule:fullerene blends in OPVs include diketopyrrolopyrroles, resulting in $\eta \sim 4.4\%$[35] and molecules with a benzodithiophene core reporting $\eta \sim 5\%$[23]. Some small molecules used in OPVs contain both electron-deficient and electron-rich functional groups, allowing them to effectively transport both electrons and holes in devices[17]. For instance, DTS($PTTh_2$)$_2$ has a pristine film field-effect mobility of around $0.1\,\mathrm{cm^2\,V^{-1}\,s^{-1}}$, and can be used to manufacture OPVs with $\eta \sim$

6.7%, when blended in a 7:3 ratio with a $PC_{71}BM$ acceptor fullerene[36]. Greater efficiencies have been achieved using the small molecule DRCN7T, which has been used in a 2:1 blend ratio with $PC_{71}BM$ to manufacture OPVs with $\eta > 9\%$[37].

Although many materials are used as the p-type donors in solution-processed OPVs, the vast majority of record-breaking devices utilise fullerene derivatives as the acceptor medium, due to energy levels that are complementary to many polymeric and small-molecule donors, as well as good solution processibility[11]. $PC_{61}BM$ and the longer-wavelength absorbing $PC_{71}BM$ are used extensively, with few substitutions demonstrating marked improvements on device efficiency[11]. These fullerene derivatives additionally have the advantage of ultrafast ($< 300\,\text{fs}$) electron transfer when combined with conjugated polymers[38] and high electron mobilities of up to $6\,\text{cm}^2\,\text{V}^{-1}\,\text{s}^{-1}$[39].

2.2.2 Conjugated Polymers

Conductive conjugated polymers consist of repeated units that allow for π-orbital overlap along the chain backbone. Some classes of polymer can be conductive from just C=C double bonds, such as oxidised, halide-doped polyacetylene[40], however most conjugated polymers used in organic electronic devices contain aromatic cycles due to the electron densities that result above and below the plane of the ring[41]. Along the chain, the orbitals overlap significantly, permitting high intra-chain mobilities, although contortions and imperfections along the backbone can break π-orbital conjugation, hampering charge transport[42]. Inter-chain mobilities tend to be lower as the orbital overlap between chains is less than along the backbone[43]. However,

the orientation of polymer chains can increase π-stacking, resulting in improved inter-chain mobility[17,44].

A key advantage of polymeric materials is that their molecular structure can be modified by including functional groups that alter the light absorption characteristics through modification of the HOMO and LUMO levels[15], or that increase π-orbital overlap and improve transport by modifying the π-stacking and lamellar separations of the structures[45,46]. Many polymers also exhibit high miscibility with commonly used acceptor materials such as fullerenes, making them suitable for solution-processing and roll-to-roll techniques in blended OPVs[47]. These do not require a vacuum or high temperatures and pressures, allowing for cheaper deposition than alternative methods[48].

There are many classes of conjugated polymer, ranging from polythiophenes such as P3HT, through carbazole-based polymers and dithienopyrroles, to fluoropolymers such as PFB[11]. These materials tend to be polydisperse and device performance depends sensitively on the processing conditions, regioregularity and molecular weight[17].

The semicrystalline polythiophene P3HT has been widely studied. It exhibits excellent self-assembly properties, arranging into three-dimensional crystals that improve the charge transport between chains, resulting in a versatile material with many uses in organic electronics[17]. As with most conjugated polymers, annealing can improve the charge transport characteristics of P3HT, with ToF hole mobilities typically increasing by an order of magnitude from $\sim 1 \times 10^{-5}\,\mathrm{cm^2\,V^{-1}\,s^{-1}}$ to $\sim 1 \times 10^{-4}\,\mathrm{cm^2\,V^{-1}\,s^{-1}}$ after thermal or solvent annealing[45,49,50]. Field-effect mobili-

ties for pristine P3HT films are generally of the order $\sim 0.1\,\mathrm{cm^2\,V^{-1}\,s^{-1}}$ [51,52], and P3HT:$PC_{60}BM$ OPVs typically exhibit $\eta \sim$ 4-5% [53,54]. Other polythiophenes, such as PBTTT and derivatives thereof, have long sidechains which can interdigitate, allowing for highly regular crystalline domains to form up to 10 nm in extent [55]. This is thought to be the reason for the high field-effect hole mobilities of around $0.6\,\mathrm{cm^2\,V^{-1}\,s^{-1}}$ [56,57]. However when blended with $PC_{61}BM$, the long, linear side chains of PBTTT intercalate with the acceptor fullerenes, producing a molecularly mixed phase that results in OPV device efficiencies of around $\eta \sim 2.3\%$ [58]. This indicates that morphology and molecular structure also strongly influence the performance characteristics of the device. The majority of this thesis studies the effects of morphology on the device properties (such as η and the carrier mobility), to clarify the relationship between them. In particular, the mixed phase is studied in chapter 5.

Polyfluorenes are commonly used in organic light-emitting diodes (OLEDs), as their bandgap typically lies in the ultraviolet (UV) part of the spectrum, allowing electroluminescence of blue light to occur [11,59]. This suggests that some of these materials in their pure form are less appropriate for OPVs, as the peak of the solar spectrum occurs in the visible range with a wavelength $400 \leq \lambda < 700\,\mathrm{nm}$, and not in the UV ($\lambda < 400\,\mathrm{nm}$). However, these materials tend to exhibit high, non-dispersive hole transport mobilities, which make them an attractive option for efficient charge transport. As an example, the UV-absorbing polyfluorene F8 exhibits a ToF mobility of $\sim 8.5 \times 10^{-3}\,\mathrm{cm^2\,V^{-1}\,s^{-1}}$ [60]. In order to access these high mobilities in OPV devices, it becomes important to modify the molecular structure of the polymer to

tune its absorption to better match the solar spectrum. One possible solution is to incorporate arylenediamine groups into the backbone to create PFB, modifying the HOMO level from −5.71 eV to −4.87 eV, while keeping the LUMO level approximately constant at around −2.05 eV [61]. This reduces the bandgap of the molecule, increasing the absorption wavelength of the photons to the visible spectrum.

As with small molecules, it is also possible to produce donor-acceptor copolymers that contain both donor and acceptor functional groups along the backbone, resulting in strong π-π stacking coherence and high carrier mobilities [62]. For example, the polymer PBDTTPD contains alternating benzodithiophene donor and thienopyrroledione acceptor moieties along its backbone, and has been blended with $PC_{71}BM$ to produce solar cells with a high $\eta = 8.3\%$ [46,63]. Such polymers are advantageous because their optical bandgap and HOMO and LUMO levels can be very precisely controlled through variation of these moieties [64]. These materials can therefore be tuned to have strong absorption spectra in a specific range, and then combined with those that absorb well in another to maximise photoabsorption and increase η. For instance, the donor-acceptor fluoro-copolymer PTB7 absorbs strongly in the range 550-750 nm, with relatively weak absorption between 300-500 nm. By blending $PC_{71}BM$ into the composition, which has strong visible absorption, the resultant device absorbs well over the range 300-800 nm. This increases the device efficiency and typical PTB7:$PC_{71}BM$ blends can produce $\eta \sim 9.0\%$ [65].

2.2.3 Other Materials

Beyond the active layer, there are still several additional components that are required in order to manufacture a functioning device. An example OPV structure is given in figure 2.4, along with some commonly used materials for each layer[66]. A high work function, transparent anode is required as devices are usually illuminated from this side. It is therefore common to use ITO, deposited onto a glass substrate to allow photo-transmission into the active layer. A low work function, reflective cathode is also required, and for this aluminium is often used. Note that interfacial layers can be deposited between the active layer and the electrodes, which permit carriers that are to be extracted from the neighbouring electrode to pass through, while simultaneously blocking the opposing carrier. For example, PEDOT:PSS is commonly used as an electron blocking interlayer at the anode, while a film of calcium can prevent holes from approaching the cathode[47,66,67]. If the active layer was in direct contact with, for example, the hole-collecting anode, then electrons could be formed at the heterojunction close to the contact, leading to surface recombination which can reduce open-circuit voltage, V_{OC}, and η. Including a blocking layer can significantly increase V_{OC}, in some cases improving η by as much as 2%, compared to a control device with no blocking layer included[68].

Within the last five years, new solar cells have emerged that use thin films of organometallic semiconductors such as methylammonium lead iodide perovskites in their composition[69,70]. These devices have demonstrated $\eta > 20\%$[71,72], effectively doubling in efficiency over two years as new deposition and mixing methodologies have been discovered that allow greater control over the mesoscale structure of

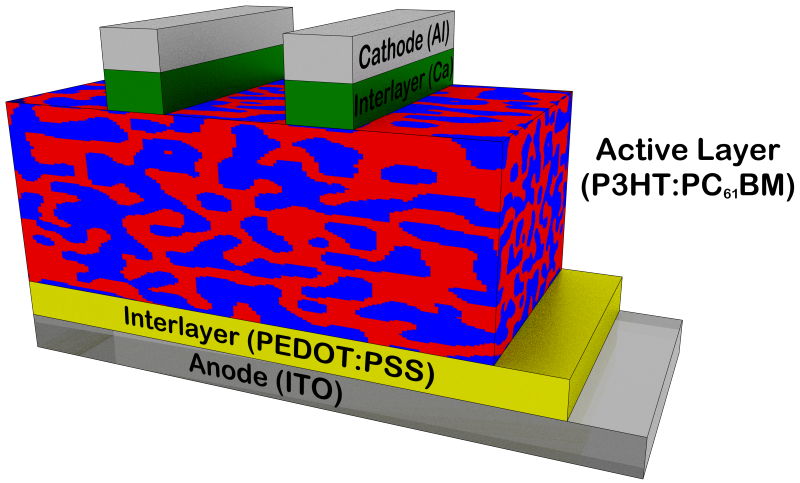

Figure 2.4: *The layers typically found in a non-inverted OPV device, along with examples of commonly-used materials.*

the perovskite crystals[73]. These extraordinary efficiencies are likely due to the high electron and hole mobilities within the perovskite crystal ($7.5\,\mathrm{cm^2\,V^{-1}\,s^{-1}}$ for electrons[74] and $>12.5\,\mathrm{cm^2\,V^{-1}\,s^{-1}}$ for holes[75]), assisted by weak exciton binding energies of around $0.03\,\mathrm{eV}$[76] ($\sim k_BT$ at room temperature) and slow recombination occurring on timescales of the order $\sim 100\,\mathrm{ns}$[77]. Despite stability and toxicity concerns arising from using a low-viscosity, fast-crystallising, water-soluble lead compound in solar cells, perovskite photovoltaics have the potential to become increasingly competitive with the conventional silicon photovoltaics that dominate the current market[78].

2.3 Field-Effect Transistors

An OFET is an electronic device that uses an electric field perpendicular to the current flow within the organic semiconductor to modulate it[79]. These are often used as on/off switches or in signal amplification, as a small variation in the gate voltage can lead to a large change in the device current[80]. An example of an OFET is shown

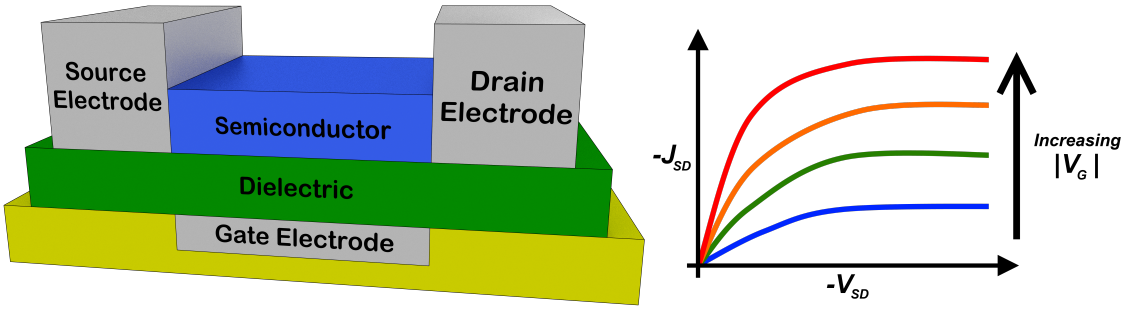

(a) OFET Material Layers *(b) Example OFET J-V curves*

Figure 2.5: *The material layers found in a FET device, along with the typical J-V output characteristics. This is a bottom-contact device, as the source and drain electrodes are in contact with the dielectric. It is operating in the p-channel because J_{SD}, V_{SD} and V_G are all negative, indicating that holes are the charge carriers in the device.*

in figure 2.5a, which includes the source and drain electrodes that charge carriers enter and exit the device from, as well as an insulating layer between the semiconductor and the gate (often consisting of SiO_2). In many OFETs, the organic layer is very thin, and so the devices are called organic thin-film transistors (OTFTs). The electrode materials used determine the carrier species that can propagate through the device, however, as many organic semiconductors have higher mobility for holes than electrons, it is more common to select electrodes for the OFET with energy levels that cause p-type behaviour, where holes are the active charge carrier[81].

Example J-V characteristics for a p-type OFET are shown in figure 2.5b. The flow of current through the semiconductor is controlled by the transverse electric field arising from an applied voltage, V_G, between the gate and the source. As $|V_G|$ is increased from zero, an 'accumulation layer' of charges forms at the semiconductor-insulator interface[42]. This forms a channel, filled with charge carriers, connecting the source and the drain. When an additional potential difference is applied between the source and the drain electrodes, V_{SD} (usually applied at the drain electrode, with

the source kept at ground[82]), a longitudinal electric field is formed within the device and the accumulated charge carriers begin to flow from the source to the drain, resulting in a current, J_{SD}. When $V_{SD} << V_G$, the device acts as a resistor and so the J-V curve is linear[83]. Increasing the magnitude of the source-drain voltage increases the output current, until the potential at the drain matches the potential at the gate. Further increments to V_{SD} result in driving the gate and drain into reverse bias. This creates a depletion region at the drain electrode where the transverse and longitudinal electric fields cancel. This is called the 'pinch-off' point[82]. Here, the current can still flow from the source to the drain, however charges that are close to the drain rely on the process of diffusion to reach the electrode as there is no resultant electric field in the depletion region. Diffusion is a slower process than drift due to an electric field, and so the current saturates[84]. Increasing V_{SD} beyond the saturation point widens the depletion region so more diffusion is required to transport charges to the drain. The current therefore remains constant, and the magnitude of the saturation current is dependent on the carrier mobility of the material[42]. Within commercial electronic devices, the materials used in OFETs typically have mobilities greater than $0.1\,\mathrm{cm^2\,V^{-1}\,s^{-1}}$[85]. Another important property is the on/off current ratio, which describes how well the transistor can switch. As V_G increases, the perpendicular electric field pinches the channel closed, increasing the impedance and restricting the current flow. The on/off ratio is then the ratio of the saturation current when $V_G = 0$ to when $|V_G|$ is high. On/off ratios for OFETs are typically around 10^6[86].

2.4 Photovoltaics

In 1839, Alexandre-Edmond Becquerel discovered that, upon exposure to light, an electrical current can be induced in semiconducting materials[87]. Incoming photons with energy greater than the work function of the semiconductor can be absorbed to promote an electron from the occupied valence band to the empty conduction band, leaving behind a hole. This is known as the photoelectric effect and a schematic is shown in figure 2.6a. The charge carriers are no longer localised onto their origin molecule and are free to move throughout the active layer of the device. In PVs, these charges can be collected at electrical contacts, generating photovoltaic current. The charges move *via* an electric field, which is induced by using at least a pair of materials arranged to create a p-n junction that combines the hole-rich donor with the electron-rich acceptor, as shown in figure 2.6b. Due to the difference in charge carrier concentrations, electrons tend to diffuse from the regions of high concentration on the acceptor side of the device to regions of low electron concentration in the donor, leaving behind positive ionic cores. The holes travel in the opposite direction, leaving an abundance of negative ionic material on the donor side. These uncompensated charge cores induce an electric field within the device that opposes the direction of diffusion. At equilibrium, these opposing forces balance, and a depletion region at the interface is formed.

2.4.1 OPV Operation

In OPVs, the end goal of operation is the same as in inorganic devices - the electron and hole must be extracted from the cathode and anode of the device respectively,

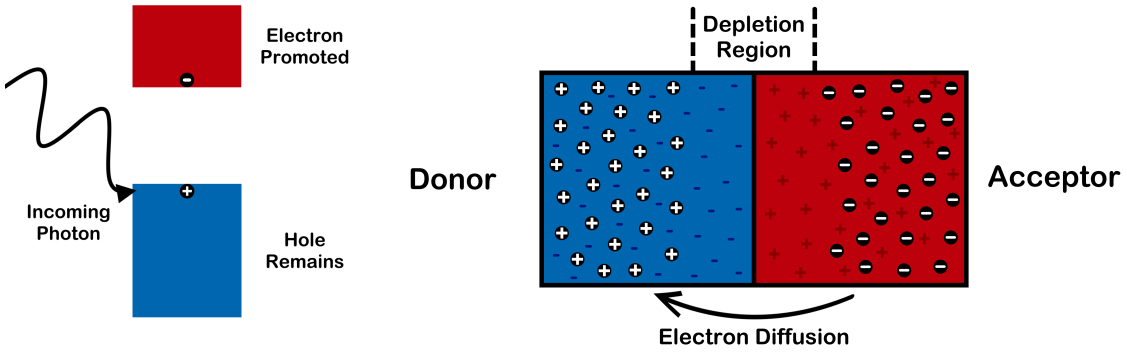

(a) The photoelectric effect

(b) A p-n junction

Figure 2.6: *Schematic of the photoelectric effect, where the band structure is as described in figure 2.1. Also shown is an example of a p-n junction of donor and acceptor material. Black circles depict free charge carriers within the system.*

in order to generate photovoltaic current. However, the process of charge extraction is more complex. An important property of the component materials of a PV is the relative electrical permittivity (quantified by the dielectric constant, ϵ_r), which can be thought of as a measure of how quickly a material can reorganise within the valence band to respond to changes in the local electric field[88]. Photoexcitation in semiconducting devices often results in an exciton - an electrostatically bound electron-hole quasi-particle, with a characteristic binding energy[89,90]. In inorganic devices, the dielectric constant is high ($\epsilon_{r,\,\text{silicon}} \sim 11.7$[7]), and charges within the valence band can reorder quickly to 'screen' the conductive electron from its hole. This results in a weakly bound exciton with binding energy typically of the order $0.01\,\text{eV}$[91]. These excitons are known as Wannier-Mott excitons, and their constituent charge carriers can be delocalised over several lattice constants[92,93]. Note that thermal fluctuations are of the order $\sim k_B T$ ($\simeq 0.025\,\text{eV}$ at $290\,\text{K}$) so, if the exciton binding energy is less than this value, the charges can be considered free and no longer Coulombically bound. Free charges can be extracted more easily at

the electrodes, resulting in high η. Conversely, organic semiconductors have a small electrical permittivity ($\epsilon_{r,\text{ organic}} \sim 3$[94]). Therefore, the opposing charges cannot be screened from each other as efficiently and excitations result in a tightly bound Frenkel exciton. Unlike Wannier-Mott excitons, Frenkel excitons are highly localised and exhibit a binding energy of the order $\sim 0.1{-}1\,\text{eV} >> k_B T$[91,95]. This high binding energy limits the exciton's lifetime, as the opposing charges will recombine back to the ground state within $\sim 0.5\,\text{ns}$, corresponding to a mean free path (called the exciton diffusion length) of around $5\,\text{nm}$[96]. Therefore, the binding energy must be overcome in order to dissociate the exciton and spatially separate the constituent charges within this time and length scale, so that they can be successfully extracted.

Both electrons and holes are fermions, in that they carry half-integer spin. Combinations of the spins of each particle result in different forms of Frenkel excitons within organic thin films[97]. A two-particle system is not only limited by whether its constituent particles are spin up and spin down, but also whether the two spins are in or out of phase. This leads to four possible spin-vector combinations. If the exciton contains one spin up carrier and one spin down carrier, both out of phase with each other, there is no resultant spin vector and both the spin and magnetic quantum numbers are zero ($S = M = 0$). This is the singlet state which, due to selection rules, is the excited state formed most commonly from photoexcitations[98]. Alternatively, if the particle spins are in phase ($S = 1$), a triplet excited species can form with magnetic moments $M = -1$, 0 or 1 depending on whether the spins of the particles are both down, opposing or both up respectively. Triplet excitons are degenerate in the absence of a magnetic field, and are generally more stable than

singlet excitons, with a lower energy and a longer lifetime (of the order ms[96]). It is not expected that triplet excitons have sufficient energy to separate into the free charge carriers needed for OPV operation, and as such, in the context of the work outlined in this thesis, they are considered as a loss mechanism[99]. For the remainder of this thesis, the term exciton will therefore be used to describe the Frenkel singlet exciton, which is expected to be the main species excited in OPVs[99].

As thermal fluctuations are generally insufficient to overcome the exciton's binding energy, the energy level difference between a pair of organic semiconductors is used instead, which is of a higher magnitude[100]. Within the active layer of OPVs, the component materials are selected so that the energy levels combine to form a 'type-II heterojunction', an example of which is shown in figure 2.2. This arrangement makes it energetically favourable for the exciton to dissociate into a charge-transfer (CT) state. In the CT state, the electron has tunnelled from a bound state in the donor material to a free state in the acceptor, but the hole remains on the donor side[101]. This involves a loss in energy of at least the exciton binding energy, as shown in figure 2.7[101]. Note that, although the example described here is for an exciton created in the donor phase, the dissociation process for an exciton propagating through the acceptor phase is equivalent, except the hole is transferred and the electron remains. It is a key requirement of the device morphology to ensure that, no matter where photons are absorbed within the device and excitons produced, as many as possible can reach the donor:acceptor interface so that dissociation can occur before the excitation decays to the ground state. Therefore, the size of morphological features should be of the same order as the exciton diffusion

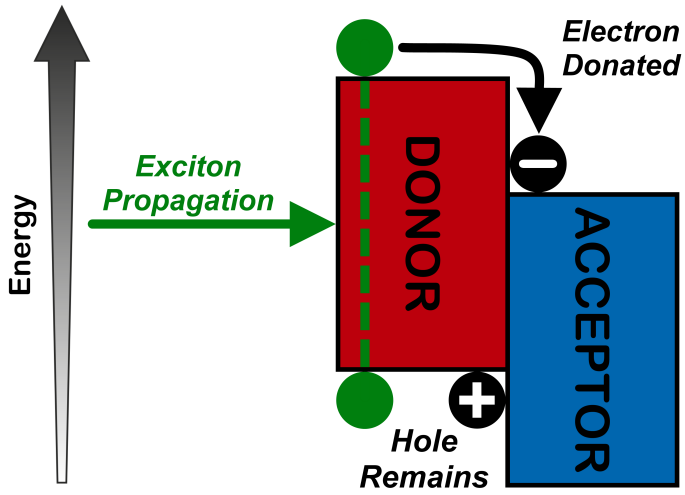

Figure 2.7: *A schematic representation of exciton dissociation at the donor:acceptor heterojunction, resulting in a CT state across the interface.*

length to ensure optimal exciton dissociation[102].

The low electrical permittivity of organic materials means that, after exciton dissociation, the opposing charges are not effectively shielded from each other and are still Coulombically bound. If the separation between the two charges is less than a critical Coulomb capture radius, r_c (estimated to be around 16 nm in OPVs at room temperature), then the dissociated charge carriers can still recombine to the ground state, across the heterojunction[103]. This is known as geminate recombination and can be an important loss mechanism within OPV devices[16,104]. A full investigation into the behaviour of charge recombination will be performed in chapter 4. If the energetic landscape surrounding the heterojunction is beneficial for charges to hop apart, carriers can increase mutual separation to the point where they are no longer Coulombically bound and thus avoid geminate recombination. Hot charge transfer states also provide a method with which to reduce the effect of geminate recombination. Due to the density of states around the heterojunction, there exists a manifold of available CT states, and it is possible for exciton dissociation to result

in a CT state of higher energy[105]. These HCTs result in a pair of charge carriers across the heterojunction with wavefunctions that are delocalised by several lattice constants[106]. As the HCTs relax, the charges become more localised, resulting in a pair of geminate charges that are spatially separated by an amount, r[107]. This reduces the Coulomb attraction between the two, permitting them to separate more easily and reducing the chance of geminate recombination. An investigation of the role HCTs play in improving the device performance characteristics will be presented in chapter 5.

The Coulomb force between two particles is given by:

$$F_{\text{Coulomb}} = \frac{1}{4\pi\epsilon_0\epsilon_r}\frac{q_1 q_2}{r^2}, \tag{2.4.2}$$

where q_1 and q_2 are the total charges carried by each particle ($\pm$ the unit charge in the case of the dissociated electron and hole) and r is the distance between them. The r^2 relationship indicates that Coulomb attraction falls off quickly as the two charges separate. When sufficient spatial separation has been attained for the charge pair, they are usually considered to be free before being swept through the device by the electric field, which is a composition of any applied voltage bias and the intrinsic field arising from the energy level arrangement of the heterojunction. However, there is a possibility that a charge might come across an opposing charge before it reaches the contact, causing them to recombine back to the ground state. This is called non-geminate or bimolecular recombination and is shown in many devices to be a more significant loss mechanism than geminate recombination[108,109]. Another key requirement of the morphology of an OPV is to provide good connectivity between

the heterojunction and the electrodes to ensure that the separated charges can be collected efficiently, reducing the effect of bimolecular recombination.

2.4.2 Morphology

OPV morphology can strongly affect η for a device. For instance, the 1986 Tang cell comprised of two layers of donor and acceptor material that were vacuum deposited on top of each other, resulting in a bilayer morphology where the heterojunction was a single plane through the middle of the device[33]. This type of morphology provides excellent charge collection characteristics, as dissociated charges have a direct path to their appropriate contact. However, photons can be absorbed anywhere within the active layer, resulting in excitons being produced throughout the morphology. Many of these excitons cannot propagate to the heterojunction plane within their lifetime, reducing the exciton dissociation efficiency and therefore the availability of free charges in the system[110,111].

In the mid 1990s, spin-coating techniques based on the miscibility of conjugated polymers and fullerene derivatives were used to create an interspersed blend of the polymer MEH-PPV and the highly soluble fullerene derivative $PC_{60}BM$, in what eventually became known as a solution processed BHJ morphology[112,113]. Some investigations have shown that forming a BHJ morphology from a P3HT:$PC_{60}BM$ blend can increase η by a factor of almost 8, compared to bilayer devices[114]. An idealised, simulated example is shown in figure 2.8, where the material phases of the blend have separated, resulting in domains of pure donor material (the red coloured sites) and pure acceptor material (coloured in blue). When the dissolved donor-

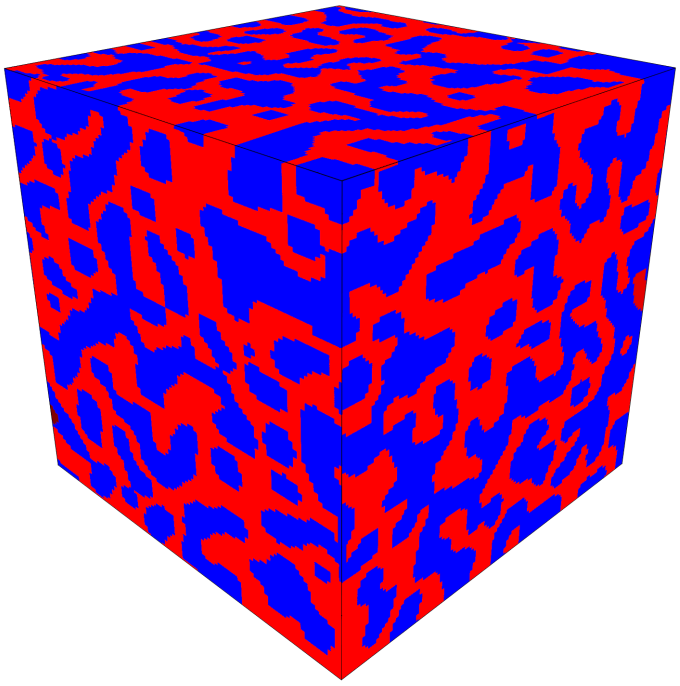

Figure 2.8: *An example bulk heterojunction morphology for a simulated P3HT:PC_{61}BM blend exhibiting complete spinodal decomposition between the donor (red) and acceptor (blue) phases.*

acceptor mixture is quenched (by, for example, heating and then quickly cooling), the mixture's composition, x, is approximately homogeneous throughout the morphology[115]. If the Gibb's free energy of the system, $G(x)$ is such that $\mathrm{d}^2G(x)/\,\mathrm{d}x^2 < 0$, then small perturbations in the local composition cause $G(x)$ to decrease. This allows regions of increased donor composition to form at the expense of acceptor material and *vice versa*. The perturbation grows to reduce $G(x)$ further, resulting in a phase-separated mixture that is commonly found within BHJ solar cells[116]. This process is dependent on the miscibility of the constituent materials, and so it is often more common that a third, mixed molecular phase forms, where significant proportions of both donor and acceptor material are present[117]. The mixed phase generally limits the device performance as both electrons and holes can propagate through the medium, without increasing mutual separation[117]. This leads to a

higher proportion of recombination events, reducing the output current[118]. The role of the mixed phase in charge separation will be characterised in more detail in chapter 5.

In general, blending the component organic materials together instead of depositing bilayers permits a larger quantity of heterojunctions (and hence interfacial area) to form throughout the entire active layer, reducing the average distance that an exciton must propagate in order to dissociate. Increasing the interfacial area from $<2 \times 10^5\,\mathrm{nm}^2$ (as might be expected in a bilayer device) to $\sim 1 \times 10^6\,\mathrm{nm}^2$ (as might be expected in an interpenetrated blend morphology) can increase the exciton dissociation efficiency by a factor of 4[119], with some blends exhibiting near unity dissociation efficiency[120–122]. However, the design of BHJs is somewhat of a compromise, as an increase in the number of heterojunctions within the active layer also restricts the domains that separated charges can move through, making it more difficult for them to reach the contacts[119]. This increases the level of morphological trapping within the device as charges can become 'stuck' on certain morphological features, risking recombination and reducing device efficiency[123]. It is therefore of paramount importance for manufacturers to optimise the morphology of BHJ devices to maximise η. To this end, it is possible to strongly affect the nanoscale structure of the active layer by varying the mixing[124] and preparation[125] methods of the constituent organic materials, or by applying a selection of post-processing methods such as solvent[126] and thermal annealing[127] to the devices to stimulate further crystallisation/interpenetration of the BHJ network. Additives can also be incorporated to stimulate crystallisation[128], or create an 'energy cascade' - a ternary

blend, formed with small molecules that exist at the donor:acceptor interface. The molecule is selected such that one of its HOMO or LUMO levels align with the donor and acceptor material, transporting one carrier species away from the interface and trapping it in a position where it cannot recombine geminately[129,130]. Device morphology can also be controlled by the synthesis of the donor and acceptor materials, as semiconductors can be constructed that optimise the π-stacking distance[131,132], miscibility[133] or planarity of the molecules to reduce twisting around the backbone vector[42]. With this knowledge it has been possible to create OPVs with $\eta > 9\%$[72,134,135]. The techniques used in the literature tend to be specific to individual materials or, as in the case of the well-documented polymer P3HT, specific to samples with the same properties, as regioregularity and molecular weight can strongly affect morphological evolution[136].

Device morphology is also important on the molecular level, particularly when using conjugated polymers which have a wide range of accessible conformations and orientations within the medium[137]. Due to the increased overlap of the molecular orbitals, charge carriers tend to have higher mobilities in crystalline or aggregated materials by at least an order of magnitude[138], with some small molecules reporting a five order of magnitude increase in mobility when compared to the amorphous state[139]. Aggregation in fullerenes can also increase the electron affinity of the molecules, leading to more efficient charge separation within the pure domains[140,141]. Therefore the size and purity of crystalline domains within the morphology can strongly affect the device efficiency[142]. Chapter 6 investigates the influence of the crystal structure of P3HT on the charge transport characteristics,

showing that the non-crystalline, amorphous regions of the morphology also play a role in the carrier mobility. Other complex morphological structures at the donor-acceptor heterojunction can also affect device performance. Resonant soft X-ray scattering measurements of PNDT-DTBT donor polymer derivatives have shown that η can increase by a factor of almost 3 in OPVs when the π-stacking structures are orientated along the plane of the heterojunction, compared to when chains are stacked perpendicular to the interface[143]. Additionally, nuclear magnetic resonance spectroscopy has suggested that there exists preferential donor-acceptor copolymer:fullerene orientations that maximise mobility when the fullerenes are docked to the electron accepting moieties[63]. Quantum chemical calculations have shown that, for small molecules and oligomers in the pure material phase, face-to-edge orientations in the form of a herringbone crystal result in larger transfer integrals and therefore improved charge transport in the system[138,144]. Further investigation of the transfer integrals in a pristine P3HT thin film is presented in chapter 6.

2.5 Characterisation

After an OPV has been manufactured, there are a variety of characterisation techniques available that can be used to compare device properties. It is common to plot a J-V characteristic curve for the system that relates the output current density of the device, J, to the applied voltage bias across the contacts, V. An example J-V curve is shown in figure 2.9. By definition, a photovoltaic must generate a photocurrent in the absence of an applied bias[145]. This is known as the short-circuit current, J_{SC}[146], the value of which can be increased by modifying the bandgap of

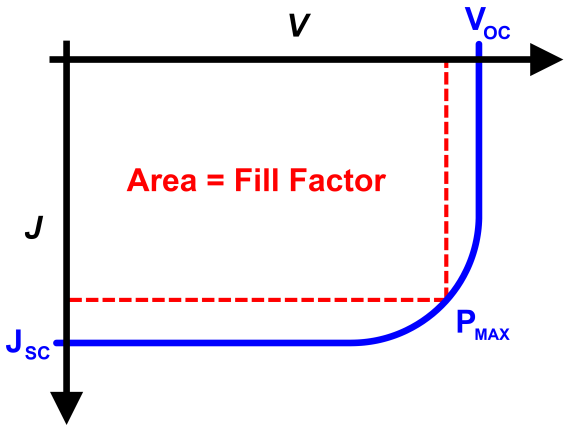

Figure 2.9: *An example J-V curve for a typical photovoltaic device. J_{SC} is the short-circuit current density, V_{OC} is the open-circuit voltage and P_{MAX} denotes the maximum power point for the device.*

the component polymers to increase the amount of harvested sunlight[147,148]. The open-circuit voltage, V_{OC}, is another important quantity in OPVs, defined as the voltage at which no current flows through the device. This value is dependent on the energy levels of the constituent materials and so is determined more by device composition than morphology[149].

The 'maximum power point', $P_{\mathrm{MAX}} = V_{\mathrm{MAX}} J_{\mathrm{MAX}}$, describes the device when it is operating optimally and the generated power is at a maximum. However, it is uncommon for the maximum power point to be discussed explicitly. Instead, the fill-factor (FF) is often used which describes the area of the J-V curve between the axes and the maximum power point:

$$\mathrm{FF} = \frac{J_{\mathrm{MAX}} V_{\mathrm{MAX}}}{J_{\mathrm{SC}} V_{\mathrm{OC}}}. \tag{2.5.3}$$

In general, efficient OPVs exhibit FFs > 0.6[150].

By using these definitions, it is possible to come up with an expression for η:

$$\eta = \frac{\mathrm{FF} \cdot V_{\mathrm{OC}} \cdot J_{\mathrm{SC}}}{P}, \tag{2.5.4}$$

where P is the input power spectrum. It is common to use the industry standard air mass index AM1.5 for the value of P, which corresponds to $P \sim 1000\,\mathrm{W\,m^{-2}}$ - the approximate power at ground level given by unobscured sunlight at the zenith.[151].

It can sometimes be useful to consider η in terms of the physical processes of exciton dissociation and subsequent charge separation, as these can be probed directly by optical techniques. For instance, the morphology-dependent exciton dissociation efficiency can be determined from PL spectroscopy[152]. When an exciton decays back to the ground state, a photon can be re-emitted. This process is called photoluminescence, and spectroscopists can use it to infer the exciton dissociation efficiency by measuring the PL emission of a material, before and after blending[153]. The technique is especially useful as the excitations are not confined to a single energy level, but in fact populate a manifold of excited states with different energies as depicted in figure 2.10a. This results in different photoluminescent wavelengths being produced, which can be analysed to determine the nature of the excited state manifold[154].

The separation efficiency, η_{SEP} corresponds to the fraction of charge transfer states that convert to spatially separated charges that are no longer considered to be Coulombically bound. This is comparable to the internal quantum efficiency (IQE) that is measured for devices experimentally, which is the ratio of collectable carriers to the number of absorbed photons (*i.e.* excluding incident photons that

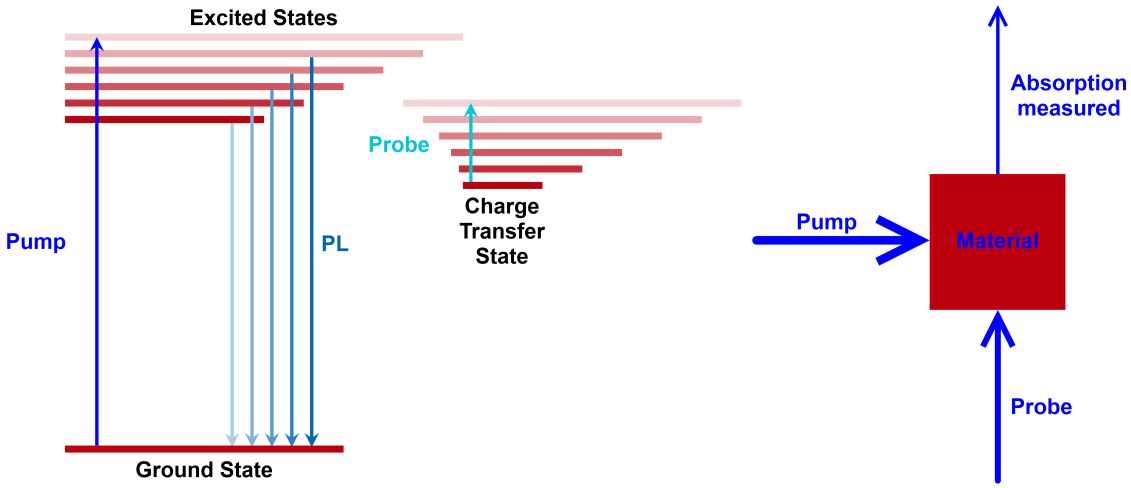

(a) Photoluminescence and Pump-probe

(b) Photoinduced Absorption

Figure 2.10: *Energy level diagram and schematic describing photoluminescence and photoinduced absorption.*

are lost through reflection or transmission)[155]. A full investigation into η_{SEP} and comparison to literature determinations of the IQE can be found in chapters 4 and 5, but, depending on the materials and methods, η_{SEP} is typically greater than 0.5[141,156], even approaching unity for some devices[121].

Both η_{DIS} and η_{SEP} can be investigated by exploring the evolution of the CT state population as a function of time, using photoinduced absorption (PIA) spectroscopy as depicted in figure 2.10b. First, the material is 'pumped' with a high-energy beam that stimulates the production of excitons and their subsequent dissociation, resulting in an increased population of CT states. Then, a second, low-energy 'probe' beam is fired at the material. By determining how much of the probe beam is absorbed, and comparing it to the absorption prior to the pump, the CT state population can be measured in real-time. Results from this 'pump-probe' technique have been used to suggest 'ultra-fast' charge generation mechanisms occurring within devices, in an attempt to explain the high IQEs that are sometimes obtained[157].

2.6 Summary

The field of organic electronics is a fast-moving area of research and active discussion. Device efficiency records are frequently broken as new materials are created or new manufacturing processes are developed. Even when the composition of the active layer is the same, subtle changes in the deposition or annealing processes can dramatically affect the morphology of the device, which is inextricably linked to its overall performance. Often, it is unclear how the morphology directly affects the power conversion efficiency, despite the wealth of experimental methods used to characterise manufactured devices. It therefore falls to alternative methodologies to bridge the gap between input morphology and output performance, which will be discussed in the next chapter.

References

[1] E. Reichmanis, H. Katz, C. Kloc, and A. Maliakal. "Plastic Electronic Devices: From Materials Design to Device Applications." *Bell Labs Techn. J.*, **10**, 87–105, 2005.

[2] Z. Bao and J. Locklin. *Organic Field-Effect Transistors*. CRC Press, 2007.

[3] S. M. Blinder. *Introduction to Quantum Mechanics: In Chemistry, Materials Science, and Biology*. Academic Press, 2012.

[4] W. Brütting and C. Adachi. *Physics of Organic Semiconductors*. John Wiley & Sons, 2012.

[5] H. Saal, T. Bredow, and M. Binnewies. "Band Gap Engineeering of ZnO via Doping with Manganese: Effect of Mn Clustering." *Phys. Chem. Chem. Phys.*, **11**, 3201–3209, 2009.

[6] N. E. Carpenter. *Chemistry of Sustainable Energy*. CRC Press, 2014.

[7] C. Kittel. *Introduction to Solid State Physics*. John Wiley and Sons, 2005.

[8] T. J. Ishii. *Components and Devices*. Academic Press, 2013.

[9] G. Parthasarathy, C. Shen, A. Kahn, and S. R. Forrest. "Lithium Doping of Semiconducting Organic Charge Transport Models." *J. Appl. Phys.*, **89**, 4986–4992, 2001.

[10] B. Lüssem, M. Riede, and K. Leo. "Doping of Organic Semiconductors." *Phys. Status Solidi A*, **210**, 9–43, 2013.

[11] C. Brabec, V. Dyakonov, and U. Scherf. *Organic Photovoltaics: Materials, Device Physics and Manufacturing Technologies*. Wiley-VCH, 2010.

[12] S. Yang, P. Olishevski, and M. Kertesz. "Bandgap Calculations for Conjugated Polymers." *Synt. Met.*, **141**, 171–177, 2004.

[13] J. O'M. Bockris and S. U. M. Khan. *Surface Electrochemistry: A Molecular Level Approach*. Springer Science & Business Media, 2013.

[14] J. Moore, C. Stanitski, and P. Jurs. *Principles of Chemistry: The Molecular Science*. Cengage Learning, 2009.

[15] Y Li. "Molecular Design of Photovoltaic Materials for Polymer Solar Cells: Toward Suitable Electronic Energy Levels and Broad Absorption." *Acc. Chem. Res.*, **45**, 723–733, 2012.

[16] H. Huang and J. Huang. *Organic and Hybrid Solar Cells.* Springer, 2014.

[17] P. M. Beaujuge and J. M. J. Fréchet. "Molecular Design and Ordering Effects in π-Functional Materials for Transistor and Solar Cell Applications." *J. Am. Chem. Soc.*, **133**, 20009–20029, 2011.

[18] A. R. Murphy and J. M. J. Fréchet. "Organic Semiconducting Oligomers for Use in Thin Film Transistors." *Chem. Rev.*, **107**, 1066–1096, 2007.

[19] M. Redecker, D. D. C. Bradley, M. Inbasekaran, W. W. Wu, and E. P. Woo. "High Mobility Hole Transport Fluorene-Triarylamine Copolymers." *Adv. Mater.*, **11**, 241–246, 1999.

[20] I. Kymissis. *Organic Field Effect Transistors: Theory, Fabrication and Characterization.* Springer Science & Business Media, 2008.

[21] R. Dost, A. Das, and M. Grell. "Time-of-flight Mobility Measurements in Organic Field-Effect Transistors." *J. Appl. Phys.*, **104**, 084519–1:084519:6, 2008.

[22] J. Roncali. "Molecular Bulk Heterojunctions: An Emerging Approach to Organic Solar Cells." *Acc. Chem. Res.*, **42**, 1719–1730, 2009.

[23] Y. Liu, X. Wan, F. Wang, J. Zhou, G. Long, J. Tian, J. You, Y. Yang, and Y. Chen. "Spin-Coated Small Molecules for High Performance Solar Cells." *Adv. Energy Mater.*, **1**, 771–775, 2011.

[24] A. C. Arias, J. D. MacKenzie, I. McCulloch, J. Rivnay, and A. Salleo. "Materials and Applications for Large Area Electronics: Solution-Based Approaches." *Chem. Rev.*, **110**, 3–24, 2010.

[25] K. Chen, A. J. Barker, M. E. Reish, K. C. Gordon, and J. M. Hodgkiss. "Broadband Ultrafast Photoluminescence Spectroscopy Resolves Charge Photogeneration via Delocalized Hot Excitons in Polymer:Fullerene Photovoltaic Blends." *J. Am. Chem. Soc.*, **135**, 18502–18512, 2013.

[26] D. J. Gundlach, Y. Y. Lin, T. N. Jackson, S. F. Nelson, and D. G. Schlom. "Pentacene Organic Thin-Film Transistors - Molecular Ordering and Mobility." *IEEE Electron Device Lett.*, **18**, 87–89, 1997.

[27] C. D. Sheraw, T. N. Jackson, D. L. Eaton, and J. E. Anthony. "Functionalized Pentacene Active Layer Organic Thin-Film Transistors." *Adv. Mater.*, **15**, 2009–2011, 2003.

[28] S. K. Park, T. N. Jackson, J. E. Anthony, and D. A. Mourey. "High Mobility Solution Processed 6,13-bis(triisopropyl-silylethynyl) pentacene Organic Thin Film Transistors." *Appl. Phys. Lett.*, **91**, 063514:1–063514:3, 2007.

[29] G. Horowitz, F. Garnier, A. Yassar, R. Hajlaoui, and Kouki F. "Field-Effect Transistor Made with a Sexithiophene Single Crystal." *Adv. Mater.*, **8**, 52–54, 1996.

[30] M. Halik, H. Klauk, U. Zschieschang, G. Schmid, W. Radlik, and S. Ponomarenko. "High-Mobility Organic Thin-Film Transistors Based on α, α', -didecyloligothiophenes." *J. Appl. Phys.*, **93**, 2977–2981, 2003.

[31] S. A. Ponomarenko, S. Kirchmeyer, M. Halik, H. Klauk, U. Zschieschang, G. Schmid, A. Karbach, D. Drechsler, and N. M. Alpatova. "1,4-bis(5-decyl-2,2'-bithien-5-yl)benzene as a New Stable Organic Semiconductor for High Performance Thin Film Transistors." *Synth. Met.*, **149**, 231–235, 2005.

[32] Y. Yuan, G. Giri, A. L. Ayzner, A. P. Zoombelt, S. C. B. Mannsfeld, J. Chen, D. Nordlund, M. F. Toney, J. Huang, and Z. Bao. "Ultra-High Mobility Transport Organic Thin Film Transistors Grown by an Off-Centre Spin-Coating Method." *Nature Commun.*, **5**, 3005:1–3005:9, 2014.

[33] C. W. Tang. "Two-Layer Organic Photovoltaic Cell." *Appl. Phys. Lett.*, **48**, 183–185, 1986.

[34] P. Peumans and S. R. Forrest. "Very-high-efficiency Double-heterostructure Copper Pthalocyanine/C_{60} Photovoltaic Cells." *Appl. Phys. Lett.*, **79**, 126–128, 2001.

[35] B. Walker, A. B. Tamayo, X.-D. Dang, P. Zalar, J. H. Seo, A. Garcia, M. Tantiwiwat, and T.-Q. Nguyen. "Nanoscale Phase Separation and High Photovoltaic Efficiency in Solution-Processed, Small-Molecule Bulk Heterojunction Solar Cells." *Adv. Funct. Mater.*, **19**, 3063–3069, 2009.

[36] Y. Sun, G. C. Welch, W. L. Leon, C. J. Takacs, G. C. Bazan, and A. J. Heeger. "Solution-Processed Small-Molecule Solar Cells with 6.7% Efficiency." *Nature Mater.*, **11**, 44–48, 2012.

[37] Q. Zhang, B. Kan, F. Liu, G. Long, X. Wan, X. Chen, Y. Zuo, W. Ni, H. Zhang, M. Li, Z. Hu, F. Huang, Y. Cao, Z. Liang, M. Zhang, T. P. Russell, and Y. Chen. "Small-Molecule Solar Cells with Efficiency Over 9%." *Nature Photon.*, **9**, 35–41, 2015.

[38] B. Kraabel, D. McBranch, N. S. Sariciftci, D. Moses, and A. J. Heeger. "Ultrafast Spectroscopic Studies of Photoinduced Electron Transfer from Semiconducting Polymers to C_{60}." *Phys. Rev. B*, **50**, 18543–18552, 1994.

[39] N. Marjanovic, G. J. MAtt, S. Günes, N. S. Sariciftci, A. M. Ramil, A. Andreev, H. Sitter, R. Schwödiauer, and S. Bauer. "Organic Thin-Film Electronics." *Mater. Res. Soc. Symp. Proc.*, **871E**, I 4.9.1, 2005.

[40] H. Shirakawa, E. J. Louis, A. G. MacDiarmid, C. K. Chiang, and A. J. Heeger. "Synthesis of Electrically Conducting Organic Polymers: Halogen Derivatives of Polyacetylene, $(CH)_x$." *J. Chem. Soc., Chem. Commun.*, **1**, 578–580, 1977.

[41] G. Hill and J. Holman. *Chemistry in Context*. Nelson Thornes, 2000.

[42] H. N. Tsao and K. Müllen. "Improving Polymer Transistor Performance *via* Morphology Control." *Chem. Soc. Rev.*, **39**, 2372–2386, 2010.

[43] S.-S. Sun and L. R. Dalton. *Introduction to Organic Electronic and Optoelectronic Materials and Devices*. CRC Press, 2008.

[44] H. Sirringhaus, P. J. Brown, R. H. Friend, M. M. Nielsen, K. Bechgaard, B. M. W. Langeveld-Voss, A. J. H. Spiering, R. A. J. Janssen, E. W. Meijer, P. Herwig, and D. M. de Leeuw. "Two-Dimensional Charge Transport in Self-Organized, High-Mobility Conjugated Polymers." *Nature*, **401**, 685–688, 1999.

[45] Y. Kim, S. Cook, S. M. Tuladhar, S. A. Choulis, J. Nelson, J. R. Durrant, D. D. C. Bradley, M. Giles, I. McCulloch, C.-S. Ha, and M. Ree. "A Strong Regioregularity Effect in Self-Organising Conjugated Polymer Films and High-Efficiency Polythiophene:Fullerene Solar Cells." *Nature Mater.*, **5**, 197–203, 2006.

[46] C. Cabanetos, A. El Labban, J. A. Bartelt, J. D. Douglas, W. R. Mateker, J. M. J. Fréchet, M. D. McGehee, and P. M. Beaujuge. "Linear Side Chains in Benzo[1,2-b:4,5-b']dithiophene-Thieno[3,4-c]pyrrole-4,6-dione Polymers Direct Self-Assembly and Solar Cells Performance." *J. Am. Chem. Soc.*, **135**, 4656–4659, 2013.

[47] F. C. Krebs, T. Tromholt, and M. Jørgensen. "Upscaling of Polymer Solar Cell Fabrication Using Full Roll-to-Roll Processing." *Nanoscale*, **2**, 873–886, 2010.

[48] Y. Liu, X. Wan, F. Wang, J. Zhou, G. Long, J. Tian, and Y. Chen. "High-Performance Solar Cells Using a Solution-Processed Small Molecule Containing Benzodithiophene Unit." *Adv. Mater.*, **23**, 5387–5391, 2011.

[49] S. S. Pandey, W. Takashima, S. Nagamatsu, T. Endo, M. Rikukawa, and K. Kaneto. "Regioregularity vs Regiorandomness: Effect on Photocarrier Transport in Poly(3-hexylthiophene)." *Jpn. J. Appl. Phys.*, **39**, L94–L97, 2000.

[50] R. Mauer, M. Kastler, and F. Laquai. "The Impact of Polymer Regioregularity on Charge Transport and Efficiency of P3HT:PCBM Photovoltaic Devices." *Adv. Funct. Mater.*, **20**, 2085–2092, 2010.

[51] H. Sirringhaus, N. Tessler, and R. H. Friend. "Integrated Optoelectronic Devices Based on Conjugated Polymers." *Science*, **280**, 1741–1744, 1998.

[52] L. Torsi, N. Cioffi, C. Di Franco, L. Sabbatini, P. G. Zambonin, and T. Bleve-Zacheo. "Organic Thin Film Transistors: From Active Materials to Novel Applications." *Solid State Electron.*, **45**, 1479–1485, 2001.

[53] G. Li, V. Shrotriya, J. Huang, Y. Yao, T. Moriarty, K. Emery, and Y. Yang. "High-Efficiency Solution Processable Polymer Photovoltaic Cells by Self-Organization of Polymer Blends." *Nature Mater.*, **4**, 864–868, 2005.

[54] C. H. Peters, I. T. Sachs-Quintana, J. P. Kastrop, S. Beaupré, M. Leclerc, and M. D. McGehee. "High Efficiency Polymer Solar Cells with Long Operating Lifetimes." *Adv. Energy Mater.*, **1**, 491–494, 2011.

[55] C. Wang, L. H. Jimison, L. Goris, I. McCulloch, M. Heeney, A. Ziegler, and A. Salleo. "Microstructural Origin of High Mobility in High-Performance Poly(thieno-thiophene) Thin-Film Transistors." *Adv. Mater.*, **22**, 697–701, 2010.

[56] I. McCulloch, M. Heeney, C. Bailey, K. Genevicius, I. MacDonald, M. Shkunov, D. Sparrowe, S. Tierney, R. Wagner, W. Zhang, M. L. Chabinyc, R. J. Kline, M. D. McGehee, and M. F. Toney. "Liquid-Crystalline Semiconducting Polymers with High Charge-Carrier Mobility." *Nature Mater.*, **5**, 328–333, 2006.

[57] J. E. Parmer, A. C. Mayer, B. E. Hardin, S. R. Scully, M. D. McGehee, M. Heeney, and I. McCulloch. "Organic Bulk Heterojunction Solar Cells Using Poly(2,5-bis(3-tetradecyllthiophen-2-yl)thieno[3,2,-b]thiophene)." *Appl. Phys. Lett.*, **92**, 113309:1–113309:3, 2008.

[58] N. C. Miller, S. Sweetnam, E. T. Hoke, R. Gysel, C. E. Miller, J. A. Bartelt, X. Xie, M. F. Toney, and M. D. McGehee. "Molecular Packing and Solar Cell Performance in Blends of Polymers with a Bisadduct Fullerene." *Nano Lett.*, **12**, 1566–1570, 2012.

[59] G. G. Wallace, P. C. Dastoor, D. L. Officer, and C. O. Too. "Conjugated Polymers: New Materials for Photovoltaics." *Chemical Innovation*, **30**, 14–22, 2000.

[60] M. Redecker, D. D. C. Bradley, M. Inbasekeran, and E. P. Woo. "Mobility Enhancement through Homogeneous Nematic Alignmnet of a Liquid-Crystalline Polyfluorene." *Appl. Phys. Lett.*, **74**, 1400–1402, 1999.

[61] K. Müllen and U. Scherf. *Organic Light Emitting Devices: Synthesis, Properties and Applications*. John Wiley & Sons, 2006.

[62] P. Sonar, S. P. Singh, Y. Li, Z.-E. Ooi, T.-J. Ha, I. Wong, M. S. Soh, and A. Dodabalapur. "High Mobility Organic Thin Film Transisitor and Efficient Photovoltaic Devices Using Versatile Donor-Acceptor Polymer Semiconductor by Molecular Design." *Energy Environ. Sci.*, **4**, 2288–2296, 2011.

[63] K. R. Graham, C. Cabanetos, J. P. Jahnke, M. N. Idso, A. El Labban, G. O. N. Ndjawa, T. Heumueller, K. Vandewal, A. Salleo, B. F. Chmelka, A. Amassian, P. M. Beaujuge, and M. D. McGehee. "Importance of the Donor:Fullerene Intermolecular Arrangement for High-Efficiency Organic Photovoltaics." *J. Am. Chem. Soc.*, **136**, 9608–9618, 2014.

[64] H. Zhou, L. Yang, and W. You. "Rational Design of High Performance Conjugated Polymers for Organic Solar Cells." *Macromolecules*, **45**, 607–632, 2012.

[65] Z. He, C. Zhong, S. Su, M. Xu, H. Wu, and Y. Cao. "Enhanced Power-Conversion Efficiency in Polymer Solar Cells Using an Inverted Device Structure." *Nature Photon.*, **6**, 591–595, 2012.

[66] S. B. Darling and F. You. "The Case of Organic Photovoltaics." *RSC Adv.*, **3**, 17633–17648, 2013.

[67] P. J. Hotchkiss, S. C. Jones, S. A. Paniagua, A. Sharma, B. Kippelen, N. R. Armstrong, and S. R. Marder. "The Modification of Indium Tin Oxide with Phosphonic Acids: Mechanism of Binding, Tuning of Surface Properties, and Potential for Use in Organic Electronic Applications." *Acc. Chem. Res.*, **45**, 337–346, 2012.

[68] M. D. Irwin, D. B. Buchholz, A. W. Hains, R. P. H. Chang, and T. J. Marks. "p-Type Semiconducting Nickel Oxide as an Efficiency-Enhancing Anode Interfacial Layer in Polymer Bulk-Heterojunction Solar Cells." *Proc. Natl. Acad. Sci. U.S.A.*, **105**, 2783–2787, 2008.

[69] A. Kojima, K. Teshima, Y. Shirai, and T. Miyasaka. "Organometal Halide Perovskites as Visible-Light Sensitizers for Photovoltaic Cells." *J. Am. Chem. Soc.*, **131**, 6050–6051, 2009.

[70] Z. Fan, K. Sun, and J. Wang. "Perovskites for Photovoltaics: A Combined Review of Organic-Inorganic Halide Perovskites and Ferroelectric Oxide Perovskites." *J. Mater. Chem. A*, **3**, 18809–18828, 2015.

[71] J. H. Noh, S. H. Im, J. H. Heo, T. H. Mandal, and S. I. Seok. "Chemical Management for Colorful, Efficient and Stable Inorganic-Organic Hybrid Nanostructured Solar Cells." *Nano Lett.*, **13**, 1764–1769, 2013.

[72] M. A. Green, K. Emery, Y. Hishikawa, W. Warta, and E. D. Dunlop. "Solar Cell Efficiency Tables (Version 45)." *Prog. Photovolt: Res Appl.*, **23**, 1–9, 2015.

[73] N. J. Jeon, J. H. Noh, Y. C. Kim, W. S. Yang, S. Ryu, and S. I. Seok. "Solvent Engineering for High-Performance Inorganic-Organic Hybrid Perovskite Solar Cells." *Nature Mater.*, **13**, 897–903, 2014.

[74] D. B. Mitzi. "Templating and Structural Engineering in Organic-Inorganic Perovskites." *J. Chem. Soc., Dalton Trans.*, **1**, 1–12, 2001.

[75] C. C. Stoumpos, C. D. Malliakas, and M. G. Kanatzidis. "Semiconducting Tin and Lead Iodide Perovskites with Organic Cations: Phase Transisitions, High Mobilities, and Near-Infrared Photoluminescent Properties." *Inorg. Chem.*, **51**, 9019–9038, 2013.

[76] C. S. Ponseca, T. J. Savenije, M. Abdellah, K. Zheng, A. Yartsev, T. Pascher, T. Harlang, P. Chabera, T. Pullerits, A. Stepanov, J.-P. Wolf, and V. Sundström. "Organometal Halide Perovskite Solar Cell Materials Rationalized: Ultrafast Charge Generation, High and Microsecond-Long Balanced Mobilities, and Slow Recombination." *J. Am. Chem. Soc.*, **136**, 5189–5192, 2014.

[77] S. D. Stranks, G. E. Eperon, G. Grancini, C. Menelaou, M. J. P. Alcocer, T. Leijtens, L. M. Herz, A. Petrozza, and H. J. Snaith. "Electron-Hole Diffusion Lengths Exceeding 1 Micrometer in an Organometal Trihalide Perovskite Absorber." *Science*, **342**, 341–344, 2013.

[78] M. D. McGehee. "Continuing to Soar." *Nature Mater.*, **13**, 845–846, 2014.

[79] R. F. Pierret. *Semiconductor Device Fundamentals*. Addison Wesley Longman, 1996.

[80] C. Bowick. *RF Circuit Design*. Newnes, 2011.

[81] R. Kelsall, I. W. Hamley, and M. Geoghegan. *Nanoscale Science and Technology*. John Wiley & Sons, 2005.

[82] S. M. Sze and K. Ng. Kwok. *Physics of Semiconductor Devices*. John Wiley & Sons, 2012.

[83] R. C. Jaeger and T. N. Blalock. *Microelectronic Circuit Design*. McGraw-Hill, 2011.

[84] Y. Li. *Organic Optoelectronic Materials*. Springer, 2015.

[85] J. Roncali, P. Leriche, and A. Cravino. "From One- to Three- Dimensional Organic Semiconductors: In Search of the Organic Silicon?" *Adv. Mater.*, **19**, 2045–2060, 2007.

[86] G. Horowitz. "Organic Field-Effect Transistors." *Adv. Mater.*, **10**, 365–377, 1998.

[87] A.-E. Becquerel. "Memoire sur les Effets Électriques Produits sous L'influence des Rayons Solaires." *C. R. Acad. Sci.*, **9**, 561–567, 1839.

[88] N. E. Hill, W. E. Vaughan, A. H. Price, and M. Davies. *Dielectric Properties and Molecular Behaviour*. van Nostrand Reinhold Company Ltd., 1969.

[89] S. F. Alvarado, P. F. Seidler, D. G. Lidzey, and D. D. C. Bradley. "Direct Determination of the Exciton Binding Energy of Conjugated Polymers Using a Scanning Tunneling Microscope." *Phys. Rev. Lett.*, **81**, 1082–1085, 1998.

[90] A. R. Blythe and D. Bloor. *Electrical Properties of Polymers*. Cambridge University Press, 2005.

[91] A. M. Fox. *Optical Properties of Solids*. Oxford University Press, 2001.

[92] G. H. Wannier. "The Structure of Electronic Excitation Levels in Insulating Crystals." *Phys. Rev.*, **52**, 191–197, 1937.

[93] D. J. Gaspar and E. Polikarpov. *OLED Fundamentals: Materials, Devices, and Processing of Organic Light-Emitting Diodes*. CRC Press, 2015.

[94] R. P. Mikalo and D. Schmeißer. "Electric Contacts on Conductive Polymers: Sodium on Poly(3-hexylthiophene-2,5-diyl)." *Synt. Met.*, **127**, 273–277, 2002.

[95] B. A. Gregg and M. C. Hanna. "Comparing Organic to Inorganic Photovoltaic Cells: Theory, Experiment, and Simulation." *J. Appl. Phys.*, **93**, 3605–3614, 2003.

[96] R. R. Lunt, N. C. Giebink, A. A. Belak, J. B. Benziger, and S. R. Forrest. "Exciton Diffusion Lengths of Organic Semiconductor Thin Films Measured by Spectrally Resolved Photoluminescence Quenching." *J. Appl. Phys.*, **105**, 053711:1–053711:7, 2009.

[97] A. Köhler and H. Bässler. "Triplet States in Organic Semicondcutors." *Mater. Sci. Eng. R-Rep.*, **66**, 71–109, 2009.

[98] C. Deibel and V. Dyakonov. "Polymer-Fullerene Bulk Heterojunction Solar Cells." *Rep. Prog. Phys.*, **73**, 096401:1–096401:68, 2010.

[99] A. Rao, P. C. Y. Chow, S. Gélinas, C. W. Schlenker, C.-Z. Li, H.-L. Yip, A. K.-Y. Jen, D. S. Ginger, and R. H. Friend. "The Role of Spin in the Kinetic Control of Recombination in Organic Photovoltaics." *Nature*, **500**, 435–439, 2013.

[100] B. A. Gregg. "The Photoconversion Mechanism of Excitonic Solar Cells." *MRS Bull.*, **30**, 20–22, 2005.

[101] P. Würfel and U. Würfel. *Physics of Solar Cells: From Basic Principles to Advanced Concepts*. John Wiley & Sons, 2009.

[102] B. P. Lyons, N. Clarke, and C. Groves. "The Relative Importance of Domain Size, Domain Purity and Domain Interfaces to the Performance of Bulk-Heterojunction Organic Photovoltaics." *Energy Environ. Sci.*, **5**, 7657–7663, 2012.

[103] M. Hilczer and M. Tachiya. "Unified Theory of Geminate and Bulk Electron-Hole Recombination in Organic Solar Cells." *J. Phys. Chem. C*, **114**, 6808–6813, 2010.

[104] C. R. McNeill, S. Westenhoff, C. Groves, R. H. Friend, and N. C. Greenham. "Influence of Nanoscale Phase Separation on the Charge Generation Dynamics and Photovoltaic Performance of Conjugated Polymer Blends: Balancing Charge Generation and Separation." *J. Phys. Chem. C*, **111**, 19153–19160, 2007.

[105] G. Grancini, M. Maiuri, D. Fazzi, A. Petrozza, H-J. Egelhaaf, D. Brida, G. Cerullo, and G. Lanzani. "Hot Exciton Dissociation in Polymer Solar Cells." *Nature Mater.*, **12**, 29–33, 2013.

[106] A. A. Bakulin, A. Rao, V. G. Pavelyev, P. H. M. van Loosdrecht, M. S. Pshenichnikov, D. Niedzialek, J. Cornil, D. Beljonne, and R. H. Friend. "The Role of Driving Energy and Delocalized States for Charge Separation in Organic Semiconductors." *Science*, **335**, 1340–1344, 2012.

[107] A. Troisi. "How Quasi-Free Holes and Electrons are Generated in Organic Photovoltaic Interfaces." *Farad. Discuss.*, **163**, 377–392, 2013.

[108] C. G. Shuttle, B. O'Regan, A. M. Ballantyne, J. Nelson, D. D. C. Bradley, and J. R. Durrant. "Bimolecular Recombination Losses in polythiophene:Fullerene Solar Cells." *Phys. Rev. B*, **78**, 113201:1–113201:4, 2008.

[109] G. F. A. Dibb, F. C. Jamieson, A. Maurano, J. Nelson, and J. R. Durrant. "Limits on the Fill Factor in Organic Photovoltaics: Distinguishing Nongeminate and Geminate Recombination Mechanics." *J. Phys. Chem. Lett.*, **4**, 803–808, 2013.

[110] J. J. M. Halls, C. A. Walsh, N. C. Greenham, E. A. Marseglia, R. H. Friend, S. C. Moratti, and A. B. Holmes. "Efficient Photodiodes from Interpenetrating Polymer Networks." *Nature*, **376**, 498–500, 1995.

[111] T. Lei. *Design, Synthesis, and Structure-Property Relationship Study of Polymer Field-Effect Transistors.* Springer, 2015.

[112] G. Yu and A. J. Heeger. "Semiconducting Polymer Diodes: Large Size, Low Cost Photodetectors with Excellent Visible-Ultraviolet Sensitivity." *Appl. Phys. Lett.*, **64**, 3422–3424, 1994.

[113] G. Yu, J. Gao, J. C. Hummelen, F. Wudl, and A. J. Heeger. "Polymer Photovoltaic Cells: Enhanced Efficiences via a Network of Internal Donor-Acceptor Heterojunctions." *Science*, **270**, 1789–1791, 1995.

[114] A. Tada, Y. Geng, Q. Wei, K. Hashimoto, and K. Tajima. "Tailoring Organic Heterojunction Interfaces in Bilayer Polymer Photovoltaic Devices." *Nature Mater.*, **10**, 450–455, 2011.

[115] P. Papon, J. Leblond, and P. H. E. Meijer. *The Physics of Phase Transitions: Concepts and Applications.* Springer Science & Business Media, 2007.

[116] D. A. Porter, K. E. Easterling, and M. Sherif. *Phase Transformations in Metals and Alloys, Third Edition*. CRC Press, 2009.

[117] N. D. Treat, A. Varotto, C. J. Takacs, N. Batara, M. Al-Hashimi, M. J. Heeney, A. J. Heeger, F. Wudl, C. J. Hawker, and M. L. Chabinyc. "Polymer-Fullerene Miscibility: A Metric for Screening New Materials for High-Performance Organic Solar Cells." *J. Am. Chem. Soc.*, **134**, 15869–15879, 2012.

[118] M. L. Jones, R. Dyer, N. Clarke, and C. Groves. "Are Hot Charge Transfer States the Primary Cause of Efficient Free-Charge Generation in Polymer:Fullerene Organic Photovoltaic Devices? A Kinetic Monte Carlo Study." *Phys. Chem. Chem. Phys.*, **16**, 20310–20320, 2014.

[119] P. K. Watkins, A. B. Walker, and G. L. B. Verschoor. "Dynamical Monte Carlo Modelling of Organic Solar Cells: The Dependence of Internal Quantum Efficiency on Morphology." *Nano Lett.*, **5**, 1814–1818, 2005.

[120] J. J. M. Halls, K. Pichler, R. H. Friend, S. C. Moratti, and A. B. Holmes. "Exciton Diffusion and Dissociation in a poly(p-phenylenevinylene)/C_{60} Heterojunction Photovoltaic Cell." *Appl. Phys. Lett.*, **68**, 3120–3122, 1996.

[121] S. H. Park, A. Roy, S. Beaupreé, S. Cho, N. Coates, J. S. Moon, D. Moses, M. Leclerc, K. Lee, and A. J. Heeger. "Bulk Hetereojunction Solar Cells with Internal Quantum Efficiency Approaching 100%." *Nature Photon.*, **3**, 297–303, 2009.

[122] R. Österbacka, A. Pivrikas, G. Juška, A. Poškus, H. Aarnio, G. Sliaužys, K. Genevičius, K. Arlauskas, and N. S. Sariciftci. "Effect of 2-D Delocalization on Charge Transport and Recombination in Bulk-Heterojunction Solar Cells." *IEEE J. Sel. Top. Quantum Electron.*, **16**, 1738–1745, 2010.

[123] Z. M. Beiley, E. T. Hoke, R. Noriega, J. Dacuña, G. F. Burkhard, J. A. Bartelt, a. Salleo, M. F. Toney, and M. D. McGehee. "Morphology-Dependent Trap Formation in High Performance Polymer Bulk Heterojunction Solar Cells." *Adv. Energy Mater.*, **1**, 954–962, 2011.

[124] M. C. Scharber, D. Mühlbacher, M. Koppe, P. Denk, C. Waldauf, A. J. Heeger, and C. J. Brabec. "Design Rules for Donors in Bulk-Heterojunction Solar Cells - Towards 10% Energy-Conversion Efficiency." *Adv. Mater.*, **18**, 789–794, 2006.

[125] S. Ulum, N. Holmes, M. Barr, A. L. D. Kilcoyne, B. B. Gong, X. Zhou, W. Belcher, and P. Dastoor. "The Role of Miscibility in Polymer:Fullerene

Nanoparticulate Organic Photovoltaic Devices." *Nano Energy*, **2**, 897–905, 2013.

[126] T. Wang, A. D. F. Dunbar, P. A. Staniec, A. J. Pearson, P. E. Hopkinson, J. E. MacDonald, S. Lilliu, C. Pizzey, N. J. Terrill, A. M. Donald, A. J. Ryan, R. A. L. Jones, and D. G. Lidzey. "The Development of Nanoscale Morphology in Polymer:Fullerene Photovoltaic Blends During Solvent Casting." *Soft Matter*, **6**, 4128–4134, 2010.

[127] W. Ma, C. Yang, X. Gong, K. Lee, and A. J. Heeger. "Thermally Stable, Efficient Polymer Solar Cells with Nanoscale Control of the Interpenetrating Network Morphology." *Adv. Funct. Mater.*, **15**, 1617–1622, 2005.

[128] X. L. Liu, S. Huettner, Z. X. Rong, M. Sommer, and R. H. Friend. "Solvent Additive Control of Morphology and Crystallization in Semiconducting Polymer Blends." *Adv. Mater.*, **24**, 669–674, 2012.

[129] L. Lu, T. Xu, W. Chen, E. S. Landry, and L. Yu. "Ternary Blend Polymer Solar Cells with Enhanced Power Conversion Efficiency." *Nature Photon.*, **8**, 716–722, 2014.

[130] C. Groves. "Suppression of Geminate Charge Recombination in Organic Photovoltaic Devices with a Cascaded Energy Heterojunction." *Energy Environ. Sci.*, **6**, 1546–1551, 2013.

[131] W. Pisula, M. Kastler, D. Wasserfallen, M. Mondeshki, J. Piris, I. Schnell, and K. Müllen. "Relation between Supramolecular Order and Charge Carrier Mobility of Branched Alkyl Hexa-peri-hexbenzocoronenes." *Chem. Mater.*, **18**, 3634–3640, 2006.

[132] W. Pisula, Ž Tomović, C. Simpson, M. Kastler, T. Pakula, and K. Müllen. "Relationship between Core Size, Side Chain Length and the Supramolecular Organization of Polycyclic Aromatic Hydrocarbons." *Chem. Mater.*, **17**, 4296–4303, 2005.

[133] Y. Liang, D. Feng, Y. Wu, S.-T. Tsai, G. Li, C. Ray, and L. Yu. "Highly Efficient Solar Cell Polymers Developed via Fine-Tuning of Structural and Electronic Properties." *J. Am. Chem. Soc.*, **131**, 7792–7799, 2009.

[134] R. F. Service. "Outlook Brightens for Plastic Solar Cells." *Science*, **332**, 293, 2011.

[135] M. Hosoya, H. Oooka, H. Nakao, S. Mori, T. Gotanda, N. Shida, M. Saito, Y. Nakano, and K. Todori. "Module Development for Polymer Solar Cells." *Grand Renewable Energy Conference*, **O-PV-6-2**, 21–37, 2014.

[136] B. C. Thompson and J. M. J. Fréchet. "Polymer-Fullerene Composite Solar Cells." *Angew. Chem. Int. Ed.*, **47**, 58–77, 2008.

[137] I. Botiz and N. Stingelin. "Influence of Molecular Conformations and Microstructure on the Optoelectronic Properties of Conjugated Polymers." *Materials*, **7**, 2273–2300, 2014.

[138] V. Coropceanu, J. Cornil, A. Demetrio, F. da Silva, Y. Olivier, R. Silbey, and J-L. Brédas. "Charge Transport in Organic Semiconductors." *Chem. Rev.*, **107**, 926–952, 2007.

[139] M. Mas-Torrent, P. Hadley, S. T. Bromley, X. Ribas, J. Tarrés, M. Mas, E. Molins, J. Veciana, and C. Rovira. "Correlation between Crystal Structure and Mobility in Organic Field-Effect Transistors Based on Single Crystals of Tetrathiafulvalene Derivatives." *J. Am. Chem. Soc.*, **126**, 8546–8553, 2004.

[140] F. C. Jamieson, E. B. Domingo, T. McCarthy-Ward, M. Heeney, N. Stingelin, and J. R. Durrant. "Fullerene Crystallisation as a Key Driver of Charge Separation in Polymer/Fullerene Bulk Heterojunction Solar Cells." *Chem. Sci.*, **3**, 485–492, 2012.

[141] B. A. Collins, Z. Li, J. R. Tumbleston, E. Gann, C. R. McNeill, and H. Ade. "Absolute Measurement of Domain Composition and Nanoscale Size Distribution Explains Performance in PTB7:$PC_{71}BM$ Solar Cells." *Adv. Energy Mater.*, **3**, 65–74, 2013.

[142] T. A. Skotheim and J. Reynolds. *Conjugated Polymers: Processing and Applications*. CRC Press, 2006.

[143] J. R. Tumbleston, B. A. Collins, L. Yang, A. C. Stuart, E. Gann, W. Ma, W. You, and H. Ade. "The Influence of Molecular Orientation on Organic Bulk Heterojunction Solar Cells." *Nature Photon.*, **8**, 385–391, 2014.

[144] W.-Q. Deng and W. A. Goddard III. "Predictions of Hole Mobilities in Oligoacene Organic Semiconductors from Quantum Mechanical Calculations." *J. Phys. Chem. B*, **108**, 8614–8621, 2004.

[145] J. Singh. *Smart Electronic Materials: Fundamentals and Applications*. Cambridge University Press, 2005.

[146] Z. He, C. Zhong, X. Huang, W.-Y. Wong, H. We, L. Chen, S. Su, and Y. Cao. "Simultaneous Enhancement of Open-Circuit Voltage, Short-Circuit Current Density, and Fill Factor in Polymer Solar Cells." *Adv. Mater.*, **23**, 4636–4643, 2011.

[147] H.-Y. Chen, J. Hou, S. Zhang, Y. Liang, G. Yang, Y. Yang, L. Yu, Y. Wu, and G. Li. "Polymer Solar Cells with Enhanced Open-Circuit Voltage and Efficiency." *Nature Photon.*, **3**, 649–653, 2009.

[148] J. Peet, J. Y. Kim, N. E. Coates, W. L. Ma, D. Moses, A. J. HEeger, and G. C. Bazan. "Efficiency Enhancement in Low-Bandgap Polymer Solar Cells by Processing with Alkane Dithiols." *Nature Mater.*, **6**, 497–500, 2007.

[149] P. W. M. Blom, V. D. Mihailetchi, L. J. A. Koster, and D. E. Markov. "Device Physics of Polymer:Fullerene Bulk Heterojunction Solar Cells." *Adv. Mater.*, **19**, 1551–1566, 2007.

[150] Y. Liang, Z. Xu, J. Xia, S. Tsai, Y. Wu, G. Li, C. Ray, and L. Yu. "For the Bright Future-Bulk Heterojunction Polymer Solar Cells with Power Conversion Efficiency of 7.4%." *Adv. Mater.*, **22**, E135–E138, 2010.

[151] H. Yan, S. Swaraj, C. Wang, I. Hwang, N. C. Greenham, C. Groves, H. Ade, and C. R. McNeill. "Influence of Annealing and Interfacial Roughness on the Performance of Bilayer Donor/Acceptor Polymer Photovoltaic Devices." *Adv. Funct. Mater.*, **20**, 4329–4337, 2010.

[152] P. Peumans, A. Yakimov, and S. R. Forrest. "Small Molecular Weight Organic Thin-Film Photodetectors and Solar Cells." *J. Appl. Phys.*, **93**, 3693–3723, 2003.

[153] K. Tvingstedt, K. Vandewal, F. Zhang, and O. Inganäs. "On the Dissociation Efficiency of Charge Transfer Excitons and Frenkel Excitons in Organic Solar Cells: A Luminescence Quenching Study." *J. Phys. Chem. C*, **114**, 21824–21832, 2010.

[154] D. M. Roundhill and J. P. Fackler. *Optoelectronic Properties of Inorganic Compounds*. Springer Science & Business Media, 2013.

[155] C. J. Brabec, V. Dyakonov, J. Parisi, and N. S. Sariciftci. *Organic Photovoltaics: Concepts and Realization*. Springer Science & Business Media, 2013.

[156] J. Jo, S.-I. Na, S.-S. Kim, T.-W. Lee, Y. Chung, S.-J. Kang, D. Vak, and D.-Y. Kim. "Three-Dimensional Bulk Heterojunction Morphology for Achieving

High Internal Quantum Efficiency in Polymer Solar Cells." *Adv. Funct. Mater.*, **19**, 2398–2406, 2009.

[157] I. A. Howard, R. Mauer, M. Meister, and F. Lacquai. "Effect of Morphology on Ultrafast Free Carrier Generation in Polythiophene:Fullerene Organic Solar Cells." *J. Am. Chem. Soc.*, **132**, 14866–14876, 2010.

Chapter 3

Simulation Methods

3.1 Introduction

With the development of computational techniques and the increased availability of high-performance computing, simulations and models are becoming useful tools with which to better understand the function of organic electronic devices. Many models are capable of accurately reproducing experimental results, or using *ab initio* calculations to predict the behaviour of devices under a variety of conditions that may not be viable using conventional experimental techniques - providing useful insights about physical processes and mechanisms that occur within devices. Of particular interest in the field of OEDs are simulations that can link together information about the morphological features of a virtual device and its corresponding performance and efficiency. In this chapter, a brief overview of the drift-diffusion (DD) and master equation (ME) modelling techniques will be given in §3.2 and §3.3 respectively. These methods consider the net flow of charge through a slice in the morphology or the probability distribution of the energy level occupation,

and therefore do not model charge carriers as individual particles. Conversely, MC methods consider the motion of charged particles through a three-dimensional morphology directly, as described in §3.4. Both mesoscale and molecular MC techniques are presented, describing the implementation of algorithms used in subsequent investigations in this thesis. A brief discussion of relevant morphology generation techniques for the MC code used in this thesis are also given. Finally, a summary is presented in §3.5.

3.2 Drift-Diffusion

DD models are based on a simplification of the more general Boltzmann transport equation, which considers the variation in the probability density function $f(\underline{\mathbf{r}}, \underline{\mathbf{p}}, t)$ for a particle with position vector, $\underline{\mathbf{r}}$, momentum, $\underline{\mathbf{p}}$, at time, t such that:

$$\frac{\partial \underline{\mathbf{p}}}{\partial t}\nabla_r f(\underline{\mathbf{r}}, \underline{\mathbf{p}}, t) - \frac{q\underline{\mathbf{F}}}{\hbar}\nabla_p f(\underline{\mathbf{r}}, \underline{\mathbf{p}}, t) + \frac{\partial f(\underline{\mathbf{r}}, \underline{\mathbf{p}}, t)}{\partial t} = -\left(\frac{f(\underline{\mathbf{r}}, \underline{\mathbf{p}}, t)}{\partial t}\right)_{\text{collisions}}, \quad (3.2.1)$$

where the first term describes the velocity of the particle due to its diffusion, the second describes the variation in its momentum due to the electric field, $\underline{\mathbf{F}}$ (∇_p is the derivative in momentum space), and the third term represents the direct time dependence of f, which is zero for steady-state[1]. The term on the right hand side describes the possible collision mechanisms of particles in the system. This equation has to be solved numerically as analytical solutions do not typically exist for electronic devices.

In general, DD methodologies omit the consideration of particle collisions for

1 dimensional devices at steady state, such that the transport of charges can be described in terms of the field-dependent drift (due to $\underline{\mathbf{F}}$) and field-independent diffusion (due to thermal motion) components[2,3]. They therefore tend not to consider the effects of morphology and time-dependent processes such as transient current on the charge transport. The main objective of the DD technique is to describe charge transport through the calculation of the charge carrier current density, J[4]. By splitting carrier motion into drift and diffusion components, J_e for electrons and J_h for holes can be calculated at position, x, by using the carrier concentrations within the device, $n_e(x)$ and $n_h(x)$ respectively:

$$J_e = -q\left[\mu_e n_e(x)\frac{\partial V(x)}{\partial x}\right] + q\left[D_e\frac{\partial n_e(x)}{\partial x}\right], \tag{3.2.2}$$

$$J_h = -q\left[\mu_e n_h(x)\frac{\partial V(x)}{\partial x}\right] - q\left[D_h\frac{\partial n_h(x)}{\partial x}\right]. \tag{3.2.3}$$

Here, the first term in the equation describes drift, which is dependent on the mobility of the carrier, μ, and the electrostatic potential $V(x)$. The second term describes diffusion, where the diffusion coefficient, D, is usually related to μ through the Einstein relation:

$$D = \frac{\mu k_B T}{q}, \tag{3.2.4}$$

where k_B is the Boltzmann constant and T is the absolute temperature of the device.

Carrier concentrations, n, are often given by the quasi-Fermi level formulation for steady-state simulations such that:

$$n_e(x) = N\exp\left(\frac{\Phi_e - qV(x)}{k_B T}\right), \tag{3.2.5}$$

$$n_h(x) = N \exp\left(\frac{qV(x) - \Phi_h}{k_B T}\right), \tag{3.2.6}$$

where N is the total intrinsic carrier density and Φ represents the quasi-Fermi level for that carrier type. The quasi-Fermi level is a material-dependent description of the population of electrons in the conduction band or holes in the valence band, when the device is out of equilibrium but still in steady state - for instance, as occurs under an applied bias voltage[5]. Furthermore, carrier concentrations must satisfy the continuity equations under steady state, which ensure that the total charge within the device is conserved, the carrier density is always positive and that densities evolve monotonically such that there are no spurious spatial oscillations[6]:

$$\frac{\partial n_e}{\partial t} = \frac{1}{q}\frac{\partial J_e(x)}{\partial x} + k_{g,e}(x), \tag{3.2.7}$$

$$\frac{\partial n_h}{\partial t} = -\frac{1}{q}\frac{\partial J_h(x)}{\partial x} + k_{g,h}(x), \tag{3.2.8}$$

where k_g is the net generation rate of the carrier. For OPVs, k_g includes photoinjection and recombination. Typically, both geminate and non-geminate recombination are treated by reducing the carrier concentrations based on an input rate that approximates the simple Onsager-Braun (OB) model with a single recombination rate coefficient, k_r[7]. The OB model is considered in more detail in chapter 4.

Charge interactions are described in terms of the electrical potential $V(x)$, which can be calculated in one dimension using the Poisson equation and the electron and hole densities $n_e(x)$ and $n_h(x)$ respectively:

$$\frac{\partial^2}{\partial x^2}V(x) = \frac{q}{\epsilon_0 \epsilon_r}\left[n_e(x) - n_h(x)\right], \tag{3.2.9}$$

where x describes the position along the device, q is the elemental charge, ϵ_0 is the permittivity of free space and ϵ_r is the relative permittivity coefficient that describes the material that is being simulated.

These core equations in the DD model are coupled, and so it is not generally possible to determine an analytical solution. Instead, numerical methods are utilised to iteratively solve the equations, based on initial guesses for the potential, V, and carrier densities $n_e(x)$ and $n_h(x)$ at each value of x[8,9]. Successive corrections to $V(x)$ can then be determined using equation 3.2.9, recalculating the carrier densities when the magnitude of the corrections are sufficiently small.

The key advantage of determining the photocurrent of a device in this way is that the iterative process does not scale with the charge carrier density of the device, allowing for larger devices to be simulated at higher charge densities without additional computational cost. Therefore, in the context of OPVs, J-V curves can be generated more quickly than would be possible using other techniques. However, in order to accomplish this, important device physics such as the processes of charge generation and recombination are reduced to analytical expressions that do not necessarily consider morphological features[10] or the effects of energetic disorder[11]. Due to this, and the difficulty in simulating multi-dimensional devices including time-dependent transient effects, DD models lend themselves to the simulation of, for example, single-carrier organic diodes in which the processes of charge generation and recombination can be ignored[12].

3.3 Master Equation

ME methods consider charge transport in terms of the occupation probability of sites based on energy levels and phonon-assisted carrier hops between them[13], achieving at least qualitative agreement with experiment for the J-V and power conversion efficiency characteristics of OPV devices[14]. These models explicitly consider the rates at which charges can move between accessible energy levels within the morphology, and then determine the time-evolution of the probability that a charge is present in a given state. As the energy levels are considered directly, the effects of a 3-dimensional morphology can be determined, as the arrangements of molecules within the device impacts the local energetic structure of the hopping destination sites.

Charges are free to 'hop' between states i and j, *via* quantum tunnelling events occurring between distinct regions of molecules in the morphology, described by energy levels and molecular orbitals. The rate at which hopping can occur, $k_{i\to j}$, is often determined by the semi-classical Marcus expression which considers the local energetic landscape[15]:

$$k_{i\to j} = \frac{\left|J_{ij}\right|^2}{\hbar}\sqrt{\frac{\pi}{\lambda_{ij}k_BT}}\exp\left[-\frac{(\Delta E_{ij}-\lambda_{ij})^2}{4\lambda_{ij}k_BT}\right], \tag{3.3.10}$$

where the first term is a hopping prefactor (often denoted as v_0) that depends on the electronic transfer integral between the initial and destination sites, J_{ij}, and the reorganisation energy, λ_{ij}. The reorganisation energy is often approximated as twice the charge carrier polaron energy[16,17] and can therefore be tuned to match

the material to be simulated[18], however an alternative description of λ_{ij}, based on explicit calculations will be discussed in more detail in chapter 6 for the case of P3HT[19]. In equation 3.3.10, $\Delta E_{ij} = E_i - E_j$ describes the difference in energy between the initial and final sites.

$k_{i\to j}$ can then be used to describe the change in the occupation probability between sites, N, using the master equation:

$$\frac{\mathrm{d}N_i}{\mathrm{d}t} = \sum_j \left[k_{i\to j} N_i(1-N_j) - k_{j\to i} N_j(1-N_i)\right], \tag{3.3.11}$$

where the first term on the right hand side of the equation describes the flux of charge carriers into a site, j, based on the availability of charges to hop, N_i, and the availability of unoccupied destination sites, $(1 - N_j)$. Similarly, the second term describes the flux of carriers leaving site j. Double occupancy is expressly prohibited to replicate some of the effects of the Coulomb interactions which prevent two carriers from occupying the same site.

In the context of OPVs, ME methods can take into account the energetic landscape, and the photoinjection of charges, without considering the exact material structure of the morphology. Beyond preventing double occupancy, this method also ignores long-range Coulomb interactions between individual charges, potentially limiting the accuracy of the model for carrier densities > 0.01 per site[20]. However, this is greater than the expected carrier densities found in OPVs, so would be unlikely to affect the results of these simulations[21].

3.4 Monte Carlo

Kinetic MC methods are event-driven modelling techniques that use a more classical representation for charge carriers within organic electronic devices than DD and ME methods, by treating carriers and excitons as individual particles and tracking their interactions and motion directly in 3-dimensional space[22]. This means that MC code is capable of obtaining the bulk device characteristics for an input morphology, usually organised into a 3D lattice of dimensions comparable to the active layer of physical thin-film devices ($\sim 100\,\mathrm{nm}$)[23]. The behaviour of each particle in the system is determined by rate equations, based on a series of rate coefficients, k, for each physical process that can occur within the device (for example hopping, recombination or exciton dissociation events). The MC algorithm determines the 'wait time', τ, to each event:

$$\tau = -\frac{\ln x}{k}, \tag{3.4.12}$$

where $0 < x \leq 1$ is a uniformly distributed random number. A queue is formed in ascending τ for each event that has been considered, with the first event in the queue representing the behaviour that will occur next chronologically. The code then steps through the queue, executing the first event and increasing the simulation time by τ. All subsequent event wait times in the queue are then decreased by τ. The particle which has just been acted upon then has its new behaviour calculated. If the event was a photo- or dark-current injection or an exciton dissociation, any new particles that have been added to the system also have their behaviour calculated. The events are then inserted into the appropriate position in the queue and the algorithm repeats many times in order to describe the average behaviour of the

entire system. This is computationally intensive, and so most MC code runs on high-performance computing clusters in order for calculations to be performed on many processor cores simultaneously.

Note that, for complete accuracy, it would be necessary to recalculate the behaviour for *all* particles in the system (not just those corresponding to the most recently executed event) as the motion of charges affects the Coulomb interactions between carriers and therefore the local energetic landscape of the device. However, as this dramatically increases the computational demand for these types of simulations, it is common for the first reaction method (FRM) approximation to be included, which only reconsiders the Coulomb interactions for particles that have just been moved[24–26]. This results in a substantial decrease in simulation runtime, while having minimal effect on the charge transport characteristics[18,27]. The algorithm then repeats until the simulation completion criteria have been met, such as a convergence of the net current flowing out of the device as charge carriers hop through the contacts, or after a certain number of photoinjections have taken place.

In this thesis, two types of kinetic MC modelling will be used in the investigations. Mesoscale MC methods will be utilised to examine the overall characteristics and performance of OPV devices, simulating active layers with total dimensions of the order 100 nm and lattice constants ~ 1 nm, for timescales varying from 1 ns to $\sim$1 µs. Morphologies for these investigations are generated using Cahn-Hilliard (CH) methodology (described in §3.4.1), with sub-lattice molecular effects treated with a simple Gaussian disorder model (GDM) model, implicitly assuming some averaging of electronic couplings between chromophores. In chapter 6, the molecular mor-

phology of organic thin-films is explored using molecular MC techniques, simulating regions of thin films with total dimensions of the order 10 nm and lattice constants $\sim$ 1 Å, for timescales varying from the force-field interaction timestep (4 fs) to $\sim$10 ps. Here, the morphologies are generated from coarse-grained (CG) molecular dynamics simulations, which use a CG force-field to describe the molecular conformation and orientation through the interactions of atom groups.

3.4.1 Mesoscale Monte Carlo

Mesoscale MC methods consider the bulk behaviour of a simulation volume of similar order to thin film thickness in organic electronic devices ($\sim$ 100 nm). Mesoscale MC techniques, and their application to charge hopping in disordered organic materials, were first made popular in 1993 [22], with subsequent investigations including frameworks for charge injection [28] and geminate pair separation [29]. In 2005, the first simulations of complete BHJ OPV devices were reported [23], the framework of which has been used to explore the effects of recombination [10,16,17,30], trapping [11] and various device-scale morphological features [26,31–34] on OPV performance.

Generally, these models operate with a lattice constant of the order 1 nm^3, which is too large to consider the molecular morphology. The sub-lattice effects of molecular orientation and conformation are therefore 'smeared out', but their effects on the energetic structure of the device can be estimated from alternative methods [35,36]. Often, a GDM is used, which assumes random, Gaussian-distributed site energies [22,37] with a typical standard deviation of $\sigma = 100$ meV [12,38], inspired by explicit quantum chemical calculations of charge carrier densities on a small number

of molecules[35,36]. These energies are kept constant throughout the entire simulation as the molecular structure is not expected to change on the simulation timescales, however it is often appropriate to repeat the investigation with several different energetic landscape selections from the same distribution to ensure that the observed phenomena are not due to a particular configuration of energetic disorder[23,27].

The MC code used in the investigations in chapters 4 and 5 are mesoscale and were developed previously by collaborators to be used as an 'experimental' method with which to computationally investigate various phenomena[11,18,26,27,30,32]. However, some enhancements and modifications to the code were made in order to better test hypotheses and explore new phenomena that did not have sufficient infrastructure in the original version of the code. In chapter 4, charge pairs are injected directly to a heterojunction in the device morphology, and simulated until recombination or separation had occurred, therefore considering only the basic behaviours of charge transport through nearest-neighbour hopping and the recombination of adjacent charges. In chapter 5, full device simulations were additionally performed, which include the processes of exciton photoinjection, transport and dissociation as well as dark current injection from the contacts. A table of all of the fiducial parameters for the mesoscale MC investigations is given in §3.4.1.

Hopping

Carrier hopping is considered using the Marcus hopping equation described in 3.3.10, where constant values are assigned to the hopping prefactor, v_0, and reorganisation energy, λ_{ij}. As the transfer integrals, J_{ij}, were not explicitly calculated, the molecular conformation was instead considered by the variation in energetic disorder of the

initial and final hopping sites which are included in the calculation of ΔE_{ij}. This also includes Coulombic potential at a site, i, for a carrier m, due to the charges in the system, n:

$$U_m(x,r) = \sum_n \left[\frac{q_m q_n}{4\pi\epsilon_0\epsilon_r r} + U'_n(z) \right], \tag{3.4.13}$$

where r is the physical separation between m and n, and $U'_n(x)$ is a term that describes the change in potential due to the image charge induced in each electrode due to the presence of the carrier, n. $U'_n(z)$ is based on the vertical position of the carrier, z, calculated to second order (*i.e.* the potential of image charges induced by image charges induced by the original charge) for both electrodes, unless $n = m$, in which case only the first order image charges are considered[28]. A final contribution to the site energies comes from the internal electric field described by the vector $\underline{\mathbf{F}}$ (often characterised as simply $F = |\underline{\mathbf{F}}|$), which modifies ΔE_{ij} by an amount $q\underline{\mathbf{F}} \cdot \underline{\mathbf{r_{i\to j}}}$, where $\underline{\mathbf{r_{i\to j}}}$ is the vector that describes the hop from site i to site j. The internal electric field is the resultant combination of the applied voltage bias and the intrinsic field associated with the difference in electrode work functions as described in §2.4.1. The expression for ΔE_{ij} to be used in equation 3.3.10 therefore becomes:

$$\Delta E_{ij} = q\underline{\mathbf{F}} \cdot \underline{\mathbf{r_{i\to j}}} + U_m(x,r)\big|_j - U_m(x,r)\big|_i . \tag{3.4.14}$$

Recombination

Recombination can be geminate (*i.e.* originating from the same photoinjected exciton) or bimolecular (*i.e.* two charges that were injected from the contacts or originated from different excitons). Often, geminate recombination is described by

OB theory, where there exists a single recombination rate, k_r, for opposing charge carriers that are adjacent or within a Coulomb capture radius that makes them sufficiently close enough to recombine[7,39]. Bimolecular recombination is often described as Langevin[40,41]:

$$k_{r,\text{Langevin}}(x) = \frac{q}{\epsilon_0 \epsilon_r} \left(\mu_e + \mu_h\right) \left[n_e(x) n_h(x)\right], \tag{3.4.15}$$

which is dependent on the availability of opposing charge carrier densities in the device (the second term in equation 3.4.15) and the diffusion-limited hopping process of these charges approaching and recombining (the first term in equation 3.4.15). Both OB and Langevin are therefore simplified, analytical expressions that aim to describe the real process of recombination. However, in OPVs, Langevin tends to overpredict the rate at which bimolecular recombination can occur by at least an order of magnitude, and so some models consider a reduction factor that arbitrarily lowers the rate of bimolecular recombination so that it agrees with experiment[42,43].

By contrast, in the mesoscale MC code, recombination is simulated directly using k_r when the electron and hole are adjacent within the morphology. At each timestep, the simulation is searched for any opposing carrier pair that is close enough to recombine, and if so, the wait period to the recombination event is calculated based on k_r, which is usually around $1 \times 10^7\,\text{s}^{-1}$ for all-polymer blends[44] and $1 \times 10^9\,\text{s}^{-1}$ for more efficient, polymer:fullerene blends[45]. While this model has been successfully fit to a variety of devices, its simplicity is unable to accurately predict the recombination behaviour in others. This will be considered in more detail in chapter 4.

It is noteworthy that many MC models that treat the morphology as completely

phase-separated donor:acceptor BHJs tend to predict geminate recombination as the main loss channel within OPVs[11,27], despite measurement suggesting that bimolecular recombination dominates (particularly in polymer:fullerene blend devices)[46,47]. This is most likely due to the approximations made when considering a completely phase-separated morphology, which can be alleviated by considering a molecularly mixed phase within the device (see chapter 5).

Some of the MC simulations reported in chapter 5 include full device simulations in order to predict a J-V curve for a simulated photovoltaic. Beyond charge carrier hopping and recombination, these simulations also include the photoinjection, hopping and dissociation of excitons, as well as the dark current injection of carriers from the contacts.

Photoinjection

Excitons are injected into the simulation volume at a rate k_{photo}:

$$k_{\text{photo}} = \Phi \frac{\lambda}{hc} A \left(1 - \exp(-\alpha(z))\right), \tag{3.4.16}$$

where Φ is the radiant fluence incident to the device, λ is the wavelength of the light, A is the area of the photosensitive area of the device that is exposed and $\alpha(z)$ is the material- and depth-dependent absorption coefficient. A and $\alpha(z)$ are determined by the size, shape and material of the active layer, but Φ and λ are free parameters that can be calibrated to a specific air mass index. For instance, it is common to utilise an air mass index of AM1.5, which most closely corresponds to the operating parameters of real photovoltaic devices[48]. In the investigations, if

the MC algorithm selected a photoinjection event to occur as the next event, the exciton was created at a random site within the morphology, as uniform absorption and injection throughout the device were assumed.

Exciton Transport

Exciton diffusion is generally modelled using Förster resonance energy transfer (FRET). This describes the motion of electronic excitation energy between similar molecules as a quantum mechanical oscillator[49]. When an excitation in one molecule relaxes to the ground state, the Coulomb interaction induces a dipole, stimulating a resonant excitation in a neighbouring molecule, effectively displacing the excitation energy[50]. Excitons also have a finite lifetime, τ_{ex}, (measured from spectroscopy to be $\sim 0.5\,\text{ns}$), whereby the excitation relaxes to the ground state before dissociation occurs and no further energy transfer can take place[26,51]. The rate of energy transfer can be given by[52]:

$$k_F = \begin{cases} \frac{1}{\tau_{\text{ex}}} \left(\frac{r_F}{r_{ij}}\right)^6 & \text{if } \Delta E_{ij} \leq 0 \\ \frac{1}{\tau_{\text{ex}}} \left(\frac{r_F}{r_{ij}}\right)^6 \exp\left(-\frac{q\Delta E_{ij}}{k_B T}\right), & \text{if } \Delta E_{ij} > 0 \end{cases} \tag{3.4.17}$$

where r_F is the exciton localisation radius. Note that a thermally activated Boltzmann penalty is applied to make exciton hops that occur 'upstream' in energy ($\Delta E_{ij} > 0$) less likely. Both τ_{ex} and r_F are treated as fitting parameters in order to give an exciton diffusion length in the region of $\sim 10\,\text{nm}$, which is typical of conjugated polymers[53]. This approach, which takes into account variations in exciton transport due to energetic disorder given by ΔE_{ij}, was shown by Scheidler *et al.* to

give excellent agreement to exciton decay dynamics in PPV[52].

Exciton Dissociation

At each destination hop site of the exciton, checks are performed to see if the local phase-structure of the surrounding material makes it permissible for the exciton to dissociate - *i.e.* if the exciton is present at a donor:acceptor heterojunction. If so, the exciton is immediately converted into an electron-hole pair, implicitly assuming that the exciton dissociation rate occurs much faster than the other rates considered. In the event of multiple dissociation options, where there is more than one interface adjacent to the current site of the exciton, the executed dissociation path is selected at random from the permitted choices.

Dark Current Injection

In order to calculate J-V curves for a device, carrier injection from the electrodes into the active layer must be considered. This dark current injection is treated within the MC code by determining the total injection rate as a Marcus carrier hop initiating from outside the morphology to a random site on either the top or bottom plane of the active layer based on the charge carrier to be injected (holes are injected from the anode, electrons from the cathode)[27]. In this case, the site-energy difference is material dependent and includes the energetic disorder: $\Delta E_{ij} = q(\text{bandgap} - \text{carrier injection barrier} - \text{disorder potential of target site})$[28].

Parameters Summary

Simulation Parameter	Value
Material Parameters	
Acceptor LUMO	−3.9 eV
Donor HOMO	−5.3 eV
Cathode Work Function	−4.2 eV
Anode Work Function	−5.0 eV
Photoabsorption Coefficient	$1.3 \times 10^6\,\mathrm{m}^{-1}$
Photoinjection rate	$6.27 \times 10^6\,\mathrm{s}^{-1}$
Dielectric Constant, ϵ	3
Charge Parameters	
Applied Electric Field, F	$5 \times 10^6\,\mathrm{V\,m}^{-1}$
Recombination Rate (all-polymer), k_r	$1 \times 10^7\,\mathrm{s}^{-1}$
Recombination Rate (polymer:fullerene), k_r	$1 \times 10^9\,\mathrm{s}^{-1}$
Exciton Lifetime, τ_{PL}	500 ps
Förster Radius, R_{F}	4.3 nm
Hopping Parameters	
Marcus Hopping Prefactor (hole), $v_{0,h}$	$1 \times 10^{11}\,\mathrm{s}^{-1}$
Marcus Hopping Prefactor (electron), $v_{0,e}$	$1 \times 10^{11}\,\mathrm{s}^{-1}$
Reorganization Energy, λ_{ij}	0.25 eV
Gaussian DoS width (all-polymer), σ	100 meV
Gaussian DoS width (polymer:fullerene), σ	50 meV
Photoinjection Parameters	
Incident Flux, Φ	$100\,\mathrm{mW\,cm}^{-2}$
Incident Wavelength, λ	500 nm
Temperature, T	298 K
Absorption Coefficient, α	$1.3 \times 10^4\,\mathrm{cm}^{-1}$

Table 3.1: *Parameters for the Monte Carlo Simulations used in later investigations.*

The simulation parameters used in the mesoscale MC investigations were based on extensive studies using previous versions of the code[11,18,26,27,30,32] and are summarised in table 3.1. Note that, in the simulations, the incident light is described by a narrow-band source with flux, Φ, at a specific wavelength $\lambda = 500\,\mathrm{nm}$, which approximates to the peak of an AM1.5 solar spectrum. The parameters shown here

correspond to a fiducial set of simulations which, unless otherwise specified, form the bulk of the investigations performed in chapters 4 and 5.

Morphology Synthesis

Alongside the simulation parameters which allow MC code to easily test a wide variety of systems accurately, the morphology is a fundamentally important input. All the morphologies used in the mesoscale investigations in chapters 4 and 5 were generated externally by collaborators using a CH based theory[54], which considers morphological evolution based on the variation of the Gibb's free-energy. This method allows for multi-component bulk heterojunction morphologies to be created for use in MC investigations[17,26,32]. In turn, this has allowed for significant advancements towards a fully predictive model for morphology formation including the effects of spinodal phase segregation through evaporation[55] and substrate-induced phase separation[26,56]. In general, such models have provided a good agreement with experimental observations of morphology evolution[57]. While research is currently taking place into incorporating material crystallisation in the morphology generation process[58], these kinetics are not yet fully described and so alternative morphology generation methods must be utilised to consider the effects of crystals (see chapter 6).

CH theory, and enhancements thereof, describe the phase-separation of a blend of two components based on the evolution of perturbations in the local concentration as the solution is cooled[59]. An example phase-separation evolution is shown in figure 3.1.

The equation of motion for the local volume fraction of a donor, ϕ, can be written

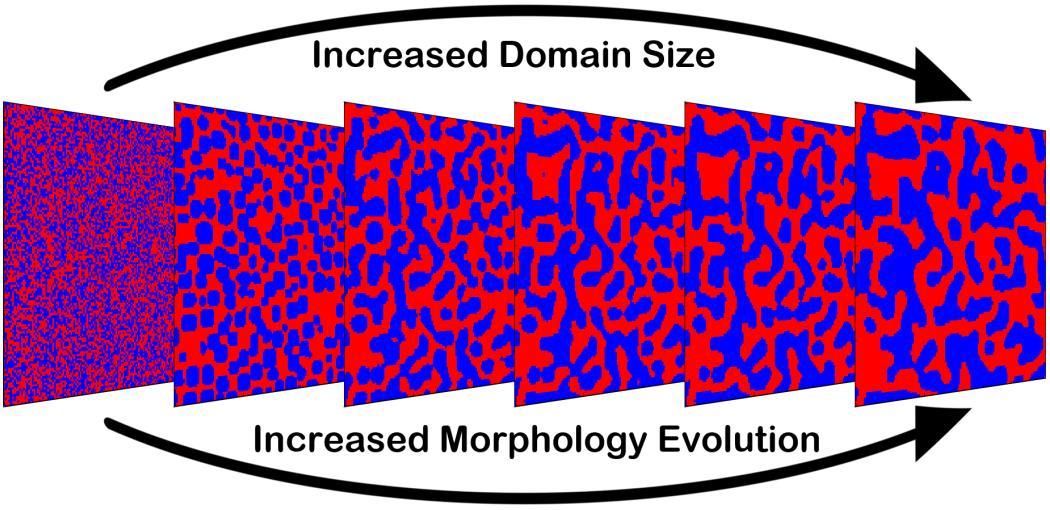

Figure 3.1: *An example morphology evolution through the first 100 timesteps of the Cahn-Hilliard equation. Red sites represent donor material, blue sites denote the acceptor phase.*

based on a dimensionless time evolution parameter τ:

$$\frac{\partial\phi(\underline{\mathbf{x}},\tau)}{\partial\tau} = \nabla_x^2\left[\frac{1}{N_D(\chi-\chi_s)}\ln\phi - \frac{1}{N_A(\chi-\chi_s)}\ln(1-\phi) - \frac{2\chi\phi}{(\chi-\chi_s)} + \frac{2\phi-1}{36\phi^2(1-\phi)^2}(\nabla\phi)^2 - \frac{1}{18\phi(1-\phi)}\nabla^2\phi\right], \tag{3.4.18}$$

where N_A and N_D are the degrees of polymerisation of the donor and acceptor phases, χ is the Flory-Huggins interaction parameter, with χ_s its value on the spinodal curve which describes the locus of points at which the second derivative of the Gibbs free energy as a function of composition is zero. If $\chi > \chi_s$, then the mixed blend is unstable and will spinodally decompose - *i.e.* the phases will separate according to the diffusive dynamics of the equation of motion. The first three terms in equation 3.4.18 arise from the free-energy of the blend as described by Flory-Huggins theory[60,61]. The 4th and 5th terms in the equation describe the energetic cost of

the composition gradients, $\nabla\phi$. The dimensionless time and space coordinates τ and $\underline{\mathbf{x}}$ are related to the canonical coordinates (t and $\underline{\mathbf{r}}$) through $\underline{\mathbf{x}} = (|\chi - \chi_s|)^{\frac{1}{2}}\underline{\mathbf{r}}/l$ and $\tau = N_A D(\chi - \chi_s)^2 t/l^2$, where D is the mutual diffusion coefficient and l is the length of a statistical segment.

To generate the morphologies used in later chapters, the CH equation was solved using a finite difference scheme with time and space-steps of $\Delta\tau = 1.25 \times 10^{-4}$ and $\Delta x = 0.04$, for a cubic lattice of side 128, with each lattice site corresponding to $1\,\mathrm{nm}^3$. In order to ensure that no material was lost through the interfaces between the morphology and the electrodes, periodic boundaries were included. Initially, each site within the morphology was composed of donor material proportion $\phi(\underline{\mathbf{x}}, 0) = \phi_0 + \delta$, where $\phi_0 = 0.5$, and δ is a uniformly distributed random number such that $-0.01 \leq \delta < 0.01$. The resultant lattice was very fine, essentially modelling white noise, with δ 'seeding' the morphology to create random perturbations in the concentration of donor material that could grow into the required morphological features. This produced a volume that is considered to be similar to a polymer melt which has been quenched so as to favour phase-separation.

Morphology evolution was permitted until domains of donor or acceptor material reached an average size $d = 7\,\mathrm{nm}$, whereupon the simulations were terminated. Mesoscale MC simulations on a variety of input morphologies have shown that $d = 7\,\mathrm{nm}$ represents the optimal domain size where competing requirements balance, as there are sufficient heterojunctions located within the exciton diffusion length to promote high dissociation efficiencies, but not so many as to hinder charge transport to the contacts[32]. The value of d was ascertained by use of a radial distribution

function which showed the distance at which the local composition was no longer linked to the initial site.

After a lattice of donor material proportion had been obtained, an additional post-processing step was necessary in order to obtain realistic morphologies. The MC simulations used here, like others, require a binary morphology where sites are defined as pure donor or pure acceptor. It was therefore necessary to assign the 3D array of ϕ values such that $\phi > 0.5 \rightarrow \phi = 1$ denoted a region of pure donor material and $\phi \leq 0.5 \rightarrow \phi = 0$ denoted a region of pure acceptor material[32]. An investigation into domain purity by Lyons *et al.* has shown that pure domains are necessary for the generation of realistic morphologies in order to successfully replicate certain experimental behaviour, such as the expected amount of exciton quenching within the system[32,62].

3.4.2 Molecular Monte Carlo

Molecular MC simulations operate on a smaller scale than their mesoscopic counterparts, explicitly including the effects of molecular orientation and conformation on the charge and energy transport mechanisms within a device[63]. Simulations of this type therefore move away from the GDM and instead calculate the transfer integrals between segments of material in the device by determining the molecular orbitals of each segment using quantum chemical calculation methods[37]. Physically, a segment is described as the region over which a polaron is expected to be delocalised, and can be determined from quantum chemical calculations of the density of states (DoS) for a polymer chain[64]. Whereas mesoscopic MC simulations can provide

comparative analysis of experimental data, determining hopping transfer integrals in this way offers a method with which to predict the charge-transport properties for materials with different physical and chemical structures[37], and have also been used to predict the distribution of traps that affect exciton transport in conjugated polymers[65].

The investigations reported in chapter 6 use molecular MC methods to determine the mobility characteristics of different thin-film morphologies for the conjugated polymer P3HT, in the style of ToF experiments. Here, an individual charge carrier is injected at a random point in the morphology and is free to hop to nearby segments for a predefined simulation time. The simulation volume consists of a small $\sim 10\,\text{nm}$ region of the single-material thin film, with no photoinjection or electrical contacts, and so treatment of the exciton and dark-injection properties is not required. Furthermore, only one charge carrier is present in the morphology at any one time, so the effects of recombination and free carrier Coulomb interaction are ignored. As such, the MC model only utilises Marcus hopping, with $\left|J_{ij}\right|$ calculated using the semi-empirical ZINDO/S method, and ΔE_{ij} determined from the variation in the HOMO level of the delocalisation segment[66].

Morphologies for molecular MC simulations can be determined in a variety of ways. Density Functional Theory (DFT) can determine the relaxed geometry of a system, resulting in an energy-minimised atomistic representation of the molecular morphology. The inputs into this DFT method could be, for example, the results of MD simulations of the material based on an atomistic interaction forcefield[67–69], however it is generally more common to assume an initial configuration of a small

number of chains or molecules to result in an idealised morphology[37,70–72]. This is primarily due to the fact that such morphologies require the forcefield to consider potentially hundreds of thousands of atoms in the simulation volume, which is computationally expensive. One possible solution to this involves 'coarse-graining' the forcefield to instead consider groups of atoms that are expected to behave in a similar way, for instance the atoms belonging to the same functional group of a molecule[70,73]. This reduces the number of interactions to be considered within the MD simulations, while still emulating realistic material behaviour. CG MD simulations will be used in chapter 6 to create morphologies that can be analysed using a molecular MC methodology.

3.5 Summary

Several computational simulation techniques have been discussed that attempt to explore the charge-transport characteristics of virtual OPV devices, including various methodologies with which to model important physical processes like injection and recombination. MC simulations stand out since, despite their large computational cost, they can consider full 3D BHJ morphologies as an active layer and take into account the effects of energetic disorder and an applied electric field. MC simulations are not necessarily independent as they can also be used to determine the important parameters for other techniques such as drift-diffusion modelling[74–76]. The investigations described in later chapters will all include some level of MC simulation, either in its mesoscale form to determine device characteristics or by using molecular MC to determine the effect of polymer chain conformation on the charge transport properties of a thin film. The details of the mesoscale and molecular MC algorithms were given, along with the fiducial parameter set and discussion of the morphology generation by using CH theory or MD simulations.

References

[1] J. Piprek. *Semiconductor Optoelectronic Devices: Introduction to Physics and Simulation*. Adademic Press, 2013.

[2] J. A. Barker, C. M. Ramsdale, and N. C. Greenham. "Modeling the Current-Voltage Characteristics of Bilayer Polymer Photovoltaic Devices." *Phys. Rev. B*, **67**, 075205:1–075205:9, 2003.

[3] L. J. A. Koster, E. C. P. Smits, V. D. Mihailetchi, and P. W. M. Blom. "Device Model for the Operation of Polymer/Fullerene Bulk Heterojunction Solar Cells." *Phys. Rev. B*, **72**, 085205:1–085205:9, 2005.

[4] B. van Zeghbroeck. *Principles of Semiconductor Devices*. Prentice Hall, 2011.

[5] A. Rockett. *The Materials Science of Semiconductors*. Springer Science & Business Media, 2007.

[6] N. Dasgupta and A. Dasgupta. *Semiconductor Devices: Modelling and Technology*. PHI Learning Pvt. Ltd., 2004.

[7] C. L. Braun. "Electric Field Assisted Dissociation of Charge Transfer States as a Mechanism of Photocarrier Production." *J. Chem. Phys.*, **80**, 4157–4161, 1984.

[8] H. K. Gummel. "A Self-Consistent Iterative Scheme for One-Dimensional Steady State Transistor Calculations." *IEEE Trans. Electron Dev.*, **11**, 455–465, 1964.

[9] T. M. Apostol. *Calculus, Vol. II, Multi-Variable Calculus and Linear Algebra*. Blaisdell, 1969.

[10] C. Groves, R. A. Marsh, and N. C. Greenham. "Monte Carlo Modelling of Geminate Recombination in Polymer-Polymer Photovoltaic Devices." *J. Chem. Phys.*, **129**, 114903:1–114903:7, 2008.

[11] C. Groves, J. C. Blakesley, and N. C. Greenham. "Effect of Charge Trapping on Geminate Recombination and Polymer Solar Cell Performance." *Nano Lett.*, **10**, 1063–1069, 2010.

[12] J. C. Blakesley, H. S. Clubb, and N. C. Greenham. "Temperature-Dependent Electron and Hole Transport in Disordered Semiconduction Polymers: Analysis of Energetic Disorder." *Phys. Rev. B*, **81**, 045210:1–045210:9, 2010.

[13] S.-S. Sun and L. R. Dalton. *Introduction to Organic Electronic and Optoelectronic Materials and Devices*. CRC Press, 2008.

[14] M. Einax, M. Dierl, and A. Nitzan. "Heterojunction Organic Photovoltaic Cells as Molecular Heat Engines: A Simple Model for the Performance Analysis." *J. Phys. Chem. C*, **115**, 21396–21401, 2011.

[15] R. A. Marcus. "Chemical and Electrochemical Electron-Transfer Theory." *Ann. Rev. Phys. Chem.*, **15**, 155–196, 1964.

[16] C. Groves. "Developing Understanding of Organic Photovoltaic Devices: Kinetic Monte Carlo Models of Geminate and Non-Geminate Recombination, Charge Transport and Charge Extraction." *Energy Environ. Sci.*, **6**, 3202–3217, 2013.

[17] L. Jones, M, B. Chakrabarti, and C. Groves. "Monte Carlo Simulation of Geminate Pair Recombination Dynamics in Organic Photovoltaic Devices: Multi-Exponential, Field-Dependent Kinetics and its Interpretation." *J. Phys. Chem. C*, **118**, 85–91, 2014.

[18] C. Groves, R. G. E. Kimber, and A. B. Walker. "Simulation of Loss Mechanisms in Organic Solar Cells: A Description of the Mesoscopic Monte Carlo Technique and an Evaluation of the First Reaction Method." *J. Chem. Phys.*, **133**, 144110:1–14410:7, 2010.

[19] E. Johansson and S. Larsson. "Electronic Structure and Mechanism for Conductivity in Thiophene Oligomers and Regioregular Polymer." *Synt. Met.*, **144**, 183–191, 2004.

[20] J. Zhou, Y. C. Zhou, J. M. Zhao, C. Q. Wu, X. M. Ding, and X. Y. Hou. "Carrier Density Dependence of Mobility in Organic Solids: A Monte Carlo Simulation." *Phys. Rev. B*, **75**, 153201:1–153201:4, 2007.

[21] C. G. Shuttle, R. Hamilton, J. Nelson, B. C. O'Regan, and J. R. Durrant. "Measurement of Charge-Density Dependence of Carrier Mobility in an Organic Semiconductor Blend." *Adv. Funct. Mater.*, **20**, 698–702, 2010.

[22] H. Bässler. "Charge Transport in Disordered Organic Photoconductors: A Monte Carlo Simulation Study." *Phys. Status Solidi B*, **175**, 15–56, 1993.

[23] P. K. Watkins, A. B. Walker, and G. L. B. Verschoor. "Dynamical Monte Carlo Modelling of Organic Solar Cells: The Dependence of Internal Quantum Efficiency on Morphology." *Nano Lett.*, **5**, 1814–1818, 2005.

[24] J. J. Lukkien, J. P. L. Segers, P. A. J. Hilbers, R. J. Gelten, and A. P. J. Jansen. "Efficient Monte Carlo Methods for the Simulation of Catalytic Surface Reactions." *Phys. Rev. E*, **58**, 2598–2610, 1998.

[25] L. Meng, Y. Shang, Q. Li, Y. Li, X. Zhan, Z. Shuai, R. G. E. Kimber, and A. B. Walker. "Dynamic Monte Carlo Simulation for Highly Efficient Polymer Blend Photovoltaics." *J. Phys. Chem. B*, **114**, 36–41, 2010.

[26] B. P. Lyons, N. Clarke, and C. Groves. "The Quantitative Effect of Surface Wetting Layers on the Performance of Organic Bulk Heterojunction Photovoltaic Devices." *J. Phys. Chem. C*, **115**, 22572–22577, 2011.

[27] R. A. Marsh, C. Groves, and N. C. Greenham. "A Microscopic Model for the Behavior of Nanostructured Organic Photovoltaic Devices." *J. Appl. Phys.*, **101**, 083509:1–083509:7, 2007.

[28] U. Wolf, V. I. Arkhipov, and H. Bässler. "Current Injection from a Metal to a Disordered Hopping System. I. Monte Carlo Simulation." *Phys. Rev. B*, **59**, 7507–7513, 1999.

[29] U. Albrecht and H. Bassler. "Yield of Geminate Pair Dissociation in an Energetically Random Hopping System." *Chem. Phys. Lett.*, **235**, 389–393, 1995.

[30] C. Groves and N. C. Greenham. "Bimolecular Recombination in Polymer Electronic Devices." *Phys. Rev. B*, **78**, 155205:1–155205:8, 2008.

[31] C. Groves, L. J. A. Koster, and N. C. Greenham. "The Effect of Morphology Upon Mobility: Implications for Bulk Heterojunction Solar Cells with Nonuniform Blend Morphology." *J. Appl. Phys.*, **105**, 094510:1–094510:6, 2009.

[32] B. P. Lyons, N. Clarke, and C. Groves. "The Relative Importance of Domain Size, Domain Purity and Domain Interfaces to the Performance of Bulk-Heterojunction Organic Photovoltaics." *Energy Environ. Sci.*, **5**, 7657–7663, 2012.

[33] C. Groves. "Suppression of Geminate Charge Recombination in Organic Photovoltaic Devices with a Cascaded Energy Heterojunction." *Energy Environ. Sci.*, **6**, 1546–1551, 2013.

[34] M. L. Jones, R. Dyer, N. Clarke, and C. Groves. "Are Hot Charge Transfer States the Primary Cause of Efficient Free-Charge Generation in Polymer:Fullerene Organic Photovoltaic Devices? A Kinetic Monte Carlo Study." *Phys. Chem. Chem. Phys.*, **16**, 20310–20320, 2014.

[35] A. A. Bakulin, A. Rao, V. G. Pavelyev, P. H. M. van Loosdrecht, M. S. Pshenichnikov, D. Niedzialek, J. Cornil, D. Beljonne, and R. H. Friend. "The Role of Driving Energy and Delocalized States for Charge Separation in Organic Semiconductors." *Science*, **335**, 1340–1344, 2012.

[36] A. E. Jailaubekov, A. P. Willard, J. R. Tritsch, W-L. Chan, N Sai, R. Gearba, L. G. Kaake, K. J. Williams, K. Leung, P. J. Rossky, and X-Y. Zhu. "Hot Charge-Transfer Excitons Set the Time Limit for Charge Separation at Donor/Acceptor Interfaces in Organic Photovoltaics." *Nature Mater.*, **12**, 66–73, 2013.

[37] S. Athanasopoulos, J. Kirkpatrick, D. Martínez, J. M. Frost, C. M. Foden, A. B. Walker, and J. Nelson. "Predictive Study of Charge Transport in Disordered Semiconducting Polymers." *Nano Lett.*, **7**, 1785–1788, 2007.

[38] W. F. Pasveer, J. Cottaar, C. Tanase, R. Coehoorn, P. A. Bobbert, P. W. M. Blom, D. M. de Leeuw, and M. A. J. Michels. "Unified Description of Charge-Carrier Mobilities in Disordered Semiconducting Polymers." *Phys. Rev. Lett.*, **94**, 206601:1–206601:4, 2005.

[39] L. Onsager. "Initial Recombination of Ions." *Phys. Rev.*, **54**, 554–557, 1938.

[40] P. Langevin. "The Recombination and Mobilities of Ions in Gases." *Ann. Chim. Phys.*, **28**, 433–530, 1903.

[41] B. P. Rand and H. Richter. *Organic Solar Cells: Fundamentals, Devices, and Upscaling.* CRC Press, 2014.

[42] G. Lakhwani, A. Rao, and R. H. Friend. "Bimolecular Recombination in Organic Photovoltaics." *Annu. Rev. Phys. Chem.*, **65**, 557–581, 2014.

[43] T. M. Burke, S. Sweetnam, K. Vandewal, and M. D. McGehee. "Beyond Langevin Recombination: How Equilibrium Between Free Carriers and Charge Transfer States Determines the Open-Circuit Voltage of Organic Solar Cells." *Adv. Energy Mater.*, **5**, 1500123:1–1500123:12, 2015.

[44] S. Westenhoff, I. A. Howard, J. M. Hodgkiss, K. R. Kirov, H. A. Bronstein, C. K. Williams, N. C. Greenham, and R. H. Friend. "Charge Recombination in Organic Photovoltaic Devices with High Open-Circuit Voltages." *J. Am. Chem. Soc.*, **130**, 13653–13658, 2008.

[45] I. A. Howard, R. Mauer, M. Meister, and F. Lacquai. "Effect of Morphology on Ultrafast Free Carrier Generation in Polythiophene:Fullerene Organic Solar Cells." *J. Am. Chem. Soc.*, **132**, 14866–14876, 2010.

[46] C. G. Shuttle, B. O'Regan, A. M. Ballantyne, J. Nelson, D. D. C. Bradley, and J. R. Durrant. "Bimolecular Recombination Losses in polythiophene:Fullerene Solar Cells." *Phys. Rev. B*, **78**, 113201:1–113201:4, 2008.

[47] G. F. A. Dibb, F. C. Jamieson, A. Maurano, J. Nelson, and J. R. Durrant. "Limits on the Fill Factor in Organic Photovoltaics: Distinguishing Nongeminate and Geminate Recombination Mechanics." *J. Phys. Chem. Lett.*, **4**, 803–808, 2013.

[48] ASTM G159-98. "Standard Tables for References Solar Spectral Irradiance at Air Mass 1.5: Direct Normal and Hemispherical for a 37° Tilted Surface.", 1998. [Online; Accessed 01-oct-2015].

[49] T. Förster. "Zwischenmolekulare Energiewanderung und Fluoreszenz." *Ann. Phys.*, **437**, 55–75, 1948.

[50] K. Feron, W. J. Belcher, C. J. Fell, and P. C. Dastoor. "Organic Solar Cells: Understanding the Role of Förster Resonance Energy Transfer." *Int. J. Mol. Sci.*, **13**, 17019–17047, 2012.

[51] J. Piris, T. E. Dykstra, A. A. Bakulin, P. H. M. van Loosdrecht, W. Knulst, M. T. Trinh, J. M. Schins, and L. D. A. Siebbeles. "Photogeneration and Ultrafast Dynamics of Excitons and Charges in P3HT/PCBM Blends." *J. Phys. Chem. C*, **113**, 14500–14506, 2009.

[52] M. Scheidler, U. Lemmer, R. Kersting, S. Karg, W. Riess, B. Cleve, R. F. Mahrt, H. Kurz, H. Bassler, E. O. Gobel, and P. Thomas. "Monte Carlo Study of Picosecond Exciton Relaxation and Dissociation in poly(phenylenevinylene)." *Phys. Rev. B*, **54**, 5536–5544, 1996.

[53] S. R. Scully and M. D. McGehee. "Effects of Optical Interference and Energy Transfer on Exciton Diffusion Length Measurements in Organic Semiconductors." *J. Appl. Phys.*, **100**, 034907:1–034907:5, 2006.

[54] I. C. Henderson and N. Clarke. "On Modelling Surface Directed Spinodal Decomposition." *Macromol. Theory Simul.*, **14**, 435–443, 2005.

[55] S. Kouijzer, J. J. Michels, M. van den Berg, V. S. Gevaerts, M. Turbiez, M. M. Wienk, and R. A. J. Janssen. "Predicting Morphologies of Solution Processed Polymer:Fullerene Blends." *J. Am. Chem. Soc.*, **135**, 12057–12067, 2013.

[56] O. Wodo and B. Ganapathysubramanian. "Modeling Morphology Evolution During Solvent-based Fabrication of Organic Solar Cells." *Comput. Mater. Sci.*, **55**, 113–126, 2012.

[57] J. J. Michels and E. Moons. "Simulation of Surface-Directed Phase Separation in a Solution-Processed Polymer/PCBM Blend." *Macromolecules*, **46**, 8693–8701, 2013.

[58] O. Wodo, S. Tirthapura, S. Chaudhary, and B. Ganapathysubramanian. "A Graph-Based Formulation for Computation Characterization of Bulk Heterojunction Morphology." *Org. Electron.*, **13**, 1105–1113, 2012.

[59] J. W. Cahn and J. E. Hilliard. "Free Energy of a Nonuniform System. I. Interfacial Free Energy." *J. Chem. Phys.*, **28**, 258–267, 1958.

[60] P. J. Flory. "Thermodynamics of High-Polymer Solutions." *J. Chem. Phys.*, **9**, 660–661, 1941.

[61] M. L. Huggins. "Theory of Solutions of High Polymers." *J. Am. Chem. Soc.*, **64**, 1712–1719, 1942.

[62] A. C. Arias, J. D. MacKenzie, I. McCulloch, J. Rivnay, and A. Salleo. "Materials and Applications for Large Area Electronics: Solution-Based Approaches." *Chem. Rev.*, **110**, 3–24, 2010.

[63] B. Walker, A. B. Tamayo, X.-D. Dang, P. Zalar, J. H. Seo, A. Garcia, M. Tantiwiwat, and T.-Q. Nguyen. "Nanoscale Phase Separation and High Photovoltaic Efficiency in Solution-Processed, Small-Molecule Bulk Heterojunction Solar Cells." *Adv. Funct. Mater.*, **19**, 3063–3069, 2009.

[64] D. P. McMahon, D. L. Cheung, L. Goris, J. Dacuña, A. Salleo, and A. Troisi. "Relation between Microstructure and Charge Transport in Polymers of Different Regioregularity." *J. Phys. Chem. C*, **115**, 19386–19393, 2011.

[65] S. Athanasopoulos, E. Hennebicq, D. Beljonne, and A. B. Walker. "Trap Limited Exciton Transport in Conjugated Polymers." *J. Phys. Chem. C*, **112**, 11532–11538, 2008.

[66] J. Kirkpatrick. "An Approximate Method for Calculating Transfer Integrals Based on the ZINDO Hamiltonian." *Int. J. Quant. Chem.*, **1**, 51–56, 2008.

[67] K. Do, D. M. Huang, R. Faller, and A. J. Moulé. "A Comparative MD Study of the Local Structure of Polymer Semiconductors P3HT and PBTTT." *Phys. Chem. Chem. Phys.*, **12**, 14735–14739, 2010.

[68] J.-M. Y. Carrillo, R. Kumar, M. Goswami, B. G. Sumpter, and W. M. Brown. "New Insights into the Dynamics and Morphology of P3HT:PCBM Active Layers in Bulk Heterojunctions." *Phys. Chem. Chem. Phys.*, **15**, 17873–17882, 2013.

[69] T. T. To and S. Adams. "Modelling of P3HT:PCBM Interface Using Coarse-Grained Forcefield Derived from Accurate Atomistic Forcefield." *Phys. Chem. Chem. Phys.*, **16**, 4653–4663, 2014.

[70] C.-K. Lee, C.-W. Pao, and C.-W. Chu. "Multiscale Molecular Simulations of the Nanoscale Morphologies of P3HT:PCBM Blends for Bulk Heterojunction Organic Photovoltaic Cells." *Energy Environ. Sci.*, **4**, 4124–4132, 2011.

[71] M. Schrader, R. Fitzner, M. Hein, C. Elschner, B. Baumeier, K. Leo, M. Riede, P. Bäuerle, and D. Andrienko. "Comparitive Study of Microscopic Charge Dynamics in Crystalline Acceptor-Substituted Oligothiophenes." *J. Am. Chem. Soc.*, **134**, 6052–6056, 2012.

[72] C. Poelking, E. Cho, A. Malafeev, V. Ivanov, K. Kremer, C. Risko, J.-L. Brédas, and D. Andrienko. "Characterization of Charge-Carrier Transport in Semicrystalline Polymers: Electronic Couplings, Site Energies and Charge-Carrier Dynamics in Poly(bithiophene-alt-thienothiophene) [PBTTT]." *J. Phys. Chem. C*, **177**, 1633–1640, 2013.

[73] D. M. Huang, R. Faller, K. Do, and A. J. Moulé. "Coarse-Grained Computer Simulations of Polymer/Fullerene Bulk Heterojunctions for Organic Photovoltaic Applications." *J. Chem. Theory Comput.*, **6**, 526–537, 2010.

[74] J. J. Kwiatkowski, J. Nelson, H. Li, J. L. Brédas, W. Wenzel, and C. Lennartz. "Simulating Charge Transport in tris(8-hydroxyquinoline) Aluminium (Alq_3)." *Phys. Chem. Chem. Phys.*, **10**, 1852–1858, 2008.

[75] J. J. Kwiatkowski, J. M. Frost, and J. Nelson. "The Effect of Morphology on Electron Field-Effect Mobility in Disordered C_{60} Thin Films." *Nano Lett.*, **9**, 1085–1090, 2009.

[76] J. Nelson, J. J. Kwiatkowski, J. Kirkpatrick, and J. M. Frost. "Modeling Charge Transport in Organic Photovoltaic Materials." *Acc. Chem. Res.*, **42**, 1768–1778, 2009.

Chapter 4

Geminate Pair Recombination Dynamics

4.1 Introduction

In order to produce useful photovoltaic current, OPV devices must efficiently convert the CT state, which results from exciton dissociation at the heterojunction, into free charges that can then separate and be collected at the electrical contacts. The efficiency at which this occurs, η_{SEP}, is therefore an important factor in determining the overall power conversion efficiency of OPVs. Given the strong Coulombic attraction between charges due to a small dielectric constant, η_{SEP} may be expected to be small or field-dependent[1,2]. While this behaviour has been reported for some OPVs[3,4], η_{SEP} has been shown to be large or field-independent in others[3,5,6]. The physical mechanisms causing this behaviour are the subject of much research[7]. Photoluminescence and photoinduced absorption spectroscopy are useful tools to help understand these mechanisms[3,8,9], although they often require kinetic models

(KMs) to interpret the data[10–13].

In this chapter, the mechanism of charge separation from the CT state will be examined, along with the issues associated with using simplified KMs to interpret the data. A brief description of the KMs currently in use to describe photoexcited state dynamics is given in §4.2. In §4.3, the mesoscale MC simulation methodology is outlined, which describes charge hopping in an energetically disordered BHJ morphology but omits HCT states - therefore only considering the most basic case of CT state dissociation. This model is then used to examine the dynamics and efficiency of CT state dissociation at a variety of electric fields in §4.4. Then, in §4.5, these MC data are interpreted using a KM, in a similar manner to how spectroscopic data is analysed. This enables examination of the relationship between the known, physical processes and rates within the MC simulations and the rates derived from the KM. The MC simulations reveal field-dependent, multi-exponential recombination dynamics in agreement with experiment. It is shown that the mean recombination time is only loosely related to the recombination rate of charges k_r. The wide range of data provided by MC, which includes separation efficiency and recombination dynamics as a function of applied electric field, could not be fitted to existing KMs. As such, an alternative KM is proposed that yields reasonable fits to all MC data; furthermore it is shown to predict qualitatively the behaviour of the MC data when the recombination rate is modified. However, it is also shown that in order to achieve quantitative fits to MC data with a modified recombination rate, the transport coefficients also have to be altered, which is not representative of the MC model. This suggests that, while KMs are useful to fit to experimental data,

they do not always have exact correspondence to the physical processes occurring in an OPV. The main conclusions of the investigation are presented in §4.6.

4.2 Kinetic Models

Analysis of excited state dynamics measured by spectroscopy commonly involves a KM in which the various excited states and transition rates are defined on an energy level (Jablonski) diagram. These diagrams represent a simplification of the charge separation process, mainly because KMs necessarily only consider a finite number of states. However, the generally observed dynamic behaviour from experiment can be reproduced by fitting the free parameters of the KM, which describe the transition rates of carriers between energy levels. Perhaps the simplest KM of excited state dynamics for an OPV is given by the OB model[1,2], shown in figure 4.1. Here, the exciton incident on the donor-acceptor interface creates a CT state which may then either recombine to the ground state (GS) with a rate k_r, or separate to free charges (FCs) with a rate k_s. The populations of these three states can be described by the following, coupled, first-order ordinary differential equations:

$$\frac{\mathrm{d[CT]}}{\mathrm{d}t} = -k_r\,[\mathrm{CT}] - k_s\,[\mathrm{CT}]\,, \tag{4.2.1}$$

$$\frac{\mathrm{d[FC]}}{\mathrm{d}t} = k_s\,[\mathrm{CT}]\,, \tag{4.2.2}$$

$$\frac{\mathrm{d[GS]}}{\mathrm{d}t} = k_r\,[\mathrm{CT}]\,, \tag{4.2.3}$$

where square brackets denote the population of each state. It is important to note that the schematic figure in the Braun paper depicts a feedback path between the FC and CT states, which would increase the rate of change of [CT] at the

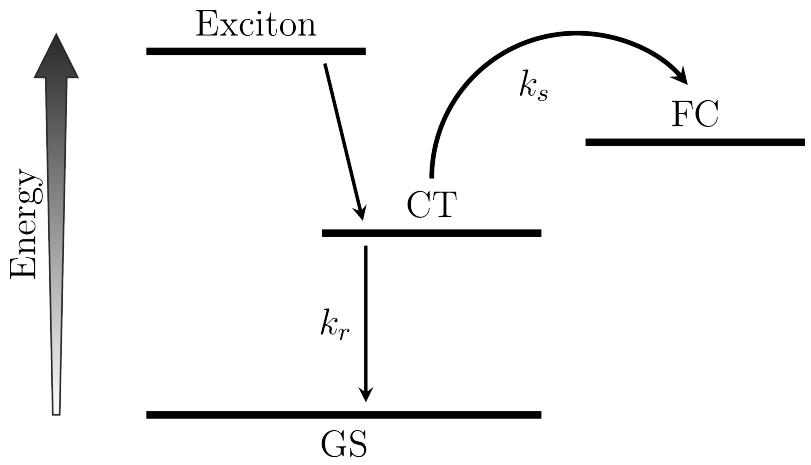

Figure 4.1: *Schematic of the Onsager-Braun (OB) description of charge generation and separation. The rate coefficients k_s and k_r describe the separation and recombination processes respectively.*

expense of [FC] by an amount k_c[FC] (where k_c is the rate of feedback between the two states) however the equation for dissociation efficiency in the subsequent analysis does not take this feedback path into account. This type of model has been successfully fitted to spectroscopy data in a range of OPV systems[14,15], although others cannot be well fit by an OB type model. To remedy this issue, modifications to the energy level diagram are often proposed, which will be studied in more detail in §4.5.

In order for a pair of charges to be considered free, a CT state must achieve a mutual separation of r >16 nm, at which point the mutual Coulomb interaction reduces to $\sim k_BT$[16]. In the absence of charge delocalisation, this occurs via a series of hops which individually may either increase or decrease the separation of the charges as described in §2.2. There are many potential hop destinations, which results in a manifold of intermediate states that is difficult to consider using a KM. In turn, this leads to difficulty in understanding complex dynamic behaviour as well as relating the fitted rate coefficients to quantum chemical determinations of the

recombination or hopping processes[17].

The degree of confidence one can have with a particular KM is somewhat dependent on the efficiency of the OPV device. In an inefficient OPV system, transport and trapping in intermediate states may be expected to be significant, and KMs will inevitably be more approximate. In efficient OPV systems, the number of hops required to separate a CT state to FC may be fewer. This can be due to, for instance, the effect of preferential energetic disorder[18,19], the driving force of entropy[20], or cascaded energy heterojunctions[21,22]. Furthermore, efficient OPVs may benefit from the delocalisation of the exciton[23] or the CT state[13,24,25] (as explored in chapter 5), which increases the initial separation of the charges, reducing both the Coulombic attraction and the distance that carriers must travel in order to be considered free. Nonetheless, even with these caveats, it is likely that the charges generated from CT states will still have to separate by a distance of some nanometres via intermediate transport states to become free.

4.3 Monte Carlo Methodology

The operating procedure of the previously developed mesoscale MC model used in this investigation is discussed in §3.4[26–31], with the aim of recreating CT state dissociation in an OPV, taking into account factors such as energetic disorder and bulk heterojunction morphology. MC simulations of the type used here have been successful in obtaining quantitative agreement with OPV systems in which these factors have been identified as key determinants for performance, particularly within all-polymer[32,33] and inefficient polymer-fullerene devices[19].

Photoinjection and dark-current were not considered throughout this investigation. Instead, simulations commenced with the photoinjection of an electron-hole pair at a random donor:acceptor interfacial site within an input Cahn-Hilliard morphology (the generation methodology of which is explained in §3.4.1). Charges were permitted to hop to nearest-neighbour cells of the appropriate material (*e.g.* electrons to the acceptor) at a rate given by the semiclassical Marcus expression, equation 3.3.10[34]. Instead of explicitly considering the electronic transfer integrals, the prefactor was set as a constant coefficient, v_0. Implicit in this assumption is the averaging of the transfer integrals across the morphology, resulting in homogeneous and time-independent site-to-site electronic couplings. To produce carrier mobilities that are similar to those reported for charges in amorphous polymers ($\mu = 4.2 \times 10^{-6}\,\mathrm{cm\,V^{-2}\,s^{-1}}$)[29], E_r was set to $4 \times 10^{-20}\,\mathrm{J}$, and $v_0 = 1 \times 10^{-11}\,\mathrm{s^{-1}}$. For the sake of simplicity, the transport of electrons and holes were assumed to be the same. Within the morphology, adjacent charges were permitted to recombine to the GS at a rate of $k_r = 1 \times 10^{7}\,\mathrm{s^{-1}}$, which is similar to that reported for all-polymer blends[35]. Simulations proceeded until each geminate charge pair had either recombined or separated - here defined as the carriers achieving a mutual separation of $r = 25\,\mathrm{nm}$. This process was repeated for at least 7×10^6 iterations over 15 different configurations of energetic disorder so as to obtain reliable statistics.

Measuring the behaviour of successive, independent charge pairs in this way most closely represents the charge kinetics of devices that are exposed to low excitation fluence in experiment. However, it is noted that a definite end point of the simulation has been defined, whereupon geminate recombination is deemed not to have

occurred. This distinction between the prompt, geminate recombination and the subsequent, delayed, bimolecular recombination is somewhat artificial, however at low pump fluence, the timescales at which both types of recombination occur are expected to be different [36,37]. It is therefore argued that it is reasonable to consider geminate and bimolecular recombination separately.

4.4 Recombination Dynamics

CT state dynamics were simulated for a range of electric fields between $1\times10^6 \leq F < 1\times10^8\,\mathrm{V\,m^{-1}}$, representing an OPV bias range extending through the operating region to a strong reverse bias (where the collection of charges is efficient). The full MC dataset is shown in figure 4.2, along with modified KM traces which will be explained in §4.5. For each electric field, the probability density function, $P_r(t)$, that a recombination event will occur at time, t, and the CT state separation efficiency, η_{SEP}, were measured.

From these data, it was possible to calculate the mean recombination time, $\langle\tau_{\mathrm{REC}}\rangle$ as

$$\langle\tau_{\mathrm{REC}}\rangle = \int_0^{t_{\mathrm{MAX}}} tP_r(t)\,\mathrm{d}t, \tag{4.4.4}$$

where t_{MAX} was defined as the time at which $P_r(t)$ had dropped by 3 orders of magnitude, corresponding to the signal range available in experiment.

The symbols in figure 4.3a show the MC-calculated $\langle\tau_{\mathrm{REC}}\rangle$ as a function of increasing electric field. It is apparent that $\langle\tau_{\mathrm{REC}}\rangle$ is field-dependent, as it is larger than the inverse recombination rate $(1/k_r)$ at fields corresponding to the operating

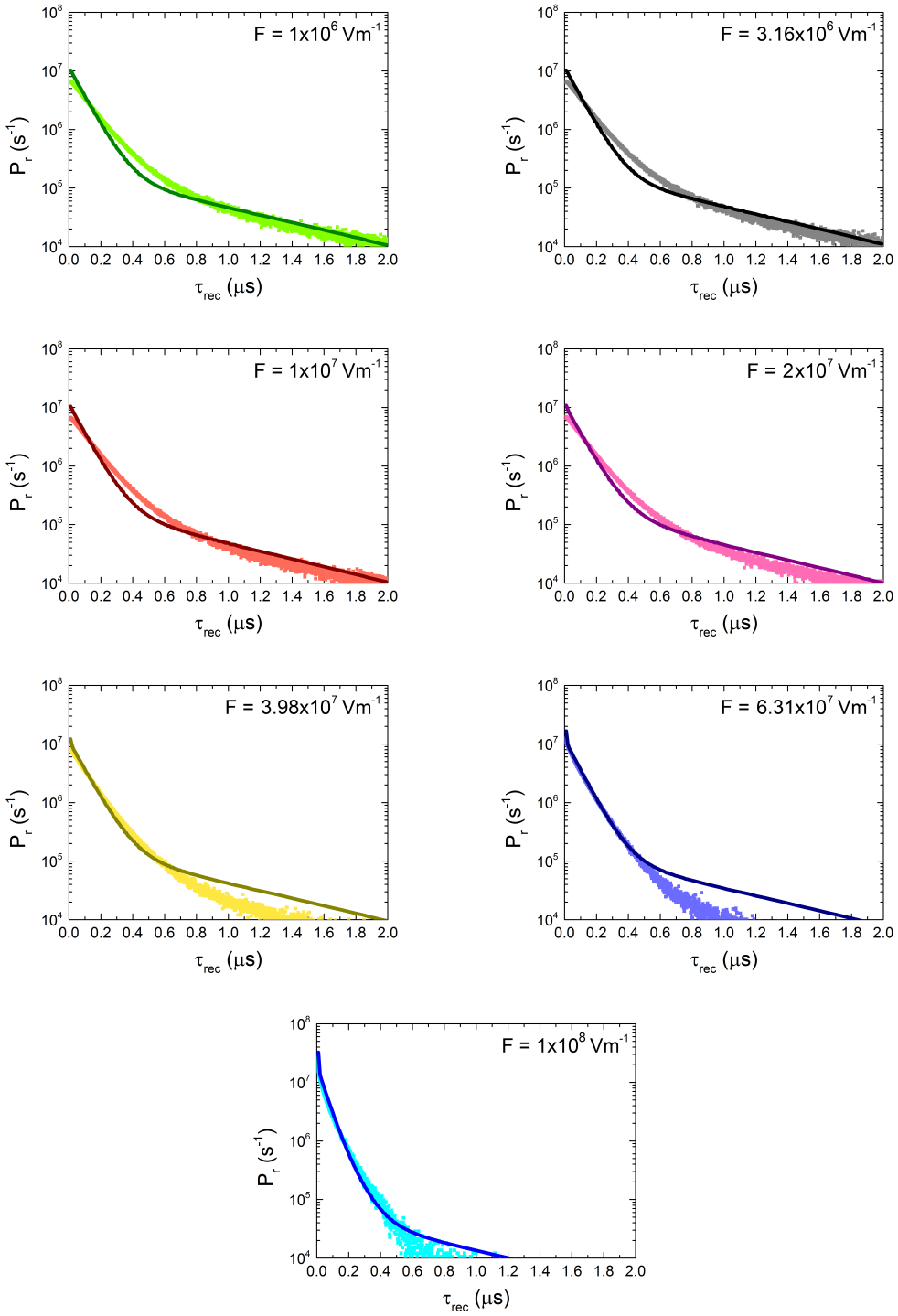

Figure 4.2: *$P_r(t)$ from the MC simulations (symbols) and KM (lines) for all explored field values using fiducial simulation parameters and given a recombination rate of $k_r = 1 \times 10^7\, s^{-1}$.*

region of an OPV ($F \simeq 1 \times 10^6\,\mathrm{V\,m^{-1}}$) and smaller than $1/k_r$ at high fields corresponding to strong reverse bias ($F \simeq 1 \times 10^8\,\mathrm{V\,m^{-1}}$). This dynamic behaviour is examined further in figure 4.3b, which shows that $P_r(t)$ is generally bi-exponential, with a slow decay component that has a characteristic rate that is smaller than k_r. This is in agreement with preliminary work using similar MC simulations[18] although, due to a larger sample size, the bi-exponential behaviour and field dependence of $P_r(t)$ are revealed more clearly for this investigation. Additionally, the prominence of the slow decay component is shown to increase as the field is reduced. Figure 4.3c shows the probability density function for the CT state lifetime, here defined as a pair of charge carriers that are located within 2 nm of each other. The MC data (solid lines) predicts qualitatively similar bi-exponential decay behaviour for the CT state population, suggesting that the field-dependence of the slow decay shown in figure 4.3b is not solely characteristic of the recombination process.

This slow decay is attributed to energetically and morphologically trapped charge carriers, which eventually detrap and are afforded another chance to recombine later, resulting in a slower transient than when the charges were first created adjacent to each other at the donor-acceptor interface. Applying an electric field to the system reduces the likelihood of this trapping, hence the prominence of the slow decay component is reduced. This mechanism has been reported elsewhere to explain experimental data[11,38]. The initial 'fast' decay of $P_r(t)$ is reasonably well-described by $1/k_r$, however the rate of decay is shown to increase with field. The fast decay component is most likely due to field-dependent charge transport 'emptying' the CT state and therefore reducing the potential for recombination.

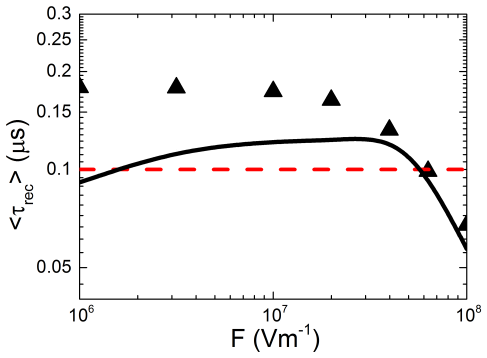

(a) *$\langle \tau_{REC} \rangle$ for both the MC simulations (black symbols) and the KM (black line), along with the inverse recombination rate $1/k_r$ (red line)*

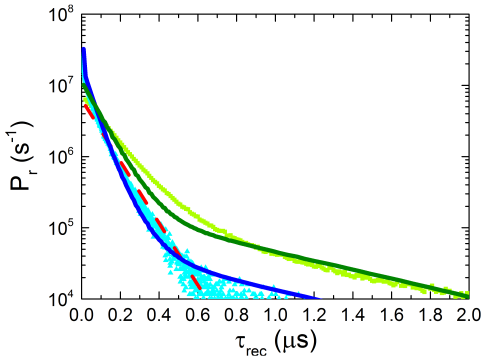

(b) *$P_r(t)$ obtained by MC (symbols) and the KM (lines) for $F = 1 \times 10^6\ V m^{-1}$ (green) and $F = 1 \times 10^8\ V m^{-1}$ (blue), along with the inverse recombination rate $1/k_r$ (red line)*

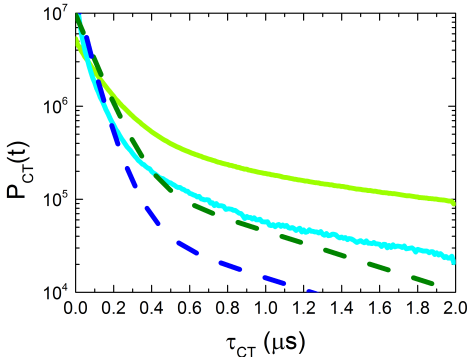

(c) *The CT state population $P_{CT}(t)$ from the MC (symbols) and KM (dashed lines) for fields $F = 1 \times 10^6\ V m^{-1}$ (green) and $F = 1 \times 10^7\ V m^{-1}$ (blue)*

Figure 4.3: *Recombination dynamics from MC simulations given $k_r = 1 \times 10^7\ s^{-1}$, including fitted KM traces.*

Multi-exponential CT state dynamics of the type shown in figure 4.2 are ubiquitous throughout the literature. In many cases, bi- or tri-exponential decays are fitted to data, although often the third decay component occurs on a faster timescale than the instrument response time, leaving two free parameters to describe the observed kinetics[4,38]. As the charge transport mechanisms seem to be able to be described by a small number of free parameters, KMs provide a useful way to interpret these types of data.

4.5 New Kinetic Model

The simplest KM is provided by the OB model shown in figure 4.1, in which the CT state branches to either the GS or FC. Under these circumstances, the lifetime of the CT state is described by

$$\tau_{\mathrm{CT}} \propto \frac{1}{k_r + k_s}. \tag{4.5.5}$$

At low fields, when $k_s \to 0$, $\tau_{\mathrm{CT}} \to 1/k_r$. At high fields, when $k_s >> k_r$, then $\tau_{\mathrm{CT}} \to 1/k_s$. Hence, a simple branching model can explain the trends in figure 4.3 which indicate $\tau_{\mathrm{CT}} < 1/k_r$ at high fields, but it cannot explain $\tau_{\mathrm{CT}} > 1/k_r$ at low field, nor a bi-exponential $P_r(t)$ as is present in the MC data, despite only a single recombination rate.

Due to the inability of simple OB-type models to describe the bi-exponential kinetics and the field dependence thereof, a variety of modifications have previously been suggested. These include the incorporation of a manifold of CT states[4,39], feedback loops *via* charge transport back to the CT state[40,41], energetic and morphological trapping resulting in a slower recombination pathway[11,38] or multiple separation/decay pathways[3,10,42].

In order to satisfactorily reproduce the MC-observed CT dynamics observed here, a new kinetic framework had to be proposed. As with OB, the GS and FC states were defined as carrier 'sinks', representing the end points of recombination and successful separation to the contacts respectively. A CT state was also introduced, which would be directly populated by exciton dissociation and from which recombination to GS

could occur. Unlike the OB model, a manifold of states intermediate between CT and FC was also considered. Within this manifold, charges were considered to be Coulombically bound but unable to recombine due to a small physical separation between the two. The manifold was then collected into a single state which was termed quasi-free (QF).

As in the MC simulation, charges within the QF state could separate further and become FC, or were permitted to 'collapse' back to the CT state where recombination could occur. This is conceptually similar to the work of Wojcik and Tachiya[43], who describe multi-exponential separation and modify OB mathematically by alleviating the constraint that recombination cannot occur unless charges are adjacent. Here, recombination occurring outside the reaction radius could be considered by increasing the recombination rate. However, for the purposes of this investigation, only adjacent charges were permitted to recombine, with spatially separated charges existing in the QF state instead, where no direct recombination path exists.

4.5.1 Single Decay Channel

Figure 4.4a depicts the most simple KM that includes the behaviour highlighted above, including just one of each category of state, and 4 total rate coefficients. This scheme provides reasonable fits to the MC predicted η_{SEP} (figure 4.4e), and also the general shape of $P_r(t)$ (figures 4.4a-d). However, the initial slope of $P_r(t)$ which denotes fast recombination is not recreated faithfully, particularly at $F = 1 \times 10^8\,\mathrm{V\,m^{-1}}$. It is important that this region of the bi-exponential decay is accurate as fast recombinations make a large contribution to $\langle \tau_{\mathrm{REC}} \rangle$.

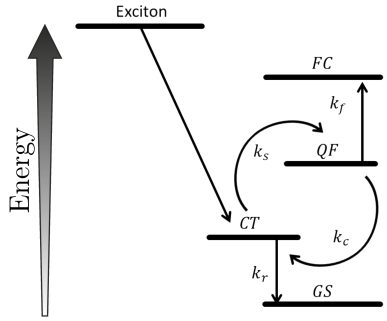

(a) KM scheme. The rate coefficients k_s, k_c, k_f and k_r describe the processes of separation, collapse, freedom and recombination respectively

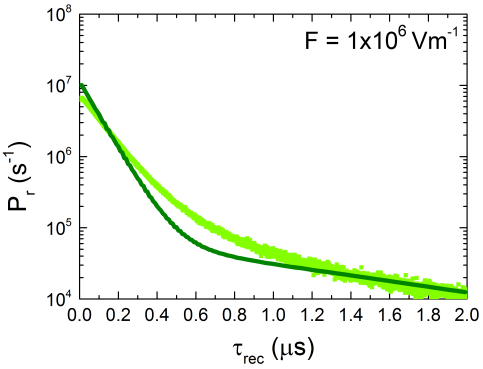

(b) P_r at $F = 1 \times 10^6\ V\,m^{-1}$

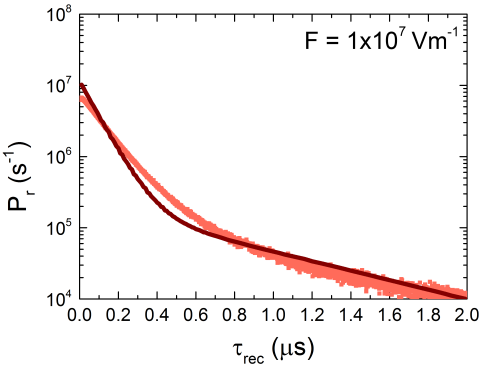

(c) P_r at $F = 1 \times 10^7\ V\,m^{-1}$

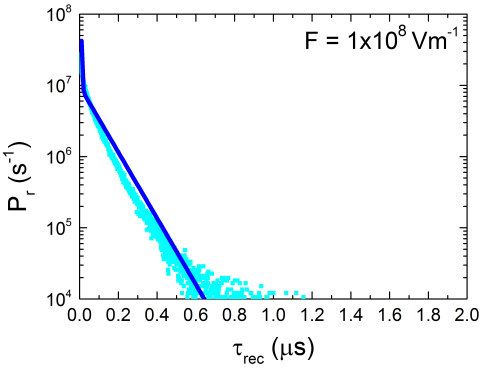

(d) P_r at $F = 1 \times 10^8\ V\,m^{-1}$

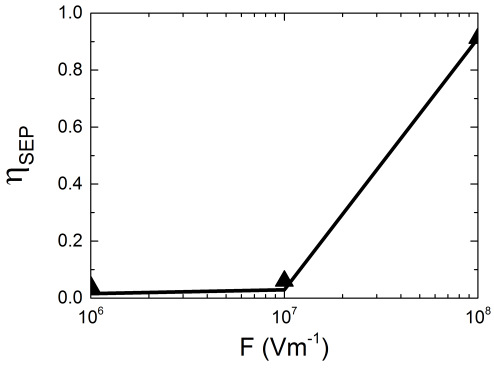

(e) The corresponding field-dependent separation efficiency, η_{SEP}

Figure 4.4: *Comparison of the MC (symbols) and KM (lines) recombination dynamics and separation efficiencies for a KM with a single set of states (and therefore a single separation/recombination pathway) in the kinetic scheme.*

4.5.2 Dual Decay Channel

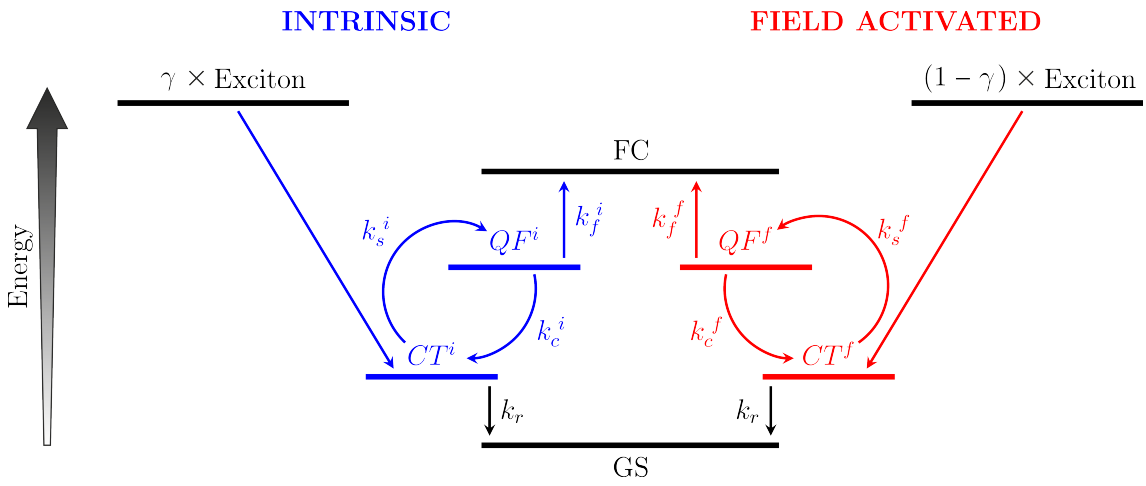

Figure 4.5: *Schematic of the proposed kinetic scheme. Two independent populations of charges are produced (with field dependent probability γ), representing intrinsic (superscript i, blue) and field-activated (superscript f, red) recombination pathways. The rate coefficients k_s, k_c, k_f and k_r describe the processes of separation, collapse, freedom and recombination respectively.*

In order to replicate the correct field-dependence for $P_r(t)$ and η_{SEP}, a combination of two recombination pathways was investigated, one related to the field-independent diffusion of carriers through the morphology and the other describing the drift of carriers within the internal electric field of the device. These were termed 'intrinsic' and 'field-activated' respectively, and the full KM is shown in figure 4.5. The fraction of excitons which dissociate *via* the intrinsic route was defined as γ, and therefore the fraction of excitons which dissociate *via* the field-activated route was $1-\gamma$. The dynamic behaviour of this scheme can therefore be described by the following equations:

$$\frac{\mathrm{d}[\mathrm{CT}^x]}{\mathrm{d}t} = -k_r^x\left[\mathrm{CT}^x\right] - k_s^x\left[\mathrm{CT}^x\right] + k_c^x\left[\mathrm{QF}^x\right], \tag{4.5.6}$$

$$\frac{\mathrm{d}[\mathrm{QF}^x]}{\mathrm{d}t} = k_s^x\left[\mathrm{CT}^x\right] - k_c^x\left[\mathrm{QF}^x\right] - k_f^x\left[\mathrm{QF}^x\right], \tag{4.5.7}$$

$$\frac{\mathrm{d}[\mathrm{FC}]}{\mathrm{d}t} = k_f^i\left[QF^i\right] + k_f^f\left[QF^f\right], \tag{4.5.8}$$

$$\frac{\mathrm{d}[\mathrm{GS}]}{\mathrm{d}t} = k_r \left[CT^i\right] + k_r \left[CT^f\right], \tag{4.5.9}$$

where the superscript x represents either the field-activated (f) or intrinsic (i) pathways and square brackets denote the population of each state. The rate coefficients k_s^x, k_c^x and k_f^x are depicted in figure 4.5. The separation efficiency η_{SEP} was calculated by solving the differential equations for the intrinsic and field-activated pathways separately to obtain the population of the GS for time $t \to \infty$ for each route. Then, the overall separation efficiency was calculated as $\eta_{\mathrm{SEP}} = \gamma\eta_{\mathrm{SEP}}^i + (1-\gamma)\eta_{\mathrm{SEP}}^f$.

In order to limit the parameter space, the rate coefficients for the intrinsic pathway were assumed to be constant with field, whereas the field-activated rate coefficients were permitted to vary linearly with the field. It was assumed that, for the inefficient OPV blends examined here, intrinsic charge generation dominates at low fields (*i.e.* $\gamma \to 1$). As the field increases, charges begin to detrap and the field-activated route becomes more dominant (*i.e.* γ decreases). Hence, γ was forced to decrease monotonically with increasing field.

A variable-timestep fourth-order Runge-Kutta method was employed to numerically solve the coupled differential equations 4.5.6-4.5.9. The free parameters in these equations were fitted to the η_{SEP}, $\langle\tau_{\mathrm{REC}}\rangle$ and $P_r(t)$ data measured by MC, subject to the constraints mentioned above. These parameters are shown in figures 4.6a and b. As can be seen from figure 4.6c, excellent fits to the MC predicted η_{SEP} are obtained. Note that the small MC prediction of $\eta_{\mathrm{SEP}} < 0.1$ below $F = 1 \times 10^7\,\mathrm{V\,m^{-1}}$ (which corresponds approximately to the operating range of an OPV) is a result of utilising model parameters that correspond to inefficient polyfluorene all-polymer devices[32], as opposed to their more efficient polymer-fullerene counterparts.

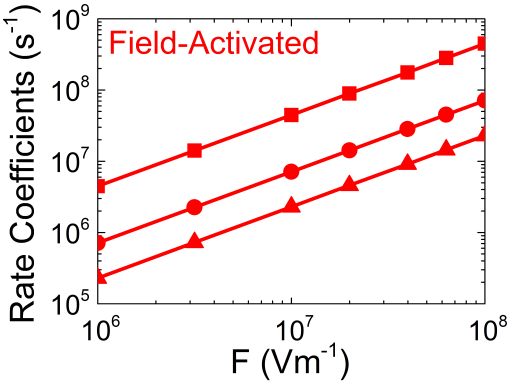

(a) The variation of the rate coefficients k_s^f (squares), k_c^f (circles), and k_f^f (triangles) as a function of F

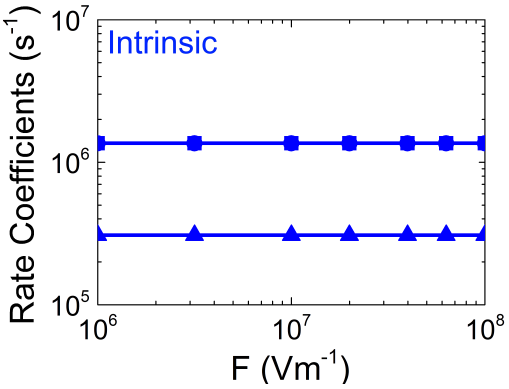

(b) The variation of the rate coefficients k_s^i (squares), k_c^i (circles), and k_f^i (triangles) as a function of F

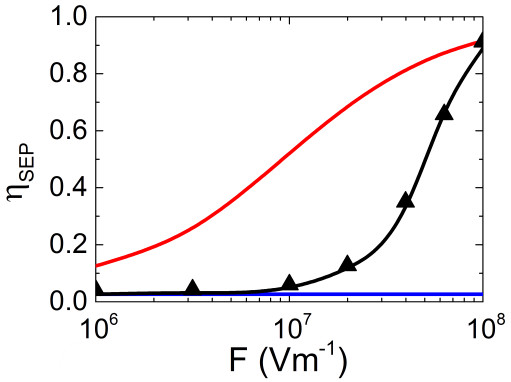

(c) η_{SEP} from MC (black symbols) along with the KM predictions for the field-activated (red), intrinsic (blue) and combined (black line) pathways

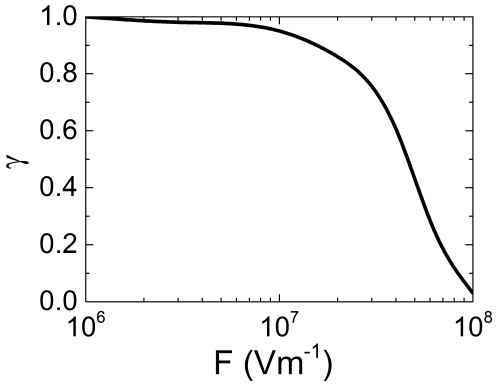

(d) Fraction of CT states in the intrinsic decay channel (γ) as a function of varying electric field (F)

Figure 4.6: *Variation in η_{SEP} (for both MC and KM) and the various free parameters of the KM for $k_r = 1 \times 10^7\, s^{-1}$.*

Figures 4.2 and 4.3b show excellent agreement between the dual-channel KM- and MC-determined $P_r(t)$ for a range of internal electric fields. In particular, the field-dependence of the initial 'fast' and delayed 'slow' component of $P_r(t)$ are recreated faithfully. The bi-exponential character of $P_r(t)$ in the context of this KM arises primarily because of feedback between the QF and CT states, which repopulates the CT state at later times and affords an additional, delayed opportunity for charge recombination to occur. Reasonable fits are also obtained for $\langle \tau_{\mathrm{REC}} \rangle$, shown

in figure 4.3a. As with the MC data, $\langle \tau_{\mathrm{REC}} \rangle$ for the KM was calculated as described in equation 4.4.4, where t_{MAX} was selected such that the KM prediction of $P_r(t)$ had dropped by 3 orders of magnitude.

Figure 4.6d shows the monotonic decay of the parameter γ as a function of internal electric field strength, F. The separation of CT states at low fields is almost solely intrinsic, until the field-activated regime of separation begins to dominate at $F \sim 2.5 \times 10^7\,\mathrm{V\,m^{-1}}$, which corresponds to the sharp increase in η_{SEP} shown in figure 4.6c.

4.5.3 Modified Recombination Rate

Given that the KM was fitted to a wider range of MC data than is generally available in experiment, it might be expected that the KM outlined in figure 4.5 would provide a more complete description of CT state dynamics for this simple system. It was therefore interesting to test the predictive capabilities of the model by performing further MC simulations with the same transport parameters and morphology, except with a modified $k_r = 1 \times 10^6\,\mathrm{s^{-1}}$. One would hope that the KM would provide similarly accurate fits to those shown in figure 4.6 if the recombination rate alone were modified. However, this was found to not be the case. Simply reducing the recombination rate in the KM to $k_r = 1 \times 10^6\,\mathrm{s^{-1}}$ and maintaining the transport parameters at the same values as the fiducial $k_r = 1 \times 10^7\,\mathrm{s^{-1}}$ system resulted in a substantial overestimation of the MC predicted η_{SEP}, as shown in figure 4.7.

It could be argued that this failure is due to a deficiency in the KM of figure 4.5, which in turn leads to errors when it is implemented in a more general fashion.

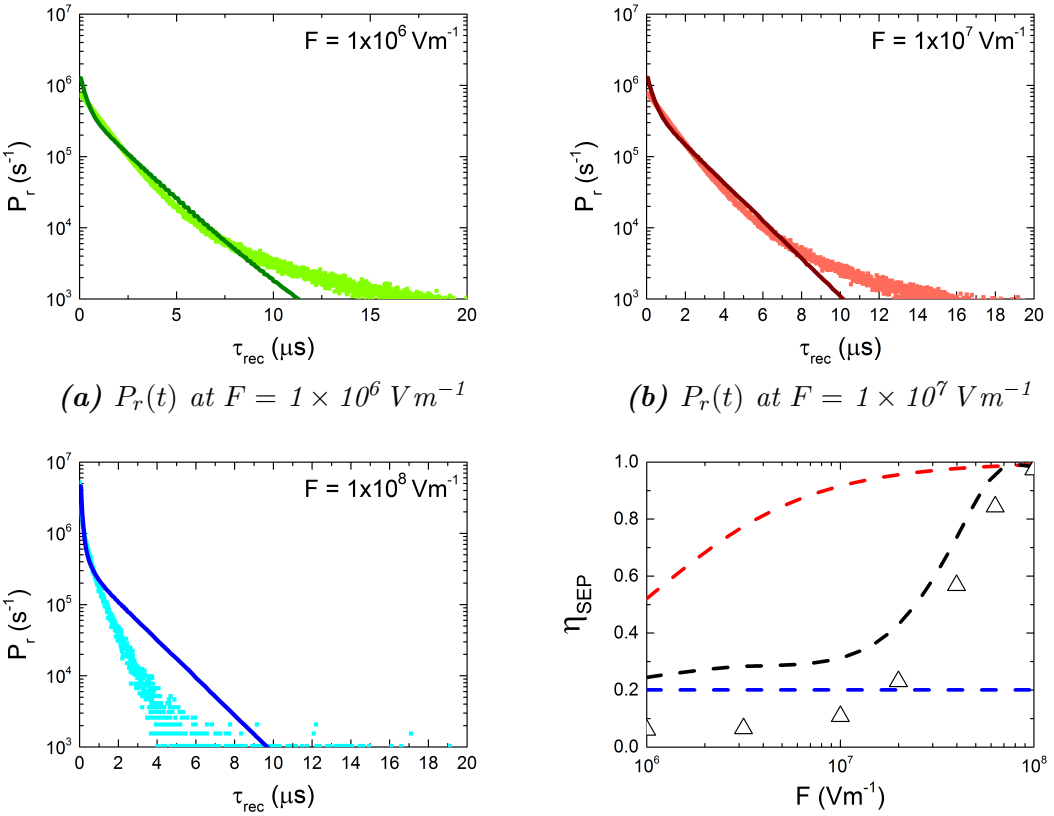

(a) *$P_r(t)$ at $F = 1 \times 10^6\ V m^{-1}$*

(b) *$P_r(t)$ at $F = 1 \times 10^7\ V m^{-1}$*

(c) *$P_r(t)$ at $F = 1 \times 10^8\ V m^{-1}$*

(d) *The corresponding η_{SEP} for the intrinsic (blue), field activated (red) and combined (black) mechanisms*

Figure 4.7: *Comparison of the MC (symbols) and KM (lines) recombination dynamics and separation efficiencies given a modified recombination rate of $k_r = 1 \times 10^6\ s^{-1}$.*

Indeed, this could be the case, however it is important to note that the KM was developed with the benefit of a wide range of charge recombination data and was shown to fit this data well. It was only after further testing by altering k_r that the KM was shown to be lacking in some respects. The wide range of data, and the subsequent tests for robustness, were made straightforward by using a MC model and would seem to be an ideal set of conditions from which to derive a robust, predictive KM. Hence, even though better KMs are possible, it is difficult to see what approach would have to be taken to first hone the alternate models to a point

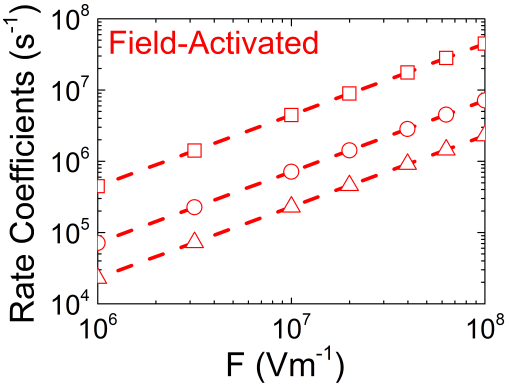

(a) The variation of the rate coefficients k_s^f (squares), k_c^f (circles), and k_f^f (triangles) as a function of F

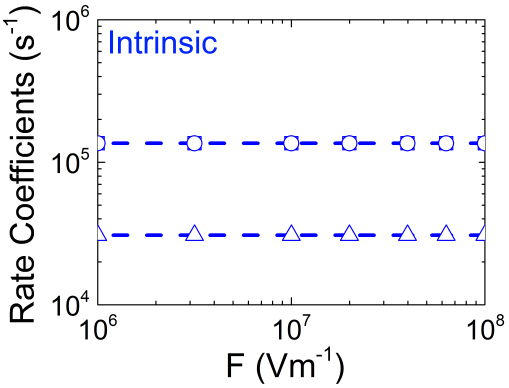

(b) The variation of the rate coefficients k_s^i (squares), k_c^i (circles), and k_f^i (triangles) as a function of F

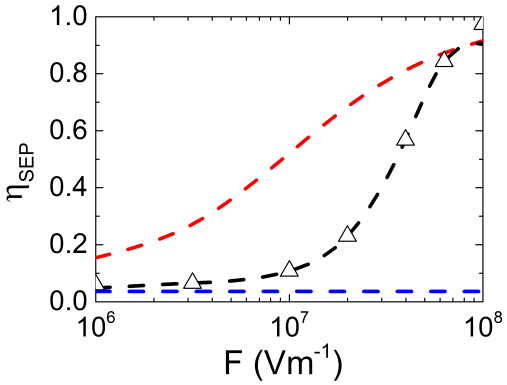

(c) η_{SEP} from MC (black symbols) along with the KM predictions for the field-activated (red), intrinsic (blue) and combined (black line) pathways

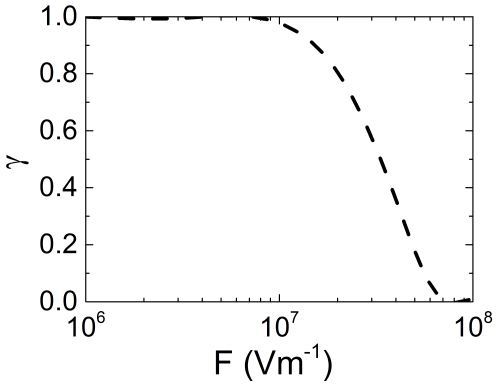

(d) Fraction of CT states in the intrinsic decay channel (γ) as a function of varying electric field (F)

Figure 4.8: *Variation in η_{SEP} (for both MC and KM) and the various free parameters of the KM given a modified $k_r = 1 \times 10^6\, s^{-1}$. All transport rates have been modified in order to give the best fit to the MC data.*

where they satisfactorily recreate the data to the same level as the one outlined in figure 4.5, and then verify the accuracy of their predictions, particularly if relying on experiment alone.

4.5.4 Modified Transport Rates

As can be seen from figures 4.8a and 4.8b, the only way in which satisfactory fits to η_{SEP} and $P_r(t)$ could be obtained was if all of the transport rates in the KM

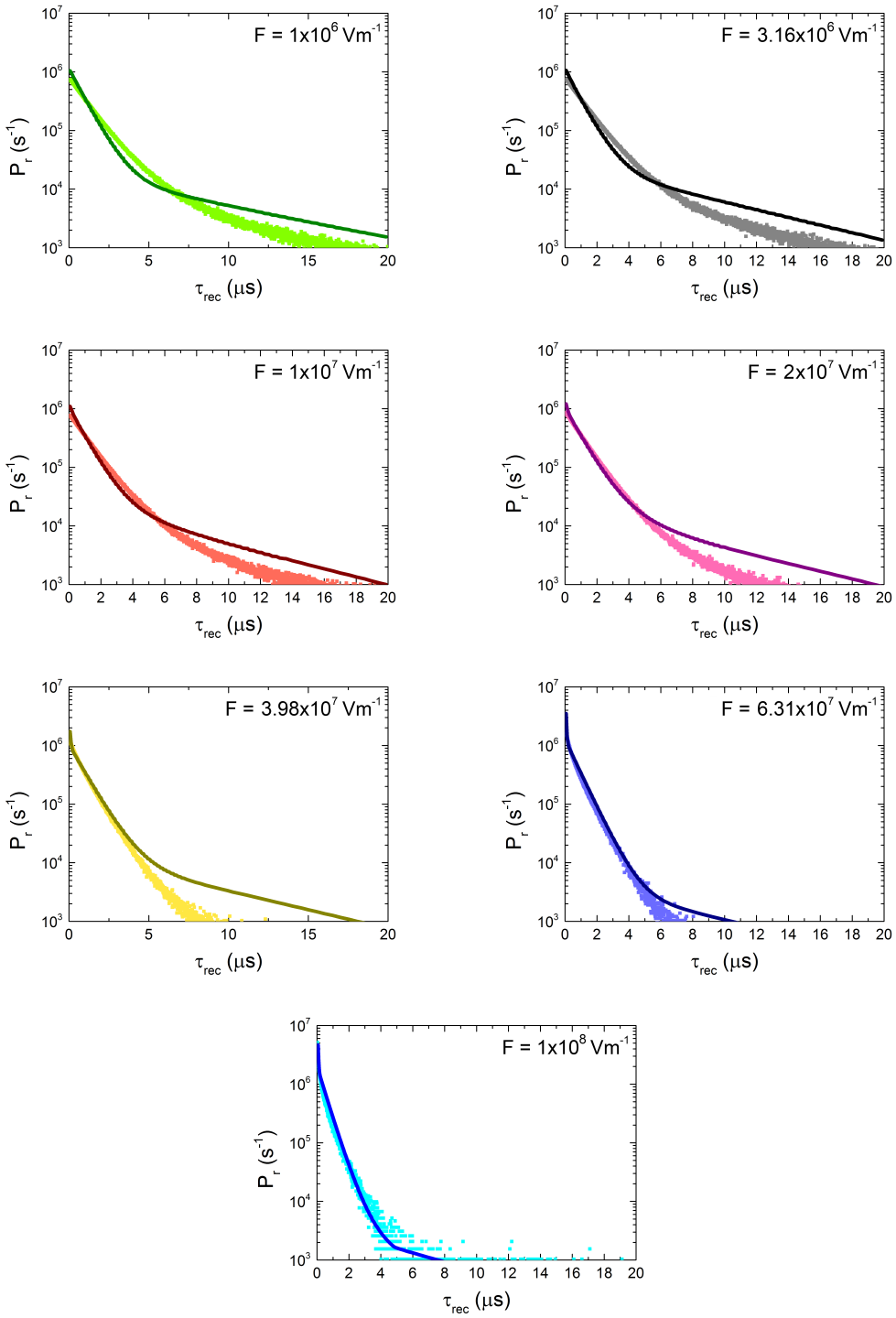

Figure 4.9: *$P_r(t)$ from the MC simulations (symbols) and KM (lines) for all explored field values given a recombination rate of $k_r = 1 \times 10^6\ s^{-1}$. Other transport rates have also been reduced by a factor of 10 from the fiducial dataset.*

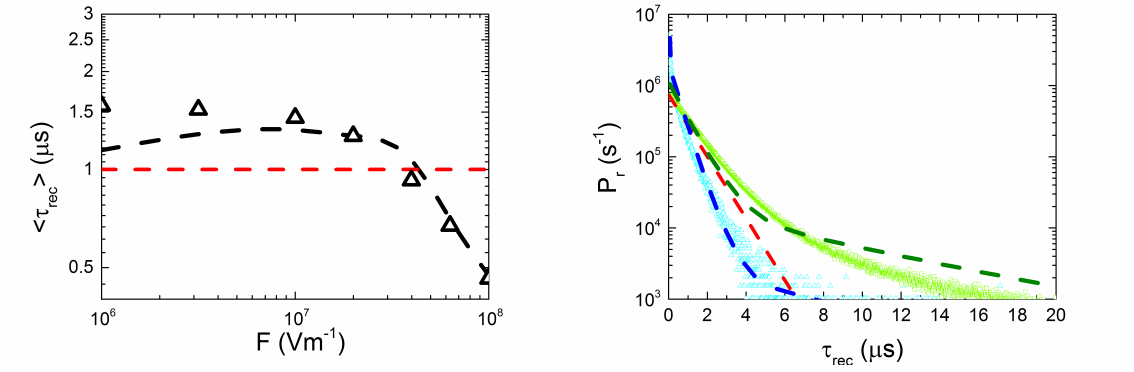

(a) *$\langle \tau_{REC} \rangle$ for both the MC simulations (black symbols) and the KM (black line), along with the inverse recombination rate $1/k_r$ (red line)*

(b) *$P_r(t)$ obtained by MC (symbols) and the KM (lines) for $F = 1 \times 10^6\ V\,m^{-1}$ (green) and $F = 1 \times 10^8\ V\,m^{-1}$ (blue), along with the inverse recombination rate $1/k_r$ (red line)*

Figure 4.10: *Recombination dynamics from MC simulations with $k_r = 1 \times 10^6\ s^{-1}$, including fitted KM traces with all transport rate coefficients modified.*

were arbitrarily reduced by a factor of 10. The fit to η_{SEP} is shown in figure 4.8c, which includes a slight modification to γ from the $k_r = 1 \times 10^7\,\mathrm{s}^{-1}$ (figure 4.8d). The resultant KM fits to the MC recombination dynamics data for all field values are shown in figure 4.9. While good fits to the MC data were achieved, there remains no physical justification for modifying the transport rates themselves as the corresponding processes within the MC model remain unchanged from the fiducial $k_r = 1 \times 10^7\,\mathrm{s}^{-1}$ simulations.

This result is perhaps surprising. Considering first the MC data, the field-dependence of the slow decay component of $P_r(t)$ shows that this feature is related to transport and trapping processes. One might therefore expect that its importance depends on the relative rates of transport and recombination. However, the MC data shows that this is not the case, because the slow decay of $P_r(t)$ is present for both $k_r = 1 \times 10^7\,\mathrm{s}^{-1}$ (shown in figure 4.3b) and $1 \times 10^6\,\mathrm{s}^{-1}$ (shown in figure 4.10b). The insensitivity of the shape of $P_r(t)$ can be attributed to the distribution of detrap-

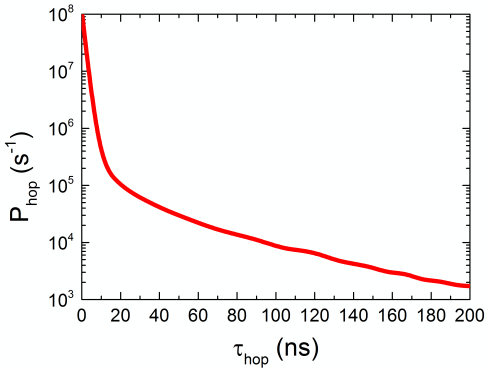

Figure 4.11: *The probability density function for the site-to-site hopping times of charges in a fiducial simulation of* $F = 1 \times 10^7\, V m^{-1}$ *and* $k_r = 1 \times 10^7\, s^{-1}$.

ping times that results from energetic disorder[44,45]. For this investigation, hopping times spanning more than 13 orders of magnitude in time were recorded (although the majority occur within 10 ns - figure 4.11), meaning that some charges would inevitably be trapped for time scales similar to $1/k_r$, irrespective of the comparatively small change to k_r considered here. Therefore, the slow decay due to trapped charges is likely to always be present.

Such a wide distribution of hopping times is often termed 'dispersive transport' and cannot be directly incorporated into the KM. Indirectly, this deficiency can be accommodated for by modifying the non-recombination transport rates within the KM, thus obtaining an acceptable fit to $P_r(t)$ for the $k_r = 1 \times 10^6\, s^{-1}$ data. In the KM, the average recombination time is determined mostly by k_r, and the shape of $P_r(t)$ depends upon the relationship between the recombination and transport rates. With these minor changes to the fitting parameters, good agreement was obtained for a variety of field-dependent dynamic data. However, this exercise has shown that the transport rates used to obtain fits of this quality do not necessarily correspond to the actual transport processes in the MC model.

4.6 Conclusions

Mesoscale Monte Carlo simulations have been utilised to examine the charge transfer separation dynamics in an OPV, including the effects of energetic disorder and bulk heterojunction morphology. Strongly bi-exponential decay of the recombination dynamics, similar to that shown in experiment was observed. The slow component of this $P_r(t)$ decay is due to the energetic or morphological trapping of charges, as increasing the electric field reduces the prominence of this feature. An alternative kinetic model was proposed, which implements an intermediate QF state between the CT and FC states to represent the CT manifold. This KM is shown to fit both the dynamic behaviour of the CT state recombination and separation efficiency as a function of electric field very well. The CT state separation behaviour was then explored further by modifying the recombination rate in both the MC and KM. The present KM was shown to give very poor fits to the MC data, when the recombination rate alone was modified. In order to obtain good fits to the MC data, the transport rate coefficients that describe the processes of separation, collapse and freedom within the KM also had to be modified - even though the description of these processes in MC was left unchanged. This shows that KMs can be used to successfully fit a wide variety of data describing CT state behaviour, but the derived rate does not always have exact correspondence with the physical processes occurring within an OPV. It is argued that this is a general shortcoming of KMs, and is attributed to the difficulty in describing dispersive hopping transport within a framework that necessarily simplifies charge transport rates.

References

[1] L. Onsager. "Initial Recombination of Ions." *Phys. Rev.*, **54**, 554–557, 1938.

[2] C. L. Braun. "Electric Field Assisted Dissociation of Charge Transfer States as a Mechanism of Photocarrier Production." *J. Chem. Phys.*, **80**, 4157–4161, 1984.

[3] I. A. Howard, R. Mauer, M. Meister, and F. Lacquai. "Effect of Morphology on Ultrafast Free Carrier Generation in Polythiophene:Fullerene Organic Solar Cells." *J. Am. Chem. Soc.*, **132**, 14866–14876, 2010.

[4] D. Veldman, Ö. Ipek, S. C. J. Meskers, J Sweelssen, M. M. Koetse, S. C. Veenstra, J. M. Kroon, S. S. van Bavel, J. Loos, and R. A. J. Janssen. "Compositional and Electric Field Dependence of the Dissociation of Charge Transfer Excitons in Alternating Polyfluorene Copolymer/Fullerene Blends." *J. Am. Chem. Soc.*, **130**, 7721–7735, 2008.

[5] G. F. A. Dibb, F. C. Jamieson, A. Maurano, J. Nelson, and J. R. Durrant. "Limits on the Fill Factor in Organic Photovoltaics: Distinguishing Nongeminate and Geminate Recombination Mechanics." *J. Phys. Chem. Lett.*, **4**, 803–808, 2013.

[6] S. H. Park, A. Roy, S. Beaupreé, S. Cho, N. Coates, J. S. Moon, D. Moses, M. Leclerc, K. Lee, and A. J. Heeger. "Bulk Hetereojunction Solar Cells with Internal Quantum Efficiency Approaching 100%." *Nature Photon.*, **3**, 297–303, 2009.

[7] T. M. Clarke and J. R. Durrant. "Charge Photogeneration in Organic Solar Cells." *Chem. Rev.*, **110**, 6736–6767, 2010.

[8] P. Peumans, A. Yakimov, and S. R. Forrest. "Small Molecular Weight Organic Thin-Film Photodetectors and Solar Cells." *J. Appl. Phys.*, **93**, 3693–3723, 2003.

[9] A. Mani, J. Schoonman, and A. Goossens. "Photoluminescence Study of Sexithiophene Thin Films." *J. Phys. Chem. B.*, **109**, 4829–4836, 2005.

[10] I.-W. Hwang, C. Soci, D. Moses, Z. Zhu, D. Waller, R. Gaudiana, C. J. Brabec, and A. J. Heeger. "Ultrafast Electron Transfer and Decay Dynamics in a Small Band Gap Bulk Heterojunction Material." *Adv. Mater.*, **19**, 2307–2312, 2007.

[11] R. D. Pensack, K. M. Banyas, L. W. Barbour, M. Hegadorn, and J. B. Asbury. "Ultrafast Vibrational Spectroscopy of Charge-Carrier Dynamics in Organic Photovoltaic Materials." *Phys. Chem. Chem. Phys.*, **11**, 2575–2591, 2009.

[12] I. A. Howard and F. Laquai. "Optical Probes of Charge Generation and Recombination in Bulk Heterojunction Organic Solar Cells." *Macromol. Chem. Phys.*, **211**, 2063–2070, 2010.

[13] A. A. Bakulin, A. Rao, V. G. Pavelyev, P. H. M. van Loosdrecht, M. S. Pshenichnikov, D. Niedzialek, J. Cornil, D. Beljonne, and R. H. Friend. "The Role of Driving Energy and Delocalized States for Charge Separation in Organic Semiconductors." *Science*, **335**, 1340–1344, 2012.

[14] P. M. Borsenberger and A. I. Ateya. "Predictions of the Onsager Theory Based on an Exponential Distribution of Electron-Hole Separation Distances." *J. Appl. Phys.*, **50**, 909–913, 1979.

[15] V. D. Mihailetchi, L. J. A. Koster, J. C. Hummelen, and P. W. M. Blom. "Photocurrent Generation in Polymer-Fullerene Bulk Heterojunctions." *Phys. Rev. Lett.*, **93**, 216601:1–216601:4, 2004.

[16] M. Hilczer and M. Tachiya. "Unified Theory of Geminate and Bulk Electron-Hole Recombination in Organic Solar Cells." *J. Phys. Chem. C*, **114**, 6808–6813, 2010.

[17] V. Coropceanu, J. Cornil, A. Demetrio, F. da Silva, Y. Olivier, R. Silbey, and J-L. Brédas. "Charge Transport in Organic Semiconductors." *Chem. Rev.*, **107**, 926–952, 2007.

[18] C. Groves, R. A. Marsh, and N. C. Greenham. "Monte Carlo Modelling of Geminate Recombination in Polymer-Polymer Photovoltaic Devices." *J. Chem. Phys.*, **129**, 114903:1–114903:7, 2008.

[19] H. van Eersel, R. A. J. Janssen, and M. Kemerink. "Mechanism for Efficient Photoinduced Charge Separation at Disordered Organic Heterointerfaces." *Adv. Funct. Mater.*, **22**, 2700–2708, 2012.

[20] B. A. Gregg. "Entropy of Charge Separation in Organic Photovoltaic Cells: The Benefit of Higher Dimensionality." *J. Phys. Chem. Lett.*, **2**, 3013–3015, 2011.

[21] D. P. McMahon, D. L. Cheung, and A. Troisi. "Why Holes and Electrons Separate So Well in Polymer/Fullerene Photovoltaic Cells." *J. Phys. Chem. Lett.*, **2**, 2737–2741, 2011.

[22] C. Groves. "Suppression of Geminate Charge Recombination in Organic Photovoltaic Devices with a Cascaded Energy Heterojunction." *Energy Environ. Sci.*, **6**, 1546–1551, 2013.

[23] D. Caruso and A. Troisi. "Long-Range Exciton Dissociation in Organic Solar Cells." *Proc. Natl. Acad. Sci. USA*, **109**, 13498–13502, 2012.

[24] A. A. Bakulin, S. D. Dimitrov, A. Rao, P. C. Y. Chow, C. B. Nielsen, B. C. Schroeder, I. McCulloch, H. J. Bakker, J. R. Durrant, and R. H. Friend. "Charge-Transfer State Dynamics Following Hole and Electron Transfer in Organic Photovoltaic Devices." *J. Phys. Chem. Lett.*, **4**, 209–215, 2013.

[25] G. Grancini, M. Maiuri, D. Fazzi, A. Petrozza, H-J. Egelhaaf, D. Brida, G. Cerullo, and G. Lanzani. "Hot Exciton Dissociation in Polymer Solar Cells." *Nature Mater.*, **12**, 29–33, 2013.

[26] R. A. Marsh, C. Groves, and N. C. Greenham. "A Microscopic Model for the Behavior of Nanostructured Organic Photovoltaic Devices." *J. Appl. Phys.*, **101**, 083509:1–083509:7, 2007.

[27] C. Groves and N. C. Greenham. "Bimolecular Recombination in Polymer Electronic Devices." *Phys. Rev. B*, **78**, 155205:1–155205:8, 2008.

[28] C. Groves, J. C. Blakesley, and N. C. Greenham. "Effect of Charge Trapping on Geminate Recombination and Polymer Solar Cell Performance." *Nano Lett.*, **10**, 1063–1069, 2010.

[29] C. Groves, R. G. E. Kimber, and A. B. Walker. "Simulation of Loss Mechanisms in Organic Solar Cells: A Description of the Mesoscopic Monte Carlo Technique and an Evaluation of the First Reaction Method." *J. Chem. Phys.*, **133**, 144110:1–14410:7, 2010.

[30] B. P. Lyons, N. Clarke, and C. Groves. "The Quantitative Effect of Surface Wetting Layers on the Performance of Organic Bulk Heterojunction Photovoltaic Devices." *J. Phys. Chem. C*, **115**, 22572–22577, 2011.

[31] B. P. Lyons, N. Clarke, and C. Groves. "The Relative Importance of Domain Size, Domain Purity and Domain Interfaces to the Performance of Bulk-Heterojunction Organic Photovoltaics." *Energy Environ. Sci.*, **5**, 7657–7663, 2012.

[32] H. Yan, S. Swaraj, C. Wang, I. Hwang, N. C. Greenham, C. Groves, H. Ade, and C. R. McNeill. "Influence of Annealing and Interfacial Roughness on the Performance of Bilayer Donor/Acceptor Polymer Photovoltaic Devices." *Adv. Funct. Mater.*, **20**, 4329–4337, 2010.

[33] R. G. E. Kimber, E. N. Wright, S. E. J. O'Kane, A. B. Walker, and Blakesley J. C. "Mesoscopic Kinetic Monte Carlo Modeling of Organic Photovoltaic Device Characteristics." *Phys. Rev. B*, **86**, 235206:1–235206:9, 2012.

[34] R. A. Marcus. "Chemical and Electrochemical Electron-Transfer Theory." *Ann. Rev. Phys. Chem.*, **15**, 155–196, 1964.

[35] S. Westenhoff, I. A. Howard, J. M. Hodgkiss, K. R. Kirov, H. A. Bronstein, C. K. Williams, N. C. Greenham, and R. H. Friend. "Charge Recombination in Organic Photovoltaic Devices with High Open-Circuit Voltages." *J. Am. Chem. Soc.*, **130**, 13653–13658, 2008.

[36] S. Massip, P. M. Oberhumer, G. Tu, S. Albert-Seifried, W. T. S. Huck, and N. C. Friend, R. H. amd Greenham. "Influence of Side Chains on Geminate and Bimolecular Recombination in Organic Solar Cells." *J. Phys. Chem. C*, **115**, 25046–25055, 2011.

[37] J. M. Hodgkiss, A. R. Campbell, R. A. Marsh, A. Rao, S. Albert-Seifried, and R. H. Friend. "Subnanosecond Geminate Charge Recombination in Polymer-Polymer Photovoltaic Devices." *Phys. Rev. Lett.*, **104**, 177701:1–177701:4, 2010.

[38] M. Tong, N. E. Coates, D. Moses, and A. J. Heeger. "Charge Carrier Photogeneration and Decay Dynamics in the Poly(2,7-carbazole) copolymer PCDTBT in Bulk Heterojunction Composites with $PC_{70}BM$." *Phys. Rev. B*, **81**, 125210:1–125210:6, 2010.

[39] Y. W. Soon, T. M. Clarke, W. Zhang, T. Agostinelli, J. Kirkpatrick, C. Dyer-Smith, I. McCulloch, J. Nelson, and J. R. Durrant. "Energy Versus Electron Transfer in Organic Solar Cells: A Comparison of the Photophysics of Two Indenofluorene:Fullerene Blend Films." *Chem. Sci.*, **2**, 1111–1120, 2011.

[40] R. H. Friend, M. Phillips, A. Rao, M. W. B. Wilson, Z. Li, and C. R. McNeill. "Excitons and Charges at Organic Semiconductor Heterojunctions." *Faraday Discuss.*, **155**, 339–348, 2011.

[41] H. Ohkita, S. Cook, Y. Astuti, W. Duffy, S. Tiemey, W. Zhang, M. Heeney, I. McCulloch, J. Nelson, D. D. C. Bradley, and J. R. Durrant. "Charge Carrier Formation in Polythiophene/Fullerene Blend Films Studied by Transient Absorption Spectroscopy." *J. Am. Chem. Soc.*, **130**, 3030–3042, 2008.

[42] J. Guo, Y. Liang, S. Xiao, J. M. Szarko, M. Sprung, M. K. Mukhopadhyay, J. Wang, L. Yu, and L. X. Chen. "Structure and Dynamics Correlation of

Photoinduced Charge Separation in Rigid Conjugated Linear Donor-Acceptor Dyads Towards Photovoltaic Applications." *New J. Chem.*, **33**, 1497–1507, 2009.

[43] M. Wojcik and M. Tachiya. "Accuracies of the Empirical Theories of the Escape Probability Based on Eigen Model and Braun Model Compared with the Exact Extension of Onsager Theory." *J. Chem. Phys.*, **130**, 104107:1–104107:9, 2009.

[44] H. Scher and E. W. Montroll. "Anomalous Transit-Time Dispersion in Amorphous Solids." *Phys. Rev. B*, **12**, 2455–2477, 1975.

[45] R. U. A. Khan, D. Poplavskyy, T. Kreouzis, and D. D. C. Bradley. "Hole Mobility Within Arylamine-Containing Polyfluorene Copolymers: A Time-of-Flight Transient-Photocurrent Study." *Phys. Rev. B*, **75**, 035215:1–035215:14, 2007.

Chapter 5

Hot Charge Transfer States

5.1 Introduction

The performance of BHJ OPV devices has improved rapidly since their invention in 1995 [1,2]. In fact, some devices have exhibited IQEs of even greater than 80% [3,4], despite strong Coulomb attraction between charges after exciton dissociation resulting in a fast recombination rate of high-performance polymer:fullerene OPVs of the order $1 \times 10^9\,\mathrm{s}^{-1}$ [5–9]. In an attempt to explain this apparent contradiction, the focus of the research community has turned to the CT state - the precursor of free charges, formed after the dissociation of the exciton. Instead of the traditional picture of a tightly bound CT state, it has been suggested that, after exciton dissociation, a delocalised, high energy, 'hot' CT state (HCT) is formed, leading to increased charge separation efficiencies. The opposing charges in the HCT are initially delocalised across regions of the molecules in the active layer but, as the state begins to cool, the charges localise to regions that are spatially separated.

In this chapter, multiple morphologies will be characterised and tested to deter-

mine the efficacy of HCTs using mescoscale MC methods, with particular emphasis on the effect of fullerene aggregation. The MC model operates on the assumption that HCTs do occur and, upon cooling, the electron and hole polaron are mutually separated by a distance, r. The subsequent charge-pair behaviour, and the consequent effect on OPV performance, are analysed in order to determine if HCTs can provide the quantum efficiencies observed in experiment for common polymer:fullerene OPV systems.

The morphologies used for this investigation are described in §5.3.1, and the MC methodology explained in §5.3. In the results section §5.4, the effect of HCTs is examined in the context of donor:acceptor blends similar to all-polymer devices in §5.4.1, and mixed:aggregate blends similar to polymer:fullerene devices in §5.4.2. Both geminate pair separation and full OPV device simulations are used to show that HCTs do indeed improve the efficiency of free-charge generation as anticipated, but in order to obtain the performance observed in OPVs, the degree of separation required is unrealistically large. The efficacy of HCTs is shown to be strongly dependent on the simulated morphology, with the most efficient results obtained from simulation volumes where the fullerene aggregates were dispersed throughout the molecularly mixed phase. However, no morphology studied here is predicted to give rise to the efficiencies expected from experiments. In §5.4.3, an examination of the optimal conditions at which HCTs provide the most significant benefit takes place. The first condition occurs when the degree of separation r is of the order $\sim 10\,\mathrm{nm}$, at which the Coulomb binding energy approaches k_BT and therefore separation becomes energetically favourable. The second occurs for small r ($\sim 4\,\mathrm{nm}$) when the

electron mobility (μ) is small and beneficial trapping means that recombination is kinetically unfavourable. It is argued that neither circumstance is expected to occur in polymer:fullerene OPVs, and that the high-efficiencies observed in these devices are most likely resultant from alternative mechanisms. The main conclusions of the investigation are presented in §5.5.

5.2 The Hot Charge Transfer State

5.2.1 Presence of the HCT State

As described in §2.4.1, the traditional picture at the donor:acceptor interface is that a tightly-bound, photoinjected exciton dissociates to yield a bound CT state, localised at the point of dissociation, as shown in figure 5.1a. The CT state can then form free charges by a series of intermolecular hops - a process which is widely expected to be comparatively slow and inefficient[10]. Bakulin *et al.*[9] measured the PIA response of a range of OPV blends in detail, explaining the results by proposing that exciton dissociation instead can create high-energy HCTs, an example of which is shown in figure 5.1b. The band-like character of these states suggests that the HCTs are more delocalised. When the state relaxes, a more localised electron and hole pair forms with a mutual spatial separation. This leads to reduced Coulomb interaction between the charges and a decreased overlap of the corresponding wavefunctions, permitting the carriers to separate to the FC state more quickly as opportunities to recombine decrease.

The concept of HCTs is consistent with other spectroscopy investigations which

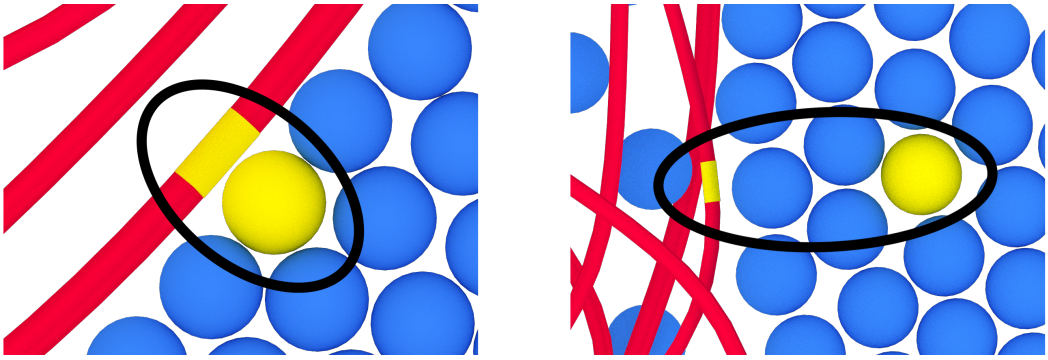

(a) *A bound CT state formed at the Donor:Acceptor Interface*

(b) *An HCT state formed at the Mixed:Aggregate Interface*

Figure 5.1: *Example bound and hot charge transfer states in a morphology containing donor polymer (red) and fullerene acceptor (blue) phases. The yellow regions depict the localised charge density of the electron and hole, and the black ring describes the extent of the CT state.*

show that an 'ultrafast' free-charge generation can occur on timescales within $\sim$ 100 fs in some material systems[11–14]. Indeed, some groups have suggested that the lifetime of the HCT state represents a maximum time for efficient free-charge generation as the HCT relaxes to a bound CT state in which the Coulomb binding energy is much larger than k_BT[14]. Quantum chemical calculations have reinforced the spatially separated nature of HCT states[9,15], in fact suggesting that excitons preferentially dissociate to yield spatially-separated electron-hole pairs[15,16]. Further work has suggested that the accessibility of HCT states is correlated to the presence of fullerene aggregates within the morphology[17,18], which is consistent with the relationship between the presence of fullerene aggregation and corresponding high performance in polymer:fullerene OPVs[19,20]. These arguments appear to offer a compelling reason why such efficient charge generation is possible in OPVs.

5.2.2 Effect of the HCT State

However, while the existence of HCTs is well established, their effect on OPV performance is still the subject of much discussion. The experiments highlighted above tend to utilise spectroscopy or the direct analysis of CT state dynamics and are therefore mostly concerned with short length and timescales ($\sim$ Å-nm, $\sim$ fs-ps). Steady-state measurements over longer time periods (implying lengthscales of $\sim$ 100 nm and timescales $\sim \mu$s) suggest that the efficiency of free-charge generation is largely independent of whether the CT states are hot (binding energy $\sim k_B T$) or bound (binding energy ~ 0.2 eV), at least at room temperature[21–24]. Additionally, other mechanisms have been suggested that could result in enhanced free-charge generation from the bound CT states[25,26].

The resulting picture is unclear, which poses difficulties when considering the best course of action for developing OPV technology further. For instance, if HCTs prove to be the primary precursor to efficient free-charge generation, then the materials development should focus on enhancing structural rigidity and suppressing geometrical relaxation to produce cleaner interfaces and better orbital overlap to maximise the bonus obtained from HCTs[9], while processing should seek to maximise fullerene aggregation to increase the quantity of HCTs in the system[17,18]. On the other hand, if HCTs prove to not affect free-charge generation significantly then other techniques and optimisation regimes may need to be employed.

5.3 Monte Carlo Simulations

5.3.1 Morphologies

The morphologies used as inputs in the MC simulations were derived from modified Cahn-Hilliard theory[27,28] as described in §3.4.1, and were generated externally by collaborators. Three main input parameters for the CH equation 3.4.18 are the molecular weight of the donor and acceptor components N_D and N_A respectively, and the initial donor:acceptor volume ratio of the blend. For this investigation, two sets of input parameters were used. One resulted in morphologies similar to an all-polymer blend, which had $N_A/N_D = 1$ and a donor volume ratio of $\phi_0 = 0.5$. In this case, the parameters $\chi = 0.065$ and $\chi_s = 0.04$. The second parameter set resulted in morphologies more closely related to a polymer:fullerene blend, where the acceptor had a higher molecular weight than the donor material such that $N_A/N_D = 30$. The donor volume ratio for these samples was $\phi_0 = 0.4$ (*i.e.* had a slight excess of a smaller molecular weight acceptor), with the other CH parameters being $\chi = 0.9$ and $\chi_s = 0.875$.

The CH simulation resulted in a regular 3D lattice in the donor volume fraction ϕ, which represents the morphology of the active layer of the device. These morphologies then underwent further processing before they were used in the MC simulations. For the all-polymer samples ($N_A/N_D = 1$), sites with $\phi \geq 0.5$ were designated as pure donor material (which holes alone could propagate through), whereas sites with $\phi < 0.5$ were denoted pure acceptor (conducting only electrons), producing morphologies of the type shown in figure 5.2a. These binary samples are referred to as donor:acceptor morphologies (D:A for brevity) and are characterised

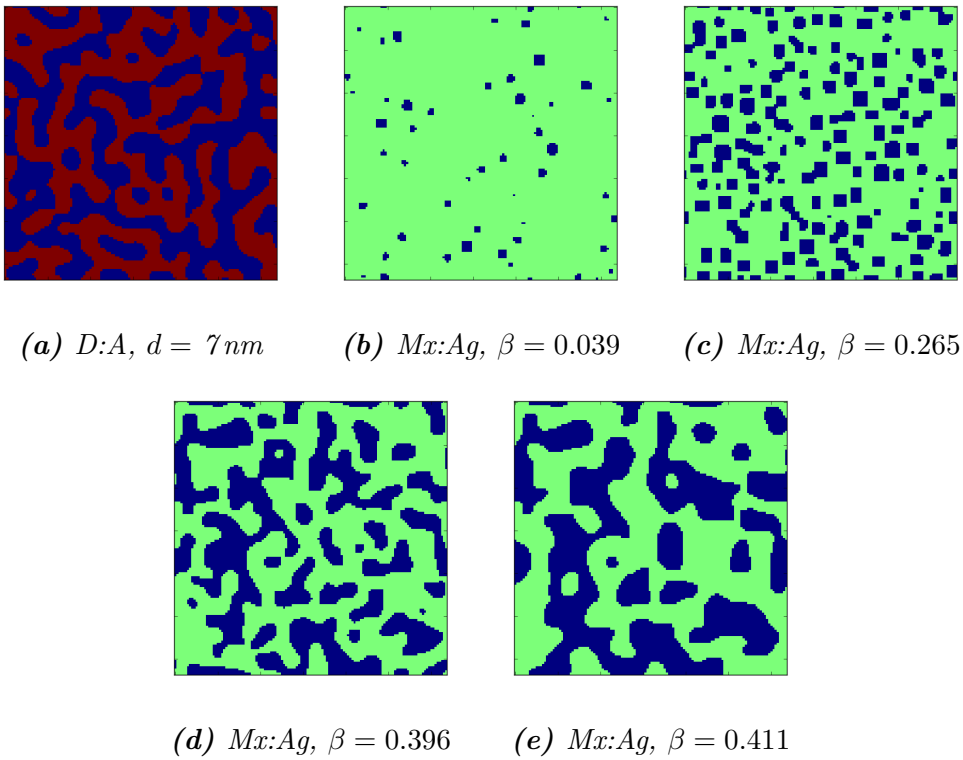

(a) *D:A, $d = 7nm$* ***(b)*** *Mx:Ag, $\beta = 0.039$* ***(c)*** *Mx:Ag, $\beta = 0.265$*

(d) *Mx:Ag, $\beta = 0.396$* ***(e)*** *Mx:Ag, $\beta = 0.411$*

Figure 5.2: *Example cross-sections of the morphologies used in this investigation. Each side is 128 nm in extent. Blue represents aggregated acceptor domains, red indicates regions of pure donor material (e.g. crystallised polymer) and green shows the location of the mixed phase where both donor and acceptor molecules are present.*

by the average size of the donor and acceptor domains d, which increased with evolution through the CH equations. For the polymer:fullerene samples ($N_A/N_D = 30$), sites with $\phi < 0.2$ were assigned as pure, aggregated acceptor, and all other sites were denoted as part of a molecularly mixed phase consisting of both donor and acceptor material as shown in figures 5.2b-e. These are referred to as mixed:aggregate morphologies (Mx:Ag), and further evolution of these through the CH equations resulted in systems with an increased proportion-by-volume of aggregated acceptor, β. Within the MC simulations of the Mx:Ag morphologies, the electrons were permitted to move freely throughout the entire volume in both the aggregate and mixed regions, but holes were confined to the mixed phase only.

Examining both D:A and Mx:Ag morphologies is of key importance as it permits analysis of the effects of the mixed phase in isolation, which can transport both charge carriers. Additional characterisation of the morphologies examined in this investigation, such as the blend ratio and average domain size, d, is provided in table 5.1. The corresponding FF and η for the devices are also given. The absolute values are lower than those expected real devices with similar energetic parameters; the most efficient all-polymer photoactive blends generally exhibit $\eta \sim 6\%$[29], whereas polymer:fullerene devices have $\eta \geq 9\%$[30]. The devices simulated here are therefore inefficient, suggesting that any benefit from the HCTs would dramatically improve the device performance, and that the platform used for this investigation represents the best-case scenario for HCT efficacy. Regardless, the relative differences between the morphologies is the most important as these indicate the conditions under which HCTs were the most beneficial.

As well as a value of ϕ, each unit cell within the morphology was additionally assigned a random, time-invariant, Gaussian distributed energetic disorder. The standard deviation of the Gaussian DoS, σ, was set to 50 meV, which is representative of the high-mobility organic materials used to construct high-performance polymer:fullerene OPVs[31,32].

Fig. 1	Blend	Ratio	*d*	Proportions		FF at	η
				D/Mx	A/Ag	r = 4 nm	%
a)	D:A	1:1	6.63 nm	0.50066	0.49934	0.25140	0.22870
b)	Mx:Ag	2:3	4.72 nm	0.96134	0.03866	0.29239	0.01360
c)	Mx:Ag	2:3	4.23 nm	0.73501	0.26499	0.26923	0.07880
d)	Mx:Ag	2:3	6.79 nm	0.60402	0.39598	0.27374	0.12740
e)	Mx:Ag	2:3	10.28 nm	0.58899	0.41101	0.27878	0.13540

Table 5.1: *A table of the key features and corresponding performance of the morphologies used in this investigation. d denotes the average domain size for the morphology, FF is the device fill factor and η the corresponding power conversion efficiency.*

5.3.2 Charge Transfer States

The mesoscopic MC simulations employed in this investigation are as described in §3.4, and have been developed previously. However, new infrastructure within the code was implemented in order to effectively model the mixed phase and HCTs. The CT was implemented in one of two ways; either a bound CT state in which an electron-hole pair was injected directly on two adjacent (separation $r = 1\,\text{nm}$) sites, or as an HCT state which, after cooling, resulted in an electron-hole pair with a separation of $r > 1\,\text{nm}$. The physics behind the process of HCT cooling was omitted from the simulations as the aim of the investigation was to predict the subsequent behaviour of the electron-hole pair at the end point of the dissociation process, as they separated and moved through the bulk of the device. While the task of explicitly modelling the cooling of the HCT state would probably be better suited to quantum chemical calculations and spectroscopic studies that can treat

the carrier delocalisation aspect of the HCT[9,11,14], mesoscale MC methods can link together the broad features of nanoscale processes with the overall OPV performance characteristics. This makes mesoscale MC simulations an appropriate technique when relating the separation of the charge carriers after HCT cooling to the device's *J*-*V* curve.

Practically, the HCT state was implemented as follows. If an exciton was generated in the mixed phase, it was assumed that there was a sufficient density of donor and acceptor material that it could dissociate immediately, yielding an electron-hole pair with a mutual separation of 1 nm as suggested by experiment[18]. This assumption was later relaxed to allow HCTs to occur more generally, as will be explained in §5.4.2. Conversely, if the exciton was generated within the donor, acceptor or aggregate phase and further diffused to an interface, it instantaneously dissociated to yield an electron-hole pair that was spatially separated by r - the cooled remains of an HCT. This process intrinsically assumed that the delocalised HCT state cooled to produce spatially separated charge carriers on a timescale that was faster than any of the other processes occurring within the device, which is in broad agreement with various experiments[11,14]. Furthermore, this assumed that the HCT is associated with the level of aggregation within the electron accepting medium, which has also been reinforced by experiments[17,18]. The position of the electron was determined by a 3-dimensional random walk of the carrier, taking care to consider the material phase of the local structure, such that the electron could only move through sites it was permitted to hop through conventionally. The random walk was terminated when the mutual separation between the electron and the hole reached the pre-

defined value, r. The hole was always created at the interface between the donor and acceptor (D:A morphologies) or mixed and aggregate (Mx:Ag morphologies) phases, and so the process resulted in the immediate injection of a charge carrier pair with the electron at a random position, separated by r from the heterojunction.

5.3.3 Charge Transport and Recombination

The dynamics of charge transport were determined by nearest-neighbour hopping at a rate given by the Marcus expression 3.3.10. As with the investigation in chapter 4, the transport of the electrons and holes was assumed to occur at the same rate, with carriers confined to regions of the morphology as explained by the material rules in §5.3.1. For simplicity in the simulation of the Mx:Ag morphologies, electron transport in the aggregate phase was taken to be the same as within the mixed phase. This approximation resulted in a 'best-case scenario' for mixed phase mobility, as it is likely that the composition of the mixed phase negatively affects the mobility of charge carriers within[33].

Adjacent charges (*i.e.* separated by $r = 1\,\mathrm{nm}$), were permitted to recombine at a rate k_r, which was set to either $1 \times 10^7\,\mathrm{s}^{-1}$ (typical of all-polymer bulk heterojunctions[34]), or $1 \times 10^9\,\mathrm{s}^{-1}$ (expected in polymer:fullerene blends such as P3HT:$PC_{61}BM$[6,7], APFO3:$PC_{61}BM$[8] and MEH-PPV:$PC_{61}BM$[35]) before the simulation began.

5.3.4 Geminate Pair Simulations

The geminate pair simulations used in this investigation followed a similar format to those described in chapter 4. For the D:A morphologies, random heterojunctions in the morphology were selected, and either bound CT states (*i.e.* adjacent carriers) or HCT states with a given r injected. The subsequent electron-hole pair was then permitted to hop through the morphology until they had either recombined to the GS, or obtained a mutual separation of 25 nm whereby the charges were said to have separated and the simulation terminated. The same process was used for the Mx:Ag morphologies, except that CT states were created when the randomly selected adjacent lattice site pair were either a mixed:aggregate interface or if both belonged to the molecularly mixed phase. CT states generated in the mixed phase were always considered bound, whereas CT states produced across a mixed:aggregate interface were HCTs.

The simulation process was repeated for over 7×10^6 iterations and for 15 different configurations of energetic disorder within the morphology, in order to obtain reliable charge separation statistics. The ratio of successfully separated charges to the number of injected geminate charge pairs was defined as the free-charge generation efficiency, η_{SEP}.

5.3.5 Device Simulations

The device simulations used in this investigation attempted to model a virtual photovoltaic, as described in §3.4, from the illumination of the active layer to stimulate photoinjection of excitons, through to dissociation and the subsequent collection of

free charges at the contacts above and below the active layer. Collected charges generated a photovoltaic current within the simulated device which was characterised by the corresponding J-V curve. The parameters used for the device simulations are shown in table 3.1. Unless otherwise specified, all simulations used this fiducial parameter set, which was selected to model a polymer:fullerene blend device such as P3HT:$PC_{61}BM$.

Device simulations proceeded until the net flow of charges leaving the device through the contacts had converged - occurring after at least 25,000 photoinjections had been recorded. The total photovoltaic current density could then be calculated, along with η as per equation 2.5.4. Simulations were repeated for at least 15 configurations of energetic disorder.

5.4 Efficacy of Hot Charge Transfer States

5.4.1 Donor:Acceptor Blends

Geminate Pair Separation

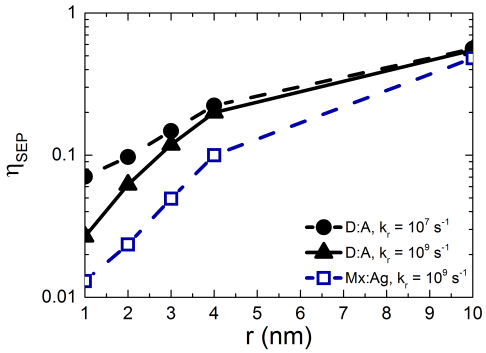

Figure 5.3: *The effect of charge transfer state separation, r, on free-charge generation efficiency, η_{SEP}, when $k_r = 1 \times 10^7\, s^{-1}$ (D:A, solid circles and dashed line) and $k_r = 1 \times 10^9\, s^{-1}$ (D:A, solid triangles and line; Mx:Ag, open squares and dashed line), given an electric field $F = 5 \times 10^6\, V\, m^{-1}$. Both morphologies exhibited an average domain size $d = 7\, nm$, and the Mx:Ag system had $\beta = 0.396$.*

Figure 5.3 shows the free-charge generation efficiency, η_{SEP}, as a function of the cooled HCT separation, r, for a D:A morphology. Two recombination rates are shown: $k_r = 1 \times 10^7\,\mathrm{s}^{-1}$, which is similar to that found in all-polymer OPVs[34], and $k_r = 1 \times 10^9\,\mathrm{s}^{-1}$, similar to that observed in polymer:fullerene blend OPVs[5–8,35]. As expected, when only bound CT states ($r = 1\,\mathrm{nm}$) were available, the system with a larger recombination rate resulted in a lower separation efficiency, as charges were unable to hop apart before the recombination process dominated. However, as r was increased, the separation efficiency increased independently of the recombination rate, with both curves intersecting for $r > 4\,\mathrm{nm}$.

The free-charge generation efficiency measured here is most closely related to the IQE of an OPV measured in experiment. As the internal quantum efficiency is the

ratio of collected charge carriers to absorbed photons, this also includes the effects of bimolecular recombination, whereas η_{sep} does not[36]. In this type of mesoscale MC model however, the effects of bimolecular recombination are small and so the two properties are comparable[37,38]. Although the values of IQE in the literature can vary substantially depending on the processing and manufacturing conditions of the device, efficient polymer:fullerene OPV systems typically exhibit IQEs greater than 50%. For example, unannealed P3HT:$PC_{61}BM$ devices produce an IQE of around 20%-30%[39], while solvent and thermally annealing devices boost their IQE to 65%[40] and 80%[41] respectively. Unannealed PTB7:$PC_{71}BM$ devices have an IQE of around 65%[20], which increases to 85%[42] after annealing. Other devices made from p-DTS($FBTTh_2$)$_2$:$PC_{71}BM$[3] and PCDTBT:$PC_{71}BM$[4] have been reported to have IQEs that reach 80% and ∼100% respectively.

In order to observe efficiencies close to even 50% in the current simulations, it was necessary to have extremely large separations of $r = 10\,\text{nm}$. This is a stark contrast to the value of $r \sim 4\,\text{nm}$ measured by electro-absorption experiment for p-DTS($FBTTh_2$)$_2$:$PC_{71}BM$ and PCDTBT:$PC_{71}BM$ blends[18]. It is therefore difficult to reconcile an IQE in excess of 80% with $r \sim 4\,\text{nm}$ based on the data depicted in figure 5.3.

Gélinas *et al.*[18] note that electro-absorption measurements are expected to be most sensitive to electron-hole separations of up to around 6 nm, due to the fact that the strength of the electro-absorption signal is proportional to the dipolar field (*i.e.* $\propto 1/r$). It is therefore possible that larger separations from the cooling of HCT states could occur within these blends that would not be detectable by the

electro-absorption technique. Quantum chemical calculations offer an alternative method to enquire about the magnitude of carrier separation after dissociation. These calculations necessarily require an atomistic representation to be realised, therefore limiting the procedure to only consider a handful of molecules at the interface in order to be computationally viable. Because of this, the maximal HCT separation is likely to be limited by the simulation volume, which is of the order 1-10 Å [9,14]. Troisi and colleagues suggest that long-range exciton dissociation occurs at a rate which depends on the local energetic disorder [16], and in the limiting case of zero disorder, the CT state separation is of order of the chain length [15]. This extent can vary greatly as the chain length distribution in samples of most semi-crystalline polymers has high polydispersity (as will be discussed in chapter 6), however it is likely to be of the order 1 nm, after considering chain conformation and coiling. Nevertheless, even if r is larger than suggested by recent experiments, the current investigation suggests that it would have to be significantly larger to be the sole precursor to large IQE values found in efficient OPVs.

Device Simulations

Figure 5.4 shows the effect of varying r on both the J-V curve and η for a D:A morphology. The shape of the various J-V curves show that there was a progressive increase in device FF and therefore η as r increased, in accordance with the approximately linear dependence of η_{SEP} on r shown in figure 5.3. Minimal changes in J-V curve shape between $r = 1\,\mathrm{nm}$ and $r = 2\,\mathrm{nm}$ suggest that there was little benefit to HCTs at these small separations, and many charges were still lost to recombination pathways. However, as r increased beyond 2 nm, η and J_{SC} improved, most likely due

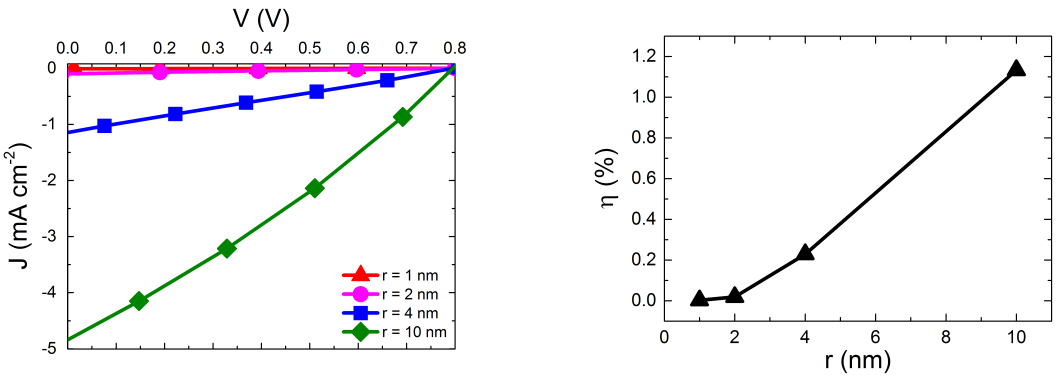

(a) *J-V Curves for varying r* ***(b)*** *The corresponding η*

Figure 5.4: *Device response characteristics for a D:A morphology with $d = 7nm$, given $k_r = 1 \times 10^9\ s^{-1}$.*

to a reduction in the proportion of recombining charge carriers, corresponding to an increase in the free-charge collection efficiency, η_{FC}. η_{FC} represents the combination of the separation efficiency of geminate charges, η_{SEP}, and the subsequent carrier collection efficiency, η_{COL}, which takes into account any bimolecular recombination. Table 5.2 confirms that the low efficiencies in the bound CT state investigations were due to increased geminate recombination over the HCT case. Modification of the value of r is expected to have minimal effect on the bimolecular recombination dynamics, as this process occurs at timescales long after the CT state has separated into free carriers. Therefore, the trend of increasing η_{FC} with increasing r is due to fewer charges undergoing geminate recombination.

System Name	$\eta_{\mathbf{FC}}$
D:A, $r = 1$, Fig 1a)	0.03273
D:A, $r = 2$, Fig 1a)	0.04827
D:A, $r = 4$, Fig 1a)	0.16120
D:A, $r = 6$, Fig 1a)	0.30310
D:A, $r = 8$, Fig 1a)	0.41491
D:A, $r = 10$, Fig 1a)	0.50521

Table 5.2: *The free-charge collection efficiencies (η_{FC}) obtained for D:A morphologies as a function of r.*

5.4.2 Mixed:Aggregate Blends

Geminate Pair Separation

Mx:Ag morphologies are commonly found in polymer:fullerene OPVs with high IQEs[19,20,43,44]. In general, it is these devices which are most strongly linked with the presence of HCT states[9,14,17,18]. The exciton dissociation and material phase limitations of charge transport assumptions described in §5.3.1, while based on the observations of experiments[17,18], would be expected to change both η and the J-V performance when compared to their D:A counterparts. Indeed, figure 5.3 shows η_{SEP} for both a $d = 7\,\mathrm{nm}$ D:A morphology and a $d = 7\,\mathrm{nm}$, $\beta = 0.396$ Mx:Ag morphology with equal recombination rates $k_r = 1 \times 10^9\,\mathrm{s}^{-1}$, clearly indicating the negative effect of the mixed phase on free-charge generation for both bound CT states ($r = 1\,\mathrm{nm}$) and HCTs ($r > 1\,\mathrm{nm}$). This is potentially expected, since there are reports that constraining the charge-transport to donor and acceptor regions can

significantly improve free-charge generation[45]. However, the presence of the mixed phase reduced η_{SEP} still further below that observed in experiment. Even when the HCT separation was set to far greater than that expected from experiment (r = 10 nm), η_{SEP} was predicted to only reach 10% for the Mx:Ag morphologies.

Device Simulations

Figure 5.5a compares the predicted J-V characteristics of these two morphologies, where HCT states were assumed to be created with $r = 4$ nm. As the average size of morphological features within each morphology were equal, this again explicitly shows that the mixed phase is especially detrimental to the short-circuit current. As an aside, the total fraction of non-geminate recombination at short circuit for the Mx:Ag morphology was measured as 14%, whereas the fraction of bimolecular recombination at short circuit for the D:A morphology was only 0.1%. While it is perhaps expected that the lack of a phase-separated structure would increase bimolecular recombination[46], it is interesting to note that, in general, MC models assuming a phase-separated D:A morphology predict geminate recombination as the major loss channel within OPVs[37,38]. Therefore the presence of the mixed phase within the current MC model, at least to a certain extent, can reconcile the predicted major mode of recombination with that measured for some polymer:fullerene OPVs[47,48].

Although HCT states appear to be somewhat beneficial to the performance of polymer:fullerene OPVs, the presence of the mixed phase can severely limit the efficiency that can be obtained. This conclusion is not sensitive to the assumptions about where the HCT forms. So far within the MC investigations, HCTs have

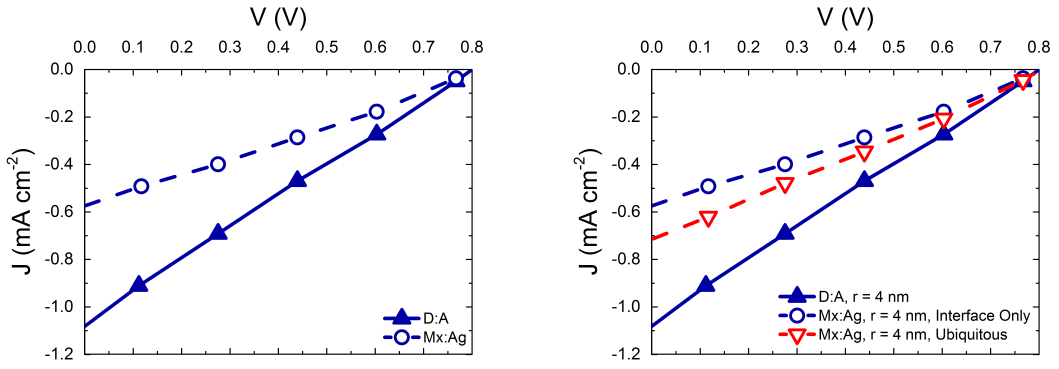

(a) *J-V curves for comparable D:A and Mx:Ag morphologies*

(b) *J-V curves when an alternative HCT methodology is used*

Figure 5.5: *J-V curves for D:A (solid symbols) and Mx:Ag morphologies (open symbols) with average domain size $d = 7\,nm$. The Mx:Ag blend additionally has $\beta = 0.396$. In both cases, $k_r = 1 \times 10^9\,s^{-1}$ and $r = 4\,nm$. Also depicted is the J-V curve when the formation of HCT states is not constrained to the aggregated acceptor regions in the Mx:Ag morphology (red open symbols).*

only been permitted to form at the interface of the aggregate material, with all other dissociations in the mixed phase leading to bound CT states with $r = 1\,\text{nm}$. Figure 5.5b examines the *J-V* characteristics when HCTs are only permitted to form at the Mx:Ag interface, compared to when this constraint is alleviated and HCTs can form throughout the morphology. The performance increase awarded by permitting HCTs to form ubiquitously through the device is small, supporting the conclusion that they are not the unique precursor to high IQEs in polymer:fullerene OPVs.

Variation in Aggregate Proportion

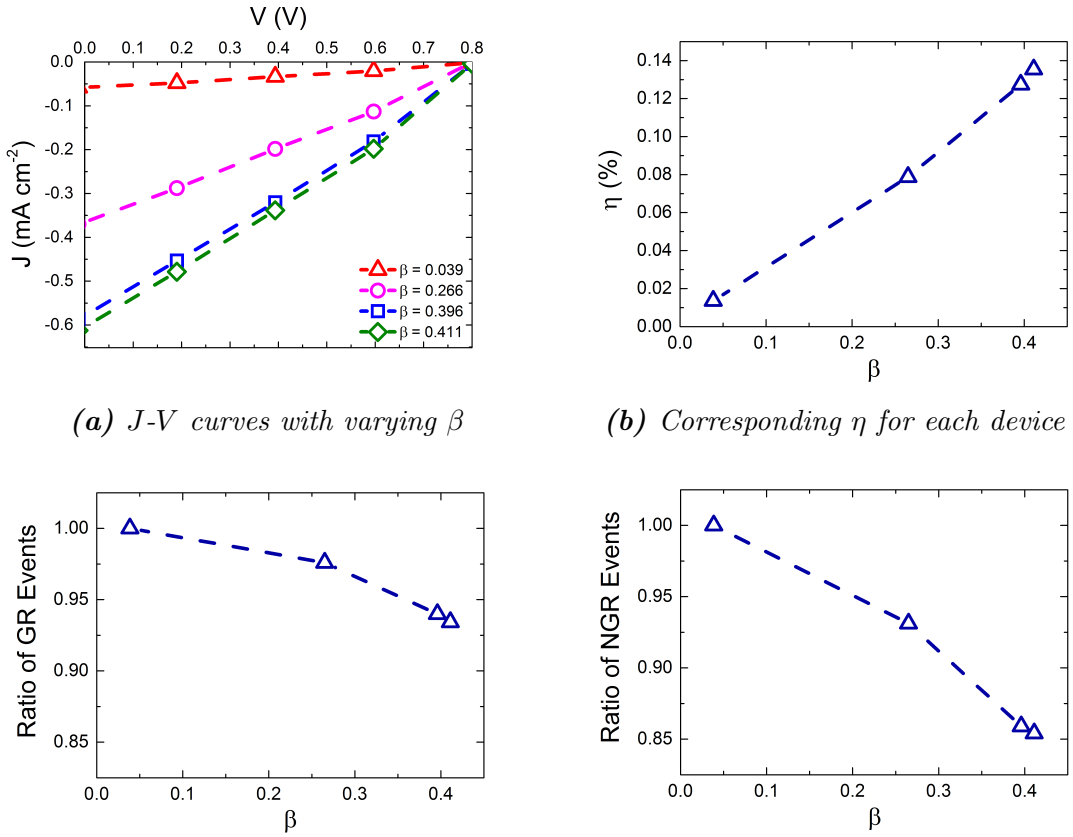

(a) *J-V curves with varying β*

(b) *Corresponding η for each device*

(c) *The variation in geminate recombination events, normalised to $\beta = 0.039$*

(d) *The variation in non-geminate recombination events, normalised to $\beta = 0.039$*

Figure 5.6: *Device response characteristics for the various Mx:Ag morphologies with varying aggregated acceptor fraction β. For all simulations, $r = 4$ nm and $k_r = 1 \times 10^9\ s^{-1}$.*

To further explore the efficacy of HCTs within polymer:fullerene devices, variations in β of the Mx:Ag morphologies were considered. Figure 5.6 examines this in more detail by showing the predicted J-V characteristics of Mx:Ag blends which varied the proportion of aggregated acceptor, β. In all cases, exciton dissociation at Mx:Ag interfaces was assumed to result in HCT states with $r = 4$ nm, while mixed-phase dissociation resulted in a bound CT state with $r = 1$ nm. Charge-collection efficiencies are shown in table 5.3.

System Name	$\eta_{\mathbf{FC}}$
Mx:Ag, $\beta = 0.039$, Fig 1b)	0.03445
Mx:Ag, $\beta = 0.266$, Fig 1c)	0.06927
Mx:Ag, $\beta = 0.396$, Fig 1d)	0.08258
Mx:Ag, $\beta = 0.411$, Fig 1e)	0.09402

Table 5.3: *The free-charge collection efficiencies (η_{FC}) obtained for Mx:Ag morphologies as a function of β.*

As the proportion of aggregated acceptor increased, the benefit from HCTs also increased, resulting in better J_{SC} and enhanced FF (figure 5.6a). This manifested as a linear increase in η with β over the range examined (figure 5.6b). Similar behaviour has been observed experimentally for P3HT:PC_{61}BM devices with varying degrees of fullerene aggregation[19]. The number of charge recombination events (figures 5.6c and d) decreased approximately linearly with increasing β. Increased aggregation permitted more HCT states to be formed, resulting in better overall free-charge generation. It also led to a reduction in the degree of bimolecular recombination due to the fact that electrons were increasingly likely to inhabit aggregated regions where they were protected from recombination, rather than propagating through the mixed phase where recombination occurred quickly[46]. Note, however, that further increases to β would eventually lead to reduced exciton dissociation efficiency and therefore OPV performance due to the lack of heterojunctions within the morphology. There is a constant compromise between maximising the proportion of aggregated acceptor to facilitate better charge transport and less recombination, but still maximising the number of heterojunctions to facilitate better exciton dis-

sociation.

These simulations therefore demonstrate that morphology plays an important role in the efficacy of HCT states, primarily by determining the fraction of generated excitons that go on to form HCT states. It has been shown, however, that even with optimised Mx:Ag morphologies and an experimentally realistic cooled HCT separation of $r = 4\,\mathrm{nm}$ associated with acceptor aggregates, the predicted η is not as high as that measured experimentally.

5.4.3 Relationship with Carrier Mobility

In order to investigate why HCT states provide only moderately efficient free-charge generation in polymer:fullerene OPVs, the free-charge generation efficiency of HCTs was simulated as a function of the electron mobility pre-factor (v_0 - the hole mobility was kept constant throughout) for both D:A and Mx:Ag morphologies as shown in figure 5.7. A range of r values were considered so that the benefit offered by the increased separation of the HCT state ($r > 1\,\mathrm{nm}$) could be identified. This therefore explored the conditions under which the energetics of free-charge generation were controlled by r, and those that were controlled by v_0.

For HCT states, the same general behaviour was observed independently of r - namely that η_{SEP} first decreased with increasing v_0, reaching a minimum before it began to increase again as v_0 increased still further. This seems counter-intuitive since it might always be expected that a larger charge-carrier mobility will result in an improvement to η_{SEP}. The minimum point varied depending on the value of r, but was around $v_0 = 1 \times 10^{12}\,\mathrm{s}^{-1}$ for most curves, which corresponds to a mobility

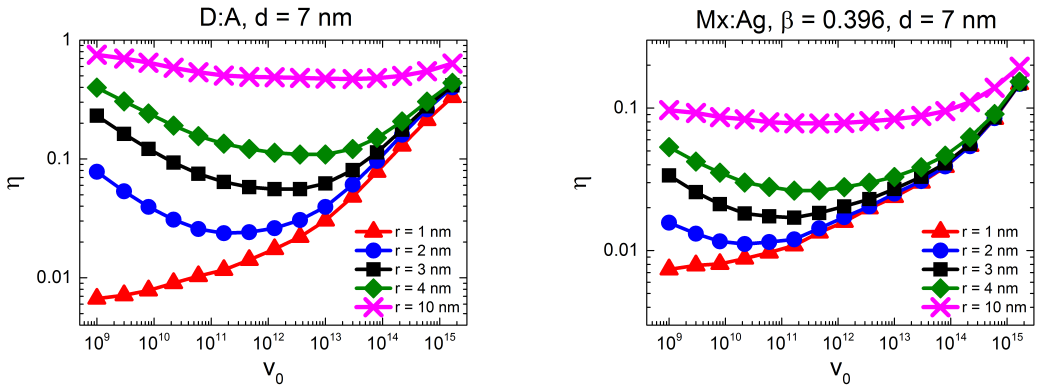

(a) *D:A morphology with $d = 7nm$* ***(b)*** *Mx:Ag morphology with $\beta = 0.396$*

Figure 5.7: *The free-charge generation efficiency, η_{SEP}, as a function of hopping rate pre-factor for electrons, v_0, for comparable D:A and Mx:Ag morphologies at a variety of HCT separations r.*

$\mu \sim 1 \times 10^{-2}\,\mathrm{cm^2\,V^{-1}\,s^{-1}}$.

Jailaubekov *et al.*[14] anticipated that the benefit of HCT states on charge-generation is time-limited, therefore somewhat dependent on the kinetics. They argue that HCT states are expected to have large Coulomb binding energies $E_C > k_BT$, and so therefore will relax to the bound CT state unless the charges separate to FC first[10,49,50]. Figure 5.7 suggests that the free-charge generation becomes less dependent on the transport kinetics (which were directly proportional to v_0) as r increases. This is attributed to E_C closely approaching k_BT, making further separation more energetically favourable. Since there are positive and negative dependencies on v_0, the HCT does not set a time-limit for free-charge generation. Instead, the trends shown in figure 5.7 can be explained as follows.

When r is small, the Coulomb binding energy is very large and so relaxation into the bound CT state is both fast and efficient. Therefore, in order to observe a benefit from the HCT state, it is beneficial to have slow electron transport (characterised by a low v_0) to allow the hole retreat from the heterojunction and escape recombination.

This seems unlikely to be applicable in polymer:fullerene OPVs, as the electron mobility within regions of aggregated fullerene is expected to be large[51]. As v_0 increases, the electron is less likely to become trapped in a position where it is shielded from recombination by the local morphology. Recombination therefore becomes more prevalent and η_{SEP} is driven down to the minimum. Increasing v_0 still further was shown to increase η_{SEP}. This improvement in the separation efficiency is due to charge transport now competing effectively with recombination, rather than an effect of HCT states - *i.e.* the electron can drift/diffuse away from the heterojunction quickly enough that recombination is suppressed. In this case, the transient benefit of HCTs is expected to be small - all of the curves converge and the difference in η_{SEP} at different r values is minimal, suggesting that efficient charge generation can still occur through the bound CT state[22–24,52]. These effects, while present, are lessened at $r = 10\,\mathrm{nm}$, as the electron becomes trapped further from the heterojunction. The increased separation suppresses recombination almost entirely, increasing η_{SEP} for all values of v_0.

Alternative Methods of Efficient Charge Generation

Since the benefit from HCTs is insufficient to explain the high efficiencies found in some devices, it seems that efficient charge generation may be obtainable from the bound CT state instead. It has been suggested that polymer packing improves further away from the donor-acceptor interface, reducing the bandgap which, in turn, creates a cascaded energy heterojunction that drives charge separation[52–54]. Additionally, fullerene aggregation can also lead to a variation in the fullerene LUMO of the order 100 meV, facilitating electron transfer to the aggregate where charge

mobility is enhanced[19]. MC simulations have been able to predict efficient (*i.e.* $\eta_{\mathrm{SEP}} > 80\%$), field-independent free-charge generation for cascaded energy heterojunctions using energy levels in the range reported by both experiments and calculations[25,50]. Furthermore, MC has shown that cascades are even more effective if the mobility of charges is large over short lengthscales[50], as may be expected from microwave conductivity measurements[31].

Efficient free-charge generation *via* cascades contrasts with that *via* HCT states in an important detail. It has been predicted that substantial improvements in the free-charge generation efficiency begin to occur when the cascade energy is in the region of $150-200\,\mathrm{meV}$[25,50]. This is approximately the same as the energy required to move a charge from a mutual separation of 1 nm to 2 nm (230 meV for a system with $\epsilon = 3$). Hence, cascaded energy heterojunctions are predicted to give efficient charge generation when charge separation is already energetically favoured, as opposed to the transient advantage offered by HCT states[14].

Cascaded energy heterojunctions appear to explain free-charge generation in systems where either the polymer packing or fullerene aggregation occurs within localised regions. It is, however, possible that similar energy gradients could be provided by other mechanisms. In particular, quantum chemical calculations have shown that electrostatic interactions between the permanent, static charges within molecules in the active layer can alter the energetic landscape in an area a few nm around the heterojunction itself, modifying the charge separation barrier depending on molecular packing[52,55] or the combination of materials used[52,56]. Perhaps more generally, the relaxation of charges within the DoS could also provide the re-

quired energetic gradient[53,57,58], although some MC investigations appear to show that relaxation alone is insufficient to obtain the high efficiencies observed in experiment[10,38].

Of course, HCT states, spatial variation in energy levels due to aggregation or packing, and electrostatic interactions between the donor and acceptor molecules are not mutually exclusive and indeed fullerene aggregation appears to be a prerequisite in providing efficient free-charge generation. It seems, then, that HCT states can be the cause of the fast, efficient charge generation observed in spectroscopy, but that it is the arrangement of energy levels in the region of the heterojunction that causes the eventual, long-term separation of charges that ultimately leads to the high quantum efficiencies in devices.

5.5 Conclusions

Mesoscale Monte-Carlo simulations have been used to show that hot charge-transfer states can enhance free-charge generation in both idealised donor:acceptor (all-polymer) and mixed:aggregate (polymer:fullerene) morphologies. Fullerene aggregation within the molecularly mixed phase was shown to enhance OPV efficiency, largely through the increased production of HCT states within the fullerene aggregate, leading to increased short-circuit current.

However, in order to obtain the free-charge generation efficiencies observed in experiment, unphysically large HCT state separations and unphysically slow charge-carrier kinetics had to be assumed. For instance, efficient device response was predicted to occur when the initial separation between the dissociated electron and

hole pair is of the order $\sim 10\,\text{nm}$, at which point the Coulomb binding energy approaches k_BT and separation becomes energetically favourable. This separation is significantly larger than has been observed experimentally ($r \sim 4\,\text{nm}$). Efficient free-charge generation was also predicted if the electron mobility is small, such that the carrier becomes energetically trapped in a position where it can not recombine with the hole, allowing the hole to retreat before the electron detraps and moves on through the system to the contacts. However, electron mobility within fullerene aggregates is expected to increase rather than decrease, compared to the mixed phase. Since neither circumstance is expected to occur, the data from this investigation indicates that HCTs are unlikely to be the sole reason why some polymer-fullerene OPVs exhibit such large internal quantum efficiencies.

Other MC simulations have considered the effect of cascaded energy heterojunctions on free-charge generation and predicted efficient operation when considering cascade parameters taken from experiment[25], and even better performance when locally high mobilities are included based on the result of microwave conductivity measurements[50]. Based on these data, it seems that regional energetic variations local to the heterojunction are more likely to produce more efficient long-term, steady-state device performance.

References

[1] G. Yu, J. Gao, J. C. Hummelen, F. Wudl, and A. J. Heeger. "Polymer Photovoltaic Cells: Enhanced Efficiences via a Network of Internal Donor-Acceptor Heterojunctions." *Science*, **270**, 1789–1791, 1995.

[2] J. J. M. Halls, C. A. Walsh, N. C. Greenham, E. A. Marseglia, R. H. Friend, S. C. Moratti, and A. B. Holmes. "Efficient Photodiodes from Interpenetrating Polymer Networks." *Nature*, **376**, 498–500, 1995.

[3] J. A. Love, C. M. Proctor, J. Liu, C. J. Takacs, A. Sharenko, T. S. van der Poll, A. J. Heeger, G. C. Bazan, and T.-Q. Nguyen. "Film Morphology of High Efficiency Solution-Processed Small-Molecule Solar Cells." *Adv. Funct. Mater.*, **23**, 5019–5026, 2013.

[4] S. H. Park, A. Roy, S. Beaupreé, S. Cho, N. Coates, J. S. Moon, D. Moses, M. Leclerc, K. Lee, and A. J. Heeger. "Bulk Hetereojunction Solar Cells with Internal Quantum Efficiency Approaching 100%." *Nature Photon.*, **3**, 297–303, 2009.

[5] I. A. Howard, R. Mauer, M. Meister, and F. Lacquai. "Effect of Morphology on Ultrafast Free Carrier Generation in Polythiophene:Fullerene Organic Solar Cells." *J. Am. Chem. Soc.*, **132**, 14866–14876, 2010.

[6] I.-W. Hwang, D. Moses, and A. J. Heeger. "Photoinduced Carrier Generation in P3HT/PCBM Bulk Heterojunction Materials." *J. Phys. Chem. C*, **112**, 4350–4354, 2008.

[7] S. C. J. Meskers, P. A. van Hal, A. J. H. Spiering, J. C. Hummelen, A. F. G. van der Meer, and R. A. J. Janssen. "Time-resolved Infrared-absorption Study of Photoinduced Charge Transfer in a Polythiophene-methanofullerene Composite Film." *Phys. Rev. B*, **61**, 9917–9920, 2000.

[8] S. De, T. Pascher, M. Maiti, K. G. Jespersen, T. Kesti, F. Zhang, O. Inganäs, A. Yartsev, and V. Sundström. "Geminate Charge Recombination in Alternating Polyfluorene Copolymer/Fullerene Blends." *J. Am. Chem. Soc.*, **129**, 8466–8472, 2007.

[9] A. A. Bakulin, A. Rao, V. G. Pavelyev, P. H. M. van Loosdrecht, M. S. Pshenichnikov, D. Niedzialek, J. Cornil, D. Beljonne, and R. H. Friend. "The Role of Driving Energy and Delocalized States for Charge Separation in Organic Semiconductors." *Science*, **335**, 1340–1344, 2012.

[10] C. Groves, R. A. Marsh, and N. C. Greenham. "Monte Carlo Modelling of Geminate Recombination in Polymer-Polymer Photovoltaic Devices." *J. Chem. Phys.*, **129**, 114903:1–114903:7, 2008.

[11] G. Grancini, M. Maiuri, D. Fazzi, A. Petrozza, H-J. Egelhaaf, D. Brida, G. Cerullo, and G. Lanzani. "Hot Exciton Dissociation in Polymer Solar Cells." *Nature Mater.*, **12**, 29–33, 2013.

[12] I.-W. Hwang, C. Soci, D. Moses, Z. Zhu, D. Waller, R. Gaudiana, C. J. Brabec, and A. J. Heeger. "Ultrafast Electron Transfer and Decay Dynamics in a Small Band Gap Bulk Heterojunction Material." *Adv. Mater.*, **19**, 2307–2312, 2007.

[13] F. Etzold, I. A. Howard, R. Mauer, M. Meister, T.-D. Kim, K.-S. Lee, N. S. Baek, and F. Laquai. "Ultrafast Exciton Dissociation Followed by Nongeminate Charge Recombination in PCDTBT:PCBM Photovoltaic Blends." *J. Am. Chem. Soc.*, **134**, 10569–10583, 2012.

[14] A. E. Jailaubekov, A. P. Willard, J. R. Tritsch, W-L. Chan, N Sai, R. Gearba, L. G. Kaake, K. J. Williams, K. Leung, P. J. Rossky, and X-Y. Zhu. "Hot Charge-Transfer Excitons Set the Time Limit for Charge Separation at Donor/Acceptor Interfaces in Organic Photovoltaics." *Nature Mater.*, **12**, 66–73, 2013.

[15] H. Vázquez and A. Troisi. "Calculation of Rates of Exciton Dissociation into Hot Charge-Transfer States in Model Organic Photovoltaic Interfaces." *Phys. Rev. B*, **88**, 205304, 2013.

[16] A. Troisi. "How Quasi-Free Holes and Electrons are Generated in Organic Photovoltaic Interfaces." *Farad. Discuss.*, **163**, 377–392, 2013.

[17] B. M. Savoie, A. Rao, A. A. Bakulin, S. Gélinas, B. Movaghar, R. H. Friend, T. J. Marks, and M. A. Ratner. "Unequal Partnership: Asymmetric Roles of Polymeric Donor and Fullerene Acceptor in Generating Free Charge." *J. Am. Chem. Soc.*, **136**, 2876–2884, 2014.

[18] S. Gélinas, A. Rao, A. Kumar, S. L. Smith, A. W. Chin, J. Clark, T. S. van der Poll, G. C. Bazan, and R. H. Friend. "Ultrafast Long-Range Charge Separation in Organic Semiconductor Photovoltaic Diodes." *Science*, **343**, 512–516, 2014.

[19] F. C. Jamieson, E. B. Domingo, T. McCarthy-Ward, M. Heeney, N. Stingelin, and J. R. Durrant. "Fullerene Crystallisation as a Key Driver of Charge Separation in Polymer/Fullerene Bulk Heterojunction Solar Cells." *Chem. Sci.*, **3**, 485–492, 2012.

[20] B. A. Collins, Z. Li, J. R. Tumbleston, E. Gann, C. R. McNeill, and H. Ade. "Absolute Measurement of Domain Composition and Nanoscale Size Distribution Explains Performance in PTB7:$PC_{71}BM$ Solar Cells." *Adv. Energy Mater.*, **3**, 65–74, 2013.

[21] M. Muntwiler, Q. Yang, W. A. Tisdale, and X.-Y. Zhu. "Coulomb Barrier for Charge Separation at an Organic Semicondcutor Interface." *Phys. Rev. Lett.*, **101**, 196403:1–196403:4, 2008.

[22] T. G. J. van der Hofstad, D. Di Nuzzo, M. van den Berg, R. A. J. Janssen, and S. C. J. Meskers. "Influence of Photon Excess Energy on Charge Carrier Dynamics in a Polymer-Fullerene Solar Cell." *Adv. Energy Mater.*, **2**, 1095–1099, 2012.

[23] K. Vandewal, S. Albrecht, E. T. Hoke, K. R. Graham, J. Widmer, J. D. Douglas, M. Schubert, W. R. Mateker, J. T. Bloking, G. F. Burkhard, A. Sellinger, J. M. J. Fréchet, A. Amassian, M. K. Riede, M. D. McGehee, D. Neher, and A. Salleo. "Efficient Charge Generation By Relaxed Charge-Transfer States at Organic Interfaces." *Nature Mater.*, **13**, 63–68, 2014.

[24] J. Lee, K. Vandewal, S. R. Yost, M. E. Bahlke, L. Goris, M. A. Baldo, J. V. Manca, and T. V. Voorhis. "Charge Transfer State Versus Hot Exciton Dissociation in Polymer-Fullerene Blended Solar Cells." *J. Am. Chem. Soc.*, **132**, 11878–11880, 2010.

[25] C. Groves. "Suppression of Geminate Charge Recombination in Organic Photovoltaic Devices with a Cascaded Energy Heterojunction." *Energy Environ. Sci.*, **6**, 1546–1551, 2013.

[26] K. Vandewal, S. Himmelberger, and A. Salleo. "Structural Factors That Affect the Performance of Organic Bulk Heterojunction Solar Cells." *Macromolecules*, **46**, 6379–6387, 2013.

[27] J. W. Cahn and J. E. Hilliard. "Free Energy of a Nonuniform System. I. Interfacial Free Energy." *J. Chem. Phys.*, **28**, 258–267, 1958.

[28] B. P. Lyons, N. Clarke, and C. Groves. "The Quantitative Effect of Surface Wetting Layers on the Performance of Organic Bulk Heterojunction Photovoltaic Devices." *J. Phys. Chem. C*, **115**, 22572–22577, 2011.

[29] T. Kim, J.-H. Kim, T. E. Kang, C. Lee, H. Kang, M. Shin, C. Wang, B. Ma, U. Jeong, T.-S. Kim, and B. J. Kim. "Flexible, Highly Efficient All-Polymer Solar Cells." *Nature Commun.*, **6**, 1–7, 2015.

[30] Q. Zhang, B. Kan, F. Liu, G. Long, X. Wan, X. Chen, Y. Zuo, W. Ni, H. Zhang, M. Li, Z. Hu, F. Huang, Y. Cao, Z. Liang, M. Zhang, T. P. Russell, and Y. Chen. "Small-Molecule Solar Cells with Efficiency Over 9%." *Nature Photon.*, **9**, 35–41, 2015.

[31] G. Dicker, M. P. de Haas, L. D. A. Siebbeles, and J. M. Warman. "Electrodeless Time-Resolved Microwave Conductivity Study of Charge-Carrier Photogeneration in Regioregular poly(3-hexylthiophene) Thin Films." *Phys. Rev. B*, **70**, 045203:1–045203:8, 2004.

[32] R. C. I. MacKenzie, T. Kirchartz, G. F. A. Dibb, and J. Nelson. "Modeling Nongeminate Recombination in P3HT:PCBM Solar Cells." *J. Phys. Chem. C*, **115**, 9806–9813, 2011.

[33] N. D. Treat, A. Varotto, C. J. Takacs, N. Batara, M. Al-Hashimi, M. J. Heeney, A. J. Heeger, F. Wudl, C. J. Hawker, and M. L. Chabinyc. "Polymer-Fullerene Miscibility: A Metric for Screening New Materials for High-Performance Organic Solar Cells." *J. Am. Chem. Soc.*, **134**, 15869–15879, 2012.

[34] S. Westenhoff, I. A. Howard, J. M. Hodgkiss, K. R. Kirov, H. A. Bronstein, C. K. Williams, N. C. Greenham, and R. H. Friend. "Charge Recombination in Organic Photovoltaic Devices with High Open-Circuit Voltages." *J. Am. Chem. Soc.*, **130**, 13653–13658, 2008.

[35] A. A. Bakulin, D. S. Martyanov, D. Y. Paraschuk, M. S. Psehnichnikov, and P. H. M. van Loosdrecht. "Ultrafast Charge Photogeneration Dynamics in Ground-State Charge-Transfer Complexes Based on Conjugated Polymers." *J. Phys. Chem. B*, **112**, 13730–13737, 2008.

[36] S. A. McDonald, G. Konstantatos, S. Zhang, P. W. Cyr, E. J. D. Klem, L. Levina, and E. H. Sargent. "Solution-Processed PbS Quantum Dot Infrared Photodetectors and Photovoltaics." *Nature Mater.*, **4**, 138–142, 2005.

[37] R. A. Marsh, C. Groves, and N. C. Greenham. "A Microscopic Model for the Behavior of Nanostructured Organic Photovoltaic Devices." *J. Appl. Phys.*, **101**, 083509:1–083509:7, 2007.

[38] C. Groves, J. C. Blakesley, and N. C. Greenham. "Effect of Charge Trapping on Geminate Recombination and Polymer Solar Cell Performance." *Nano Lett.*, **10**, 1063–1069, 2010.

[39] R. A. Marsh, J. M. Hodgkiss, S. Albert-Seifried, and R. H. Friend. "Effect of Annealing on P3HT:PCBM Charge Transfer and Nanoscale Morphology Probed by Ultrafast Spectroscopy." *Nano Lett.*, **10**, 923–930, 2010.

[40] J. Jo, S.-I. Na, S.-S. Kim, T.-W. Lee, Y. Chung, S.-J. Kang, D. Vak, and D.-Y. Kim. "Three-Dimensional Bulk Heterojunction Morphology for Achieving High Internal Quantum Efficiency in Polymer Solar Cells." *Adv. Funct. Mater.*, **19**, 2398–2406, 2009.

[41] S. Honda, T. Nogami, H. Ohkita, H. Benten, and S. Ito. "Improvement of the Light-Harvesting Efficiency in Polymer/Fullerene Bulk Heterojunction Solar Cells by Interfacial Dye Modification." *ACS Appl. Mater. Interfaces*, **1**, 804–810, 2009.

[42] H. Zhou, Y. Zhang, J. Seifter, S. D. Collins, C. Luo, G. C. Bazan, T.-Q. Nguyen, and A. J. Heeger. "High-Efficiency Polymer Solar Cells Enhanced by Solvent Treatment." *Adv. Mater.*, **25**, 1646–1652, 2013.

[43] B. A. Collins, J. R. Tumbleston, and H. Ade. "Miscibility, Crystallinity, and Phase Development in P3HT/PCBM Solar Cells: Toward an Enlightened Understanding of Device Morphology and Stability." *J. Phys. Chem. Lett.*, **2**, 3135–3145, 2011.

[44] S. Shoaee, S. Subramaniyan, H. Xin, C. Keiderling, P. S. Tuladhar, F. Jamieson, S. A. Jenekhe, and J. R. Durrant. "Charge Photogeneration for a Series of Thiazolo-Thiazole Donor Polymers Blended with the Fullerene Electron Acceptors PCBM and ICBA." *Adv. Funct. Mater.*, **23**, 3286–3298, 2013.

[45] P. Peumans and S. R. Forrest. "Separation of Geminate Charge-Pairs at Donor-Acceptor Interfaces in Disordered Solids." *Chem. Phys. Lett.*, **398**, 27–31, 2004.

[46] C. Groves and N. C. Greenham. "Bimolecular Recombination in Polymer Electronic Devices." *Phys. Rev. B*, **78**, 155205:1–155205:8, 2008.

[47] C. G. Shuttle, B. O'Regan, A. M. Ballantyne, J. Nelson, D. D. C. Bradley, and J. R. Durrant. "Bimolecular Recombination Losses in polythiophene:Fullerene Solar Cells." *Phys. Rev. B*, **78**, 113201:1–113201:4, 2008.

[48] G. F. A. Dibb, F. C. Jamieson, A. Maurano, J. Nelson, and J. R. Durrant. "Limits on the Fill Factor in Organic Photovoltaics: Distinguishing Nongeminate and Geminate Recombination Mechanics." *J. Phys. Chem. Lett.*, **4**, 803–808, 2013.

[49] R. G. E. Kimber, A. B. Walker, G. E. Schröder-Turk, and D. J. Cleaver. "Bicontinuous Minimal Surface Nanostructures for Polymer Blend Solar Cells." *Phys. Chem. Chem. Phys.*, **12**, 844–851, 2010.

[50] T. M. Burke and M. D. McGehee. "How High Local Charge Carrier Mobility and an Energy Cascade in a Three-Phase Bulk Heterojunction Enable >90% Quantum Efficiency." *Adv. Mater.*, **26**, 1923–1928, 2014.

[51] D. Veldman, Ö. Ipek, S. C. J. Meskers, J Sweelssen, M. M. Koetse, S. C. Veenstra, J. M. Kroon, S. S. van Bavel, J. Loos, and R. A. J. Janssen. "Compositional and Electric Field Dependence of the Dissociation of Charge Transfer Excitons in Alternating Polyfluorene Copolymer/Fullerene Blends." *J. Am. Chem. Soc.*, **130**, 7721–7735, 2008.

[52] S. R. Yost and T. van Voorhis. "Electrostatic Effects at Organic Semiconductor Interfaces: A Mechanism for "Cold" Exciton Breakup." *J. Phys. Chem. C*, **117**, 5617–5625, 2013.

[53] G. D'Avino, S. Mothy, L. Muccioli, C. Zannoni, L. Wang, J. Cornil, D. Beljonne, and F. Castet. "Energetics of Electron-Hole Separation at P3HT/PCBM Heterojunctions." *J. Phys. Chem. C*, **117**, 12981–12990, 2013.

[54] D. P. McMahon, D. L. Cheung, and A. Troisi. "Why Holes and Electrons Separate So Well in Polymer/Fullerene Photovoltaic Cells." *J. Phys. Chem. Lett.*, **2**, 2737–2741, 2011.

[55] J. Idé, R. Mereau, L. Ducasse, F. Castet, H. Bock, Y. Olivier, J. Cornil, D. Beljonne, G. D'Avino, O. M. Roscioni, L. Muccioli, and C. Zannoni. "Charge Dissociation at Interfaces between Discotic Liquid Crystals: The Surprising Role of Column Mismatch." *J. Am. Chem. Soc.*, **136**, 2911–2920, 2014.

[56] S. Mothy, M. Guillaume, J. Ide, F. Castet, L. Ducasse, J. Cornil, and D. Beljonne. "Tuning the Interfacial Electronic Structure at Organic Heterojunctions by Chemical Design." *J. Phys. Chem. Lett.*, **3**, 2374–2378, 2012.

[57] H. van Eersel, R. A. J. Janssen, and M. Kemerink. "Mechanism for Efficient Photoinduced Charge Separation at Disordered Organic Heterointerfaces." *Adv. Funct. Mater.*, **22**, 2700–2708, 2012.

[58] U. Albrecht and H. Bassler. "Yield of Geminate Pair Dissociation in an Energetically Random Hopping System." *Chem. Phys. Lett.*, **235**, 389–393, 1995.

Chapter 6

Relating Morphology to Mobility

6.1 Introduction

So far, this thesis has considered mostly mesoscopic MC simulations of OPVs. The morphologies used in each investigation have been created by collaborators using a Cahn-Hilliard technique (§3.4.1), in which the details of sublattice structure are treated using a Gaussian disorder model, instead of determining the molecular conformation explicitly. Here, the focus is switched to the conjugated polymer within thin-film electronic devices (not just relevant to photovoltaics), with the aim of determining how polymer chain packing and crystallinity on the molecular level can affect macroscopic device properties such as the bulk carrier mobility.

In this chapter, realistic P3HT morphologies are simulated using MD simulations, which are then used in a MC charge transport model. Populations of chains are simulated, with commercially available weight-averaged molecular weights ($19.4\,\mathrm{kDa} \leq M_w < 69.9\,\mathrm{kDa}$) and polydispersity indices ($1.5 \leq \mathrm{PDI} \leq 2.4$), for a realistic thin film density ($\rho = 1.1\,\mathrm{g\,cm^{-3}}$). By fitting each of these variables to commercially

available values, this allows the simulations to produce realistic morphologies without assuming an initial configuration. The chains are then subjected to various annealing protocols to understand how the thin film morphology evolves. These diverse, realistic morphologies are input to a new, molecular MC charge transport framework in which hopping rates along and between the chains are determined by semi-empirical quantum chemical ZINDO/S calculations.

The process of producing realistic morphologies from a calibrated CG forcefield is explained in §6.3, along with the subsequent characterisation methodologies employed for the investigation. §6.4 explains how the charge transport simulations were implemented which, when combined with the MD morphologies, allowed the morphology dependence of the zero-field hole mobility to be investigated in §6.5. Finally, the conclusions from this investigation are presented in §6.6.

6.2 Conjugated Polymers

6.2.1 Mobility

A fundamental property of the constituent polymers within organic electronic devices is the charge-carrier mobility (μ), which often determines performance in electronic devices[1] such as OTFTs[2], OLEDs[3,4] and OPVs[5–8]. It is therefore vital to exert control over the mobility in order to enable conjugated polymers to achieve their maximum potential. This has led to the design of high-mobility polymers and subsequent processing techniques as very active areas of research[9–11], in an attempt to produce morphologies that exhibit a high charge mobility[12–14]. However, it is

a significant challenge to understand the relationship between the morphology on the molecular level and the resultant mobility[15]. This is demonstrated by the plentiful investigations of P3HT - a semicrystalline polymer that is frequently used in OTFTs[12,16] and OPVs[14,17].

As is the case for many conjugated polymers, the electronic properties of P3HT are strongly dependent on the morphology of the thin film[18]. When 'as-cast' in its amorphous phase, P3HT exhibits a ToF mobility, $\mu \sim 1 \times 10^{-5}\,\mathrm{cm^2\,V^{-1}\,s^{-1}}$[19]. However, P3HT chains can self-assemble into crystals when the film is subjected to thermal or solvent vapour annealing or high pressure[20,21], with the resultant semicrystalline morphology exhibiting hole mobilities at least an order of magnitude larger[19,22,23]. The degree to which crystals form depends also on the properties of the polymer chains themselves such as the regioregularity[20], molecular weight[24] and polydispersity[25], all of which can affect the resultant film mobility. Many aspects of the molecular morphology have been linked to high mobility within P3HT, such as an increased proportion of crystalline material[25,26], improved crystalline order in the π-stacking[27] or chain backbone[24,28,29] directions, or, more recently, the presence of tie-chains within the morphology that link crystals together, forming 'mobility highways', along which the hole can travel more quickly than through the surrounding amorphous medium[15,30,31]. This highlights the challenge of demonstrating causal relationships for mobility as, even with the benefit of a wide array of carefully performed experiments on an extensively-studied polymer, the underlying physics is still very much the subject of debate.

6.2.2 Molecular Dynamics Simulations

Simulations offer a useful method with which to examine the relationship between molecular morphology and bulk charge transport in greater detail than is generally available by a single experiment. While there are a range of morphology simulation techniques available[32,33], MD methods stand out as being able to produce atomistically detailed morphologies for experimentally relevant molecular weights and polydispersities. MD simulations employ a calibrated force-field that replicates the bulk behaviour of chains under different processing conditions and annealing temperatures[34–36]. While some MD simulations model samples atomistically, an alternative method involves grouping together atoms into a single coarse-grained site to reduce the computational overhead of calculating the forces acting between the potentially hundreds of thousands of particles in the system[37,38]. This is especially important as computational cost limits the amount of simulated material to be considered. CG models have been used to successfully reproduce the experimental data of the chain conformation that influences phase behaviour in conjugated polymers[39], the miscibility and interpenetration of the various constituent molecules of OPV blends[40], and predicting microstructure architectures[41] that can be linked to mesoscopic morphological features[42]. However, to date, the detailed film morphologies generated by these techniques have not been joined with charge transport simulations. Instead, studies have focussed solely on the film morphology alone[38], or only considered charge transport after assuming an initial configuration of chains that resulted in an idealised morphology - influencing the subsequent charge transport characteristics[43,44].

6.3 Molecular Dynamics Simulations

6.3.1 Coarse-Grained Forcefield

The forcefield used in this investigation was created by a collaborator[37,39,40]. Figure 6.1 shows the location of the CG sites used in the MD simulations, based on the positions of the three main functional groups of the 3-hexylthiophene monomer. Each CG 'superatom' represents the average behaviour of several atoms that are expected to behave in a similar way to the other atoms within the group. Details of the production and calibration of the forcefield can be found in appendix A. Importantly, the resultant forcefield successfully predicted the atomistic bond length, angle, and dihedral potentials, as well as the non-bonded pair distribution functions and average film densities for a variety of thermodynamic states, making it well suited to this investigation.

6.3.2 Picking Chain Lengths

With the framework for a suitable CG methodology in place, the behaviour of P3HT chains could be simulated in order to determine how the different effects of processing affect morphological characteristics. P3HT is polydisperse due to variability in the degree of polymerisation for each chain. The length of a chain can affect many of the physical and electronic properties of a chain, as well as strongly affecting the self-reorganisation of the sample[30]. It is therefore useful to describe the molecular weight of the polymer, which must take into account some level of averaging over the chains within the whole polydisperse sample.

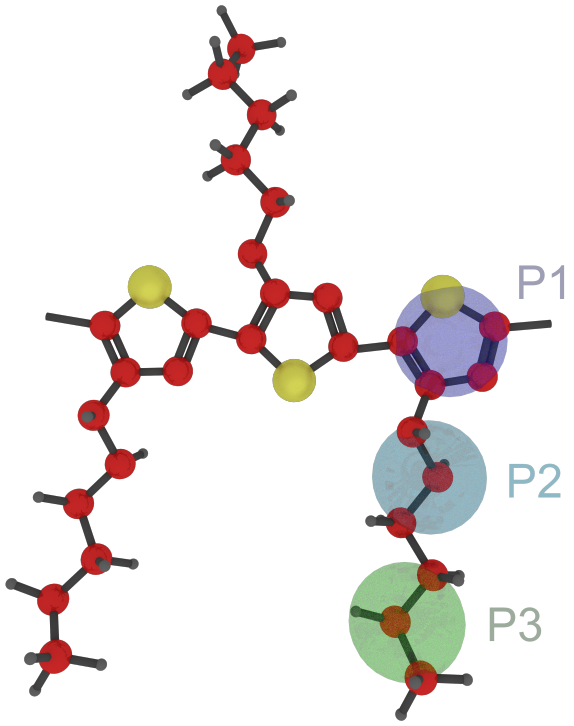

Figure 6.1: *The coarse-grained model used to simulate P3HT. The sites P1, P2 and P3 are located at the centres-of-mass of the thiophene ring, first three methyl groups of the hexyl sidechain and the second three methyl groups respectively.*

The molecular weight can be defined in a number of ways. Perhaps the most simple is the number-average molecular weight $\mathrm{M_n}$:

$$\mathrm{M_n} = \frac{\sum_i n_i M_i}{\sum_i n_i}, \tag{6.3.1}$$

where M_i is the molecular weight of a chain, and n_i is the number of chains with that molecular weight. $\mathrm{M_n}$ therefore represents the mean of the molecular weights of the chains within the sample.

Alternatively, it can be useful to calculate the weight-averaged molecular weight, $\mathrm{M_w}$:

$$\mathrm{M_w} = \frac{\sum_i n_i M_i^2}{\sum_i n_i M_i}. \tag{6.3.2}$$

Due to the M_i^2 term, $\mathrm{M_w}$ is more sensitive to chains with a higher degree of polymerisation, which can have more of an effect on phase transition temperatures and mechanical properties such as stiffness[45]. Both $\mathrm{M_n}$ and $\mathrm{M_w}$ can be determined by rheometry or gel permeation chromatography[46,47]. Knowledge of both allows the polydispersity of a sample to be calculated, which is defined as:

$$\mathrm{PDI} = \frac{\mathrm{M_w}}{\mathrm{M_n}}. \tag{6.3.3}$$

The polydispersity is an important quantity because it describes the breadth of the chain-length distribution of a particular sample, which is strongly dependent on the polymerisation technique used[48]. The PDI of P3HT can vary between 1.15-5[49,50], with many manufacturers quoting PDI < 2.5[51]. A realistic simulation of P3HT films must therefore take into account the polydispersity.

A commonly used mathematical description of the relative ratios of polymer lengths in a sample is the Schulz-Flory distribution, which has the form:

$$P_{D,SF} = \alpha^2 D_p \left((1-\alpha)^{D_p - 1} \right), \tag{6.3.4}$$

where D_p is the degree of polymerisation for a particular chain, $P_{D,SF}$ the probability at which it occurs and α is a tunable parameter that affects the shape of the distribution. The blue line in figure 6.2 shows the shape of the Schulz-Flory distribution for $\alpha = 0.2$. The nature of the function implies that shorter polymers are favoured over longer chains, with the selection probability of long chains decaying to 0 quickly. Even with the tuning of α, it was found that, at the correct $\mathrm{M_w}$, the

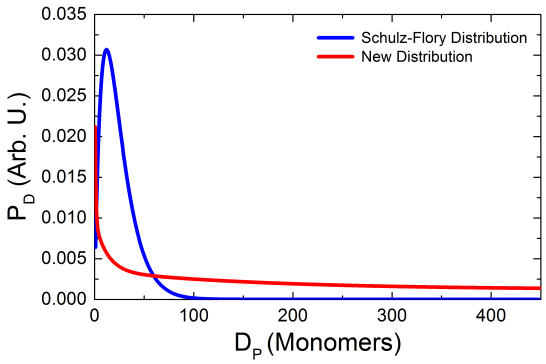

Figure 6.2: *A comparison of examples of the Schulz-Flory distribution (blue line, $\alpha = 0.2$) and the new distribution (red line, $A = 0.0192$, $B = 0.0044$, $C = 0.0016$, $\kappa_1 = 0.5754$, $\kappa_2 = 0.0176$) used for this investigation.*

obtained PDI was significantly smaller than those available commercially for P3HT, suggesting that a wider distribution of both short and long chains was required.

As such, an alternative distribution was used:

$$P_{D,NEW} = A\exp(-\kappa_1 D_p) + B\exp(-\kappa_2 D_p) + C, \tag{6.3.5}$$

where A, B, C, κ_1 and κ_2 are free parameters that could be tuned to recreate the commercial M_w and PDI. The shape of the distribution is shown in figure 6.2 as the red line. In this distribution, short chains are still favoured (as in $P_{D,SF}$), but long chains can be selected at a probability tending towards the non-zero constant C, thereby increasing the PDI. In this investigation, samples of 40 chains were selected at random from $P_{D,NEW}$, and those with unrealistic M_w or PDI discarded. The accepted samples are shown in table 6.1. This dataset had a range of molecular weights $19 \leq M_w < 70\,\text{kDa}$, and were named *S-19* to *S-70* for identification.

Name	S-19	S-37	S-46	S-51	S-57	S-70
M_w (kDa)	19.4	37.0	45.7	51.1	56.8	69.9
M_n (kDa)	12.6	20.0	27.8	29.5	30.1	45.0
PDI	1.5	1.9	1.6	1.7	1.9	1.6

Table 6.1: *The P3HT samples considered in this investigation with weight- and number-averaged molecular weights (M_w, M_n) and polydispersity indices (PDI). The naming convention is "S-$\langle M_w \rangle$", where the 'S' denotes that only a single sample is present, selected from the distribution in equation 6.3.5.*

6.3.3 LAMMPS Simulations

After an appropriate distribution of chain lengths had been selected, samples could be generated to form the input morphologies for the molecular dynamics simulations. All simulations performed at constant volume and temperature, maintained using a Nosé-Hoover thermostat and barostat[52], using the LAMMPS simulation suite[53].

Chain Database

For each chain in the samples shown in table 6.1, a coarse-grained chain of corresponding polymerisation was selected from a lookup database, consisting of P3HT chains with lengths ranging from 2 (M_n = 330 Da) to 1000 monomers (M_n = 164 kDa). Chains for the database began as a P3HT dimer consisting of two monomers in a head-to-tail configuration, with an energetically optimised atomic structure determined by the DL_POLY program suite[54]. As in the coarse-grained forcefield configuration, the terminating hydrogen atoms were removed for simplicity. The dimer was then coarse-grained by calculating the centres-of-mass of each

of the functional groups according to the schematic in figure 6.1. The CG dimer was then copied and translated in a direction corresponding to the chain's backbone vector by a distance equal to the current length of the chain, resulting in a 100% regioregular, completely straight chain of the required polymerisation. In order to mimic the contortions of chains in solution, each chain in the database was simulated at 290 K in isolation for a period of 1 ns, thereby permitting it to relax according to the intramolecular components of the forcefield.

Shrinking Process

Selected chains from the database that represented a particular P3HT sample were then inserted at random positions and orientations into a large, periodically bounded simulation box, with sufficient empty space between chains to avoid interactions with neighbouring polymers. This created a sample with a very low film density, which was then compressed at 290 K over a period of 40 ps, until the simulation reached the experimental film density of $\rho = 1.1\,\mathrm{g\,cm^{-3}}$ [55]. This shrinking process forced chains together on a timescale faster than the interaction timescales dictated by the forcefield, and was a necessary step to prevent physical instabilities within the forcefield that occurred when trying to populate the simulation volume at the correct density directly. This method mimicked the effect of solvent evaporation of the solution, producing a CG morphology consisting of a sample of CG P3HT chains with realistic M_w, PDI and ρ, occupying a cube with sides of the order of 10 nm. The exact simulation volumes varied with M_w, but were all of similar order to the thin film thickness in real devices [14,38].

Annealing, Cooling and Equilibration

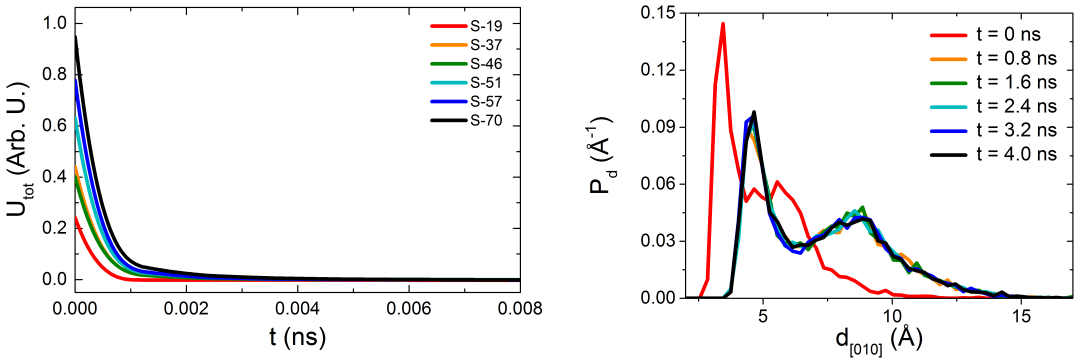

(a) *Total Potential Energy* ***(b)*** $d_{[010]}$ *for S-51*

Figure 6.3: *The time evolution of the total potential energy and* $d_{[010]}$ *distribution functions for samples annealed at* $T_a = 423\,K$ *for the annealing simulation phase.*

The CG morphologies were then subjected to a series of annealing and equilibration MD simulations, utilising both the intra- and inter-molecular components of the forcefield in LAMMPS. Morphologies were first simulated at a temperature T_a, varying from $T_a = 290\,\mathrm{K}$ (no annealing) through to $T_a = 623\,\mathrm{K}$ for a period of 4 ns. Of course, real devices are annealed for a much longer period, however, the total potential energy and structural distribution functions stabilised within this timescale (figure 6.3), suggesting that some level of thermally activated chain reorganisation had taken place. Therefore, the annealing process was limited to 4 ns in the interest of computational cost. To mitigate the effect of the reduced annealing time, T_a values here exceed those frequently used in experiment in order to maximise the transfer of energy to the system during this time[38,56]. It was found that $T_a > 623\,\mathrm{K}$ resulted in numerical instabilities in the MD simulations for the chosen timestep.

The CG site positions from the outputs of each annealing simulation were then converted back into LAMMPS inputs, and resubmitted for a 4 ns cooling phase.

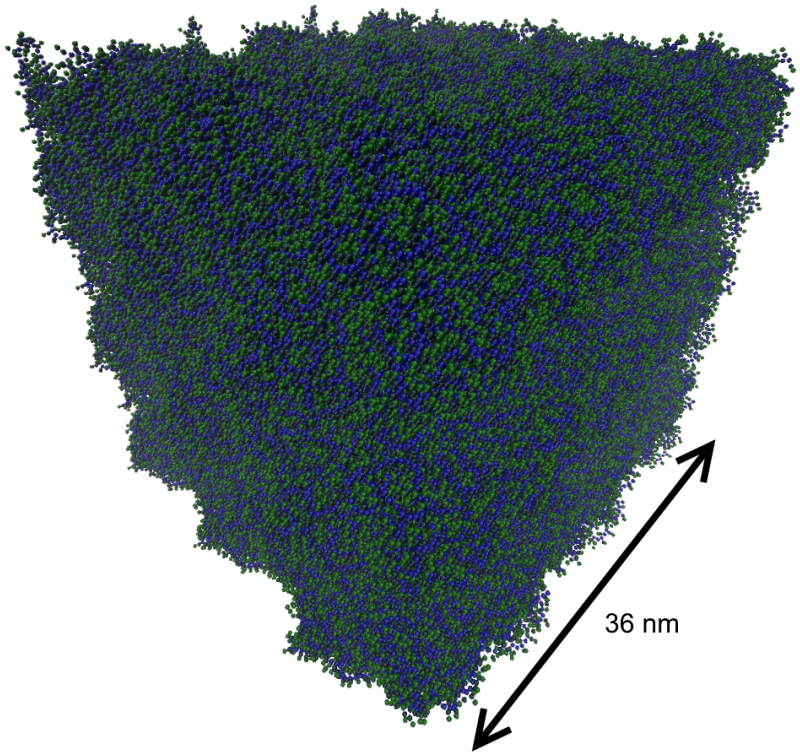

Figure 6.4: *An example of the heated, cooled and equilibrated S-51 morphology, with $M_w = 51\,kDa$ and $T_a = 423\,K$. The coarse-grained sites are coloured as shown in figure 6.1. Unit cells are repeated due to the periodic boundary conditions to form a larger 3x3x3 cubic domain of side 36 nm.*

During this phase, the temperature was linearly reduced from T_a to 290 K, allowing the polymer chains to crystallise out of the melt. The rate of temperature reduction varied depending on the initial value of T_a, but all samples reached 290 K after 4 ns. Finally, the morphology was permitted to equilibrate for a further 4 ns period at 290 K to settle the morphology. An example of the final CG morphology is shown in figure 6.4, including the periodic boundary conditions in all 3 directions.

6.3.4 Characterisation methodology

The physical conformation of the chains in each equilibrated system was analysed to determine the crystal structure of each sample. Crystals in the morphology were defined based on the proximity of pairs of conjugated subunits (in the case of

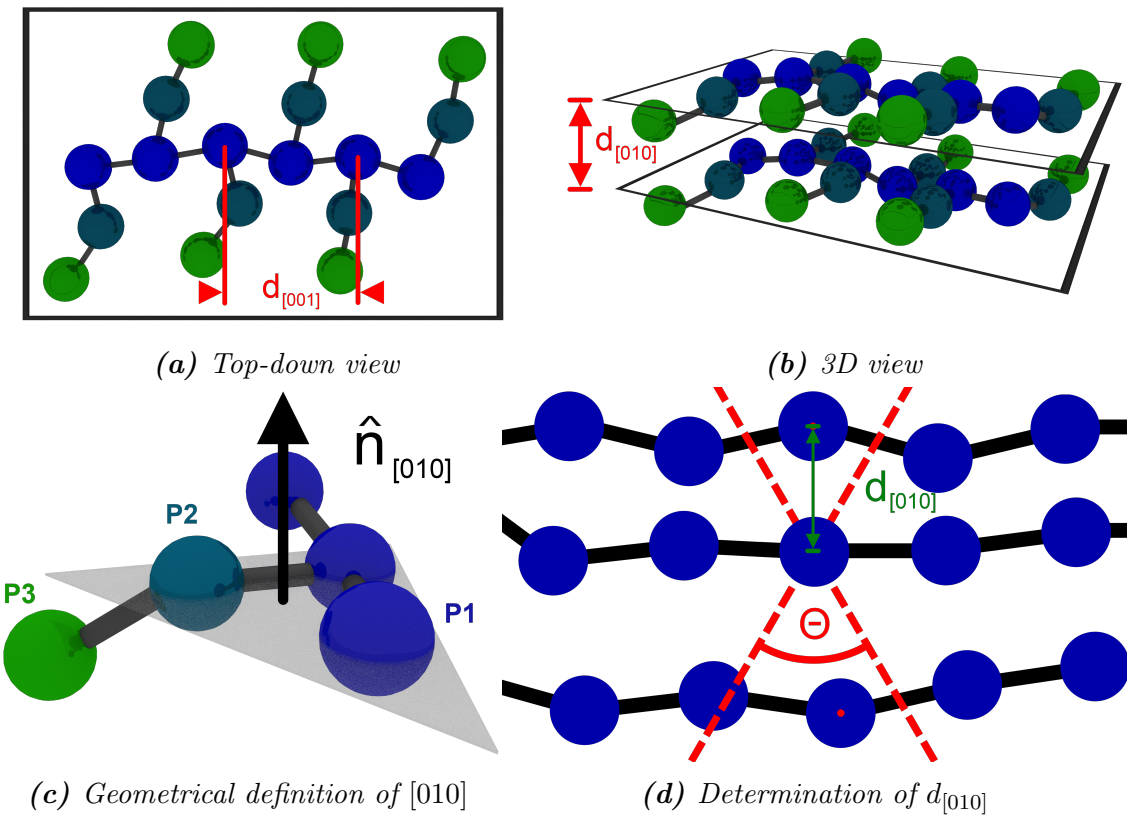

(a) Top-down view *(b) 3D view*

(c) Geometrical definition of [010] *(d) Determination of* $d_{[010]}$

Figure 6.5: *Schematics of the two crystal directions used in the characterisation of the CG P3HT morphologies.*

P3HT, the thiophene ring at CG site P1) along a given direction denoted by the Miller index $[hkl]$, specifically the first order π-stacking ($[hkl] = [010]$) and backbone ($[hkl] = [001]$) axes, as shown in figures 6.5a and b. The definition of the π-stacking axis, which was based on the positions of bonded CG sites, is given in figure 6.5c. For each subunit, $d_{[hkl]}$ was defined as the separation to the closest thiophene ring lying within a cone of apex angle $\Theta = 30°$ protruding both above and below the CG site in the $[hkl]$ direction. An example determination of $d_{[010]}$ is given in figure 6.5d, where the centre-points of two CG sites are present within the cone (depicted by red dots), but only the separation to the closest site defines $d_{[010]}$.

Figure 6.6 shows the $d_{[hkl]}$ histogram for the *S-51* sample annealed at $T_a = 423\,\mathrm{K}$.

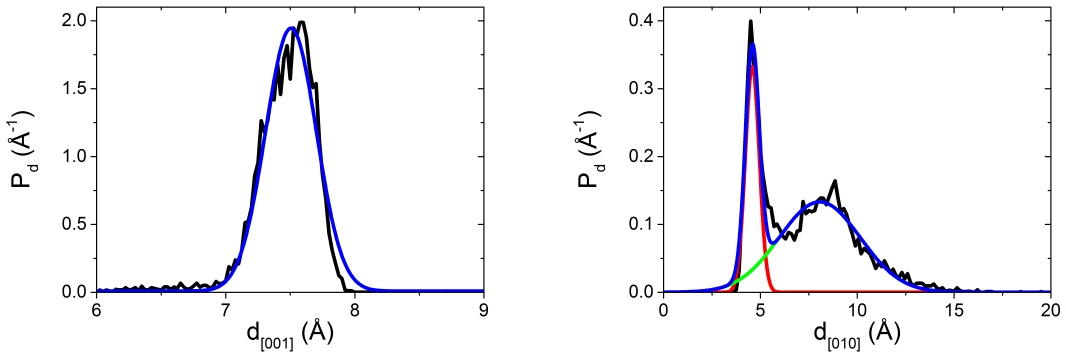

(a) *[hkl] = [001], backbone* ***(b)*** *[hkl] = [010], π-stacking*

Figure 6.6: *$d_{[hkl]}$ histograms for the S-51 sample annealed at 423 K. The combined Gaussian fits to the data are depicted as blue lines.*

The $d_{[001]}$ data (panel **(a)**), which measures order along the chain backbone, is unimodal and can be fit by a single Gaussian distribution with $\bar{d}_{[001]} = 7.5\,\text{Å}$ and $\sigma_{[001]} = 0.2\,\text{Å}$. However, the π-stacking $d_{[010]}$ data is better fitted by a bimodal distribution consisting of two separate Gaussians. The peak at small $d_{[010]}$ has $\bar{d}_{[010]} = 4.6\,\text{Å}$ and $\sigma_{[010]} = 0.4\,\text{Å}$, and is attributed to the crystalline portion of the morphology where the neighbouring thiophenes are closely separated. The second peak is therefore attributed to the less-ordered, amorphous regions of the morphology, where there is a greater mean separation between the thiophene rings. This is characterised by a much broader distribution with $\bar{d}_a = 8.1\,\text{Å}$ and $\sigma_a = 2.1\,\text{Å}$.

These data agree well with the literature, since both $\bar{d}_{[001]}$ and $\bar{d}_{[010]}$ relate to the grazing-incidence wide-angle x-ray scattering (GIWAXS) data which report $\bar{d}_{[001]} = 7.7\,\text{Å}$ and $\bar{d}_{[010]} = 3.8\,\text{Å}$ [57], as well as atomistic MD simulation data which report $\bar{d}_{[001]} = 7.9\,\text{Å}$ and $\bar{d}_{[010]} = 4.0\,\text{Å}$ [44]. Hence, the generated morphologies show crystal packing in agreement with experiment.

From the $d_{[010]}$ distributions, it was possible to determine the paracrystallinity, which quantifies the disorder by describing the proportion of crystal defects within

the lattice structure[58]. The backbone and π-stacking paracrystallinities were calculated as $g_{[001]} = \sigma_{[001]}/\bar{d}_{[001]}$ and $g_{[010]} = \sigma_{[010]}/\bar{d}_{[010]}$ respectively, where only the narrow, crystalline distribution was considered for the π-stacking direction, as this is the region probed by XRD methods. The paracrystallinity data is shown in §6.5.2.

Additionally, the proportion of crystalline material within the morphology (γ) can be simply estimated by determining the integral underneath the crystalline Gaussian curve as a proportion of the integral of the whole distribution. These results will be discussed in §6.5.3, where γ is shown to be affected by both M_w and T_a. However, despite the realistic dimensions of the morphologies used in this investigation, it is still important to note that γ was limited by the short anneal times, as there was reduced opportunity for the crystals themselves to form. Due to the simulation dimensions, the crystals formed here were necessarily smaller than 10 nm in extent which, although directly relevant for some devices[59] is smaller than others[60,61].

The molecular dynamics simulations described in this section were executed on the Hamilton high-performance computing cluster at the University of Durham. Each phase of the annealing, cooling and equilibrating process for each annealing temperature and average molecular weight utilised 16 parallel processing cores on Intel Xeon E5-2650 v2 2.6 GHz Ivybridge processors, taking between 2 and 4 hours to complete. Scripts that completed the coarse-graining process and analysed the final crystal structure were single-threaded and each took 1-2 hours to complete for each input morphology.

6.4 Charge Transport Simulations

Using the above methodologies, it was possible to relate the supramolecular structure of the CG morphologies to variations in both M_w and T_a. However, an important feature of this investigation is identifying links between these properties and the hole-mobility of the morphologies that form the active layer in OEDs. This was accomplished through the use of a newly developed molecular MC simulation, which first required knowledge of the electronic couplings between the chains. These couplings are strongly related to the chain's frontier molecular orbitals, which are usually determined through DFT or quantum chemical calculations. However, no method is applicable to CG chains as each requires the knowledge of the atomic positions within the morphology in order to calculate the orbitals. In order to proceed therefore, the CG morphologies were returned to an atomistic representation for these calculations to take place.

6.4.1 Fine-Graining Procedure

The 'fine-graining' procedure was implemented as follows. Firstly, the original atomistic template that was used to generate the CG chains was split up into the three main functional groups that each CG superatom describes (figure 6.1). The atoms of the thiophene ring were then rotated around the ring's centre of mass so to minimise the distance, r, between the carbon atom bonding to the first half of the hexyl group (P2) and P2's centre of mass (figure 6.7a). This flipped the thiophene ring into the correct head-to-tail orientation to maintain the regioregularity of the chain.

The plane of the ring was then selected by an algorithm that mapped (*via* the

shortest possible rotation to ensure the thiophene ring was not flipped out of the correct head-to-tail position) the normal vector of the ring to the normal vector that described the plane between the centres of mass of the ring and its two neighbouring thiophene CG sites. For end-of-chain monomers, the rotation plane was instead described by the neighbouring CG site and the first bonded alkyl group. Rotations were performed using the following equation which uses a rotation matrix R, to rotate a vector $\underline{\mathbf{a}}$ onto a vector $\underline{\mathbf{b}}$:

$$R = I + [v]_{\times} + [v]_{\times}^{2} \frac{1 - (\underline{\mathbf{a}} \cdot \underline{\mathbf{b}})}{(||\underline{\mathbf{a}} \times \underline{\mathbf{b}}||)^{2}}, \tag{6.4.6}$$

where I is the identity matrix, and $[v]_{\times}$ is the skew-symmetric cross-product matrix of $v = \underline{\mathbf{a}} \times \underline{\mathbf{b}} = \big(v_x, v_y, v_z\big)$:

$$[v]_{\times} \equiv \begin{bmatrix} 0 & -v_z & v_y \\ v_z & 0 & -v_x \\ -v_y & v_x & 0 \end{bmatrix}. \tag{6.4.7}$$

The thiophene plane calculation algorithm is depicted in 2D without sidechains in figure 6.7b. The numbered stages are considered as follows:

1. Beginning at the end of the chain, the vector to the adjacent, bonded monomer (the second CG site) was determined ($\underline{\mathbf{a}}$). The first ring was then rotated such that its planarity matched the vector $\underline{\mathbf{a}}$.

2. $\underline{\mathbf{b}}$ was defined as the vector between the positions of the first and third CG

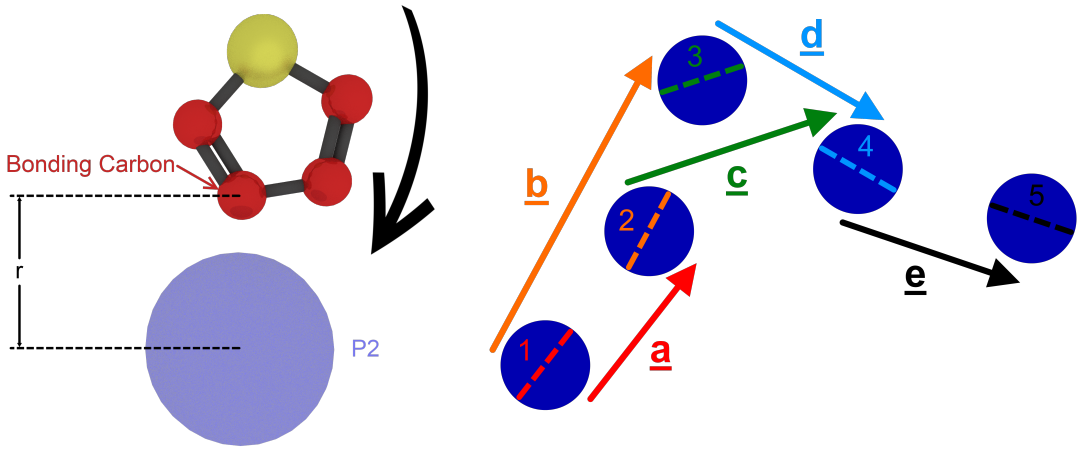

(a) First rotation algorithm *(b) Second rotation algorithm*

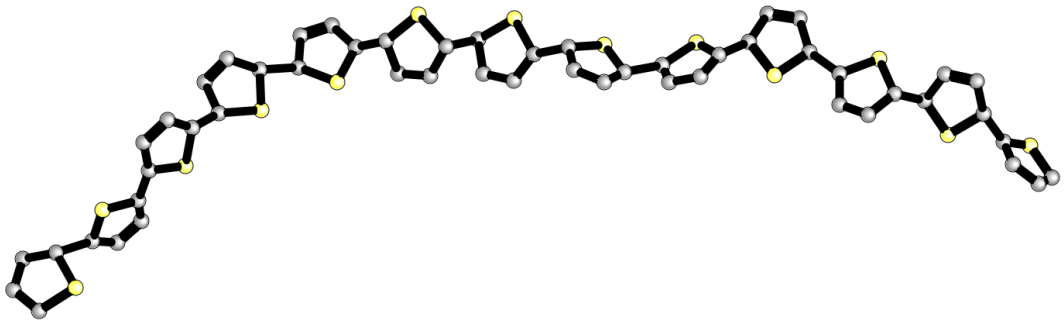

(c) A cartoon of the fully rotated thiophene rings, modelling the coarse-grained chain in an atomistic representation

Figure 6.7: *The rotations required to complete the fine-graining process of the P3HT morphologies. The first rotation flips the thiophene ring into the correct head-to-tail orientation to preserve regioregularity. The second uses the locations of nearby monomers to determine the optimal ring planarity.*

sites in the chain. The second ring was then rotated such that its planarity matched the vector **b**.

3. The planarity of the third ring was determined by **c** - the vector between the second and fourth rings in the chain,

and so on until all of the thiophene rings in the chain had been properly rotated.

This process resulted in an atomistic polythiophene chain with thiophene ring positions and orientations corresponding to the CG MD outputs. An example of

the resultant chain backbone is shown in figure 6.7c. Other works have shown that the solubilising alkyl sidechains affect the charge mobility characteristics only through constraining the self-organisation properties of the backbone itself[45,62,63]. As the final morphology already considered the impact of the sidechains within the MD simulations, they were omitted from consideration for the transfer integral calculations in order to simplify the fine-graining process.

6.4.2 Chain Segments

Calculations of the DoS for P3HT have shown that the orbital density localisation (L), is a segment of around 7 monomers in length[56,64]. It was therefore decided that a hole, present on a particular region of the chain, can be considered as delocalised across the segment, hopping between neighbouring segments as it moves through the morphology. Thus, the fine-grained polythiophene chains were split into segments by considering the chain 'backbone axis vector' between the centres of mass of adjacent thiophene rings with respect to a tolerance angle θ_c. The algorithm for the segmentation of chains is depicted in figure 6.8. The numbered stages depicted are as follows:

1. A chain was selected and the first atom at the end of the chain considered. The vector between the atom and the next bonded thiophene was denoted the backbone axis vector ($\underline{\mathbf{a}}$). Both atoms were added to the current 'segment'.

2. Consideration then moved to the bonded thiophene used to calculate the backbone axis vector. The separation vector to the next bonded thiophene along the chain was calculated ($\underline{\mathbf{b}}$). The angle between both the separation and the

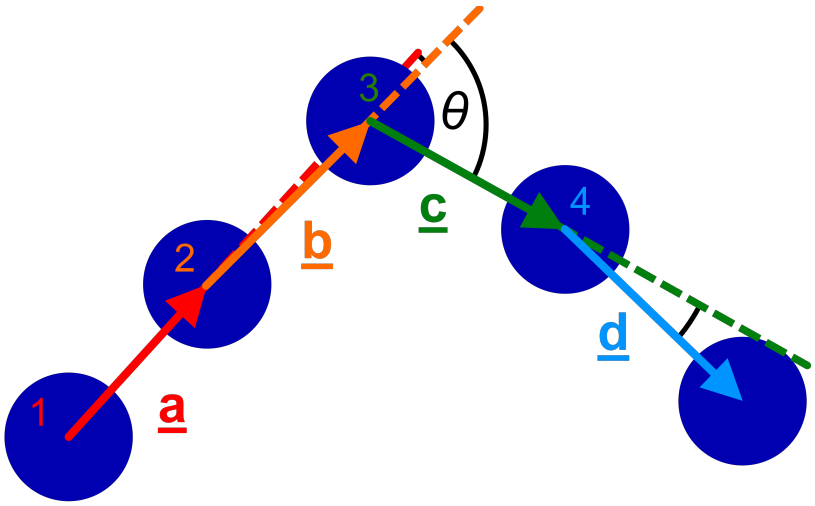

Figure 6.8: *A depiction of the segmentation algorithm used on atomistic polythiophene chains to split them into regions of strong orbital coherence.*

backbone axis vectors was determined using $\underline{\mathbf{a}} \cdot \underline{\mathbf{b}} = |\underline{\mathbf{a}}|\,|\underline{\mathbf{b}}| \cos\theta$. In this case, $\theta < \theta_c$. This suggests that the vector between these two thiophenes was similar enough to the backbone orientation of the chain and so the orbitals were likely to be continuous. This thiophene was therefore added to the current segment, and the new backbone axis vector set to be the calculated separation vector ($\underline{\mathbf{b}}$).

3. Stepping along the chain again, the new separation vector to the next thiophene was calculated ($\underline{\mathbf{c}}$). In this case, $\theta > \theta_c$, therefore backbone conjugation was considered broken, and the segment complete.

4. The next thiophene along the chain then started a new segment and the process repeated until all thiophenes had been considered.

The value of $\theta_c = \pi/6\,\text{rad}$ was selected such that the hole was, on average, delocalised over 7 monomers for the *S-57* sample, as shown in figure 6.9, and was fixed for the calculations on the other morphologies. Note that this method represents an

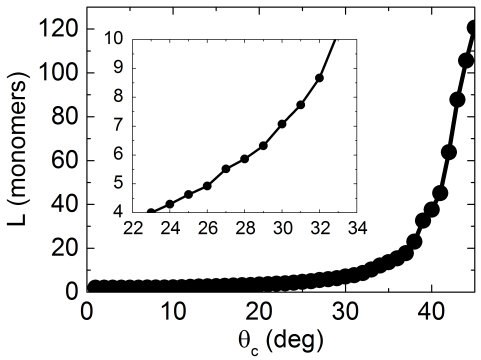

Figure 6.9: *The variation in the number of S-57 monomers in each segment with tolerance angle θ_c.*

approximation as the HOMO wavefunctions were not directly calculated. However, the resultant mean delocalisation was matched to more rigorous calculations[56,65] through this utilisation of θ_c.

6.4.3 Hopping Rate Calculation

The segments were then sorted into pairs of hopping partners - *i.e.* two segments located within $r_{\max} = 20\,\text{Å}$ of each other, taking into account the periodic boundary conditions of the morphology. Note that $r_{\max}$ was set to be significantly larger than the $\bar{d}_{[010]}$ and $\bar{d}_a$ spacings for all morphologies. Quantum Chemical ZINDO/S calculations that determine the molecular orbitals were then performed on each segment individually, as well as all of the hopping partner pairs for the entire morphology, using the ORCA program suite[66,67]. These calculations allowed the electronic coupling transfer integral $\left|J_{ij}\right|$ between segments to be calculated:

$$\left|J_{ij}\right| = \frac{1}{2}\sqrt{\left(E_{\text{HOMO}} - E_{\text{HOMO-1}}\right)^2 - \left(\Delta E_{ij}\right)^2}, \tag{6.4.8}$$

where ($E_{\text{HOMO}} - E_{\text{HOMO-1}}$) denotes the HOMO splitting energy for the dimer containing the two hopping partners and ΔE_{ij} is the difference in HOMO levels between the initial and final sites. Like some other quantum chemical calculations[65], it was found that the DoS was significantly broader than those expected in real devices[23,28,68]. Using HOMO levels directly from the DoS to calculate ΔE_{ij} led to imaginary transfer integrals which made the charge transport simulations unrealistic. Some studies have utilised Koopmans' approximation[69], *i.e.* set $\Delta E_{ij} = 0$[70,71]. While this approximation provides good agreement with DFT results for a variety of systems[72,73], it nonetheless discards relevant information about the energy levels of the segments, which in turn are dependent on the morphologies of interest and argued to be important when determining the mobility[15]. To resolve this issue, an approximation was employed where the ZINDO/S-calculated HOMO levels were mapped onto the experimentally determined DoS, such that the sigma within the distribution (*e.g.* +1 standard deviation from the mean) was retained. This mapping was only used to determine ΔE_{ij}; the HOMO splitting calculation was left unmapped from the simulated molecular orbitals.

An example Gaussian mapping is given in figure 6.10. Both Gaussians exhibit an identical mean (at -7.32 eV), but the standard deviation of values from the mean has been reduced from $\sigma_{\text{unmapped}} = 1.31\,\text{eV}$ to $\sigma_{\text{mapped}} = 70\,\text{meV}$, as determined by experiment[23,28,68].

The transfer integral was then used to determine the rate at which hops were permitted to take place, given by the semiclassical Marcus expression, described in equation 3.3.10[74]. The reorganisation energy, λ_{ij}, was estimated using a model

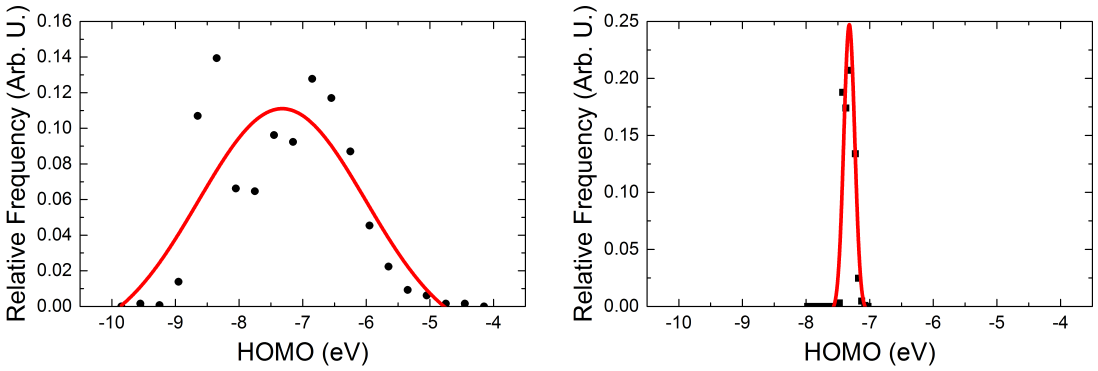

(a) *Unmapped HOMO levels* ***(b)*** *Mapped HOMO levels*

Figure 6.10: *An example of the Gaussian mapping implemented to reduce the standard deviation of HOMO levels determined by ZINDO/S calculations.*

predicted from DFT calculations based on the length of the host segment[75]. Note that because all segment pairs in the morphology with separation $r < r_{\max}$ were considered, variable range hopping[76] was therefore implicitly permitted.

λ_{ij} is a measure of the energy required to polarise and repolarise the molecule as the charge-carrier hops onto and subsequently off the site - effectively forming a polaron in the surrounding molecule. It consists of two contributions: the 'internal' (λ_{int}) and 'external' (λ_{ext}) reorganisation energies, which correspond to the various normal frequency modes of the molecule and the contribution due to the reorientation of the surrounding molecules respectively[77]. λ_{ext} is usually described to be independent of the length of the molecule in question and so for this investigation was kept constant at 0.11 eV[78]. Both DFT and alternative numerical models predict λ_{int} to vary with hole delocalisation segment length[75]. The internal reorganisation energies used in this investigation are shown in figure 6.11a. $\lambda_{ij} = \lambda_{\text{int}} + \lambda_{\text{ext}} \sim 0.25$ eV which is in good agreement with quantum chemical calculations in the literature[79], as well as other MD simulations[43,44].

Figure 6.11b shows an example transfer integral distribution, using the method

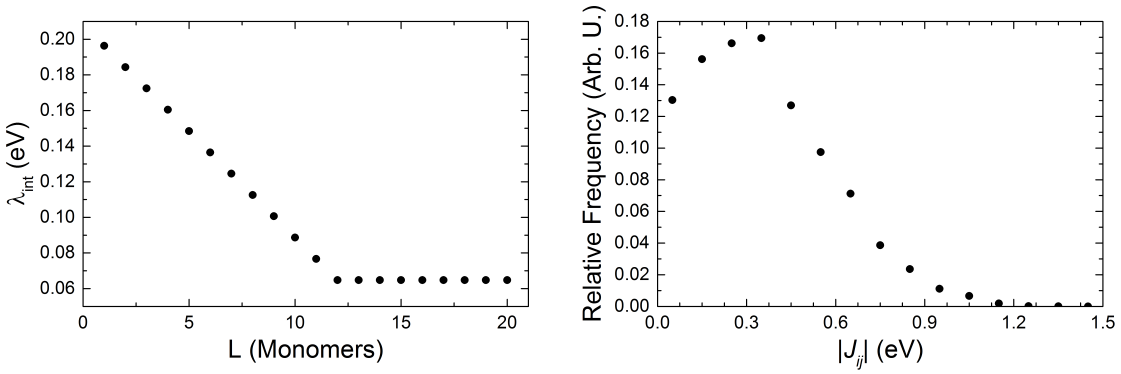

(a) *Internal reorganisation energy as a function of segment length*

(b) *Distribution of Transfer Integrals*

Figure 6.11: *Variation in the internal reorganisation energies, λ_{int}, as a function of segment length, L, as well as an example transfer integrals distribution for the for S-51 morphology with $T_a = 423\,K$.*

described above for the *S-51* morphology annealed at $T_a = 423\,\mathrm{K}$. It is encouraging to note that some quantum chemical calculations report transfer integrals of around 0.35-0.37 eV for $L \sim 5$, after alleviating Koopmans' approximation and directly computing the transfer integral by expanding the molecular orbitals in terms of atomic contributions[79]. This corresponds to the centre of the distribution shown in figure 6.11b.

6.4.4 Molecular Monte Carlo Algorithm

The molecular charge transport simulations consisted of a MC algorithm similar to those described in chapter 3.4, determining the wait time until the next hopping event using the MC equation described in equation 3.4.12, and hopping events described by k_{hop} were considered using Marcus theory. A hole was then injected onto a randomly selected segment within each morphology and permitted to hop through the system for a total time, t. The mean squared displacement ($\langle x^2 \rangle$) was calculated for each value of t and the results averaged over 10,000 carriers, which was sufficient

to obtain an adjusted R-squared value > 0.999. $\langle x^2 \rangle$ was shown to be directly proportional to t, with proportionality corresponding to the 3D diffusion coefficient D. The zero-field hole mobility μ_0 for the morphology was calculated using the Einstein relation:

$$\mu_0 = \frac{qD}{k_B T}, \tag{6.4.9}$$

where q is the elementary charge.

The fine-graining and segmentation processes were treated by single-threaded scripts that typically took several hours to run for each morphology at each annealing temperature and average molecular weight studied. The resultant files contained the positions of each atom within the hopping partner pairs and were input into the ZINDO/S calculations performed using ORCA. Each of these took from 10 seconds to 10 minutes to complete, depending on the complexity of the segments, with more complex hopping pairs requiring multiple runs to obtain converged results. Although each calculation could only be run on a single core, a script was written to treat the simultaneous submission of many calculations, as each morphology contained up to 40,000 combinations of segment pairs, taking several hours to complete. The Monte Carlo charge transport simulations themselves were comparatively fast, with a runtime of generally less than an hour on a single core.

6.5 Morphology Dependence of Charge Transport

6.5.1 Zero-Field Mobility

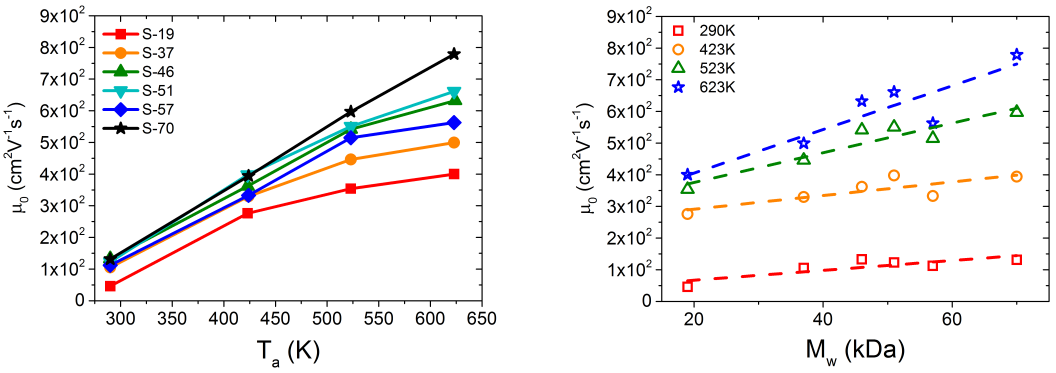

(a) *Annealing temperature dependence*

(b) *Weight-averaged molecular weight dependence*

Figure 6.12: *Zero-field hole mobilities for the samples created for the polymer investigation listed in table 6.1.*

Figure 6.12 shows the simulated mobilities for $F = 0\,\mathrm{V\,m^{-1}}$, μ_0, for the various P3HT samples created for this investigation (table 6.1) as functions of T_a and $\mathrm{M_w}$. Firstly, note that the absolute values of the mobilities recorded here are several orders of magnitude greater than those determined from real devices, where mobilities within the range of 2×10^{-4}-$2\times10^{-3}\,\mathrm{cm^2\,V^{-1}\,s^{-1}}$ are reported for highly regioregular pristine P3HT films at zero to low fields ($\mathrm{F} \simeq 4\times10^{6}\,\mathrm{V\,m^{-1}}$), depending on the processing regime[19,22,23]. However, performing *ab initio* calculations of mobility is challenging, especially for disordered structures[80,81]. For this reason, the remainder of this investigation will focus on the *relative* differences between μ_0 calculated for different sample conditions, and how these compare with experiment.

While the data in figure 6.12 does show some scatter, there is a monotonic trend of increasing μ_0 with both $\mathrm{M_w}$ and T_a. The improvement in μ_0 is shown to saturate

beyond $\sim 450\,\mathrm{K}$ to an extent that depends on M_w, with smaller M_w showing more pronounced saturation. $T_a = 423\,\mathrm{K}$ is a common annealing temperature, for which it has been shown that μ_0 increases by a factor of 2-3 when compared to as-cast films[82,83]. These data agree reasonably well with the predicted improvement in μ_0 by a factor of 3.5 shown here when T_a was increased from 290 K to 423 K.

The mobility is also sensitive to M_w, as increasing M_w from 19-70 kDa increased μ_0 by a factor of 3.2 for unannealed samples and a factor of 2.1 for morphologies annealed at 623 K. Some field-effect mobility measurements on samples of unannealed P3HT have reported that an increase in M_w from 11-51 kDa results in an increase in saturation mobility of around one order of magnitude[84]. Others have demonstrated an increase in field-effect mobility of a factor of ~ 5 over the range $21 \leq M_w < 61\,\mathrm{kDa}$[85]. For transistors annealed at $T_a = 370\,\mathrm{K}$, the mobility increase has been reported as a factor of around 3 for the range $20 \leq M_w < 76\,\mathrm{kDa}$[86]. However, ToF mobility measurements similar to those implemented in this investigation show that the mobility decreases by a factor of 5 as M_w is increased from 26-72 kDa[28]. It is difficult to be exact when comparing the current data to those found in the literature due to the variety of experimental protocols used. However, it is clear that at least the general trend of increasing μ_0 with M_w is reproduced. The order of magnitude increase in μ_0 with increasing M_w is smaller than most reports over similar weight ranges, however this might be expected due to shorter annealing times restricting crystallisation and therefore the mobility samples consisting of longer chains.

Focus now turns to the morphological structure of the P3HT film in order to explain the observed mobility trends in figure 6.12 and indeed those in previous

studies.

6.5.2 Paracrystallinity

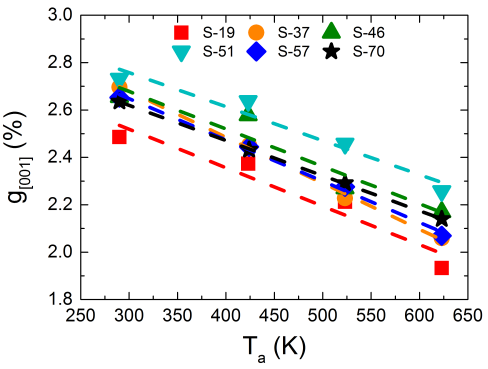

(a) Backbone ([001]) direction

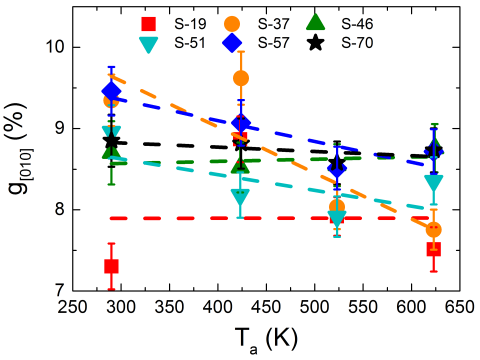

(b) π-stacking ([010]) direction

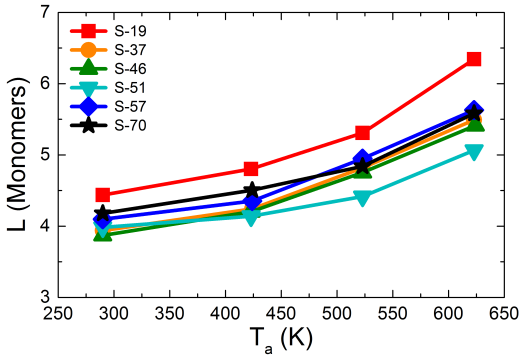

(c) Average segment length

Figure 6.13: *Paracrystallinity measurements and average segment length for the investigated samples as a function of T_a. Note that the highly uniform Gaussian distributions for the along-chain $d_{[001]}$ data results in very small error bars that are not visible on these axes.*

The results of the paracrystallinity measurements for all the investigated samples are shown in figure 6.13. Along the polymer backbones, there is reduced disorder as the annealing temperature is increased, characterised by the narrowing of the $d_{[001]}$ distribution. Regular lattice spacings in this direction result in strong coherence between adjoining chain segments, enhancing hole mobility along the intra-chain direction. This additionally manifests as an increase in the average segment length,

L (figure 6.13c). A combination of these factors could explain the observed trend in μ_0 as a function of T_a in figure 6.12, however, figure 6.13a does not clearly show a monotonic decrease in $g_{[001]}$ as a function of increasing M_w.

The $g_{[010]}$ data shown in figure 6.13b are within $7\% \leq g_{[010]} < 10\%$, show a slight reduction with increasing T_a, and no clear trend with M_w. This is in agreement with sources in the literature that suggest that P3HT π-stacking disorder is high and mostly independent of the degree of polymerisation beyond 100 monomer units corresponding to $M_w = 16\,\text{kDa}$[15]. The trend is also characteristic of x-ray diffraction data for semicrystalline polymer films[44,87] such as PBTTT[88,89]. GIWAXS measurements on thick ($\sim 100\,\text{nm}$) films annealed at 413 K have shown that P3HT generally exhibits a slightly more ordered crystal structure resulting in a paracrystallinity $\sim 5\%$[90], suggesting that the morphologies used in this investigation are slightly more disordered than equivalent experiments, but still lie in the semicrystalline regime[87,88].

Although there are correlations between $g_{[001]}$ and T_a (and hence μ_0), there is no clear dependence of $g_{[001]}$ or $g_{[010]}$ on M_w, even though μ_0 has a strong dependence on M_w. This indicates that not all of the mobility trends observed in figure 6.12 can be solely explained by the paracrystallinity along either axis, in agreement with morphological studies that have suggested that the π-stacking paracrystallinity does not affect the mobility[15,43].

6.5.3 Crystal Proportion

The $d_{[010]}$ distributions shown in figure 6.6b also allow for an estimation of the volume occupied by the crystal regions. A 'crystal cut-off' (d_{cut}) was defined for the morphology as the value of $d_{[010]}$ at which the bimodal distribution, P_d, was at a minimum. This value is around 6 Å for all morphologies considered. Thiophene spacings $d_{[010]} < d_{\text{cut}}$ were considered as belonging to a crystal, whereas thiophenes with $d_{[010]} > d_{\text{cut}}$ belonged to the amorphous region of the morphology. The crystal proportion, γ could then be defined as the integral of the $d_{[010]}$ distribution up to d_{cut} as a fraction of the integral of the whole distribution.

Figure 6.14 shows γ as functions of both T_a and M_w. The absolute values of γ are around 0.2 lower than those reported from melting enthalpy calculations[25], again likely because those devices were annealed for a much longer period than the current simulations. In general, figure 6.14 shows that γ increases linearly with annealing temperature as expected. By contrast, γ shows no clear dependence on M_w.

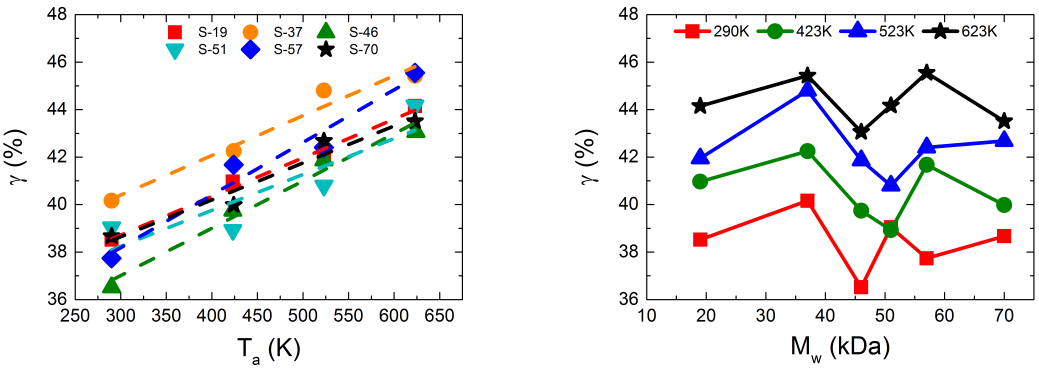

(a) *Annealing temperature dependence*

(b) *Weight-averaged molecular weight dependence*

Figure 6.14: *Variation in π-stacking crystal proportion (γ) for the investigated samples as functions of T_a and M_w. Linear fits are also depicted for the temperature response.*

Differential scanning calorimetry (DSC) measurements of the enthalpy of fusion have shown that the expected degree of crystallinity remains approximately constant for $17 \leq M_w < 93\,kDa$ at room temperature[91]. Over a smaller molecular weight range, the melting enthalpies from DSC thermograms of deuterated P3HT show an increase in the volume occupied by crystals from 4.5% at $M_w = 2.6\,kDa$ to 18% at $M_w = 27\,kDa$[26]. Perhaps then it is unsurprising that, for the data in this investigation, γ varies by a maximum of 5% for unannealed devices and even less for films annealed at increased T_a.

As with the paracrystallinity measurements, increasing T_a has been found to be correlated to an increased crystal proportion in the film, which may partly explain the observed increase in μ_0 with respect to T_a. However, there is no clear trend relating γ to M_w for the examined conditions, even though μ_0 clearly increases with M_w.

6.5.4 Tie Chains

It has been argued that high mobility is not only caused by the quantity of well-ordered crystals in the morphology, but also by the presence of 'tie-chains' that form efficient connections between them[15]. To explore the impact of tie chains in the current data, figure 6.15 shows the number of crystals that each chain in the same participates in (ζ) as a function of the degree of polymerisation, D_p. Increasing M_w increases the likelihood that individual chains will participate in more crystals. Furthermore, this trend is largely unaffected by the annealing temperature. Since the M_w dependence of μ_0 has not been satisfactorily explained by the crystalline

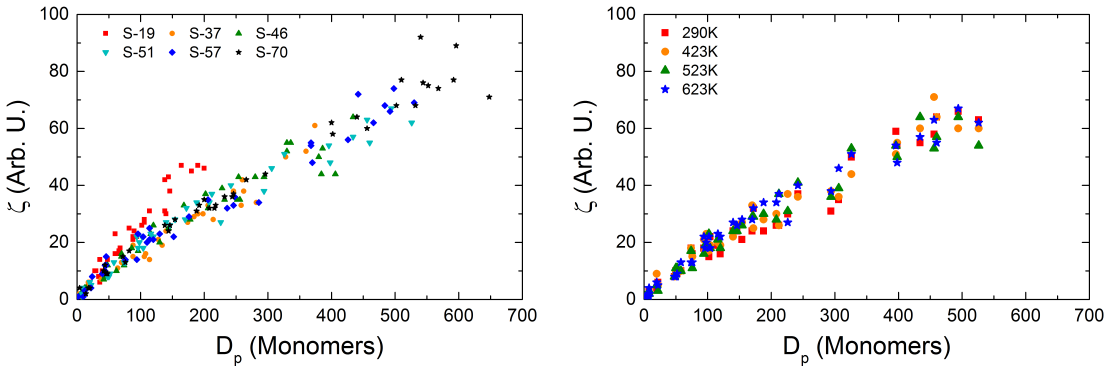

(a) *Varying M_w annealed at $T_a = 623\,K$* ***(b)*** *Varying T_a for the S-51 samples*

Figure 6.15: *The functional relationship between the number of participant crystals for each chain in the single morphologies, ζ, and its degree of polymerisation D_p.*

order or crystallite size, it is instead likely due to the population of long polymer chains linking together the many crystallites - the length of which are of course independent of the temperature of the system. This is in agreement with prior studies by Noriega *et al*[15]. Implicit in this argument is that the non-crystalline regions of the film are divided into tie-chains which are members of many crystals and increase mobility, and other shorter chains that are members of only a few crystals and do not. This therefore suggests that semi-crystalline conjugated polymer mobility can be optimised by increasing the number of tie-chains in the non-crystalline phase.

To test this hypothesis, additional films were generated, which included an increased population of tie-chains in an otherwise small molecular sample. These were formed by randomly substituting a number of chains from the *S-70* sample into the *S-19* sample, ensuring that each morphology still consisted of 40 chains after mixing. This process was completed multiple times so that all the considered mixed samples had approximately the same polydispersity index as each other (around 2.3), and comparable molecular weights to the single-distribution samples described in table

Name	M-5	M-10	M-20	M-50
***S-19*:*S-70* Ratio**	1:19	1:9	1:4	1:1
Effective M_w (kDa)	37.3	45.7	51.2	57.0
Effective M_n (kDa)	15.9	18.8	21.8	26.4
PDI	2.3	2.4	2.3	2.2

Table 6.2: *The mixed P3HT samples considered in this investigation, showing the S-19:S-70 ratio, effective weight- and number-averaged molecular weights (M_w, M_n) and polydispersity indices (PDI). The naming convention is "M-⟨Proportion of S-70⟩", where the 'M' denotes that a mixture of S-19 and S-70 chains are present.*

6.1. The resultant mixed samples are shown in table 6.2.

Figure 6.16 shows that the population of high-ζ tie-chains has been successfully increased by adding a small number of chains from the *S-70* morphology to the *S-19* sample. The tie-chains in the mixed morphologies are generally longer and belong to more crystals than those within the single-distribution morphologies of an equivalent M_w. As with the single-distribution samples, there is no T_a dependence, suggesting that the effect of the added chains is largely to join crystals together rather than modify the crystal properties.

The comparison between the mobilities of the resultant mixed morphologies and single-distributions of equivalent M_w is shown in figure 6.17. It seems clear that incorporating long chains into the system affects the mobility, as there is an increase in μ_0 as the proportion of *S-70* chains in the mixture increases. The noise in the simulation is significant enough that it is not possible to reliably conclude that mixed morphologies result in *better* mobilities than a single-distribution sample of equivalent M_w, however the data show that it is possible to force a low M_w sample

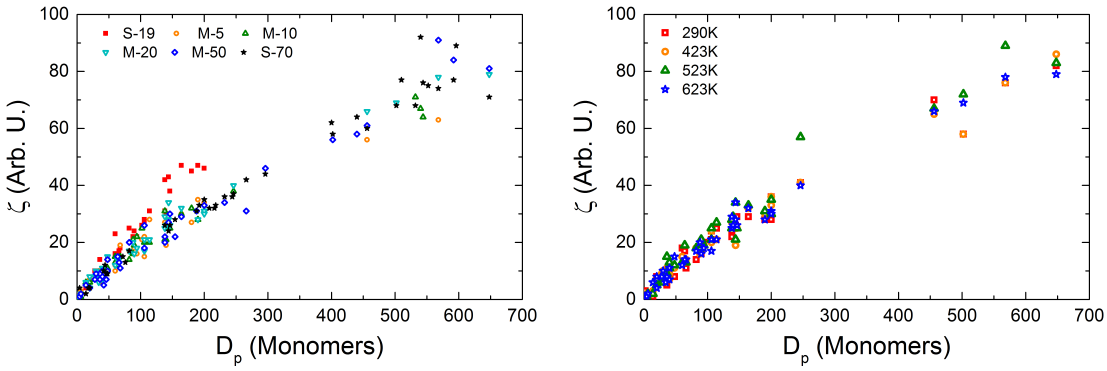

(a) *Varying M_w annealed at $T_a = 623\,K$* ***(b)*** *Varying T_a for the M-20 samples*

Figure 6.16: *The functional relationship between the number of participant crystals for each chain in the mixed morphologies, ζ and its degree of polymerisation D_p.*

to behave like a high M_w sample through the addition of longer chains which act as tie-chains within the morphology. The added chains require a larger degree of polymerisation and a greater ζ than the longest chains already present in the single-distribution of equivalent M_w in order to achieve similar mobility characteristics. This suggests that increasing the polydispersity of chain lengths within a sample is not detrimental to the performance of the active layer. While tie-chains have been introduced here by engineering the distribution of M_w, we note that similar effects could be achieved in conjugated polymers with increased persistence length and rigidity[92].

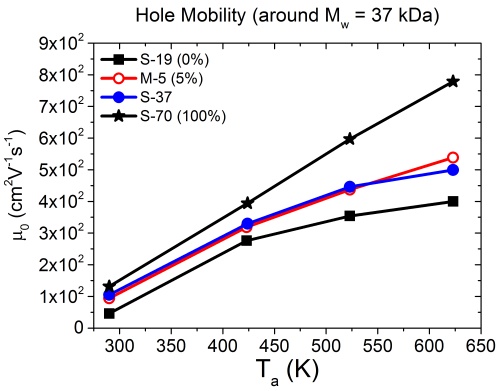

(a) M-5 (effective $M_w = 37\,kDa$)

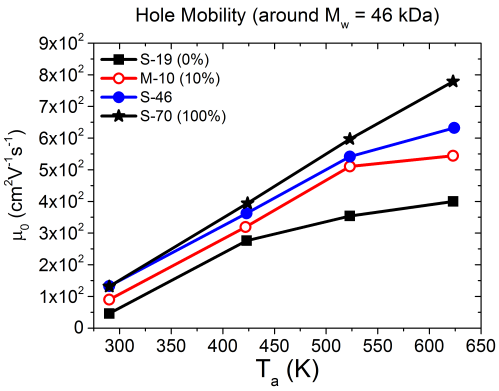

(b) M-10 (effective $M_w = 46\,kDa$)

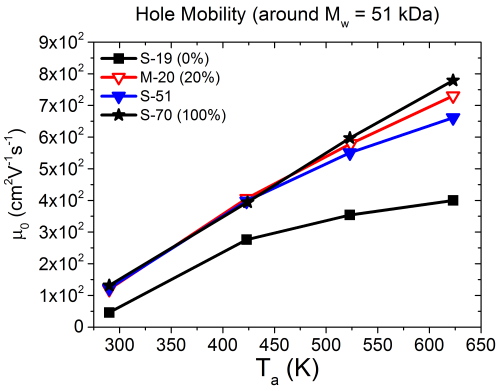

(c) M-20 (effective $M_w = 51\,kDa$)

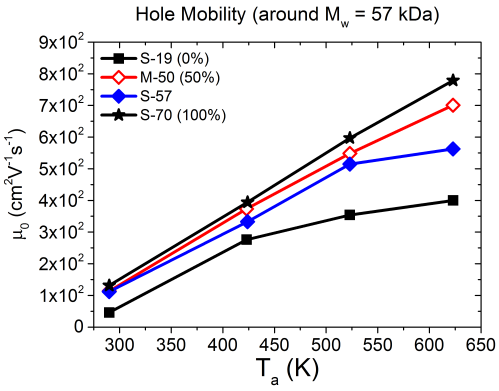

(d) M-50 (effective $M_w = 57\,kDa$)

Figure 6.17: *Comparisons of the hole mobilities for mixed (red, closed symbols) and single samples of comparable molecular weights (blue, open symbols) as a function of T_a.*

6.6 Conclusions

Coarse-grained molecular dynamics simulations were implemented to create samples of P3HT chains with experimentally realistic molecular weights (selected by a new length distribution), polydispersities and film densities. The resultant thin film morphologies were subjected to a variety of annealing protocols without assuming any initial configurations for the chains. A fine-graining procedure was then employed to return the morphologies to the atomistic representation such that the semi-empirical ZINDO/S method could be used to determine the charge-transport characteristics for each sample. Hole mobilities at zero field were calculated and showed that the mobility increased when either the annealing temperature or the weight-averaged molecular weight of the sample were increased, in accordance with experimental results. The crystal structure for each morphology was then analysed to help explain these mobility trends.

Both the along-chain crystalline order and the volume proportion of crystals within the morphology were shown to increase with increasing annealing temperature, suggesting that, as devices were annealed at higher temperatures, more and better ordered crystals were produced, providing some benefit to the hole mobility. The π-stacking crystalline order was shown to increase slightly with increasing temperature indicating that, although well-ordered π-stacking crystals can contribute slightly to the observed mobility dependence on temperature, it is less important than the other crystal properties, as determined by some experimental investigations.

The molecular weight dependence of the mobility was less clear. No obvious trend

existed between the along-chain, π-stacking paracrystallinities or crystal proportion, suggesting that the crystallinity and crystal order are not the main precursors to high mobility within the thin film as the molecular weight is increased. Instead it was found that, as the molecular weight increases, the average number of crystals that each chain belongs to also increases, resulting in better connected crystals. It is therefore predicted that the bulk, long-range mobility in semi-crystalline polymers is limited below the short-range crystal mobilities, by the availability of tie-chains within the system. This, in turn, suggests that the non-crystalline sections of a morphology perform a useful function, although not all of these regions are useful tie-chains.

As an example to show how the utility of the non-crystalline parts of a morphology can be improved, samples were engineered that included a proportion of longer chains, acting as tie-chains, to an otherwise low-mobility morphology. It was shown that the resultant zero-field hole mobility could be improved and was indeed comparable to a single-distribution sample of the same molecular weight, as more tie-chains were added. The added chains were shown to have enhanced crystal connectivity, supporting the conclusion that tie-chains are the main contributor to the molecular weight dependence of the mobility, simultaneously suggesting that a high polydispersity is not necessarily detrimental to charge transport within the active layer.

While these conclusions were for a test system of P3HT, the processes involved in this investigation are not molecule specific and so they could still be generally true for all semi-crystalline polymers.

References

[1] H. Sirringhaus. "25th Anniversary Article: Organic Field-Effect Transistors: The Path Beyond Amorphous Silicon." *Adv. Mater.*, **26**, 1319–1335, 2014.

[2] A. Tsumura, H. Koezuka, and T. Ando. "Macromolecular Electronic Device: Field-Effect Transistor with a Polythiophene Thin Film." *Appl. Phys. Letts.*, **49**, 1210–1212, 1986.

[3] J. H. Burroughes, D. D. C. Bradley, A. R. Brown, R. N. Marks, K. Mackay, R. H. Friend, P. L. Burns, and Holmes A. B. "Light-Emitting Diodes Based on Conjugated Polymers." *Nature Lett.*, **347**, 539–541, 1990.

[4] R. H. Friend, R. W. Gymer, A. B. Holmes, J. H. Burroughes, R. N. Marks, C. Taliani, D. D. C. Bradley, D. A. Dos Santos, J. L. Brédas, M. Lögdlund, and W. R. Salaneck. "Electroluminescence in Conjugated Polymers." *Nature*, **397**, 121–128, 1999.

[5] N. S. Sariciftci, L. Smilowitz, A. J. Heeger, and F. Wudl. "Photoinduced Electron Transfer from a Conducting Polymer to Buckminsterfullerene." *Science*, **258**, 1474–1476, 1992.

[6] A. Abrusci, S. D. Stranks, P. Docampo, Yip H.-L., A. K.-Y. Jen, and H. J. Snaith. "High-Performance Perovskite-Polymer Hybrid Solar Cells via Electronic Coupling with Fullerene Monolayers." *Nano Lett.*, **13**, 3124–3128, 2013.

[7] A. Facchetti. "Polymer Donor-Polymer Acceptor (All-Polymer) Solar Cells." *Mater. Today*, **16**, 123–132, 2013.

[8] S. Günes, H. Neugebauer, and N. S. Sariciftci. "Conjugated Polymer-Based Organic Solar Cells." *Chem. Rev.*, **107**, 1324–1338, 2007.

[9] H. Bronstein, Z. Chen, R. S. Ashraf, W. Zhang, J. Du, J. R. Durrant, P. S. Tuladhar, K. Song, S. E. Watkins, Y. Geerts, M. M. Wienk, R. A. J. Janssen, T. Anthopoulos, H. Sirringhaus, M. Heeney, and I. McCulloch. "Thieno[3,2-b]thiophene-Diketopyrrolopyrrole-Containing Polymers for High-Performance Organic Field-Effect Transistors and Organic Photovoltaic Devices." *J. Am. Chem. Soc.*, **133**, 3272–3275, 2011.

[10] I. McCulloch, M. Heeney, C. Bailey, K. Genevicius, I. MacDonald, M. Shkunov, D. Sparrowe, S. Tierney, R. Wagner, W. Zhang, M. L. Chabinyc, R. J. Kline, M. D. McGehee, and M. F. Toney. "Liquid-Crystalline Semiconducting Polymers with High Charge-Carrier Mobility." *Nature Mater.*, **5**, 328–333, 2006.

[11] H. N. Tsao, D. M. Cho, I. Park, M. R. Hansen, A. Mavrinskiy, D. Y. Yoon, R. Graf, W. Pisula, H. W. Spiess, and K. Müllen. "Ultrahigh Mobility in Polymer Field-Effect Transistors by Design." *J. Am. Chem. Soc.*, **133**, 2605–2612, 2011.

[12] H. Sirringhaus, N. Tessler, and R. H. Friend. "Integrated Optoelectronic Devices Based on Conjugated Polymers." *Science*, **280**, 1741–1744, 1998.

[13] C. Scharsich, R. H. Lohwasser, M. Sommer, U. Asawapirom, U. Scherf, M. Thelakkat, D. Neher, and A. Köhler. "Control of Aggregate Formation in Poly(3-hexylthiophene) by Solvent, Molecular Weight, and Synthetic Method." *J. Polym. Sci. Part B Polym. Phys.*, **50**, 442–453, 2011.

[14] G. Li, V. Shrotriya, J. Huang, Y. Yao, T. Moriarty, K. Emery, and Y. Yang. "High-Efficiency Solution Processable Polymer Photovoltaic Cells by Self-Organization of Polymer Blends." *Nature Mater.*, **4**, 864–868, 2005.

[15] R. Noriega, J. Rivnay, K. Vandewal, F. P. V. Koch, N. Stingelin, P. Smith, M. F. Toney, and A. Salleo. "A General Relationship Between Disorder, Aggregation and Charge Transport in Conjugated Polymers." *Nature Mater.*, **12**, 1038–1044, 2013.

[16] M. M. Voigt, A. Guite, D.-Y. Chung, R. U. A. Khan, A. J. Campbell, D. D. C. Bradley, F. Meng, J. H. G. Steinke, S. Tierney, I. McCulloch, H. Penxten, L. Lutsen, O. Douheret, J. Manca, U. Brokmann, K. Sönnichsen, D. Hülsenberg, W. Bock, C. Barron, N. Blanckaert, S. Springer, J. Grupp, and A. Mosley. "Polymer Field-Effect Transistors Fabricated by the Sequential Gravure Printing of Polythiophene, Two Insulator Layers and a Metal Ink Gate." *Adv. Funct. Mater.*, **20**, 239–246, 2010.

[17] S. Fabiano, Z. Chen, S. Vahedi, A. Facchetti, B. Pignataro, and M. A. Loi. "Role of Photoactive Layer Morphology in High Fill Factor All-Polymer Bulk Heterojunction Solar Cells." *J. Mater. Chem.*, **21**, 5891–5896, 2011.

[18] H. Sirringhaus, P. J. Brown, R. H. Friend, M. M. Nielsen, K. Bechgaard, B. M. W. Langeveld-Voss, A. J. H. Spiering, R. A. J. Janssen, E. W. Meijer, P. Herwig, and D. M. de Leeuw. "Two-Dimensional Charge Transport in Self-Organized, High-Mobility Conjugated Polymers." *Nature*, **401**, 685–688, 1999.

[19] Y. Kim, S. Cook, S. M. Tuladhar, S. A. Choulis, J. Nelson, J. R. Durrant, D. D. C. Bradley, M. Giles, I. McCulloch, C.-S. Ha, and M. Ree. "A Strong

Regioregularity Effect in Self-Organising Conjugated Polymer Films and High-Efficiency Polythiophene:Fullerene Solar Cells." *Nature Mater.*, **5**, 197–203, 2006.

[20] M. Surin, P. Leclère, R. Lazzaroni, J. D. Yuen, G. Wang, D. Moses, A. J. Heeger, S. Cho, and K. Lee. "Relationship Between the Microscopic Morphology and the Charge Transport Properties in Poly(3-hexylthiophene) Field-Effect Transistors." *J. Appl. Phys.*, **100**, 033712:1–033712:6, 2006.

[21] D. H. Kim, Y. D. Park, Y. Jang, S. Kim, and K. Cho. "Solvent Vapor-Induced Nanowire Formation in Poly(3-hexylthiophene) Thin Films." *Macromol. Rapid Commun.*, **26**, 834–839, 2005.

[22] S. S. Pandey, W. Takashima, S. Nagamatsu, T. Endo, M. Rikukawa, and K. Kaneto. "Regioregularity vs Regiorandomness: Effect on Photocarrier Transport in Poly(3-hexylthiophene)." *Jpn. J. Appl. Phys.*, **39**, L94–L97, 2000.

[23] R. Mauer, M. Kastler, and F. Laquai. "The Impact of Polymer Regioregularity on Charge Transport and Efficiency of P3HT:PCBM Photovoltaic Devices." *Adv. Funct. Mater.*, **20**, 2085–2092, 2010.

[24] A. Zen, J. Pflaum, S. Hirschmann, W. Zhuang, F. Jaiser, U. Asawapriom, J. P. Rabe, U. Scherf, and D. Neher. "Effect of Molecular Weight and Annealing of Poly(3-hexylthiophene)s on the Performance of Organic Field-Effect Transistors." *Adv. Funct. Mater.*, **14**, 757–764, 2004.

[25] P. Kohn, S. Huettner, H. Komber, V. Senkovskyy, R. Tkachov, A. Kiriy, R. H. Friend, U. Steiner, W. T. S. Huck, J.-U. Sommer, and M. Sommer. "On the Role of Single Regiodefects and Polydispersity in Regioregular Poly(3-hexylthiophene): Defect Distribution, Synthesis of Defect-Free Chains, and a Simple Model for the Determination of Crystallinity." *J. Am. Chem. Soc.*, **134**, 4790–4805, 2012.

[26] A. Zen, M. Saphiannikova, D. Neher, J. Grenzer, S. Grigorian, U. Pietsch, U. Asawapirom, S. Janietz, U. Scherf, I. Lieberwirth, and G. Wegner. "Effect of Molecular Weight on the Structure and Crystallinity of Poly(3-hexylthiophene)." *Macromolecules*, **39**, 2162–2171, 2006.

[27] P. Schilinsky, U. Asawapirom, U. Scherf, M. Biele, and C. J. Brabec. "Influence of the Molecular Weight of Poly(3-hexylthiophene) on the Performance of Bulk Heterojunction Solar Cells." *Chem. Mater.*, **17**, 2175–2180, 2005.

[28] A. M. Ballantyne, L. Chen, J. Dane, T. Hammant, F. M. Braun, M. Heeney, W. Duffy, I. McCulloch, D. D. C. Bradley, and J. Nelson. "The Effect of Poly(3-hexylthiophene) Molecular Weight on Charge Transport and the Performance of Polymer:Fullerene Solar Cells." *Adv. Funct. Mater.*, **18**, 2373–2380, 2008.

[29] D. L. Cheung, D. P. McMahon, and A. Troisi. "Computational Study of the Structure and Charge-Transfer Parameters in Low-Molecular-Mass P3HT." *J. Phys. Chem. B*, **113**, 9393–9401, 2009.

[30] F. P. V. Koch, J. Rivnay, S. Foster, C. Müller, J. M. Downing, E. Buchaca-Domingo, P. Westacott, L. Yu, M. Yuan, M. Baklar, Z. Fei, C. Luscombe, M. A. McLachlan, M. Heeney, G. Rumbles, C. Silva, A. Salleo, J. Nelson, P. Smith, and N. Stingelin. "The Impact of Molecular Weight on Microstructure and Charge Transport in Semicrystalline Polymer Semiconductors - poly(3-hexylthiophene), a Model Study." *Prog. Polym. Sci.*, **38**, 1978–1989, 2013.

[31] M. Brinkmann and P. Rannou. "Molecular Weight Dependence of Chain Packing and Semicrystalline Structure in Oriented Films of Regioregular Poly(3-hexylthiophene) Revealed by High-Resolution Transmission Electron Microscopy." *Macromolecules*, **42**, 1125–1130, 2009.

[32] P. Peumans, S. Uchida, and S. R. Forrest. "Efficient Bulk Heterojunction Photovoltaic Cells Using Small-Molecular-Weight Organic Thin Films." *Nature*, **425**, 158–162, 2003.

[33] I. C. Henderson and N. Clarke. "On Modelling Surface Directed Spinodal Decomposition." *Macromol. Theory Simul.*, **14**, 435–443, 2005.

[34] K. Do, D. M. Huang, R. Faller, and A. J. Moulé. "A Comparative MD Study of the Local Structure of Polymer Semiconductors P3HT and PBTTT." *Phys. Chem. Chem. Phys.*, **12**, 14735–14739, 2010.

[35] J.-M. Y. Carrillo, R. Kumar, M. Goswami, B. G. Sumpter, and W. M. Brown. "New Insights into the Dynamics and Morphology of P3HT:PCBM Active Layers in Bulk Heterojunctions." *Phys. Chem. Chem. Phys.*, **15**, 17873–17882, 2013.

[36] T. T. To and S. Adams. "Modelling of P3HT:PCBM Interface Using Coarse-Grained Forcefield Derived from Accurate Atomistic Forcefield." *Phys. Chem. Chem. Phys.*, **16**, 4653–4663, 2014.

[37] D. M. Huang, R. Faller, K. Do, and A. J. Moulé. "Coarse-Grained Computer Simulations of Polymer/Fullerene Bulk Heterojunctions for Organic Photovoltaic Applications." *J. Chem. Theory Comput.*, **6**, 526–537, 2010.

[38] C.-K. Lee, C.-W. Pao, and C.-W. Chu. "Multiscale Molecular Simulations of the Nanoscale Morphologies of P3HT:PCBM Blends for Bulk Heterojunction Organic Photovoltaic Cells." *Energy Environ. Sci.*, **4**, 4124–4132, 2011.

[39] K. N. Schwarz, T. W. Kee, and D. M. Huang. "Coarse-Grained Simulations of the Solution-Phase Self-Assembly of poly(3-hexylthiophene) Nanostructures." *Nanoscale*, **5**, 2017–2027, 2013.

[40] D. M. Huang. "Computational Study of P3HT/C_{60}-Fullerene Miscibility." *Aust. J. Chem.*, **67**, 585–591, 2014.

[41] H. S. Marsh, E. Jankowski, and A. Jayaraman. "Controlling the Morphology of Model Conjugated Thiophene Oligomers through Alkyl Side Chain Length, Placement, and Interactions." *Macromolecules*, **47**, 2736–2747, 2014.

[42] E. Jankowski, H. S. Marsh, and A. Jayaraman. "Computationally Linking Molecular Features of Conjugated Polymers and Fullerene Derivatives to Bulk Heterojunction Morphology." *Macromolecules*, **46**, 5775–5785, 2013.

[43] M. Schrader, R. Fitzner, M. Hein, C. Elschner, B. Baumeier, K. Leo, M. Riede, P. Bäuerle, and D. Andrienko. "Comparitive Study of Microscopic Charge Dynamics in Crystalline Acceptor-Substituted Oligothiophenes." *J. Am. Chem. Soc.*, **134**, 6052–6056, 2012.

[44] C. Poelking and D. Andrienko. "Effect of Polymorphism, Regioregularity and Paracrystallinity on Charge Transport in Poly(3-hexylthiophene) [P3HT] Nanofibers." *Macromolecules*, **46**, 8941–8956, 2013.

[45] N. R. Tummala, C. Risko, C. Bruner, R. H. Dauskardt, and J.-L. Brédas. "Entanglements in P3HT and Their Influence on Thin-Film Mechanical Properties: Insights from Molecular Dynamics Simulations." *J. Polym. Sci. Part B Polym. Phys.*, **53**, 934–942, 2015.

[46] G. H. Lathe and C. R. Ruthven. "The Separation of Substances on the Basis of their Molecular Weights, Using Columns of Starch and Water." *Biochem. J.*, **60**, 34, 1955.

[47] S. Holdcroft. "Determination of Molecular Weights and Mark-Houwink Constants for Soluble Electronically Conducting Polymers." *J. Polym. Sci. Part B Polym. Phys.*, **29**, 1585–1588, 1991.

[48] M. Rogošić, H. J. Mencer, and Z. Gomzi. "Polydispersity Index and Molecular Weight Distributions of Polymers." *Eur. Polym. J.*, **32**, 1337–1344, 1996.

[49] M. Trznadel, A. Pron, M. Zagorska, R. Chrzaszcz, and J. Pielichowski. "Effect of Molecular Weight on Spectroscopic and Spectroelectrochemical Properties of Regioregular Poly(3-hexylthiophene)." *Macromolecules*, **31**, 5051–5058, 1998.

[50] R. Miyakoshi, A. Yokoyama, and T. Yokozawa. "Synthesis of Poly(3-hexylthiophene) with a Narrower Polydispersity." *Macromol. Rapid Commun.*, **25**, 1663–1666, 2004.

[51] Sigma-Aldrich. "Poly(3-hexylthiphene-2,5-diyl).", 2015. [Online; Accessed 01-oct-2015].

[52] W. Shinoda, M. Shiga, and M. Mikami. "Rapid Estimation of Elastic Constants by Molecular Dynamics Simulation Under Constant Stress." *Phys. Rev. B*, **69**, 134103:1–134103:8, 2004.

[53] S. J. Plimpton. "Fast Parallel Algorithms for Short-Range Molecular Dynamics." *J. Comput. Phys.*, **117**, 1–19, 1995.

[54] I. T. Todorov, W. Smith, K. Trachenko, and M. T. Dove. "DL_POLY_3 New Dimension in Molecular Dynamics Simulations via Massive Parallelism." *J. Mater. Chem.*, **16**, 1911–1918, 2006.

[55] T. J. Prosa, M. J. Winokur, J. Moulton, P. Smith, and A. J. Heeger. "X-ray Structural Studies of poly(3-alkylthiophenes): an Example of an Inverse Comb." *Macromolecules*, **25**, 4364–4372, 1992.

[56] D. P. McMahon, D. L. Cheung, L. Goris, J. Dacuña, A. Salleo, and A. Troisi. "Relation between Microstructure and Charge Transport in Polymers of Different Regioregularity." *J. Phys. Chem. C*, **115**, 19386–19393, 2011.

[57] Z. Wu, A. Petzold, T. Henze, T. Thurn-Albrecht, R. H. Lohwasser, M. Sommer, and M. Thelakkat. "Temperature and Molecular Weight Dependent Hierarchical Equilibrium Structures in Semiconducting Poly(3-hexylthiophene)." *Macromolecules*, **43**, 4646–4653, 2010.

[58] A. M. Hindeleh and R. Hosemann. "Paracrystals Representing the Physical State of Matter." *J. Phys. C: Solid State Phys.*, **21**, 4155–4170, 1988.

[59] M. Shin, H. Kim, J. Park, S. Nam, K. Heo, M. Ree, C.-S. Ha, and Y. Kim. "Abrupt Morphology Change upon Thermal Annealing in Poly(3-hexylthiophene)/Soluble Fullerene Blend Films for Polymer Solar Cells." *Adv. Mater.*, **20**, 748–754, 2010.

[60] T. Erb, U. Zhokhavets, G. Gobsch, S. Raleva, B. Stühn, P. Schilinsky, C. Waldauf, and C. J. Brabec. "Correlation Between Structural and Optical Properties of Composite Polymer/Fullerene Films for Organic Solar Cells." *Adv. Mater.*, **15**, 1193–1196, 2005.

[61] M.-Y. Chiu, U-.S. Jeng, C.-H. Su, K. S. Liang, and K.-H. Wei. "Simultaneous Use of Small- and Wide-Angle X-ray Techniques to Analyze Nanometerscale Phase Separation in Polymer Heterojunction Solar Cells." *Adv. Mater.*, **20**, 2573–2578, 2008.

[62] S. B. Darling and M. Sternberg. "Importance of Side Chains and Backbone Length in Defect Modeling of Poly(3-alkylthiophenes)." *J. Phys. Chem. B*, **113**, 6215–6218, 2009.

[63] A. Babel and S. A. Jenekhe. "Alkyl Chain Length Dependence of the Field-Effect Carrier Mobility in Regioregular poly(3-alkylthiophene)s." *Synt. Met.*, **148**, 169–173, 2005.

[64] D. H. K. Murthy, M. Gao, M. J. W. Vermeulen, L. D. A. Siebbeles, and T. J. Savenije. "Mechanism of Mobile Charge Carrier Generation in Blends of Conjugated Polymers and Fullerenes: Significance of Charge Delocalisation and Excess Free Energy." *J. Phys. Chem. C*, **116**, 9214–9220, 2012.

[65] N. Vukmirovic and L. W. Wang. "Electronic Structure of Disordered Conjugated Polymers: Polythiophenes." *J. Phys. Chem. B*, **113**, 409–415, 2009.

[66] J. Ridley and M. Zerner. "An Intermediate Neglect of Differential Overlap Technique for Spectroscopy: Pyrrole and the Azines." *Theoret. Chim. Acta*, **32**, 111–134, 1973.

[67] F. Neese. "The ORCA Program System." *WIREs Comput. Mol. Sci.*, **2**, 73–78, 2011.

[68] A. J. Mozer and N. S. Sariciftci. "Negative Electric Field Dependence of Charge Carrier Drift Mobility in Conjugated, Semiconducting Polymers." *Chem. Phys. Lett.*, **389**, 438–442, 2004.

[69] T. Koopmans. "Über die Zuordnung von Wellenfunktionen und Eigenwerten zu den Einzelnen Elektronen Eines Atoms." *Physica*, **1**, 104–113, 1934.

[70] V. Coropceanu, J. Cornil, A. Demetrio, F. da Silva, Y. Olivier, R. Silbey, and J-L. Brédas. "Charge Transport in Organic Semiconductors." *Chem. Rev.*, **107**, 926–952, 2007.

[71] Y.-K. Lan and C.-I. Huang. "A Theoretical Study of the Charge Transfer Behaviour of the Highly Regioregular Poly-3-hexylthiophene in the Ordered State." *J. Phys. Chem. B*, **47**, 14857–14862, 2008.

[72] H.-Y. Chen and I. Chao. "Effect of Perfluorination on the Charge-Transport Properties of Organic Semiconductors: Density Functional Theory Study of Perfluorinated Pentacene and Sexithiophene." *Chem. Phys. Lett.*, **401**, 539–545, 2005.

[73] L. Blancafort and A. A. Voityuk. "CASSCF/CAS-PT2 Study of Hole Transfer in Stacked DNA Nucleobases." *J. Phys. Chem. A*, **110**, 6426–6432, 2006.

[74] R. A. Marcus. "Chemical and Electrochemical Electron-Transfer Theory." *Ann. Rev. Phys. Chem.*, **15**, 155–196, 1964.

[75] E. Johansson and S. Larsson. "Electronic Structure and Mechanism for Conductivity in Thiophene Oligomers and Regioregular Polymer." *Synt. Met.*, **144**, 183–191, 2004.

[76] B. Hartenstein and H. Bassler. "Transport Energy for Hopping in a Gaussian Density-of-States Distribution." *J. Non-Cryst. Solids*, **190**, 112–116, 1995.

[77] T. Liu and A. Troisi. "Absolute Rate of Charge Separation and Recombinaiton in a Molecular Model of the P3HT/PCBM Interface." *J. Phys. Chem. C*, **115**, 2406–2415, 2011.

[78] T. Liu, D. L. Cheung, and A. Troisi. "Structural Variability and Dynamics of the P3HT/PCBM Interface and its Effects on the Electronic Structure and the Charge-Transfer Rates in Solar Cells." *Phys. Chem. Chem. Phys.*, **13**, 21461–21470, 2011.

[79] B. M. Medina, A. van Vooren, P. Brocorens, J. Gierschner, M. Shkunov, M. Heeney, I. McCulloch, R. Lazzaroni, and J. Cornil. "Electronic Structure and Charge-Transport Properties of Polythiophene Chains Containing Thienothiophene Units: A Joint Experimental and Theoretical Study." *Chem. Mater.*, **19**, 4949–4956, 2007.

[80] Y.-K. Lan and C.-I. Huang. "Charge Mobility and Transport Behavior in the Ordered and Disordered States of the Regioregular Poly(3-hexylthiophene)." *J. Phys. Chem. B*, **113**, 14555–14564, 2009.

[81] S. Dag and L.-W. Wang. "Packing Structure of Poly(3-hexylthiophene) Crystal: Ab Initio and Molecular Dynamics Studies." *J. Phys. Chem. B*, **114**, 5997–6000, 2010.

[82] S. Cho, K. Lee, J. Yuen, G. Wang, D. Moses, A. J. Heeger, M. Surin, and R. Lazzaroni. "Thermal Annealing-Induced Enhancement of the Field-Effect Mobility of Regioregular Poly(3-hexylthiophene) Films." *J. Appl. Phys.*, **100**, 114503:1–114503:6, 2006.

[83] V. D. Mihailetchi, H. Xie, B. de Boer, J. A. Koster, and P. W. M. Blom. "Charge Transport and Photocurrent Generation in Poly(3-hexylthiophene):Methanofullerene Bulk-Heterojunction Solar Cells." *Adv. Funct. Mater.*, **16**, 699–708, 2006.

[84] R. J. Kline, M. D. McGehee, E. N. Kadnikova, J. Liu, and J. M. J. Fréchet. "Controlling the Field-Effect Mobility of Regioregular Polythiophene by Changing the Molecular Weight." *Adv. Mater.*, **15**, 1519–1522, 2003.

[85] J.-M. Verilhac, R. Pokrop, G. LeBlevennec, I. Kulszewicz-Bajer, K. Buga, M. Zagorska, S. Sadki, and A. Pron. "Molecular Weight Dependent Charge Carrier Mobility in Poly(3,3"-dioctyl-2,2':5',2"-terthiophene)." *J. Phys. Chem. B.*, **110**, 13305–13309, 2006.

[86] J.-F. Chang, J. Clark, N. Zhao, H. Sirringhaus, D. W. Breiby, J. W. Andreasen, M. M. Nielsen, M. Giles, M. Heeney, and I. McCulloch. "Molecular-Weight Dependence of Interchain Polaron Delocalization and Exciton Bandwidth in High-Mobility Conjugated Polymers." *Phys. Rev. B*, **74**, 115318:1–115318:12, 2006.

[87] A. M. Hindeleh and R. Hosemann. "A review Microparacrystals: The Intermediate Stage Between Crystalline and Amorphous." *J. Mater. Sci.*, **26**, 5127–5133, 1991.

[88] J. Rivnay, R. Noriega, R. J. Kline, A. Salleo, and M. F. Toney. "Quantitative Analysis of Lattice Disorder and Crystallite Size in Organic Semiconductor Thin Films." *Phys. Rev. B*, **84**, 045203:1–045203:20, 2011.

[89] C. Poelking, E. Cho, A. Malafeev, V. Ivanov, K. Kremer, C. Risko, J.-L. Brédas, and D. Andrienko. "Characterization of Charge-Carrier Transport in Semicrystalline Polymers: Electronic Couplings, Site Energies and Charge-Carrier Dynamics in Poly(bithiophene-alt-thienothiophene) [PBTTT]." *J. Phys. Chem. C*, **177**, 1633–1640, 2013.

[90] S. Lilliu, T. Agostinelli, E. Pires, M. Hampton, J. Nelson, and J. E. Macdonald. "Dynamic of Crystallization and Disorder During Annealing of P3HT/PCBM Bulk Heterojunctions." *Macromolecules*, **44**, 2725–2734, 2011.

[91] O. G. Reid, J. A. Nekuda Malik, G. Latini, S. Dayal, N. Kopidakis, C. Silva, N. Stingelin, and G. Rumbles. "The Influence of Solid-State Microstructure on the Origin and Yield of Long-Lived Photogenerated Charge in Neat Semiconducting Polymers." *J. of Polym. Sci. Part B Polym. Phys.*, **50**, 27–37, 2012.

[92] S. A. Mollinger, B. A. Krajina, R. Noriega, A. Salleo, and A. J. Spakowitz. "Percolation, Tie-Molecules, and the Microstructural Determinants of Charge Transport in Semicrystalline Conjugated Polymers." *ACS Macro Lett.*, **4**, 708–712, 2015.

Chapter 7

Conclusions and Suggestions for Future Work

7.1 Conclusions

The aim of this thesis was to elucidate the effect of morphological features on organic electronic device operation.

Organic photovoltaic devices are an attractive alternative to their inorganic counterparts due to their comparatively inexpensive manufacturing processes, although the power conversion efficiencies tend to be significantly lower. In order to optimise devices to maximise their efficiencies, it is vital to determine how the morphology of the active layer can affect the charge transport within. This requires a complete understanding of the governing physical processes.

Geminate charge recombination is one such process. By using mesoscale Monte Carlo simulations, the probability density function for charge recombination within OPV devices was shown to exhibit biexponential behaviour, even though only a

single recombination rate was present in the simulations. The presence of two decay transients implied that some geminate charge pairs undergo a fast recombination soon after exciton dissociation, whereas others initially spatially separate a short distance, before collapsing back down again and recombining at later times. This process inspired a modification to the frequently used Onsager-Braun model for recombination to include a quasi-free state, where charges are sufficiently close to be Coulombically bound, but too separated to immediately recombine. The resultant kinetic model fit the recombination dynamics data well, and additionally predicted the correct internal quantum efficiency for that device. However, the predictive qualities of the new theoretical framework were insufficient to fit the MC data when the recombination rate was modified, suggesting that it is difficult to describe the fundamentally dispersive mechanism of hopping transport using KMs which necessarily simplify the system to a small set of physical states and rate coefficients.

An investigation into the impact of hot charge-transfer states on device performance to determine whether they can be the sole precursor to the fast, efficient, free-charge generation observed in some bulk-heterojunction devices was reported. HCTs are formed when an exciton dissociates into a spatially separated electron and hole pair, reducing Coulombic attraction between the two and facilitating more efficient separation. They were shown to improve the device performance in both fully phase-separated, idealised donor:acceptor morphologies similar to those found in all-polymer devices, and in more generalised mixed:aggregate morphologies similar to those found in polymer:fullerene blends. In particular, increased fullerene aggregation was shown to improve the effect of HCTs, largely due to the increased

production of HCT states on the interface of the aggregated acceptor. However, it was also shown that, in order to obtain the free-charge generation efficiencies observed in experiment, unrealistically large HCT separations or slow charge transport kinetics had to be assumed that were not reflected by experimental investigations. HCTs, therefore, are not expected to be the sole precursor to high device efficiencies, but rather a supplementary mechanism that affects short-range charge separation.

A range of simulation techniques were utilised to examine the effects of polymer crystallisation on charge mobility, combining the results of coarse-grained molecular dynamics simulations with quantum chemical calculations and molecular MC. In accordance with experimental results, the zero-field hole mobilities were shown to increase with both increasing annealing temperature and increasing average molecular weight for a range of realistic morphologies with expected polydispersities, thin film densities and without any assumed initial configuration of chains. The annealing temperature trend could be explained by increased crystalline order along the chain backbone and increased proportion of crystals within the morphology at higher temperatures, although, as some experimental investigations have shown, the π-stacking crystalline order is less important. On the other hand, there was no obvious trend between the mobility and the backbone order, π-stacking order or crystal proportion. Instead, it was found that, as the average molecular weight of the sample increased, the average number of crystals that each chain belonged to also increased, resulting in a greater quantity of better connected crystals. Longer chains therefore act as tie chains within the morphology, while the short chains in a sample restrict charge transport because they belong to fewer crystals. This hy-

pothesis was reinforced when low and high molecular weight samples were mixed, which forced more tie chains to form, improving the mobility to at least that of an unmixed distribution of comparable molecular weight. Therefore, a high polydispersity is not necessarily detrimental to charge transport within the active layer, as the presence of tie-chains appears to be the main contributor to the molecular weight dependence of the mobility.

7.2 Suggestions for Future Work

7.2.1 Molecular Dynamics for Alternative Materials

The techniques outlined in chapter 6 were trialled on a test system of P3HT, which is one of the most widely studied polymers used in organic electronics. However, the techniques are not limited to this system. Given a calibrated forcefield, it would be relatively straightforward to simulate a wide variety of alternative polymers and complete the same analysis. Of particular interest would be the high-efficiency fluoropolymers used in the most efficient OPV devices such as PTB7[1,2]. The technique could even be applied to small molecules and fullerene derivatives - or indeed any single-phase material - as long as the degree of delocalisation of the charges is known for the material that is to be simulated. This is potentially not limited to organic materials, and applications of this method could be useful to the recent discussions of perovskite crystals as a new material to improve photovoltaic efficiency.

7.2.2 Mixed Phase and Heterojunction Molecular Dynamics Simulations

Beyond a single phase, it should also be possible to simulate blend morphologies using the methods in chapter 6, at least to a certain extent. Molecules could be distributed randomly around the simulation volume in order to effectively model the mixed phase, and it could even be possible to model a donor:acceptor heterojunction, although this would likely be difficult to achieve without assuming an initial orientation or configuration for the molecules. A significant challenge here would be the calibration of an appropriate forcefield, which gets more complex as the interactions between additional coarse-grained site types are included.

7.2.3 Incorporation of Polymer Crystallisation into Full Device Simulations

The molecular MC simulations used in chapter 6 could also be combined with the mesoscale code used in chapters 4 and 5 in order to determine the effects of nanoscale molecular structure on the bulk device performance. It would be challenging to scale up the MD simulations to model an entire active layer, so perhaps it would be possible to model small regions with certain phase behaviour - *i.e.* obtain average behaviour for regions containing aggregated/amorphous acceptor, crystallised/amorphous donor, or a molecularly mixed phase. The relative charge transport characteristics of each could then be implemented by use of a mobility factor or energetic variation for a carrier moving through a comparable region of the Cahn-Hilliard morphology.

References

[1] C. Brabec, V. Dyakonov, and U. Scherf. *Organic Photovoltaics: Materials, Device Physics and Manufacturing Technologies*. Wiley-VCH, 2010.

[2] K. R. Graham, C. Cabanetos, J. P. Jahnke, M. N. Idso, A. El Labban, G. O. N. Ndjawa, T. Heumueller, K. Vandewal, A. Salleo, B. F. Chmelka, A. Amassian, P. M. Beaujuge, and M. D. McGehee. "Importance of the Donor:Fullerene Intermolecular Arrangement for High-Efficiency Organic Photovoltaics." *J. Am. Chem. Soc.*, **136**, 9608–9618, 2014.

Appendix A

Coarse-Grained Forcefield

A.1 Coarse-Grained Site Interactions

Interactions between each site were characterised by a number of potential energy functions that described all the possible inter- and intra-molecular combinations of the sites. The intra-molecular potential energy functions are given in equations 1.1.1-1.1.4.

$$U_{\text{bond}}(l) = \sum_{i=2}^{4} c_i (l - l_0)^i, \tag{1.1.1}$$

$$U_{\text{angle}}(\theta) = \sum_{i=2}^{4} c_i (\theta - \theta_0)^i, \tag{1.1.2}$$

$$U_{\text{dihedral}}(\phi) = \sum_{i=0}^{4} c_i \cos^i(\phi), \tag{1.1.3}$$

$$U_{\text{improper}}(\zeta) = 45.3281\zeta^2, \tag{1.1.4}$$

where l is the physical separation of the two bonded sites, θ is the angle between the two in-plane vectors describing the three connected sites and ϕ is the dihedral angle between the two planes that describe all 4 linked sites. Pictorial representa-

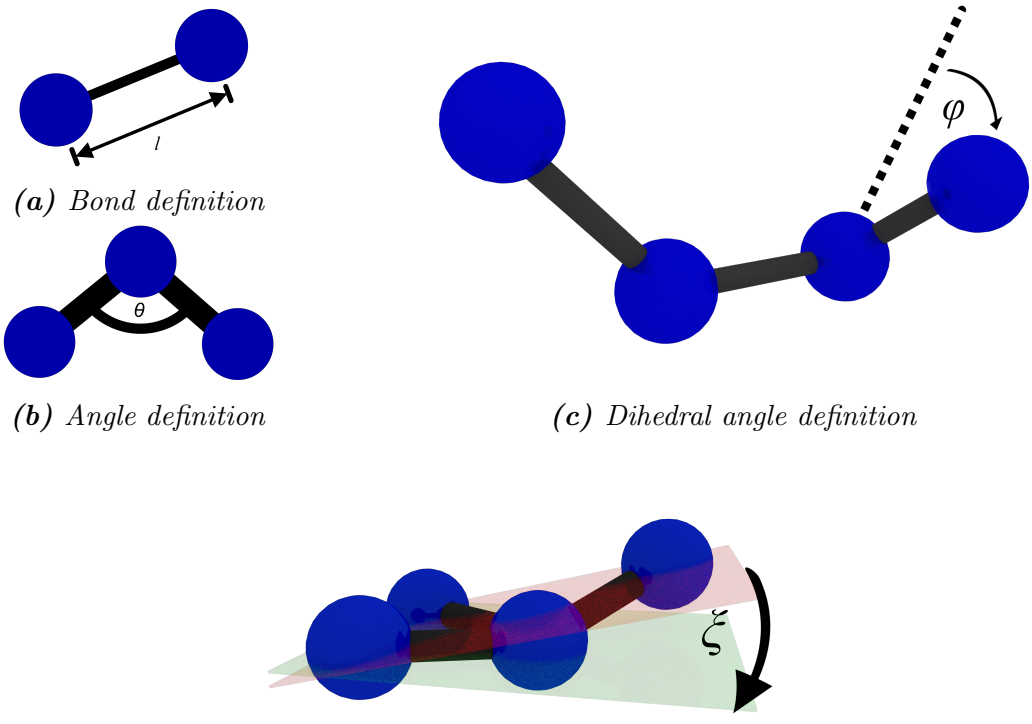

(a) Bond definition

(b) Angle definition

(c) Dihedral angle definition

(d) Improper dihedral angle definition

Figure A.1: *Definitions of each forcefield descriptor used in the polymer investigation.*

tions of each force-field descriptor are given in figure A.1, along with their defining arguments.

In the forcefield, c_i, l_0 and θ_0 are free parameters that were varied iteratively to best fit the probability distributions for each potential in an accurate, atomistic simulation model[1–3]. The values of the free-parameters used in this investigation are given in tables A.2-A.3. Note that due to P3HT chain directionality, the P1-P1-P2 and P2-P1-P1 angle potentials differ and so were parametrised separately, as with the P1-P1-P2-P3 and P3-P2-P1-P1 dihedrals. Additionally, there is no need to define a P1-P1-P1-P2 dihedral as the P2 site is kept in the plane of the closest 3

P1 sites by the sole P1-P2-P1-P1 improper dihedral potential instead.

Parameter	P1-P1	P1-P2	P2-P3
l_0(Å)	3.8817	4.0773	3.8297
c_2 (kcal/mol/Å^2)	58.2280	56.4094	44.6180
c_3 (kcal/mol/Å^3)	0	175.5560	278.2030
c_4 (kcal/mol/Å^4)	0	148.7330	436.2700

Table A.1: *Coefficients for the coarse-grained description of the bond length potentials in P3HT,* $U_{bond}(l) = \sum_{i=2}^{4} c_i (l - l_0)^i$.

Parameter	P1-P1-P1	P1-P2-P3	P1-P1-P2	P2-P1-P1
$\theta_0(deg.)$	166.7460	158.0860	129.0940	76.2600
c_2 (kcal/mol/Å^2)	26.5042	12.3621	2.7338	22.9487
c_3 (kcal/mol/Å^3)	109.8370	16.5460	17.5095	-6.7598
c_4 (kcal/mol/Å^4)	148.8830	6.9452	73.6114	0.4978

Table A.2: *Coefficients for the coarse-grained description of the bond angle potentials in P3HT,* $U_{angle}(\theta) = \sum_{i=2}^{4} c_i (\theta - \theta_0)^i$.

Parameter	P1-P1-P1-P1	P2-P1-P1-P2	P1-P1-P2-P3	P3-P2-P1-P1
c_0 (kcal/mol)	0.6403	1.4924	0.1583	0.0090
c_1 (kcal/mol/Å)	0.3851	0.2473	-0.5142	0.1154
c_2 (kcal/mol/Å^2)	0.1643	-2.1492	0.2498	0.3792
c_3 (kcal/mol/Å^3)	-0.7109	0.1257	0.3353	0.0405
c_4 (kcal/mol/Å^4)	-0.4787	1.0298	-0.0729	-0.0753

Table A.3: *Coefficients for the coarse-grained description of the proper dihedral angle potentials in P3HT,* $U_{angle}(\phi) = \sum_{i=0}^{4} c_i \cos^i(\phi)$.

In addition to the intra-molecular interaction potentials, the non-bonded interactions between molecules were also considered as a 9/6 Lennard-Jones potential, with a maximum interaction cut-off of 15 Å:

$$U_{\text{non-bonded}}(r) = \begin{cases} 4\epsilon \left[\left(\frac{\sigma}{r}\right)^9 - \left(\frac{\sigma}{r}\right)^6 \right] & \text{if } r \leq 15\,\text{Å} \\ 0, & \text{if } r > 15\,\text{Å} \end{cases} \tag{1.1.5}$$

where r is the physical separation between the non-bonded site pair and ϵ, σ are the two free parameters, calibrated according to the values in table A.4.

Parameter	P1, P1	P1, P2	P1, P3	P2, P2	P2, P3	P3, P3
ϵ (kcal/mol)	0.3500	1.4500	0.5100	1.5700	0.9000	0.5500
σ (Å)	4.6000	4.3000	4.7100	4.7000	4.8000	4.8900

Table A.4: *Coefficients for the coarse-grained description of the non-bonded sites in P3HT, separated by $r \leq 15\,Å$, $U_{non\text{-}bonded}(r) = 4\epsilon\left[\left(\frac{\sigma}{r}\right)^9 - \left(\frac{\sigma}{r}\right)^6\right]$.*

A.2 Fitting to Atomistic Forcefield

The atomistic model for P3HT that the CG forcefield was calibrated to was derived from a model of tetrathiophene[4], based on parameters from the widely used OPLS-AA forcefield[5], while using atomic partial charges from density functional theory (DFT) calculations[6]. The tetrathiophene model was then modified to include an OPLS-AA hexyl side-chain, and an inter-monomer torsional potential derived from the DFT calculations of methylthiophene oligomers[7]. This resulted in an atomistic P3HT forcefield that was expected to have good agreement with the experimental properties of crystal structure and heat of sublimation[4], while providing excellent agreement with the monomer density under ambient conditions[6], as well as the thermodynamic and nanoscale structural properties of solution-phase P3HT predicted by experiment[6,8].

The parameters for the CG forcefield were optimised to match the structural distribution functions from constant temperature and pressure (NPT) for atomistic simulations of 72 regioregular P3HT decamers heated to 550 K at a pressure of 1 atm.

This ensured that the polymer chains described a melt, ensuring that the spherically symmetric non-bonded pair interactions (equation 1.1.5) were isotropic[3]. All simulations were carried out using a modified version of the LAMMPS simulation package[9]. Constant temperature and pressure were maintained using a Nosé-Hoover thermostat and barostat[10], with carbon-hydrogen bond lengths constrained using the SHAKE algorithm[11] and long-range electrostatic interactions calculated through the use of the particle-particle-mesh method[12]. The atomistic simulations ran for 30 ns with a timestep of 2 fs. To ensure that the system was in thermodynamic equilibrium, the first 5 ns of simulation data was discarded, and statistical averaging performed on the remaining dataset. The coarse-grained simulations were performed a constant temperature (NVT) at the same average density, and proceeded for 8 ns with a 8 fs timestep, with the first half of the dataset discarded before statistical averaging took place. Additionally, the chain-ends of the oligomers were omitted for the distribution function calculations for simplicity.

It is important to note that the non-bonded coarse-grained interaction parameters from equation 1.1.5 and table A.4 do not describe a unique solution. Therefore, to ensure that the coarse-grained model was dynamically consistent with the atomistic representation, the interaction strength parameter, ϵ, was scaled for all interaction pairs such that the average pressure was 1 atm - the same as the atomistic simulation. This had minimal impact on the pair distribution function, while increasing the accuracy of the coarse-grained interaction parameters compared to the atomistic model.

After parameter optimisation was complete, a final NPT coarse-grained simula-

tion was executed for 16 ns at 550 K and 1 atm in order to compare the probability distributions of bond lengths, angles, proper and improper dihedral angles and non-bonded pair interactions to the atomistic representation. The results are shown in figures A.2 and A.3a.

Although the coarse-grained parameters highlighted here were derived for a single thermodynamic state (550 K and 1 atm), the model is robust enough to accurately predict the atomistic model behaviour under different conditions - making it ideally suited to exploring the effects of different annealing processes on the thin film morphology. To this end, further atomistic NPT simulations were run for 72 P3HT decamers at 450 K, 500 K and 600 K, along with equivalent coarse-grained simulations. The CG model reported average densities within 3% of those obtained by the atomistic model over this temperature range, as well as reproducing the non-bonded pair distribution functions of the atomistic model very well (figure A.3b).

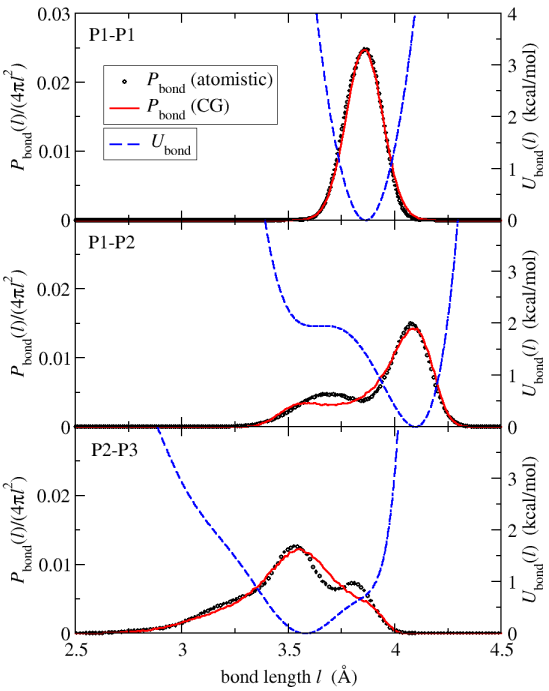

(a) Bond lengths

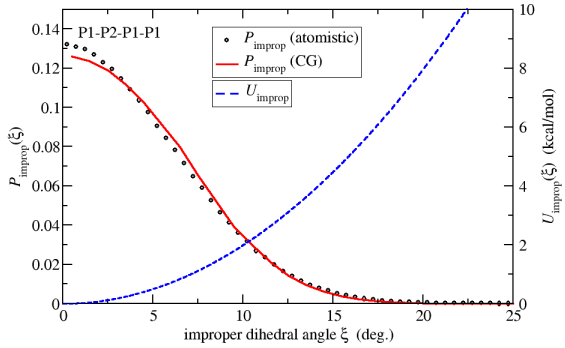

(b) Improper dihedral angles

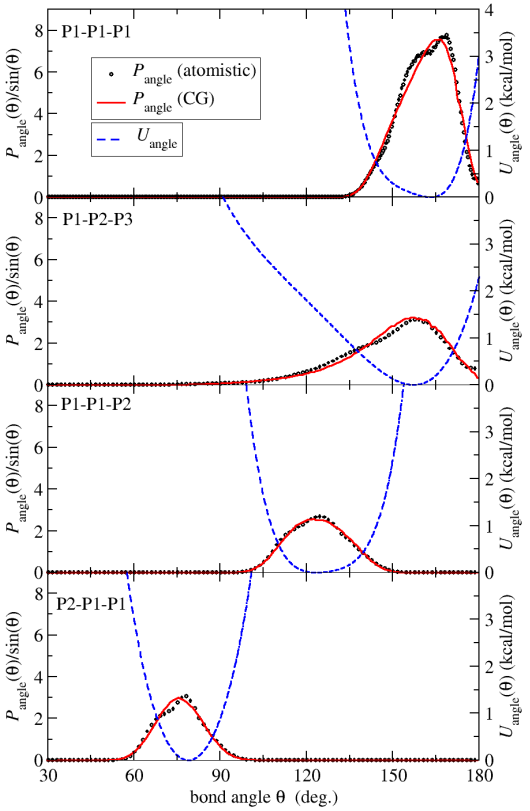

(c) Bond angles

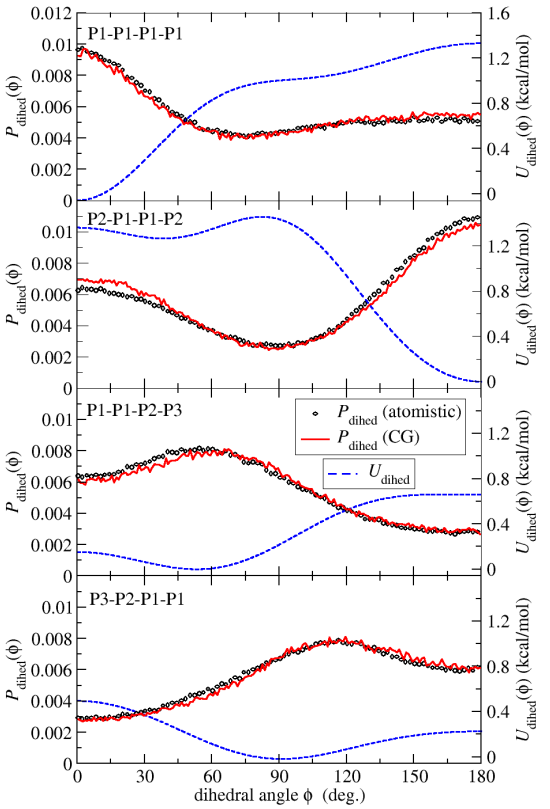

(d) Proper dihedral angles

Figure A.2: *Comparisons of the intra-chain interaction probability distributions for atomistic NPT simulations of 72 P3HT decamers at 550 K and 1 atm and an equivalent, optimised coarse-grained model.*

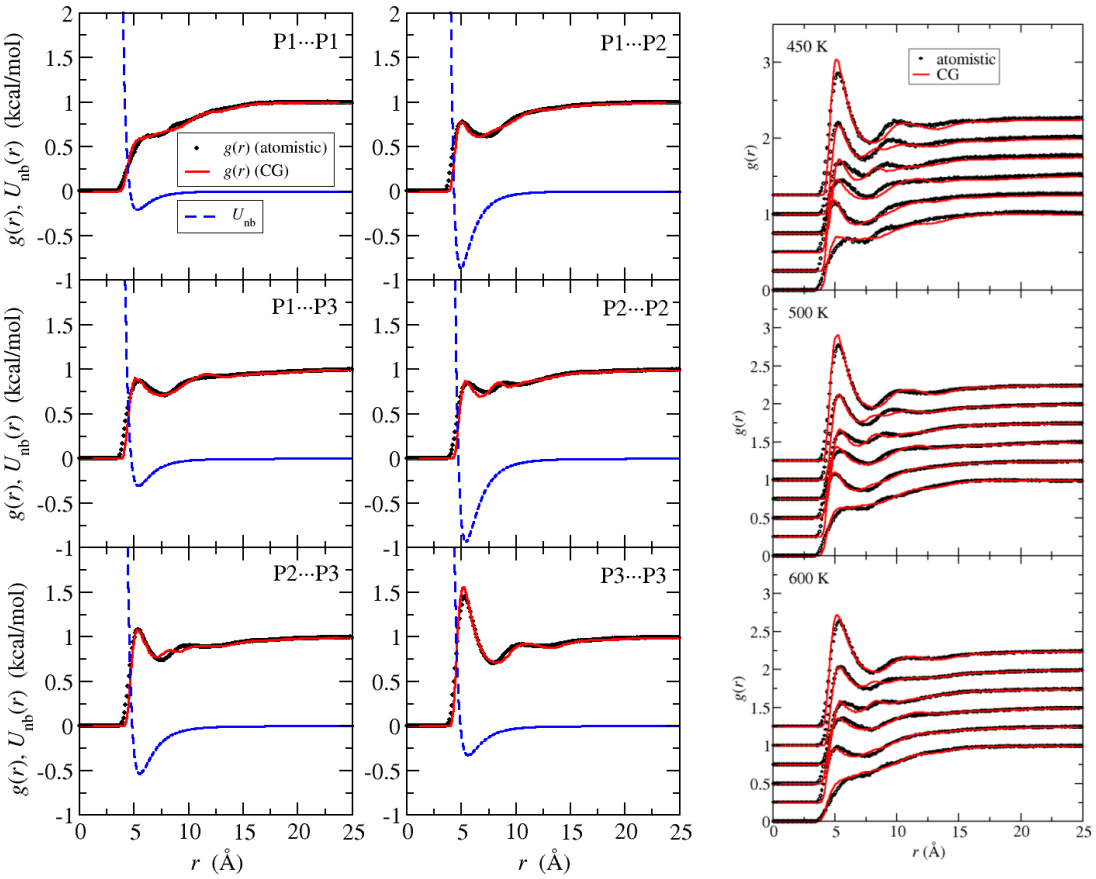

(a) *Fiducial simulation (550 K)*

(b) *Predictions with varying temperature*

Figure A.3: *Comparisons of the inter-chain, non-bonded radial distribution functions for atomistic NPT simulations of 72 P3HT decamers at 1 atm and equivalent, optimised coarse-grained models.*

References

[1] D. Reith, M. Pütz, and F. Müller-Plathe. "Deriving Effective Mesoscale Potentials from Atomistic Simulations." *J. Comput. Chem.*, **24**, 1624–1636, 2003.

[2] R. Faller and D. Reith. "Properties of poly(isoprene): Model Building in the Melt and in Solution." *Macromolecules*, **36**, 5406–5414, 2003.

[3] D. M. Huang, R. Faller, K. Do, and A. J. Moulé. "Coarse-Grained Computer Simulations of Polymer/Fullerene Bulk Heterojunctions for Organic Photovoltaic Applications." *J. Chem. Theory Comput.*, **6**, 526–537, 2010.

[4] V. Marcon and G. Raos. "Free Energies of Molecular Crystal Surfaces by Computer Simulation: Application to Tetrathiophene." *J. Am. Chem. Soc.*, **128**, 1408–1409, 2006.

[5] W. L. Jorgensen, D. S. Maxwell, and J. Tirado-Rives. "Development and Testing of the OPLS All-Atom Force Field on Conformational Energetics and Properties of Organic Liquids." *J. Am. Chem. Soc.*, **118**, 11225–11236, 1996.

[6] K. N. Schwarz, T. W. Kee, and D. M. Huang. "Coarse-Grained Simulations of the Solution-Phase Self-Assembly of poly(3-hexylthiophene) Nanostructures." *Nanoscale*, **5**, 2017–2027, 2013.

[7] S. B. Darling and M. Sternberg. "Importance of Side Chains and Backbone Length in Defect Modeling of Poly(3-alkylthiophenes)." *J. Phys. Chem. B*, **113**, 6215–6218, 2009.

[8] P. C. Tapping, S. N. Clafton, K. N. Schwarz, T. W. Kee, and D. M. Huang. "Molecular-Level Details of Morphology-Dependent Exciton Migration in Poly(3-hexylthiophene) Nanostructures." *J. Phys. Chem. C*, **119**, 7047–7059, 2015.

[9] S. J. Plimpton. "Fast Parallel Algorithms for Short-Range Molecular Dynamics." *J. Comput. Phys.*, **117**, 1–19, 1995.

[10] W. Shinoda, M. Shiga, and M. Mikami. "Rapid Estimation of Elastic Constants by Molecular Dynamics Simulation Under Constant Stress." *Phys. Rev. B*, **69**, 134103:1–134103:8, 2004.

[11] J. P. Ryckaert, G. Ciccotti, and H. J. C. Berendsen. "Numerical Integration of the Cartesian Equations of Motion of a System with Constraints: Molecular Dynamics of *n*-alkanes." *J. Comput. Phys.*, **23**, 327–341, 1977.

[12] R. W. Hockney and J. W. Eastwood. *Computer Simulation Using Particles*. Taylor & Francis, Bristol, 1988.